INFORMATION TO USERS

The Physics and Chemistry of Metal Oxide Composites
as Anode Materials for Lithium-Ion Batteries

by

Ian Anthony Courtney

B.Sc., The Royal Military College of Canada, Kingston, Ontario, Canada, 1992

M.Sc., Dalhousie University, Halifax, Nova Scotia, Canada, 1997

Submitted in partial fulfillment of the requirements

for the degree of Doctor of Philosophy

in the Department of Physics

Dalhousie University

Halifax, Nova Scotia, Canada

February 1999

The author has granted a non-exclusive licence allowing the National Library of Canada to reproduce, loan, distribute or sell copies of this thesis in microform, paper or electronic formats.

The author retains ownership of the copyright in this thesis. Neither the thesis nor substantial extracts from it may be printed or otherwise reproduced without the author's permission.

L'auteur a accordé une licence non exclusive permettant à la Bibliothèque nationale du Canada de reproduire, prêter, distribuer ou vendre des copies de cette thèse sous la forme de microfiche/film, de reproduction sur papier ou sur format électronique.

L'auteur conserve la propriété du droit d'auteur qui protège cette thèse. Ni la thèse ni des extraits substantiels de celle-ci ne doivent être imprimés ou autrement reproduits sans son autorisation.

Canada

DALHOUSIE UNIVERSITY

FACULTY OF GRADUATE STUDIES

The undersigned hereby certify that they have read and recommend to the Faculty of

Graduate Studies for acceptance a thesis entitled "The Physics and Chemistry of Metal

Oxide Composites as Anode Materials for Lithium-Ion Batteries"

by   Ian Anthony Courtney

in partial fulfillment of the requirements for the degree of Doctor of Philosophy.

Dated: _____ February 18, 1999 _____

External Examiner

Research Supervisor

Examining Committee

ii
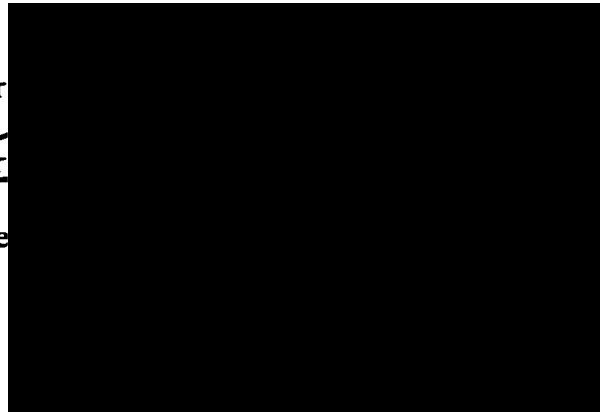
DALHOUSIE UNIVERSITY

DATE: 18 February 1999
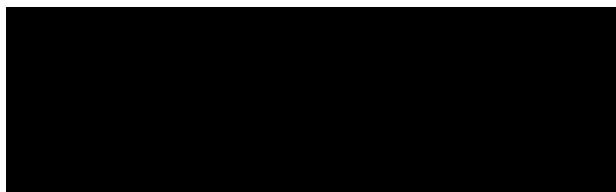
AUTHOR: _____ Ian Anthony Courtney _____

TITLE: _____ The Physics and Chemistry of Metal Oxide Composites as _____
_____ Anode Materials for Lithium-Ion Batteries _____

DEPARTMENT OR SCHOOL: _____ Physics _____

DEGREE: ____ PhD ____ CONVOCATION: ____ May ____ YEAR: ____ 1999 ____

Permission is herewith granted to Dalhousie University to circulate and have copies for non-commercial purposes, at its discretion, the above title upon the requests of individuals or institutions.

Signature of Author

Dedication

For my wife, Debbie, and our children, Micheal and Hannah.

I love you all very much.

Table of Contents

List of figures

List of Tables

Abstract

Tin oxide composite (SnO:X, X = $(B_2O_3)_x(P_2O_5)_y$, SiO_2) glasses represent a new class of material for the anode of lithium-ion rechargeable cells. These materials demonstrate discharge capacities on the order of 1000 mAh/(g Sn), which is consistent with the alloying limit of 4.4 Li atoms per Sn atom. These materials also demonstrate significant irreversible capacities, which is proportional to the oxygen content (i.e O in SnO:X). It is shown (by electrochemical data, in-situ x-ray diffraction studies and in-situ Mössabuer effect studies) that during the first discharge, the oxygen intimately bonded to Sn reacts with lithium to give Li_2O, leaving small clusters of metallic Sn that subsequently alloy with lithium. The Li_2O and X atoms (collectively known as 'Spectator Atoms') are inert to lithium. The subsequent cycling, or reversibility, of these materials is linked to the size of the Sn clusters that form during the first discharge. Those materials with high spectator atom count (as in SnO:$(B_2O_3)_{0.5}(P_2O_5)_{0.5}$ glass) produce smaller Sn clusters during first discharge than those materials with low spectator atom count (as in SnO:$(B_2O_3)_{0.1}(P_2O_5)_{0.1}$ glass). Furthermore, it is observed that these Sn clusters grow in size by the repeated discharge and charge of the cell. This explains the capacity loss in these types of materials after many cycles. The size of the Sn clusters reach a steady state size, and a speculative model that links the steady state cluster size to the number of spectator atoms is proposed. The rate of aggregation of Sn clusters can be controlled by several factors: the voltage range chosen for discharge and charge, the number of spectator atoms in the matrix, and the temperature. Studies of other alloying metal oxide composites (i.e PbO:X and Sb_2O_3:X) are also presented. These materials follow a similar reaction mechanism as SnO:X composites do, but the rate of aggregation of the alloying metal differs between all three.

List of Symbols and Abbreviations used

a, b, c, α, β, and γ – Lattice constants

a_i, b_i and c ($i = 1, 4$) – Atomic form factor coefficients

B – Applied magnetic field

BCC – Body centered cubic

c – Speed of light in vacuum

CS – Center shift

CCP – Cubic close packed

d – Plane spacing

DSC – Differential scanning calorimetry

e – Magnitude of charge on the electron

EC – Ethylene carbonate

E_R – Recoil energy

E_D – Doppler effect energy

E_γ – Energy of gamma-ray photon

E – Energy

ΔE – Change in energy

DEC – Diethyl carbonate

f – Recoil free fraction

f_n – Atomic form factor of the nth atom

F – Geometrical structure factor

FWHM – Full width at half maximum intensity

ΔG – Change in Gibb's free energy

G_f^o – Standard Gibb's free energy of formation

h, k, and l – Miller indices

h – Thickness of a layer of atoms on crystallite surface

ℏ – Planck's constant divided by 2π

I – Total scattered intensity

i – Current

IS – Isomer shift

k_B – Boltzman constant

L – Grain size in Scherrer equation

m – Electrode active mass

M - Magnetization

ME – Mössbauer effect

Me – Alloying metal

NMP – N-methyl pyrrolidinone

PDF – Powder diffraction file (PDF-2, JCPDS – ICCDD, © 1993)

PVDF – Polyvinylidene flouride

p – Probability

ΔP – Change in pressure

q - Capacity

RF – Radio frequency

RFF – Recoil free fraction

SCP – Simple cubic packing

SOD – Second order doppler shift

ΔS – Change in entropy

t - Time

T – Temperature

T_m – Melting temperature

UHP – Ultra high pure

v – Doppler shift velocity

V – Voltage

ΔV – Change in volume

$x(n)$, $y(n)$ and $z(n)$ – Atomic coordinates of nth atom

Δx – change in number of lithium

XRD – X-ray diffraction

ZBH – Zero background holder

α - Ratio of the mean atomic displacements of surface atoms to bulk atoms

$\langle x^2 \rangle$ - mean atomic displacement squared

$\langle v^2 \rangle$ - mean squared lattice vibrational velocity

Θ_D – Debye Temperature

χ_T – Isothermal magnetic susceptibility

θ - Bragg angle

2θ - Scattering angle

s – Scattered x-ray vector

s_o – Incident x-ray vector

r_{mn} – Vector between m^{th} and n^{th} atom in Debye scattering formalism

μ - Chemical potential

λ - Wavelength

Acknowledgements

Chapter 1

Introduction

1.1 Scope

Materials research brings together different divisions of science, setting common goals for physicists, chemists, engineers, and biologists. Materials scientists strive to produce materials with useful properties. Materials for pharmaceuticals, biomedical engineering, genetic engineering, semiconductor device technology and battery technology are examples. The process of materials development must be based on sound scientific progression, otherwise one would require either extreme luck or infinite resources. The periodic table is, after all, a large place.

This thesis is a study of a new class of materials and an investigation of how to manipulate their characteristics.

1.2 Portable energy storage

Our society, apparently, has a need for mobility. We desire transportation, portable communications and 'stand-alone' computer and electronics devices. These devices need energy to operate. One method by which to provide portable energy is to store the energy in a battery. The use of rechargeable, or secondary, batteries is a means to efficiently store energy because these batteries can be discharged and charged many times while delivering the same energy during each discharge cycle.

1

1.3 Lithium ion cells

The electrochemical cell is not a new concept. In 1800 Volta, although unbeknownst to him at the time, invented the first primary, or non-rechargeable, battery. Battery technology has progressed since then, and there are now batteries that can deliver greater charge per unit time, per unit weight and per unit volume.

The *discharge capacity*, quoted in amp-hours, of a battery is equal to the amount of charge that can be delivered during discharge. The *voltage* at which this charge is delivered defines the *energy* of the battery. *Specific energy* and *energy density* are quantities that measure the energy per unit mass (Watt-hours per kilogram) and energy per unit volume (Watt-hours per liter), respectively, of a battery. The *reversibility* of a rechargeable battery is the ratio of subsequent discharge capacities to the first discharge capacity. Reversibility is usually quoted in terms of *cycle life*, which is typically the number of cycles at which the discharge capacity has deteriorated to 80% of the first discharge capacity. The lithium ion battery currently leads its competitors by these conventional methods of comparison.

1.3.1 A comparison of current technologies

Butler and Klassen (1995) compare various advanced rechargeable battery systems. Table 1-1 is a summary of the most relevant systems and methods of comparison. If we exclude those systems that have poor cycle life, contain hazardous materials, operate at high temperatures and are high cost, then we are left with nickel-metal hydride and lithium ion. Lithium ion outperforms the former in both cycle life and specific energy. Lithium ion is not, however, without its disadvantages. An important potential disadvantage of lithium ion is safety. Lithium metal, or lithium-containing carbon, is reactive, and in certain situations can

lead to the 'self-heating' and ignition of cell components. The safety of lithium ion is an important issue, particularly in larger batteries such as those that would power an electric vehicle, for instance. Several research groups are conducting fundamental safety studies on

Table 1-1 A comparison of several advanced rechargeable battery systems

Technology	Voltage (V)	Specific Energy (Wh/kg)	Energy Density (Wh/L)	Cycle Life [c]	Comments
Lead-acid	1.98	35	80	800	Environmental concerns [a]
Nickel-Cadmium	1.20	50	100	1000	Environmental concerns [a] and high cost
Nickel-metal hydride	1.20	80	300	500	
Zinc / silver oxide	1.55	90	180	50	High cost
Zinc / air	1.1	150	160	400 hrs	Low cycle life
Lithium-aluminum / iron disulfide	1.68	180	350	1000	High operating temperature (450 °C) [b]
C / $LiCoO_2$ (lithium ion)	3.6	135	320	1200	Safety concerns

[a] The environmental concerns are to do with the disposal of and the toxicity of lead and cadmium.
[b] A high operating temperature battery would not be very practical in a laptop computer or cellular phone.
[c] The cycle number at which the capacity is 80% of the initial capacity.

lithium ion battery materials (e.g., Richard and Dahn, 1998, and references therein).

1.3.2 The lithium ion electrochemical cell

Figure 1-1(a) is a schematic of a lithium ion cell during discharge. The present day commercial lithium ion cell incorporates a carbon anode, typically graphite, versus a lithium transition metal oxide cathode, such as $LiCoO_2$ (Hossain, 1995). The two electrodes are immersed in a non-aqueous electrolyte containing a dissolved lithium salt (e.g. $LiPF_6$). The electrolyte solvent is an organic liquid or mixture of several, such as ethylene carbonate (EC)

Figure 1-1(a) Schematic of a lithium ion cell (during discharge)
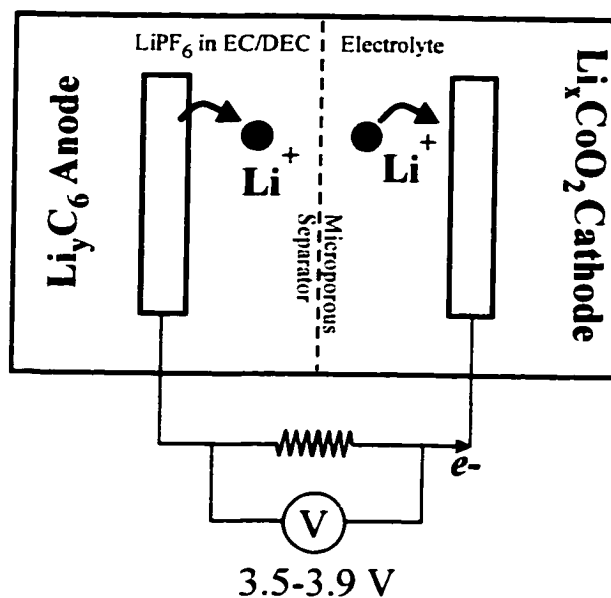
and di-ethyl carbonate (DEC). The discharge half-cell reactions for this cell are given in equations 1-1 and 1-2.

$$Li_yC_6 \rightarrow C_6 + yLi^+ + ye^-$$

Anode reaction (1-1)

$$Li_{1-x}CoO_2 + yLi^+ + ye^- \rightarrow Li_{1-x+y}CoO_2$$

Cathode reaction (1-2)
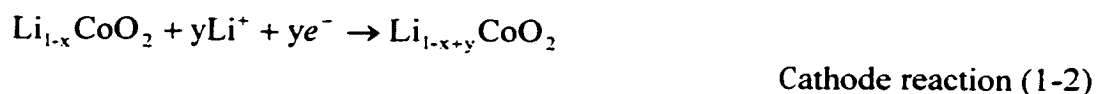
In a lithium ion cell, those electrode materials that have a high binding energy for lithium, such as $LiCoO_2$, are referred to as cathode materials, and those materials that have low binding energy for lithium, such as graphite, are called anode materials.

In all experiments reported in this work, however, cells with a lithium metal anode (not lithium ion cells) are used. Then the variation of the *voltage profile* (voltage versus specific capacity graph) of a material can be attributed to that material alone, and not to a combination of both electrode materials. A lithium metal anode is discharged and charged versus the cathode material under investigation. A schematic of a cell with a lithium anode

and a carbon cathode is shown in figure 1.1(b).

Figure 1-1(b) Schematic of a lithium/graphite cell (during discharge)
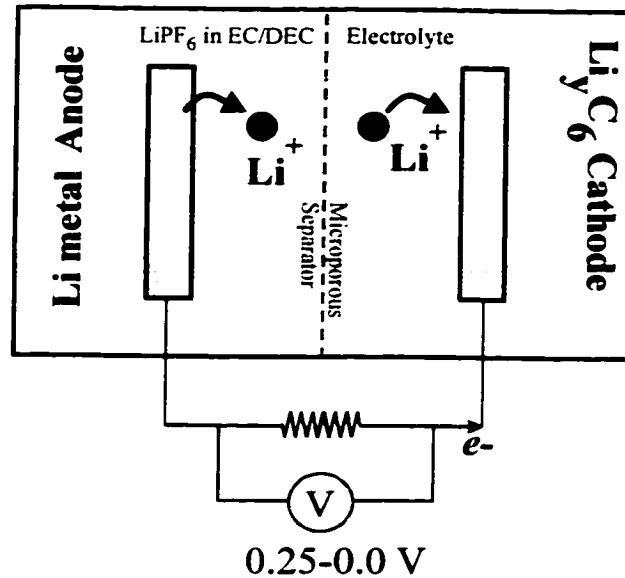
1.3.3 Desirable characteristics of electrode materials

Graphite and $LiCoO_2$ are not the only choices for the electrode materials of a lithium ion cell. Many other materials have been investigated. Figure 1-2, a lithium binding energy diagram for lithium containing compounds (Dahn et al., 1991), shows some of the key ones.

There are several characteristics that are used to compare electrode materials, such as, but not limited to, the average voltage over which the material reacts with lithium, the capacity of the electrode, and the reversibility of the electrode. The reversibilities of electrode materials will be referred to often in the chapters to follow.

Under ambient conditions one mole of graphite reacts with $1/6^{th}$ moles of lithium (Herold, 1955). Therefore, the capacity of the following reaction,

$$6C + Li^+ + e^- \rightarrow LiC_6$$

<div align="right">(1-3)</div>

results from transferring one mole of Li^+ from anode to cathode, and one mole of charge through the external circuit. Equation 1-4 shows how to calculate the theoretical specific capacity of graphite.

$$\text{specific capacity (graphite)} = \frac{96500 \frac{A \cdot s}{mol}}{3.6 \times 10^3 s \cdot h^{-1} \times 12.011 g \cdot mol^{-1} \times 6} = 372 mAh/g$$

<div align="right">(1-4)</div>

The theoretical volumetric capacity of graphite, which is based on the density of graphite (2.2g/ml, Wyckoff, 1982), is 800Ah/L. The specific and volumetric capacities of graphite are the benchmark comparison for all new anode materials. We attempt to maximize capacity when developing new electrode materials.

Figure 1-2 Lithium binding energy diagram for various compounds, quoted relative to lithium metal.

The lithium in the compounds in the air stable region will not react with the components of air.
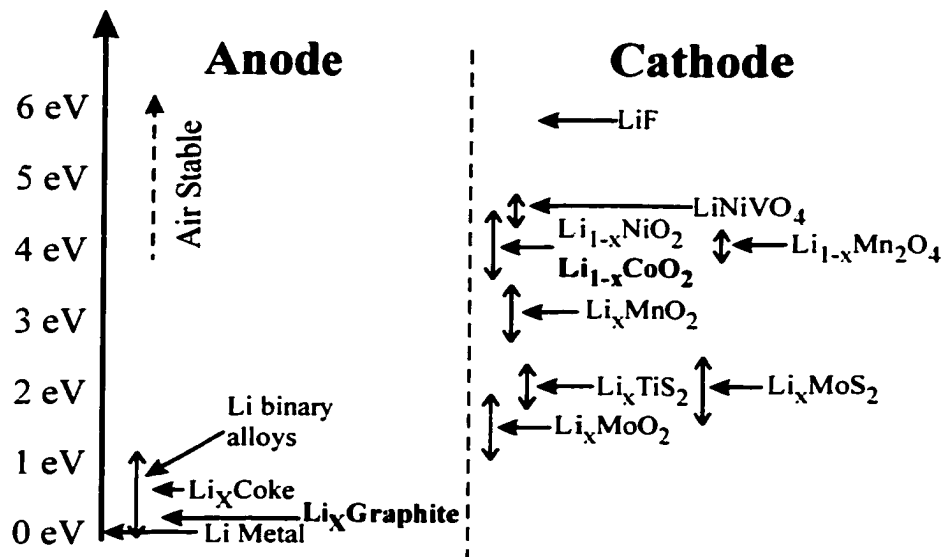
The voltage of a particular anode-cathode pair is derived in terms of the chemical potentials of lithium in the two materials. The voltage is then given by (McKinnon, 1995),

$$V = -\frac{(\mu_{cathode} - \mu_{anode})}{e}$$

(1-5)

where e is the magnitude of the charge on an electron. The chemical potentials vary with lithium composition, since different amounts of lithium in a host result in different chemical potentials for lithium in that host (McKinnon, 1995). Section 2.2 contains the results of an ab-initio calculation of the lithium-tin voltage profile. That section develops further the ideas of energy, chemical potential and voltage.

Estimates of the potential difference between various anode-cathode pairs can be made from figure 1-2. The voltage of a C-LiCoO$_2$ cell will be between 3.5 and 4.2 V. Desirable cathode materials, therefore, will have high binding energies for lithium and anode materials will have low binding energies for lithium. So why not use LiF as a cathode material? After all, its potential for lithium is the largest on figure 1-2, at around 5.8 V. If the cathode is at a potential (relative to lithium metal) greater than about 4.5V, based on current technology, then various side-reactions will occur in the electrolyte. These side-reactions will result in poor performance of the cell. LiF does not react reversibly with Li, which is another reason why it is not suitable.

In summary, there are three key factors, notwithstanding other issues such as safety, price and toxicity, which determine the suitability of a particular electrode material. The remainder of this thesis will focus on anode materials, so the factors to consider are, high capacity, low voltage in reference to lithium metal and good reversibility as lithium is

inserted and removed from the material.

1.4 Anode materials for lithium ion cells

Over the past 20 years, research into the anode materials used in lithium metal and lithium ion batteries has focussed on lithium metal, lithium binary alloys, carbon in various forms and, more recently, tin oxide composites. The best choice of anode material to date is graphitic carbon, which is used in almost all commercially available cells on the market.

1.4.1 Lithium metal

The obvious choice for an anode material in a lithium battery is lithium metal. It has zero voltage versus lithium metal and has a very large capacity (3860 mAh/g, Fauteaux and Koksbang, 1993). In fact, one of the first commercial rechargeable lithium systems was the Li metal anode versus MoS_2 cathode cell (Hossain, 1995). However, this use of lithium metal as the anode material was flawed. When lithium electroplates during a charge it tends to form dendrites that can grow to the extent that the separator is pierced, which can subsequently lead to a short. The dentrite formation can also result in poor cycle life. The tendency of the lithium metal to plate in structures of large surface area creates a situation where the lithium becomes very reactive. The heat associated with an internal short coupled with the increased heat produced by a larger and more reactive surface can result in a runaway exothermic reaction. Ultimately, this can lead to the ignition of the cell's components.

1.4.2 Carbon

The safety problems associated with using metallic lithium as an anode material prompted researchers to consider alternatives. Graphitic carbon is an *intercalation* material for lithium. This means that lithium can be inserted and removed from graphite without causing a significant change in the host structure (McKinnon, 1995). Intercalation materials are well suited as electrode materials for rechargeable batteries; a host structure that does not change implies good reversibility.

Figure 1-3 Schematic of the structure of graphite. (a) One graphene sheet showing honeycomb arrangement of carbon atoms, (b) ABABAB stacking of 2H graphite, (c) Lithium intercalated between graphene sheets, and (d) Lithium in relation to the honeycomb structure
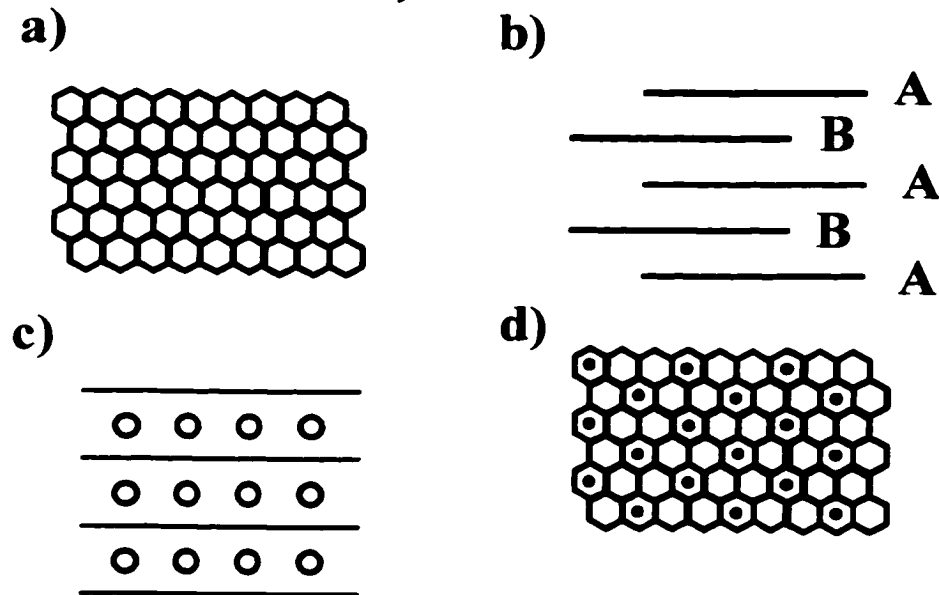
The most common form of graphite is that of the so-called 2H stacking of adjacent graphene sheets (Zheng, 1996). Carbon atoms are arranged in a honeycomb structure, or on the edges of inter-connected hexagons (figure 1-3 (a)). One layer (in the c-direction) of this arrangement is called a graphene sheet. Successive layers are stacked with an ABABAB registry. Adjacent layers of A and B are shifted by 1/3 of a unit cell along the 110 crystal

direction with respect to one another (figure 1-3(b)). When lithium is intercalated into graphite, the carbon layers shift from ABABAB to AAAAAA stacking (Way, 1995). The lithium resides between successive graphene sheets (figure 1-3(c)). A completely lithiated graphitic carbon will have lithium on next-nearest-neighbour sites, resulting in one lithium per six carbon atoms (figure 1-3(d)). The total volume expansion associated with this process is less than 8%. The intercalation of lithium into graphite is perfectly reversible. On lithium removal, the graphite re-adopts the initial ABABAB structure.

Figure 1-4 Voltage profile (Voltage versus specific capacity) for graphite for the first three half-cycles
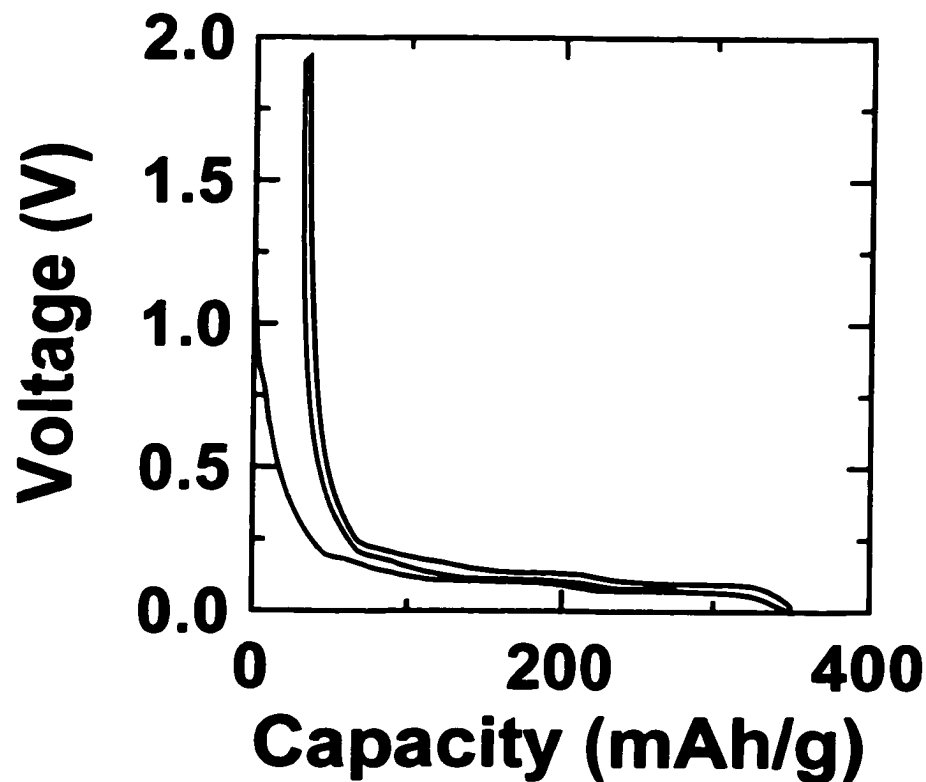
Figure 1-4 shows a voltage profile for a lithium/graphite cell. Graphite exhibits all the desirable characteristics of anode materials, high capacity (372mAh/g), low voltage in reference to lithium metal (0.2V average) and good reversibility (graphite retains 80% of its first discharge capacity for 1200 cycles). New materials that might replace graphite as anode

materials for lithium ion cells are usually measured against graphite.

1.4.3 Binary lithium alloys

Lithium alloys with metals such as tin, lead and silicon, in structures with high lithium content; for example, $Li_{4.4}Sn$, $Li_{4.4}Pb$ and $Li_{4.4}Si$, which have far greater lithium contents than $Li_{1/6}C$. Moreover, the packing density of lithium in these materials is very close to, and sometimes higher than, the packing density of lithium in lithium metal. For example, the packing density of lithium in; $Li_{4.4}Si$ is 0.0851 mol/ml, in $Li_{4.4}Sn$ it is 0.0724 mol/ml, in $Li_{4.4}Pb$ it is 0.0718 mol/ml, whereas in Li it is 0.0769 mol/ml (Besenhard, 1996). The chemical potential of lithium in the alloy materials is also close to the chemical potential of lithium in lithium metal. Therefore, it is possible to design a high-voltage, high-capacity battery using an alloy anode versus an intercalating cathode material.

Table 1-2 Comparison of the theoretical capacities of various alloy anode materials, carbon, and lithium metal

Compound	Gravimetric Capacity (mAh/(g starting material))	Volumetric Capacity (Ah/(l starting material))
$Li_{4.4}Si$	4199	9784
$Li_{4.4}Sn$	994	7266
$Li_{4.4}Pb$	569	6458
Li_3As	1073	6148
Li_3Sb	660	4416
LiAl	993	2680
LiC_6	372	818
Li	3861	2062

The theoretical specific capacities of the lithium alloys can be calculated by applying equation 1-4 and the known stoichiometries of the end products (Moffat, 1990). Table 1-2 compares the gravimetric and volumetric capacities of several Li-alloy compounds with graphite and lithium metal. One can see the reason for the interest in such materials.

Graphite, as mentioned in the previous section, with a density of 2.2g/ml would have a volumetric capacity of the order of 800 Ah/l. This capacity is far short of the theoretical volumetric capacities of silicon and tin.

The problem, however, with lithium alloy anodes is that they don't cycle well. The main reason that they don't cycle well is that the alloys are not lithium intercalation compounds. There is a large volume expansion associated with the insertion of lithium into these metals (Anani et al., 1988). For example, the crystal structures of Sn (Wyckoff, 1982) and $Li_{22}Sn_5$ (Gladyeshevski et al., 1964) show that there is at least a 300% increase in volume between Sn and $Li_{4.4}Sn$ (compared to 8% for C to $Li_{1/6}C$). More important, perhaps, is the fact that the Li-Sn phase diagram contains seven inter-metallic phases of generally different structures (Moffat, 1990). It is impossible to believe that the transformations between each of these structures are benign processes. The transformation from C to $Li_{1/6}C$ is a benign process, as shown in the previous section. Chapter 2 contains more detailed structural information on all of the Li-Sn alloy phases.

The failure mechanism of the alloys has to do with the loss of the morphological integrity of the grain structure through cycling. The grains of tin, for example, within a particle before lithium insertion, are well connected and so the electrical conduction between the grains is good. As lithium is added the volume of the grains increases. The transformation between two phases of different structures puts large stresses on the connections between the grain boundaries, and some of them become disjointed when the lithium is removed during charging. The grains also experience catastrophic internal stresses that result in the pulverization of the grains. The grain boundaries of the product are poorly connected and the grains are pulverized, and as a result, the grains and particles do not conduct electrons and

ions as well as before lithium was inserted. The conduction of electrons must be maintained across the grain boundary if lithium is to be re-inserted during the subsequent discharge. In some cases, grains may become electrically detached and will not conduct electrons across the grain boundaries that had previously connected this grain to others. The internal resistance increase as a result of the lithium insertion and removal is cumulative through subsequent cycles. Eventually the anode can no longer react with appreciable amounts of lithium and is therefore not useful as an energy storage material.

1.4.4 Alloying-metal-oxide composite glass

In March 1996, Fuji Film Company announced its plans for the manufacture and sale of a new generation of lithium ion cells. Surprisingly, these cells used an anode material that is based on tin oxide and not carbon. The material, an amorphous tin oxide composite, was claimed to have theoretical volumetric and gravimetric capacity advantages over carbon of four and two times, respectively (Idota et al., 1997).

Idota et al. (1994), in one of approximately 200 patent applications surrounding the Fuji cell, describe the preparation and electrochemical behaviour of hundreds of tin, as well as other group IV, oxides and oxide composite glasses. Investigation into the Fuji materials followed shortly after the Fuji press release. Courtney and Dahn (1997a) provide the first published scientific explanation of the reaction mechanism of these materials. The reaction mechanism of lithium with these materials is essentially reduced to the alloying and de-alloying of lithium with the constituent binary alloy. Figure 1-5 is a voltage profile comparison between graphite and SnO. It is obvious why the Fuji announcement created such interest in these new materials.

Figure 1-5 Voltage profile for lithium versus graphite (solid) and SnO (dashed)
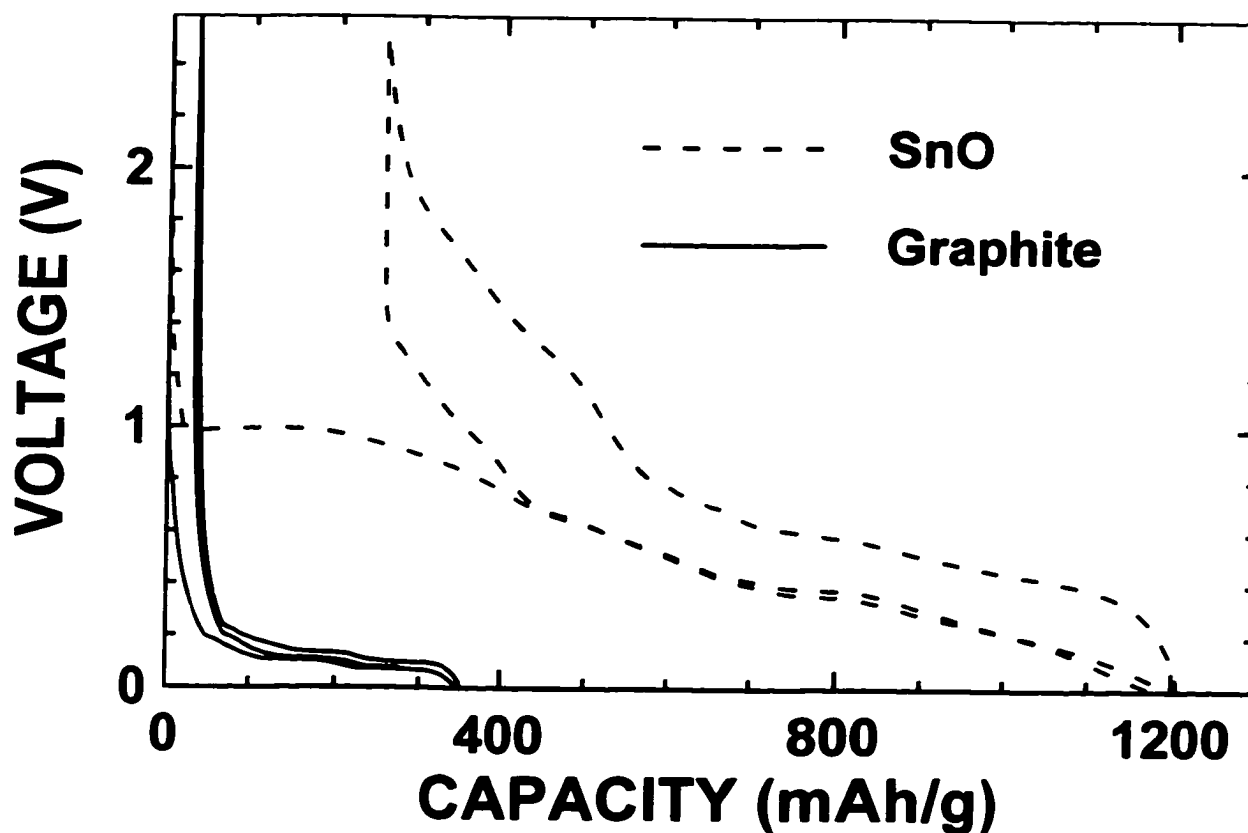
Apparently Fuji had found a way by which to react materials with large amounts of lithium, while maintaining the morphological integrity of the material. This thesis summarizes what has been learned at Dalhousie since the original Fuji announcement.

1.5 Organization of thesis

Chapter 2 provides a detailed explanation of the experimental techniques used in this work; notably, electrochemical methods, x-ray diffraction (XRD) and the Mössbauer effect (ME) spectroscopy. The electrochemical reaction of lithium with tin is important to this thesis, and chapter 3 is devoted to various aspects of it. This chapter contains, among other information, the results of an ab-initio calculation of the lithium-tin electrochemical voltage profile.

It became apparent that grain-size was an important factor in investigating these materials. The effects of grain size on XRD, ME spectroscopy and electrochemical voltage (specifically the Li-Sn electrochemical voltage profile) are discussed in chapter 4. By this point, one is well prepared to investigate the reaction mechanism of lithium with the Fuji materials.

The reaction mechanism is broken down into two main areas: the first cycle reaction mechanism (chapter 5) and the subsequent cycles and reversibility (chapter 6). The first cycle reaction mechanism of lithium with SnO, initially, is surmised from basic thermodynamic considerations. Electrochemical, in-situ XRD and in-situ ME spectroscopy experiments confirm the initial assumption. This reaction mechanism is extended to SnO-containing glasses, whose preparation is discussed in section 5.3. The subsequent reaction, or the failure mechanism for the Fuji materials (after many cycles), is investigated in chapter 6. Chapters 5 and 6 focus on tin-containing materials, and chapter 7 shows the results of similar experiments on antimony and lead containing materials. Finally, chapter 8 concludes and gives suggestions for future work in this area.

Chapter 2

Experimental techniques

2.1 Electrochemical measurement

The electrochemical characterization of a material is a three-step process, electrode coating, cell fabrication and electrochemical testing. The following explains these general steps for all the materials studied. Individual variations are described in later sections and chapters, as appropriate.

An electrode of the material under investigation is prepared as follows. Materials are manually ground and sieved (-325 mesh), producing particle sizes of less than 40 μm. A slurry is prepared from a ground powder of the material, a conducting additive, (typically 'Super S' carbon black, Chemetals, USA) usually added at a level of 10% of the mass of the cathode, and a binder (typically polyvinylidene fluoride (PVDF), Aldrich), usually added at a level of 5% of the mass of the cathode. The PVDF is dissolved in N-methyl pyrrolidinone (NMP) (Aldrich). The conducting additive, a filamentary carbon, helps to connect the individual particles of the cathode together electrically. The binder holds the mass together in a workable form and helps it adhere to the copper substrate. The slurry, which has a consistency similar to molasses, is mixed in a sealed plastic bottle with ceramic mixing beads by shaking vigorously for 10-15 minutes. The uniform slurry is coated on a thin copper foil substrate using a doctor blade spreader. The thickness of the coated foil is typically 150 μm. Mass loadings are typically 5-15 mg/cm^2. The foils are heated in air at 110 °C for a period of not less than 4 hours. The binder solvent NMP evaporates and the resultant film generally has a composition of, 85% by weight active material, 10% by weight Super S and 5% by weight

PVDF binder. The dried foils are pressed between flat stainless-steel plates using a pressure of 1.36×10^7 Pa for 30 seconds. Cathodes of 13mm diameter are punched from the foil. These are weighed and taken into an inert atmosphere glove box for cell construction.

Figure 2-1 shows an exploded view of a coin cell. The cathode is placed on the stainless-steel can (2325 coin cell hardware - 23mm outer diameter and 2.5mm thick) and wetted with a few drops of electrolyte (1M $LiPF_6$ dissolved in a 30:70 vol % mixture of ethylene carbonate (EC) and diethyl carbonate (DEC), Mitsubishi Chemical). A microporous polypropylene separator (Celgard 2502) is placed on top of the cathode. Next, a 14mm-diameter, 125μm-thick lithium foil is located on top of the separator and centered with

Figure 2-1 Exploded view of a coin cell

	Cell Top (Negative Terminal)
	Polypropylene Gasket
	Steel Spring
	Stainless-Steel Spacer
	Lithium Metal Anode
	Celgard 2502 Separator
	Cathode
	Cell Bottom (Positive Terminal)
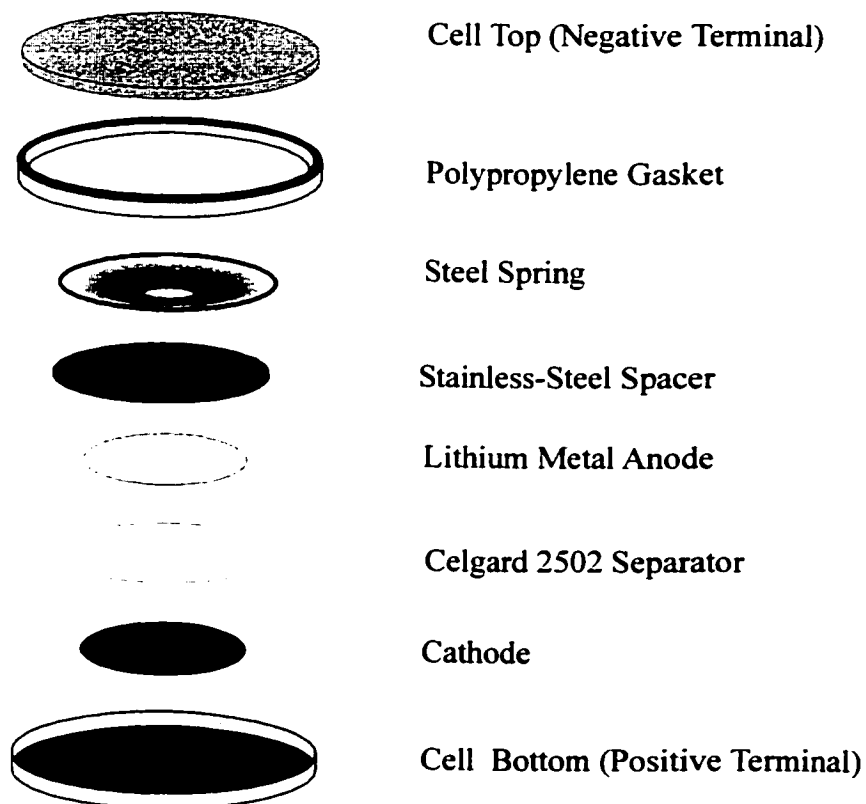
respect to the cathode. A stainless steel spacer disc is placed on top of the lithium. A cone-

shaped mild-steel spring is placed next. When the cell is sealed, the cone-shaped spring is compressed and applies force to the cell can and spacer disc, which keeps the electrodes under pressure. This 'stack pressure', as it is called, assists in maintaining good electrical contact between the particles of the cathode and the copper foil current collector. Finally, a stainless-steel cap, which has a polypropylene gasket along its circumference, is placed onto the stack. Then the cell is 'crimped' closed. The sides of the can fold over onto the gasket and seal the cell. The cell is then taken out of the glove box and stainless-steel tabs are spot-welded to the top and bottom of the coin cell. The tabs are connected to the charger by alligator clips and wires.

The currents chosen for charge and discharge are based on the active electrode mass. The active mass is typically 85% of the mass of the cathode minus substrate. A 'low-rate' cell is charged and discharged using a specific current of 9.3 mA/g and a 'high-rate' cell is charged and discharged using a specific current of 37.2 mA/g. The cells are housed in temperature controlled environments (30.0 ± 0.1°C) and are connected to a computer controlled charger system (Moli Energy 1990 Ltd., Burnaby, B.C.). The charger system measures voltage versus time. The voltage measurement is made by a Keithley 196 DMM, which has 6.5 digit precision. The charger is programmed to discharge and charge the cells to pre-set voltage limits. The system maintains a constant current (to within 1%) during discharge.

The first discharge capacity can be calculated from the data that the charger logs, as follows.

$$\text{first discharge capacity (mAh/g)} = \frac{-i \times t}{m} \quad ; i = \text{current}, t = \text{time and } m = \text{the active electrode mass}$$

(2-1)

Data were logged with 10 μV precision whenever the cell voltage changed by 5 mV or more and time is measured to the nearest second. The lower voltage-trip chosen for discharge was between 0.0 V and 0.3 V and the upper voltage-trip chosen for charge was between 0.8 V and 2.5 V. The specific voltage ranges chosen for the discharge and the charge of a particular cell will be provided in subsequent chapters.

2.2 X-ray diffraction technique

Powder X-ray diffraction (XRD) can be used by novices to match the crystal structure of a material to a known pattern. This application of XRD is particularly relevant for materials preparation. Cullity (1967) and Warren (1969) describe powder XRD in detail.

2.2.1 Powder XRD

The diffractometer used was a Siemens D5000 θ - θ diffractometer with a copper target x-ray tube. The diffractometer is configured for flat-plate samples. In this set-up, the sample is fixed and the tube and detector arms are each set at an angle θ (with respect to the plane of the flat-plate sample holder), providing a scattering angle of 2θ. The typical slits used were $0.5°$ divergence, $0.5°$ anti-scattering, and 0.6mm receiving, providing a resolution of $\Delta 2\theta \sim 0.2°$ full-width half-maximum. The machine has a diffracted beam monochromater.

A stainless-steel holder, with well dimensions of 12mm long by 20mm wide by 2mm deep, was used to hold the powder samples. Powders were manually ground and sieved (-325 mesh) before measuring. Scan ranges were between $10°$ - $90°$ (quoted in 2θ), the step size was generally $0.05°$/step, and the count time was between 3 and 16 seconds/step.

When the amount of available powder was small ($\sim$ 100 mg) a zero background

holder (ZBH) was used. This is a single crystal of silicon cut along its 510 plane. The silicon 510 plane has a structure factor of zero, so the sample holder produces no coherent scattering. Powders were first mixed with acetone and spread evenly on the ZBH. When the acetone evaporated a uniformly distributed powder remained.

In situations where the materials to be measured were air sensitive, an airtight holder was used (Obrovac, 1997). Electrode materials containing lithium are good examples of such samples. This holder employed a ZBH located in this airtight environment.

2.2.2 In-situ XRD for electrochemical cells

Changes in the structure of the cathode material can be monitored as lithium is inserted or removed from it, by the use of an in-situ XRD technique. This 'bird's-eye' view of the material under investigation can provide a fairly conclusive picture as to the reaction mechanism that a particular material adopts. The method was described by Dahn et al. (1981) and has been refined into a more convenient form by Richard et al. (1996). The latter method is used in this work.

The in-situ cell is a modified coin cell that has an appropriate window. The window must be fairly transparent to x-rays. Beryllium is used since it has a low mass absorption coefficient for x-rays and is mechanically workable. The coin cell, shown in figure 2-1, is easily transformed into an in-situ cell. A centered hole (17.5 mm) is machined on the cell bottom and an inserted Be window becomes the cell bottom. The beryllium window (Brush Wellman Electrofusion Products, Freemont, CA. Material Grade PF-60) has a diameter of 22.6 mm and a thickness of 0.254 mm. Leaks can occur at the beryllium-steel interface so a thin layer of a pressure sensitive adhesive (Roscobond, Rosco, Port Chester, NY) is applied

between the remaining steel on the can bottom and the beryllium.

An electrode that is coated on copper, such as the one described in section 2.1, cannot be used in an in-situ XRD experiment. The copper, which would be placed inside the cell on top of the Be, will absorb an appreciable amount of x-rays. One solution to this problem is to coat the electrode slurry directly onto the Be. Another solution is to use an electrode coating technique that does not require coating onto a metallic substrate. The process chosen uses a 'Bellcore' plasticized electrode technique.

To prepare a Bellcore electrode, a slurry of the active material was prepared as follows. The active material (11.6% by weight), Kynar Flex 2801 (88% vinylidene fluoride and 12% hexafluoro-propylene) polymer (5.5% by weight), 'Super S' carbon black (1.4% by weight), EC/PC (ethylene carbonate/propylene carbonate 50:50 volume %) (9.5% by weight), and acetone (72.0% by weight) were mixed in a sealed glass vial with a stirring bar. The slurry was stirred in a water bath at 50°C for 4 hours and was then spread on a glass plate in air using a doctor blade spreader set to 0.635 mm thickness. The cathodes were then cut (13 mm diameter), weighed, and immersed in diethyl-ether (Aldrich) for 5 minutes to remove the EC/PC. In-situ XRD cells employing cathodes of selected materials opposite Li metal anodes of 125 μm thickness and 14 mm diameter were constructed in an argon-filled glove box. The cathodes were first submersed for 5 minutes in 1M LiPF$_6$ dissolved in a 30:70 volume % mixture of ethylene carbonate (EC) and diethyl carbonate (DEC), and were then centered on the beryllium window. The rest of the cell is constructed as described in section 2.1.

The cells are placed in a specially designed holder, which is then located inside the diffractometer. The depth of the well of the holder was machined such that the cathode inside

the cell would align with the goniometer axis. Figure 2-2 is a picture of a cell and a cell in its holder.

The in-situ cell is repeatedly x-rayed, while being discharged and subsequently re-charged. Figure 2-3 is a picture of the cell and holder, inside the diffractometer.

Figure 2-2 Picture of an in-situ XRD cell and a cell mounted in the holder

In-situ cell in holder

In-situ cell
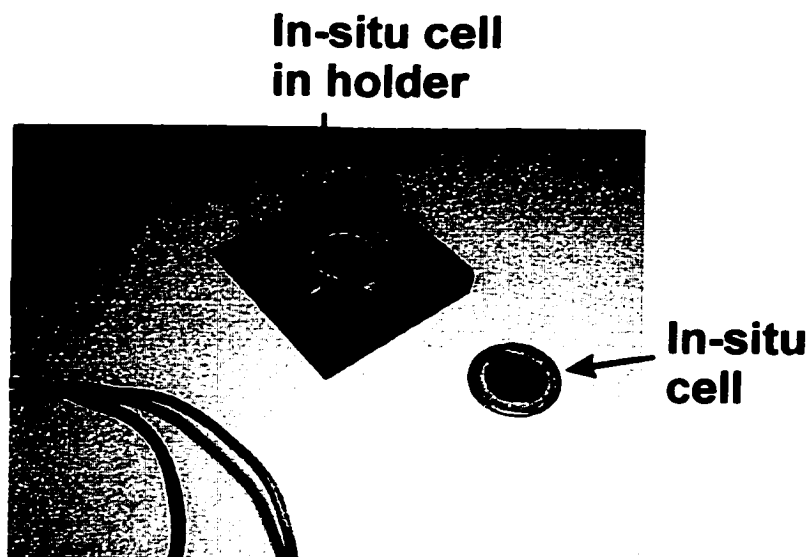
Figure 2-3 Picture of cell and holder inside the diffractometer

Holder and cell in diffractometer
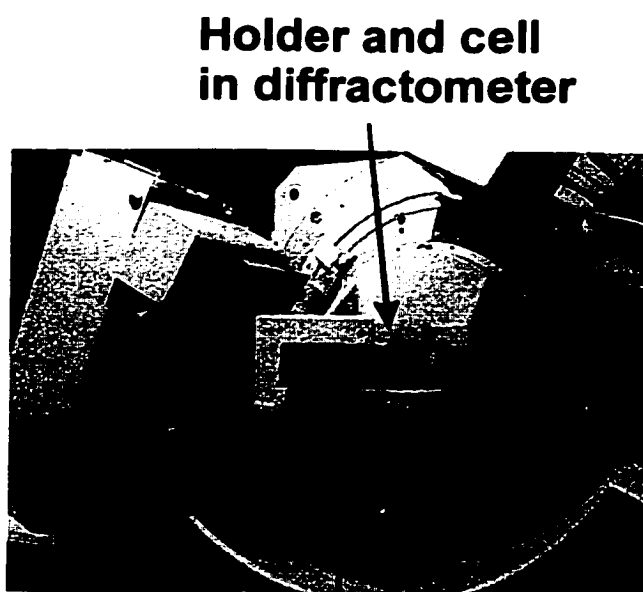
2.2.3 Theory of XRD

The information that is needed for the calculation of the powder pattern is the coordinates and types of the atoms contained in the unit cell of the crystal, and the lattice constants of that unit cell. A crystal that is oriented with similar atomic planes aligned (at an angle θ with respect to a beam of incident x-rays of wavelength λ), will cause constructive interference in the diffracted beam according to Bragg's law (equation 2-2). For a particular set of Miller indices, hkl, there will be a particular spacing, d_{hkl}, between each of these parallel atomic planes. This plane spacing can be calculated from the lattice constants of the unit cell.

$$\lambda = 2d_{hkl}\sin\theta$$

(2-2)

The wavelength of the incident x-ray, in our case Cu-K_α, is known ($\lambda = 1.541$ Å). Therefore the angles $\theta(h,k,l)$ can be easily calculated. The beam is deflected a total of 2θ, which is referred to as the scattering angle. These are the angles at which an intensity maximum on a powder diffraction pattern could be located. For a powder sample, random orientation of grains is assumed; therefore the sample does not have to be rotated in three dimensions. The next step is to calculate the relative intensity (if any) for each of these reflections.

There are, according to Cullity (1967), six factors that affect the relative intensity of peaks of a powder pattern; the polarization factor, the structure factor, the multiplicity factor, the Lorentz factor, the absorption factor and the temperature factor.

The multiplicity factor recognizes the fact that different crystallographic planes can give rise to reflections located at the same angle of reflection. This multiplicity can be derived from the particular Bravais lattice. For example, the 100, 010, and 001 planes in a

cubic lattice will result in a diffraction peak at the same angle since the spacing of these planes is equal. Consideration of the multiplicity factor can make a manual calculation more efficient.

The absorption factor describes the incident intensity absorbed (i.e. not reflected) by the sample itself. The absorption factor is related to the linear absorption coefficients of the atoms in the material. In the flat-plate geometry, where we assume 'infinite' sample thickness, the angular dependence of absorbed incident intensity is eliminated. Therefore, the absorption factor is not important for the present discussion. The only exception to this is the Be window used in the in-situ cell, as the Be window has a finite thickness. This will result in greater absorption of x-rays at lower incident angle than at higher incident angle. The effect is relatively small, however, so it need not concern us.

The temperature factor describes another relationship between the peak intensity and the angle of reflection. Atoms are, in reality, not fixed points in a mathematical lattice, as they vibrate about their equilibrium positions. The mathematical derivation of the Bragg condition assumes parallel planes separated by a constant distance. Atoms that are moving about their mean positions do not sit on planes of constant separation. The fractional effect will be stronger for planes of small spacing than for planes of large spacing, which is the source of the angular dependence. Reflection from planes of low spacing occur at large Bragg angle, so the effect of the temperature factor is greater at high angle than at low angle. A detailed determination of the temperature factor, such as a Debye-Waller calculation (Warren, 1969), is not a simple process. Atoms do not necessarily vibrate independently as there is coupling to the other atoms in the surroundings. This effect becomes even more difficult to quantify for structures composed of different types of atoms. The temperature

factor, as it pertains to XRD, is not useful to the work in this thesis, so it is not discussed further.

Electrons scatter x-rays in all directions, but the intensity of the scattered ray is dependent on the scattering angle. This dependence is known as the polarization factor for the intensity of a diffracted x-ray. The Lorentz factor is an angularly dependent factor based on the geometry of an experimental measurement. Both the polarization factor and the Lorentz factor are grouped together into the Lorentz-polarization factor given in equation 2-3 (for a machine employing a monochromator),

$$Lorentz\text{-}polarization\ factor = \frac{(1 + \cos^2 2\theta \cos^2 2\theta_m)}{(\sin^2 \theta \cos\theta)}$$

(2-3)

where the monochromator scattering angle is θ_m.

The structure factor, F, determines the intensity of a particular Bragg reflection based on the types and positions of the atoms that make up the unit cell. The structure factor is defined as,

$$F_{hkl} = \sum_n f_n e^{2\pi i (hx(n) + ky(n) + lz(n))}$$

(2-4)

where the sum is over all n atoms, of atomic coordinates $x(n)$, $y(n)$ and $z(n)$, in the unit cell. The atomic form factor, f_n, of the nth atom, is specific to each element and defines the intensity of scattered radiation from the electrons in that particular atom. The atomic form factor is also dependent on the angle of reflection.

The atomic form factor is provided in *The International Tables for X-Ray Crystallography, Vol. 4* (Ibers and Hamilton, 1974) by an analytic expression, which fits the results of quantum mechanical calculations, as follows,

$$f_n\left(\frac{\sin\theta}{\lambda}\right) = \sum_{i=1}^{4} a_i \exp\left[-b_i\left(\frac{\sin\theta}{\lambda}\right)^2\right] + c$$

(2-5)

Table 2-1 Atomic form factor coefficients for Sn and Li (Ibers and Hamilton, 1974)

Atom	a_1	b_1	a_2	b_2	a_3	b_3	a_4	b_4	c
Sn	19.1889	5.83030	19.1005	0.50310	4.45850	26.8909	2.46630	83.9571	4.78210
Li	1.12820	3.95460	0.75080	1.05240	0.61750	85.3905	0.46530	168.261	0.03770

The coefficients for Sn and Li are given in table 2-1.

The total intensity of a particular Bragg reflection, is proportional to,

$$I \propto F \times F^*$$

(2-6)

Calculation of a XRD pattern, without the other intensity correction factors described previously, involves applying 2-6 over the sets of Miller indices for the crystal. All possible combinations of Miller index from -9 to 9 would typically be an appropriate calculation to perform on a computer. Other factors, such as the temperature factor and the Lorentz-polarization factor, can be included for calculations where the exact intensity of the pattern is required.

2.2.3.1 The Debye scattering formalism

The method of calculating the intensity in the previous section, however, applies to an 'infinite' lattice. In order to examine the effects of finite (i.e. very small) grain size on the scattered intensity, the *Debye scattering formalism* (Warren, 1969) is used.

Equation 2-4 can be expressed in its vector form,

$$F = \sum_m f_m e^{(2\pi i/\lambda)(\vec{s}-\vec{s}_0)\cdot\vec{r}_m}$$

(2-7)

where the position of each atom, m, is now expressed as a vector, r_m, and the direction of the scattered and incident waves are expressed as vectors s and s_0, respectively. The scattered intensity, introducing a dummy index n, is then,

$$I = F \times F^* = \sum_m f_m e^{(2\pi i/\lambda)(\vec{s}-\vec{s}_0)\cdot\vec{r}_m} \sum_n f_n e^{-(2\pi i/\lambda)(\vec{s}-\vec{s}_0)\cdot\vec{r}_n}$$

(2-8)

Consider the vector, $r_{mn} = r_m - r_n$, simplifying 2-8 to,

$$I = \sum_m \sum_n f_m f_n e^{(2\pi i/\lambda)(\vec{s}-\vec{s}_0)\cdot\vec{r}_{mn}}$$

(2-9)

Equation 2-9 is the intensity due to an array of atoms, m and n, where the vector between each pair is r_{mn}. We can examine the consequences of a powder average of this structure by assuming a sample of the structure contains many grains of random orientation. That is, we assume that r_{mn} has equal probability of being in any orientation in space. The average of the exponential term in equation 2-9, is then (introducing $k = (4\pi\sin\theta)/\lambda$),

$$\left\langle e^{(2\pi i/\lambda)(\vec{s}-\vec{s}_0)\cdot\vec{r}_{mn}} \right\rangle = \frac{1}{4\pi r_{mn}^2} \int_{\phi=0}^{\pi} e^{ikr_{mn}\cos\phi}\, 2\pi r_{mn}^2 \sin\phi\, d\phi = \frac{\sin kr_{mn}}{kr_{mn}}$$

(2-10)

The intensity, therefore, for a collection of atoms (m and n), whose grains are randomly oriented in space and where the distance between m and n is r_{mn} is,

$$I = \sum_m \sum_n \frac{f_m f_n \sin kr_{mn}}{kr_{mn}}$$

(2-11)

Equation 2-11 is known as the Debye scattering formalism.

2.2.3.2 The Scherrer equation

A way in which to estimate grain size from a XRD pattern that is often used is the Scherrer equation (Warren, 1969). A peak having a full-width half-maximum (FWHM) of $\Delta 2\theta$ will correspond to a grain size of L, given by,

$$L = \frac{0.94\lambda}{\Delta 2\theta \cos\theta}$$

(2-12)

2.3 Mössbauer spectroscopy

The Mössbauer effect (ME) is '...the phenomenon of the emission or absorption of a γ-ray photon without loss of energy due to recoil of the nucleus and without thermal broadening...' (Greenwood and Gibb, 1971). It is a resonant effect where the probed nucleus absorbs and re-emits a photon of a narrowly defined energy band. The small line widths, which for Sn $\approx 2.5 \times 10^{-8}$ eV (FWHM), are useful for probing very slight differences in nuclear energy levels due to different electronic environments ($\sim 8 \times 10^{-7}$ eV for the entire range of Sn-containing materials). The ME can be applied to a number of different nuclei, but for the purposes of this work we shall restrict ourselves to its use in tin-containing materials.

Figure 2-4 is a schematic of one particular decay scheme for the Sn ME. A meta-stable parent state (^{119m}Sn, half-life 250 days) decays to a ^{119}Sn excited state. The excited state decays to a ^{119}Sn ground state producing a photon of approximately 24 keV. The energy change of the three-halves (spin) to one-half (spin) transition is generally different for tin nuclei in different electronic environments.

Figure 2-4 A decay scheme to produce Sn ME photons

Note the fraction at the left-hand side of each energy line. This refers to the nuclear spin of that particular nucleus.

$^{119m}_{50}$Sn(meta stable parent state)

11/2 —————————————— 90keV

$t_{1/2}$ = 250 days

$^{119}_{50}$Sn Excited state

3/2 —————————————— 24keV = E_0

Mössbauer transition $^{119}_{50}$Sn Ground state

1/2 —————————————— 0
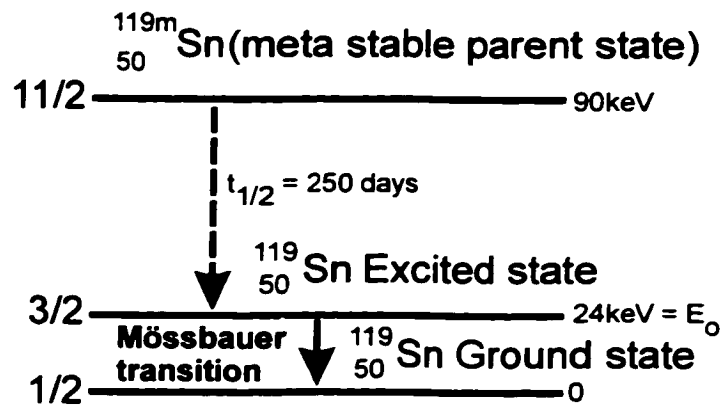
About 8% of naturally occurring Sn nuclei are the ^{119}Sn isotope. In the ME a source (in our case Ca^{119m}SnO₃) that decays according to figure 2-4 is used. The 24 keV photon produced impinges on the absorber material, for example ^{119}Sn$_{8\%}$O. If the ^{119}Sn nuclei in the absorber are in exactly (that is, within the range of the natural line-width) the same electronic environment as the ^{119}Sn nuclei in the source then the incident photon will be absorbed producing a one-half to three-halves transition in the ^{119}Sn nuclei in the absorber. This will subsequently decay and re-emit another photon. In general, however, the absorber and source nuclei are usually not in the same environments. In order to probe different tin environments the energy of the source photon must be varied over a range of energies.

2.3.1 ME spectroscopy experimental set-up

The photons produced by the source in the ME are doppler shifted so as to encompass a range of energies. The doppler shift, in this experimental set-up, is achieved by moving the source back and forth relative to the stationary absorber material. For tin-containing nuclei the source is moved back and forth at velocities between -8 mm/s and 8 mm/s, which translates to energy changes of about $\pm 6 \times 10^{-7}$ eV. That is, the 24keV photon produced by the ME is shifted in energy by an amount,

$$\Delta E = \frac{v}{c} 24 \, \text{keV}$$

(2-13)

where, c, is the speed of light and v is the velocity of the source. Figure 2-5 is a picture of a ME spectroscopy experimental set-up.

Figure 2-5 Picture of ME spectroscopy experimental set-up
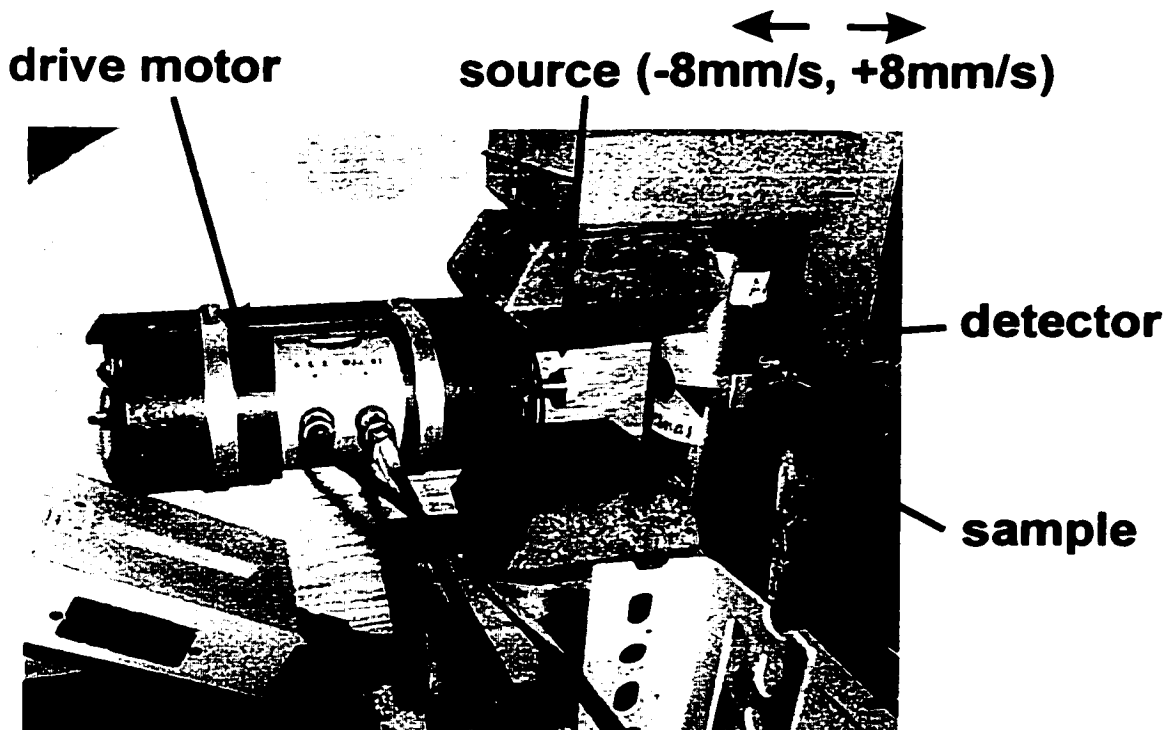
Room temperature ME measurements were made with a Wissel system II constant acceleration spectrometer (operating at a frequency of 23 Hz) and a krypton/CO_2 x-ray proportional counter (Reuter-Stokes Inc.). The detector employed a Pd filter. Data were collected using an Ortec ACE multi-channel scaling board. The $Ca^{119m}SnO_3$ source had an intrinsic line-width of 0.78mm/s (FWHM), and the velocity scale was calibrated using the peak-to-peak splitting of the outer lines of Co_2MnSn (Dunlap et al., 1998).

Powder samples were prepared as follows. Powders were manually ground and sieved (−325 mesh). Typically 150 mg of powder was uniformly distributed over a 30 mm diameter piece of tape ('Scotch-Brand', 3M Co.), and was kept in place by another piece of tape on top. Total measurement times were between 3 and 24 hours, depending on the availability of the spectrometer.

Figure 2-6 ME spectroscopy vs. XRD;
(a)ME spectroscopy of Sn, SnO and SnO Glass, (b)XRD of same
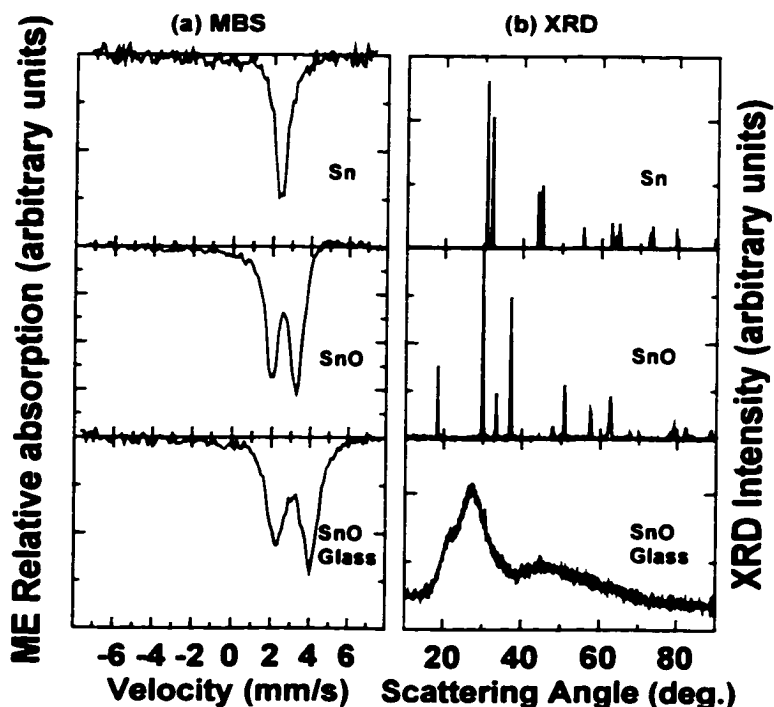
Figure 2-6 shows the results of XRD and ME spectroscopy for similar materials. It is generally accepted that the ME is useful for studying amorphous materials (Greenwood and Gibb, 1971), as the ME does not depend on detecting a signal that is coherent. An XRD pattern of a glass is essentially featureless (bottom panel, figure 2-6(b)) in comparison to crystalline SnO and Sn, as the detected signal in XRD measurements is preferably coherent. This feature of the ME is particularly useful in the in-situ experiments on the amorphous materials. The information gained from the diffracted x-rays in the in-situ experiment is significantly reduced from the crystalline materials. The in-situ ME experiment for the amorphous materials is complementary to the in-situ XRD experiment.

2.3.2 In-situ ME spectroscopy for an electrochemical cell

A cell for in-situ ME spectroscopy, which is a slight modification of the in-situ XRD cell as described in section 2.2.2, was designed (Mao et al., December 1998). A diagram of this cell is shown in figure 2-7. The in-situ ME cell is designed for maximum transmission of γ-rays. As such, all steel parts were removed (spacer and spring), and a second hole (diameter 13mm) was cut in the cell top. A second piece of beryllium (diameter 15mm, thickness 1mm) was placed over the hole, and was held in place by Roscobond pressure sensitive adhesive. A thin bead of Torr Seal (high vacuum, Varian) was applied after the cell was assembled at the (cell bottom/Be) and (cell top/Be) interfaces. The electrodes, prepared as described in 2.1, were coated directly onto the beryllium in this case.

This cell was held in place approximately 10 cm from the detector and 1 cm from the source. Charging and discharging currents were controlled by a Keithley 220 Programmable Current Source that was interfaced to a computer with a GPIB. The cell voltage was

measured by a Keithly 196 Digital Voltmeter, and also recorded through the GPIB. The current was sequentially decreased near the bottom of discharge and the top of charge to give the reactions adequate time to equilibrate. Spectra were obtained continuously while the cell was discharged and subsequently charged. The total experiment time was approximately 300 hours, during which 100 three-hour ME spectra were recorded.

Figure 2-7 Diagram of in-situ ME spectroscopy cell

cell bottom (2325) with hole

Gasket

cell top with hole

Thick Be Window

Lithium

Separator

Cathode

Thin Be window
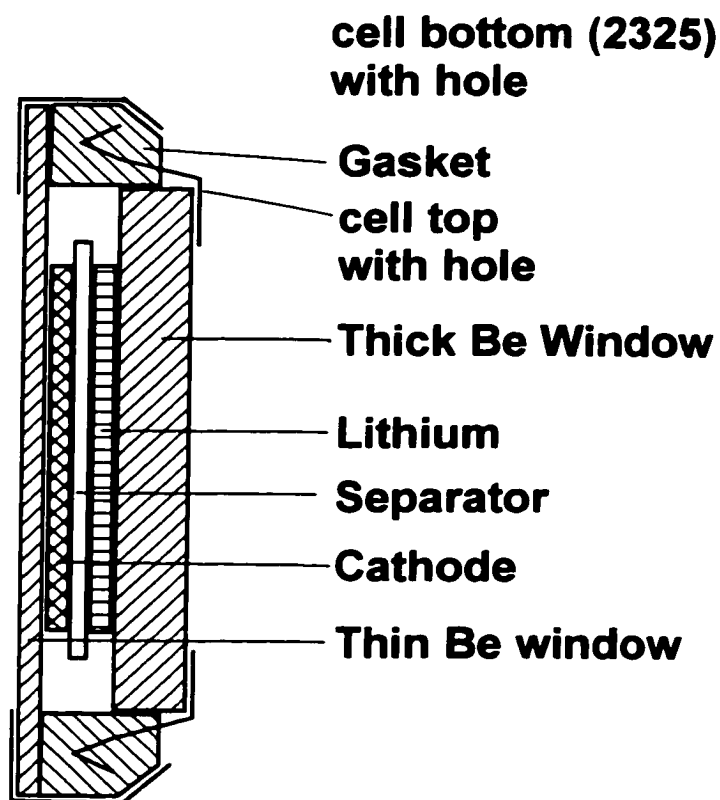
Chapter 3

A study of the reaction of lithium with tin

3.1 The Li-Sn phase diagram

The electrochemical reaction of lithium with tin is integral to this thesis. so an understanding of it is important. The electrochemical reaction of lithium and tin has been previously studied (see for example, Anani et al., 1982; Wang et al., 1986; and, Yang et al., 1996). In equilibrium, as Li is added to Sn, the lithium-tin binary phase diagram is followed. In other words, the discharge of a Li-Sn cell corresponds to moving from the right to the left of the phase diagram, as shown in figure 3-1. Each of the inter-metallic phases: Sn, Li_2Sn_5. LiSn, Li_7Sn_3, Li_5Sn_2, $Li_{13}Sn_5$, Li_7Sn_2 and $Li_{22}Sn_5$, should form sequentially, in such an experiment.

3.1.1 XRD and ME spectroscopy of crystalline Li-Sn phases

All compounds of the Li-Sn phase diagram were made (Dunlap et al., 1998) and were studied by XRD and ME spectroscopy. These results are gratefully reproduced here. as background, not as new results.

Figure 3-2 shows the XRD patterns of the Li-Sn alloy phases, as well as the reference powder diffraction file (PDF) (PDF-2 JCPDS-ICDD, © 1993) file for Li. Structural information, for the Li-Sn alloy phases, is provided in tables 3-1, 3-2 and 3-4.

The Li_2Sn_5 and $Li_{22}Sn_5$ samples were matched. by Reitveld analysis, to their expected crystallographic structures. All remaining phases were found to contain small amounts of impurities from neighbouring phases. For example, the LiSn sample contained a small

amount of Li_2Sn_5. The structures of the LiSn, Li_7Sn_3 and Li_5Sn_2 samples were matched to their respective reported structures. According to Dunlap et al., the $Li_{13}Sn_5$ and Li_7Sn_2 samples, however, did not quite match their expected structures. The XRD patterns of the materials in figures 3-2 (d) to (h) exhibit a similar underlying structure with a prominent peak at around $38°$ and several strong peaks at lower angle ($20°$ to $25°$). These shall be referred to as 'lithium-rich' alloys in this and in subsequent chapters. The peak at $38°$ is due to a body centered cubic (BCC) sub-structure. Section 3-4 will show that in a cell of Li and Sn, under ambient conditions, this sub-structure remains, but it is the long-range ordering of Sn atoms that is lost. The XRD patterns of figure 3-2 strengthen this argument.

Figure 3-1 The Li-Sn binary phase diagram (From Moffat, 1990)
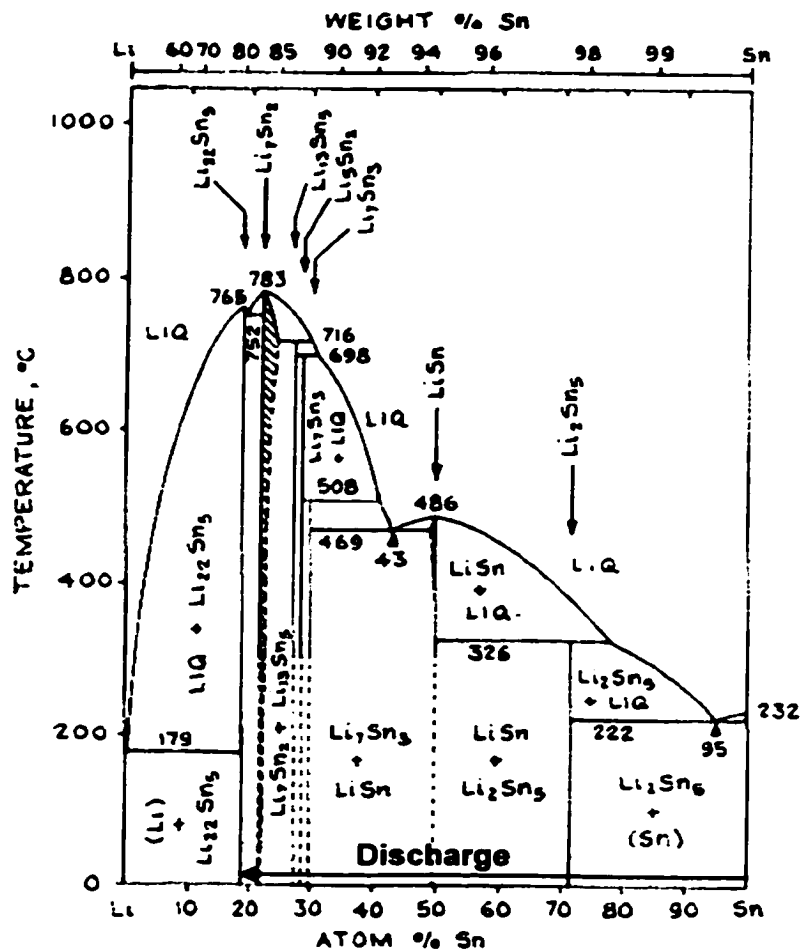
Figure 3-2 Powder XRD patterns of (a) Sn, (b) Li$_2$Sn$_5$, (c) LiSn, (d) Li$_7$Sn$_3$, (e)Li$_5$Sn$_2$, (f)Li$_{13}$Sn$_5$, (g) Li$_7$Sn$_2$, (h) Li$_{22}$Sn$_5$ and reference pattern for Li (PDF) in (i)

The Li-Sn alloys were made (Dunlap et al., 1998) by solid state reaction. Li$_2$Sn$_5$ and Li$_{22}$Sn$_5$ confirmed to be pure by Reitveld analysis. LiSn, Li$_7$Sn$_3$ and Li$_5$Sn$_2$ contained small amounts of neighbouring phases. Li$_{13}$Sn$_5$ and Li$_7$Sn$_2$ do not match their accepted patterns, and also contain small amounts of neighbouring phases.
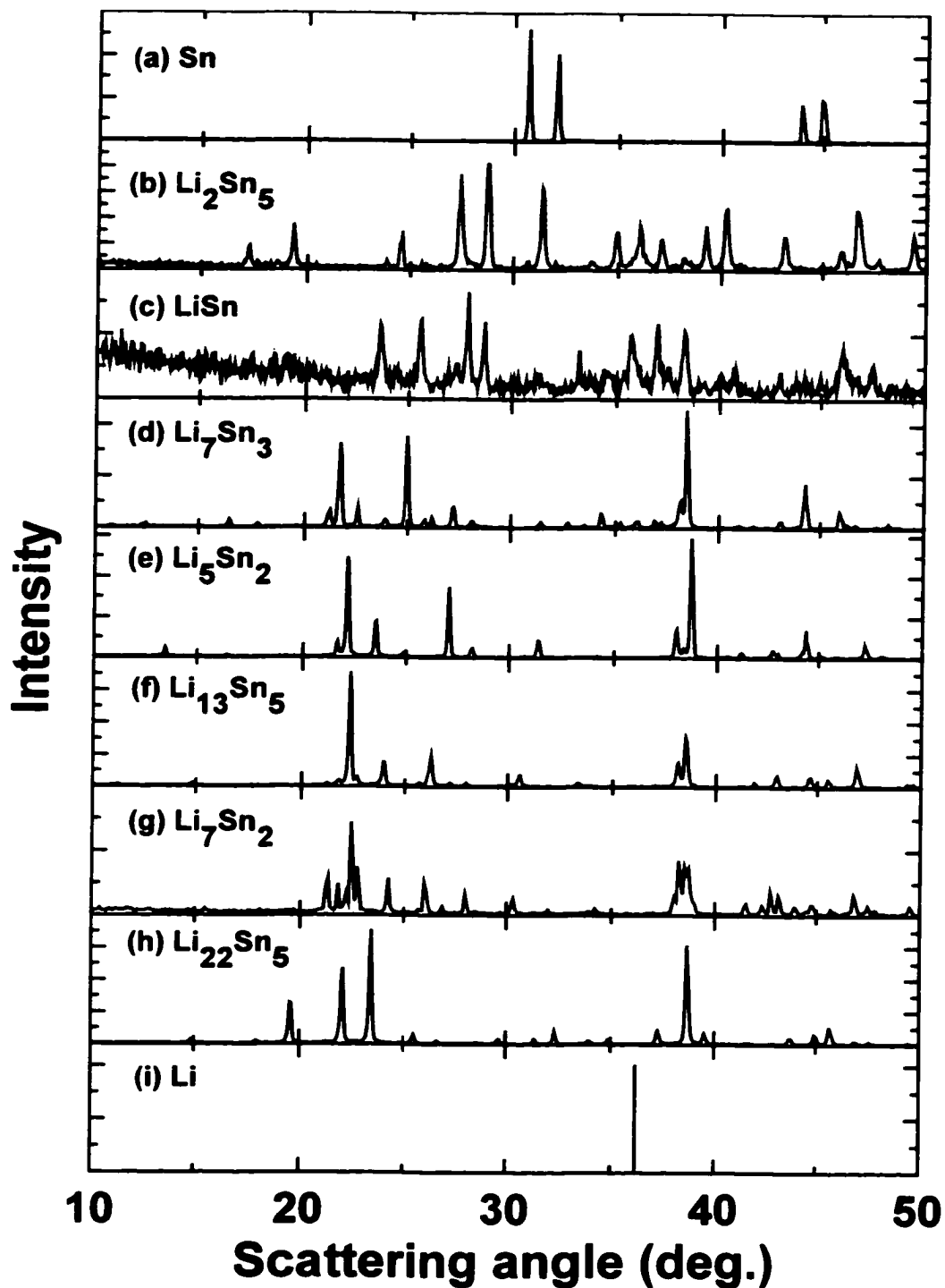
Figure 3-3 Powder ME spectra of (a) Sn, (b) Li₂Sn₅, (c) LiSn, (d) Li₇Sn₃, (e)Li₅Sn₂,
(f)Li₁₃Sn₅, (g) Li₇Sn,and (h) Li₂₂Sn₅

The Li-Sn alloys were made (Dunlap et al., 1998) by solid state reaction. Li_2Sn_5 and $Li_{22}Sn_5$ confirmed to be pure by Reitveld analysis. LiSn, Li_7Sn_3 and Li_5Sn_2 contained small amounts of neighbouring phases. $Li_{13}Sn_5$ and Li_7Sn_2 do not match their accepted XRD patterns, and also contain small amounts of neighbouring phases.
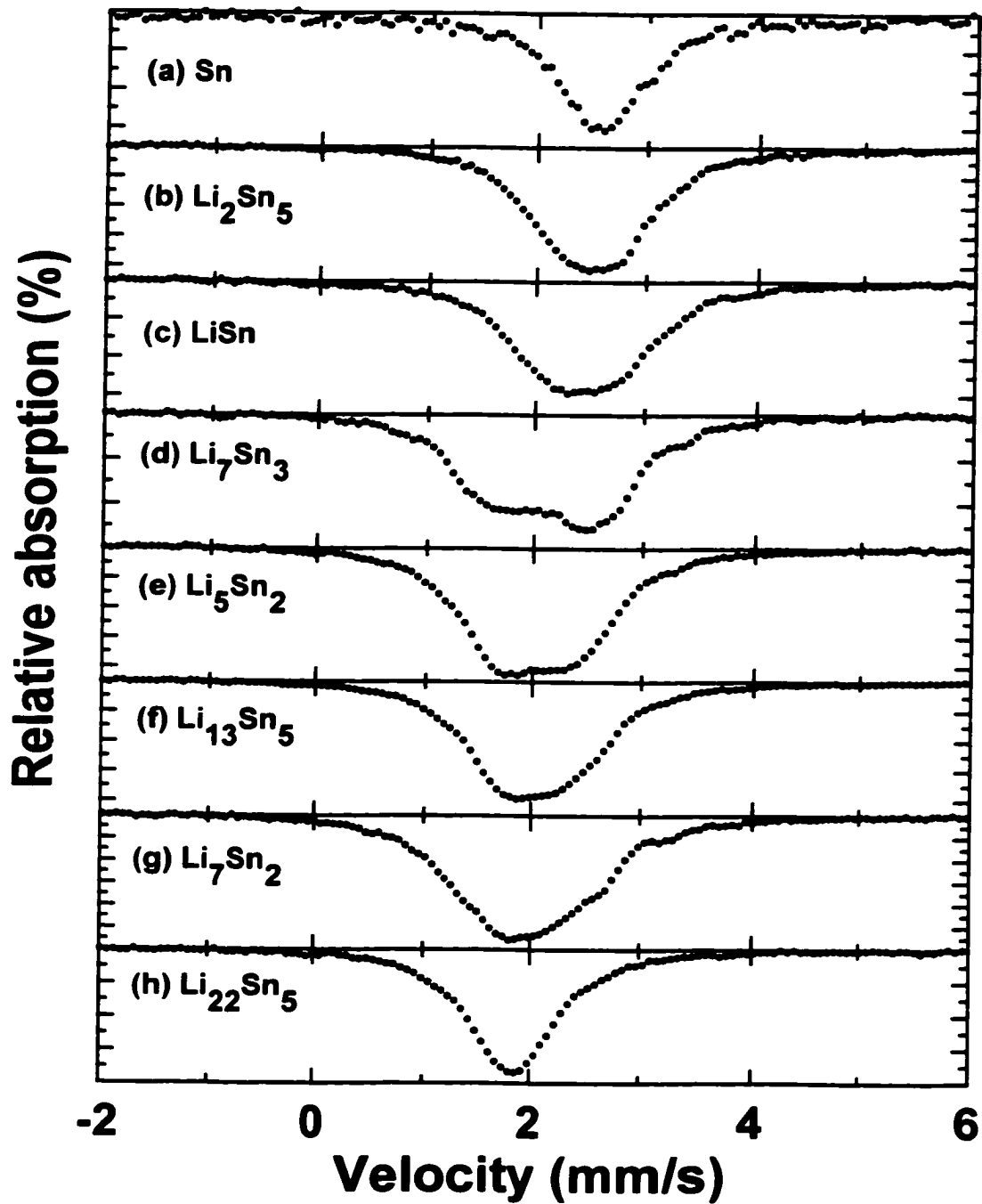
Figure 3-3 shows the ME spectra of the lithium-tin alloy phases, as well as metallic Sn. Notice the general shift of the absorption to lower velocity as lithium is added.

The method of velocity scale calibration for the spectra in figure 3-3 had changed from that reported in chapter 2. The new scale is based on the relative peak separation of a Sn-BaSnO3 composite. As such, all spectra to be reported in this thesis that were analyzed with a Co2MnSn calibration scale have been re-scaled to the new scale of Sn-BaSnO3. To re-scale, the spectra have been multiplied (in velocity) by a factor of 1.06 (Dunlap, private conversation, October 1998). The spectra of figure 3-3 will be used, in chapter 5, as 'fingerprints' for the in-situ ME experiments.

3.2 First order phase transitions and the electrochemical response

Figure 3-4 Schematic of a first order phase transition and how it leads to a plateau in an equilibrium voltage profile.
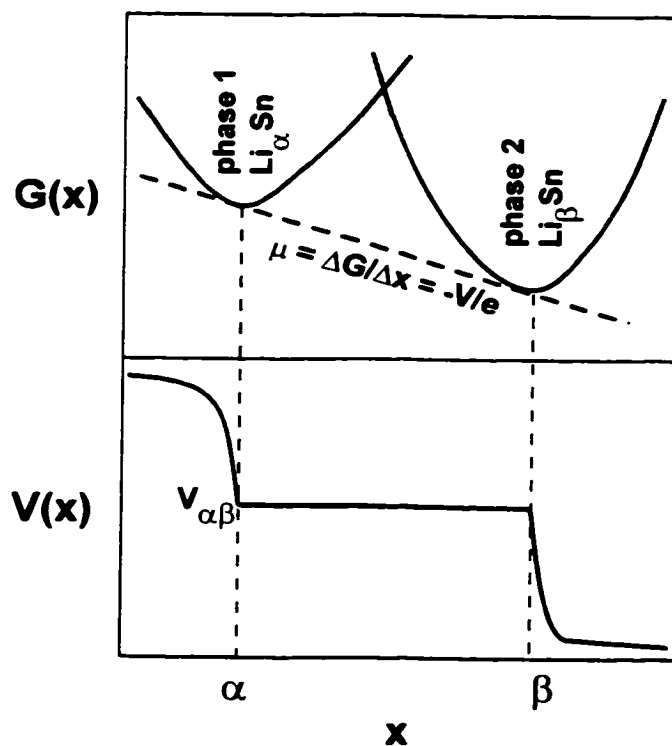
If the Li-Sn phase diagram is followed during the electrochemical reaction of Li with Sn, then at each of the phase boundaries there will be a first order phase transition. A general first order phase transition (e.g. Li_2Sn_5 to LiSn) is characterized in the schematic of figure 3-4. In order to minimize free energy (as lithium is added), the lithium and tin atoms will organize themselves as a phase mixture of the two line phases (McKinnon, 1995). For average compositions between α and β, particles will not be found as a homogeneous phase of average composition, instead they will be a mixture of $Li_\alpha Sn$ and $Li_\beta Sn$. Therefore, the change in free energy (with respect to composition), or chemical potential (at constant temperature and pressure), will be constant. The voltage, with respect to a lithium reference electrode, is the negative of the slope of the line connecting the two local minima on the free energy curve divided by the magnitude of the charge on the electron. Thus, a first-order phase transition appears as a plateau on the voltage profile. In the case of several two-phase regions, for example, $Li_2Sn_5/LiSn$, $LiSn/Li_7Sn_3$, etc., there will be several voltage plateaus corresponding to each region. If all of the inter-metallics of the Li-Sn phase diagram form under ambient conditions, then there will be seven such voltage plateaus in the voltage profile of a Li-Sn cell.

Figure 3-5 is an experimental voltage profile for a lithium-tin cell, where the capacity axis has been re-scaled to x in Li_xSn. The cathode of this cell was made with a Sn powder (99.9%, Aldrich) active material. This cell did not achieve the maximum theoretical capacity of $Li_{4.4}Sn$, but instead achieved a stoichiometry of $Li_{3.8}Sn$. Notice the well-defined voltage plateaus, corresponding to a first-order phase transition at each of the two-phase regions: Sn-Li_2Sn_5, Li_2Sn_5-LiSn and LiSn-Li_7Sn_3, as indicated on the graph. After x=2.33, however, the voltage slopes gradually to zero voltage. We attempted to understand this.

Figure 3-5 Voltage versus x in Li$_x$Sn for a Li-Sn cell

The discharge portion of the plot is lower in voltage than the charge segment, as shown. For each of the voltage plateaus, a reaction is suggested. A reaction arrow to the right corresponds to the discharge reaction, whereas a reaction arrow pointing to the left corresponds to the charge reaction.
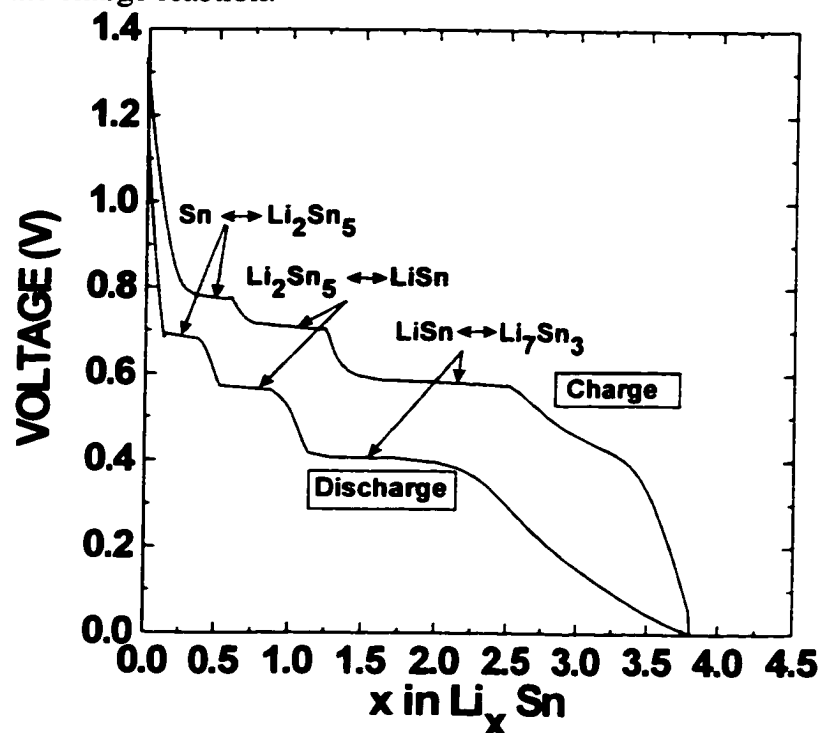
3.3 Ab-initio calculation of the Li-Sn voltage profile

The equilibrium cell voltage can be obtained from first principles energy calculations. The increased computing ability, reduced cost and the development of more sophisticated algorithms, have allowed accurate numerical solutions to the Schrödinger equation (Reimers, 1995). This section reports the results of an ab-initio calculation of the lithium-tin voltage profile. This work was a collaborative effort with a computational chemist at the National Research Council of Canada (Dr. John Tse). The goal of the collaboration was to attempt to utilize expertise and equipment to develop further understanding of the experimental problem at hand, not to become expert in quantum mechanical calculations or to fully understand

them. Of course, if the measured heats of formation were available for the Li-Sn alloys, this particular calculation would be irrelevant.

Several groups have performed first principles calculations for various electrode materials. Deiss et al. (1997) calculated the average voltage and energy density for $LiC_6/LiMoO_2$ (anode/cathode) and $LiC_6/LiNiO_2$ cells. Aydinol et al. (1997) calculated the average voltages for $Li/LiMO_2$ and $Li/LiCoX_2$ (M=Ti, V, Mn, Co, Ni, Cu, Zn, Al; X=O, S, Se) cells.

Consider the general first-order phase transition shown in the reaction of equation 3-1.

$$Li_x Y + \Delta xLi \rightarrow Li_{(x+\Delta x)} Y$$

(3-1)

The voltage plateau of the reaction of equation 3-1 is then,

$$V = \frac{-\Delta G}{\Delta x}$$

(3-2)

A further approximation can be made given that,

$$\Delta G = \Delta E + P\Delta V - T\Delta S$$

(3-3)

The change in internal energy, ΔE, will be the order of 0.1-4.0 (eV/Li atom). $P\Delta V$ is of the order of 10^{-5} (eV/Li atom), and $T\Delta S$ is the order of the thermal energy ($k_B T$) which is also much smaller than ΔE at ambient temperatures. Therefore,

$$V = \frac{-\Delta E}{\Delta x}$$

(3-4)

is a good approximation for the equilibrium cell voltage of the general two-phase reaction

shown in equation 3-1.

The energy difference, ΔE, is defined as,

$$\Delta E = E_{total} (Li_{(x+\Delta x)}Y) - E_{total} (Li_xY) - \Delta x[E_{total} (Li)]$$

(3-5)

where the total energies are obtained from the ab-initio calculation. Thus, the cell voltage is given by,

$$V = \frac{[E_{total} (Li_x Y) - E_{total} (Li_{(x+\Delta x)}Y)]}{\Delta x} - E_{total} (Li)$$

(3-6)

The seven two-phase regions of the Li-Sn phase diagram, and the structural complexity of some of these phases, made a first principles calculation of the lithium-tin voltage profile a large undertaking. The experimentally determined structures of the Li-Sn alloy phases, as well as lithium and tin, are listed in table 3-1. The most lithium rich phase, $Li_{22}Sn_5$, was not calculated as it proved to be too complex a structure to obtain a convergent solution.

Table 3-1 - Crystal structure information for the bulk Li-Sn phases

Name	Space Group	Lattice Constants	Reference
Sn	I4/amd	a=5.83Å, c=3.18Å	Wyckoff, 1982
Li_2Sn_5	P4/mbm	a=10.274 Å, c=3.125 Å	Hansen and Chang, 1975
LiSn	P2/m	a=5.17 Å, b=7.74 Å, c=3.18 Å, γ=104.5°	Muller and Schafer, 1975
Li_7Sn_3	$P2_1/m$	a=9.45 Å, b=8.56 Å, c=4.72 Å, γ=105.95°	Muller, 1974
Li_5Sn_2	R$\bar{3}$m	a=4.74 Å, c=19.83 Å	Frank et al., 1975
$Li_{13}Sn_5$	P$\bar{3}$m1	a=4.70 Å, c=17.12 Å	Frank et al., 1975
Li_7Sn_2	Cmmm	a=9.80 Å, b=13.80 Å, c=4.75 Å	Frank and Muller, 1975
Li	Im3m	a=3.51 Å	Wyckoff, 1982

The ab-initio calculations that were performed were based on 6 two-phase regions according to equation 3-1. The seven line phases have x = 0.0, 0.4, 1.0, 2.3333, 2.5, 2.6, and 3.5; so the width of the two-phase regions, Δx, are Δx=0.4, 0.6, 1.3333, 0.1667, 0.1, and 0.9.

Table 3-2 Optimized and experimental atomic coordinates for the Li-Sn alloy phases
Numbers in parenthesis are the experimental values if the value was changed during optimization.

Name	Space Group	Atom (site)	x	y	z
Li$_2$Sn$_5$	P4/mbm	Sn (8i)	0.0698 (0.0676)	0.2054 (0.2046)	0.0
		Sn (2d)	0.0	½	0.0
		Li (4h)	0.174 (0.172)	0.674 (0.672)	½
LiSn	P2/m	Sn (1a)	0.0	0.0	0.0
		Sn (2m)	0.234 (0.234)	0.0	0.658 (0.666)
		Li (1e)	½	½	0.0
		Li (2n)	0.271 (0.263)	0.5	0.328 (0.336)
Li$_7$Sn$_3$	P2$_1$/m	Sn (2e)	0.2228 (0.2251)	0.4013 (0.3995)	¼
		Sn (2e)	0.9153 (0.9179)	0.1955 (0.1974)	¼
		Sn (2e)	0.4304 (0.4318)	0.1974 (0.1979)	¼
		Li (2e)	0.724 (0.732)	0.397 (0.392)	¼
		Li (2e)	0.126 (0.134)	0.007 (0.007)	¼
		Li (2e)	0.620 (0.622)	0.995 (0.998)	¼
		Li (2e)	0.312 (0.318)	0.801 (0.803)	¼
		Li (2e)	0.830 (0.821)	0.812 (0.810)	¼
		Li (2e)	0.533 (0.533)	0.600 (0.601)	¼
		Li (2e)	0.015 (0.021)	0.602 (0.606)	¼
Li$_5$Sn$_2$	R$\bar{3}$m	Sn (6c)	0.0	0.0	0.0727 (0.0727)
		Li (6c)	0.0	0.0	0.355 (0.352)
		Li (6c)	0.0	0.0	0.213 (0.210)
		Li (3b)	0.0	0.0	½
Li$_{13}$Sn$_5$	P$\bar{3}$ m1	Sn (1a)	0.0	0.0	0.0
		Sn (2d)	1/3	2/3	0.7772 (0.7764)
		Sn (2d)	1/3	2/3	0.6090 (0.6091)
		Li (1b)	0.0	0.0	½
		Li (2c)	0.0	0.0	0.672 (0.668)
		Li (2c)	0.0	0.0	0.837 (0.836)
		Li (2d)	1/3	2/3	0.946 (0.943)
		Li (2d)	1/3	2/3	0.446 (0.445)
		Li (2d)	1/3	2/3	0.281 (0.284)
		Li (2d)	1/3	2/3	0.109 (0.117)
Li$_7$Sn$_2$	Cmmm	Sn (4i)	0.0	0.3189 (0.3127)	0.0
		Sn (4h)	0.161 (0.153)	0.0	½
		Li (2a)	0.0	0.0	0.0
		Li (2c)	½	0.0	½
		Li (4g)	0.342 (0.359)	0.0	0.0
		Li (4j)	0.0	0.172 (0.179)	½
		Li (8p)	0.187 (0.187)	0.159 (0.154)	0.0
		Li (8q)	0.342 (0.349)	0.161 (0.165)	½

An average voltage was calculated for each reaction in accordance with equation 3-6.

The pseudopotential planewave method (Kresse and Hafner, 1994) implemented in the Vienna ab initio simulation package (VASP) was used to compute the total energies of the Li-Sn alloy phases (Courtney et al., 1998). Initial calculations showed that a meaningful voltage profile could not be obtained with the experimental unit cell sizes and fractional atomic coordinates. The optimization of the atomic positions in the experimental unit cell led to more satisfactory results. The optimized, as well as experimental, atomic positions are shown in table 3-2. A tabulation of the calculated total energies for Li, Sn and the Li-Sn alloy phases is shown in table 3-3.

Table 3-3 Calculated total energies for Li-Sn phases

Name	Number of k-points	Total Energy (eV/formula unit)	Total Energy per Li_xSn (eV/formula unit)
Li	220	-2.034	N/A
Sn	196	-4.511	-4.511
Li_2Sn_5	144	-28.254	-5.651
LiSn	250	-7.294	-7.294
Li_7Sn_3	250	-32.296	-10.764
Li_5Sn_2	182	-22.389	-11.194
$Li_{13}Sn_5$	310	-57.292	-11.458
Li_7Sn_2	216	-27.135	-13.568

The calculated and experimental Li-Sn voltage profiles have been plotted in figure 3-6. The results show reasonable agreement. The true equilibrium voltage profile would be single valued with respect to charge and discharge, and would lie somewhere in between the charge and discharge curves. Since the experiment was not performed at an infinitesimally slow rate, then we do not measure the true equilibrium voltage profile. The calculation, on the other hand, assumes the equilibrium condition. There is a 'voltage-spike' in the calculation at around x=2.6, which is physically impossible. In addition, for 2.6<x<3.6, the

calculation predicts another two phase region and a corresponding plateau, which is not well

formed in experiment. In section 3.4 the discrepancies between experiment and theory shall

be discussed. Obviously, the initial assumption that the Li-Sn cell, at ambient temperature,

follows the Li-Sn phase diagram needs to be refined.

Figure 3-6 Experimental and calculated voltage profiles
for the electrochemical reaction of lithium with tin

The voltage of the two phase region Li_7Sn_2 to $Li_{22}Sn_5$ was not calculated, but a likely general location for this voltage is shown as a dashed line.
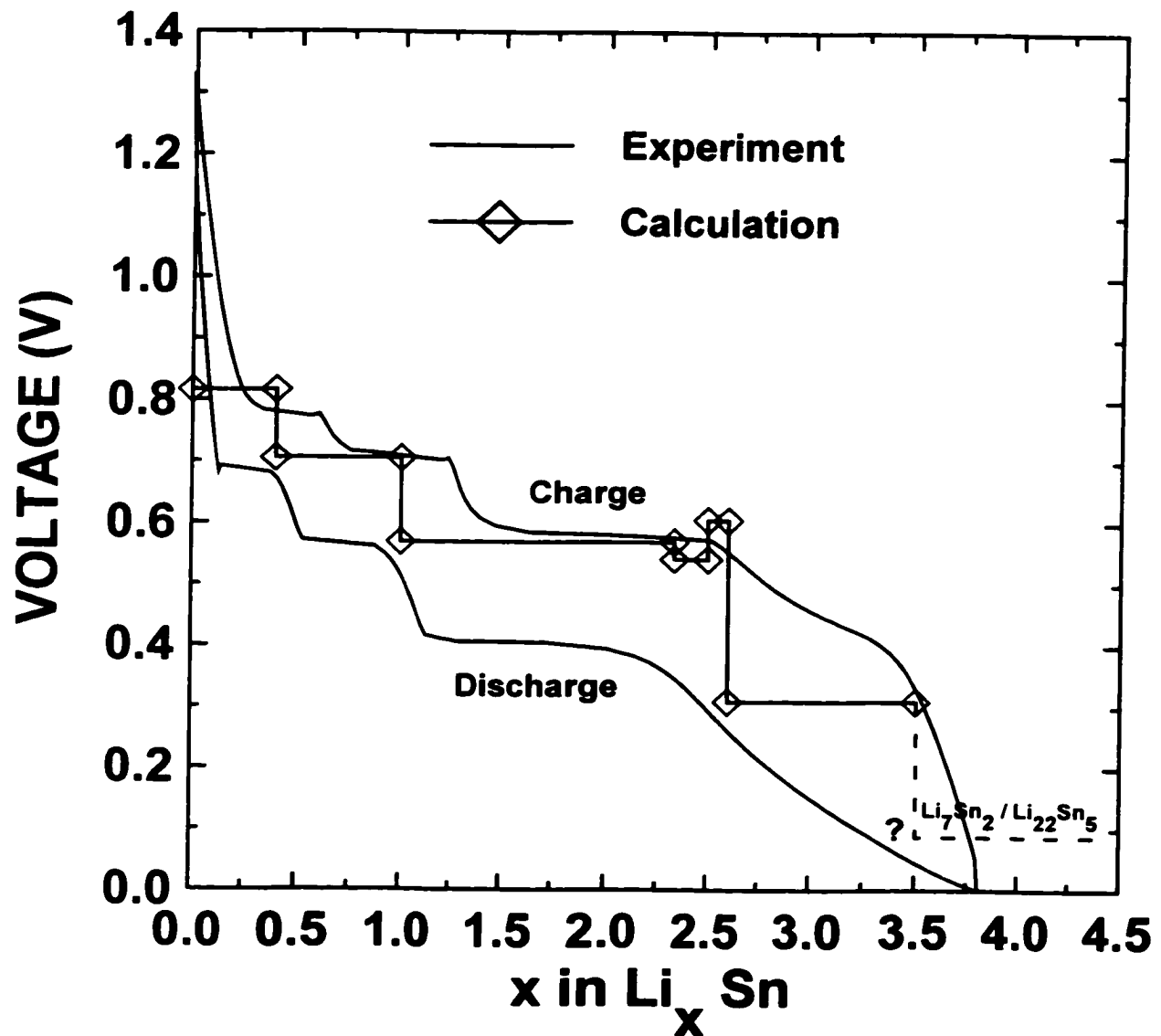
3.4 Short range ordering of lithium rich Li-Sn alloys prepared at ambient temperature in an electrochemical cell

The ab-initio calculation presented in the last section showed a departure from experiment for $2.6 < x < 3.6$ (in Li_xSn). Theory predicts two additional two-phase regions that are not well formed in experiment. This section will explain why the voltage plateaus for these regions are not observed in the experiment.

Figure 3-7 Ex-situ XRD pattern for an electrode at 0.0V, corresponding to $Li_{3.8}Sn$
Small Sn peaks arise from incomplete alloying reaction. Sharp peaks are indexed to a body centered cubic (BCC) structure of lattice constant $a= 3.30$ Å.
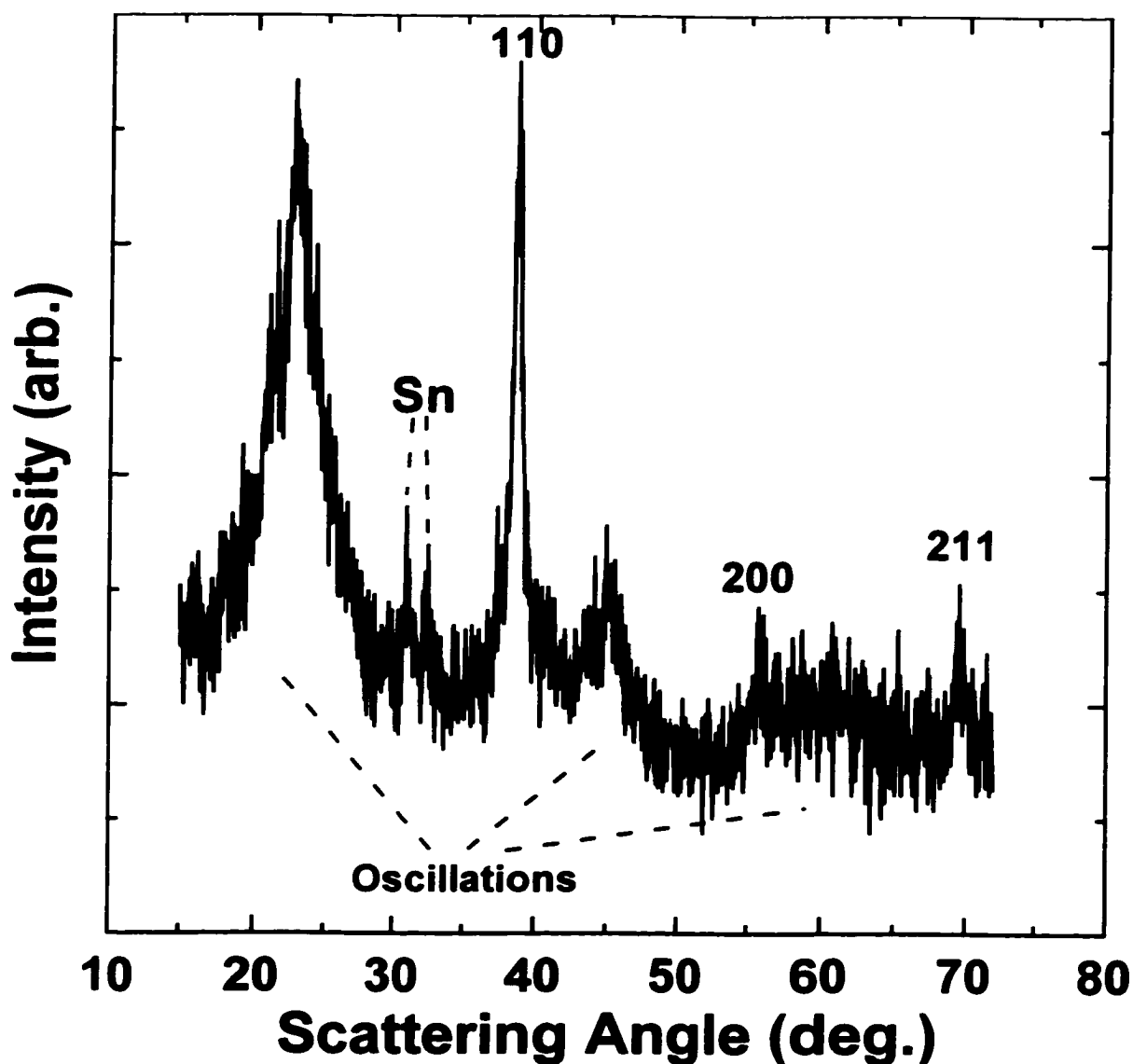
Figure 3-7 is a XRD pattern taken of a Li_xSn electrode at 0.0 volts, equivalent to the compound $Li_{3.8}Sn$. To obtain the electrode for this measurement, a cell that had been slowly discharged to 0.0 V was taken into an argon-filled glove box. It was then carefully opened and the electrode material was mounted in an air-tight x-ray holder. The holder was then taken out of the glove box and the XRD pattern of the electrode was measured. According to the Li-Sn phase diagram, this x-ray pattern should show both $Li_{22}Sn_5$ and Li_7Sn_2. However, the diffraction pattern does not agree with this prediction. The pattern shows both sharp peaks and broad oscillations from the sample. The sharp peaks are well indexed to a body centered cubic (BCC) structure with a lattice constant of a=3.30 Å, and the Miller indices of the BCC structure are shown next to each peak on figure 3-7. This interesting XRD pattern will be seen throughout this thesis, so it is worthwhile to understand it. This understanding has been previously presented by Dahn et al. (1998).

Table 3-4 Atomic positions for $Li_{22}Sn_5$. Space group F23, a=19.78 Å

Atom	Special Position	x	y	z
Li	4a	0	0	0
Li	4b	½	½	½
Li	4c	¼	¼	¼
Li	4d	¾	¾	¾
Li	16e	1/12	1/12	1/12
Li	16e	1/6	1/6	1/6
Li	16e	1/3	1/3	1/3
Li	16e	5/12	5/12	5/12
Li	16e	7/12	7/12	7/12
Li	16e	5/6	5/6	5/6
Li	24f	1/6	0	0
Li	24g	7/12	¼	¼
Li	48h	5/6	1/6	0
Li	48h	2/3	1/6	0
Li	48h	¼	1/12	1/12
Li	48h	¾	1/12	1/12
Sn	16e	0.914	0.914	0.914
Sn	16e	0.664	0.664	0.664
Sn	24f	0.321	0	0
Sn	24g	0.0711	¼	¼

In order to understand the pattern in figure 3-7, consider the structure of $Li_{22}Sn_5$ as given in the literature (Gladyeshevski et al., 1964). Table 3-4 gives the atomic positions for the structure of $Li_{22}Sn_5$. The structure is based on a BCC sub-cell with lattice constant a=3.296 Å. The tin and lithium atoms are arranged on this BCC network to give a 6x6x6 superstructure with a=19.78 Å. The arrangement of Sn atoms is most interesting. All the tin atoms are found on tetrahedra as shown in figure 3-8(a). The atom at the center of the Sn tetrahedron is a Li atom, and in figure 3-8(b) the tetrahedron itself is shaded, obscuring the Li atom in its centre. Figure 3-8(c) shows a portion of the $Li_{22}Sn_5$ unit cell containing 64 BCC sub-cells, with Sn tetrahedra indicated. Figure 3-8(d) shows all the tin atoms in a complete unit cell, and does not show the lithium atoms. All the tin atoms are contained in tetrahedra, which are either isolated, share edges or share corners.

Given the complex superstructure adopted by the Sn tetrahedra in $Li_{22}Sn_5$, it is likely that $Li_{4.4}Sn$ prepared at room temperature, by the electrochemical reaction of a solid material in an electrode, would not show well developed long-range order of the Sn tetrahedra. Model calculations were therefore undertaken to explore whether a simple random arrangement of Sn tetrahedra on the underlying BCC lattice could explain the observed pattern in figure 3-7.

The Debye scattering formalism, was used to calculate the powder pattern of the model lattices. Figure 3-9(a) shows the calculated powder diffraction pattern of a tin tetrahedron with an edge length of 4.67 Å, which is the size and shape of the tetrahedron in figure 3-8(b). The first and second peaks in the calculation are at about $23°$ and $42°$, close to the broad peaks observed in the data. This suggests that tin tetrahedra can be responsible for the broad peaks in the experimental pattern of figure 3-7.

Figure 3-8 The structure of Li₂₂Sn₅. *(a) a BCC unit of the structure which has 4 tin atoms.*
(b) showing how the 4 tin atoms in a) are on the corners of a tetrahedron. (c) a portion of
the unit cell of Li₂₂Sn₅ showing the arrangement of tin tetrahedra and Li atoms. Individual
tin atoms are shown where they are in tetrahedra which are not entirely included in the
view. Some Li atoms are omitted on the faces of the diagram. (d) All the tin atoms which
reside in a unit cell of Li₂₂Sn₅ shown in their tetrahedra.
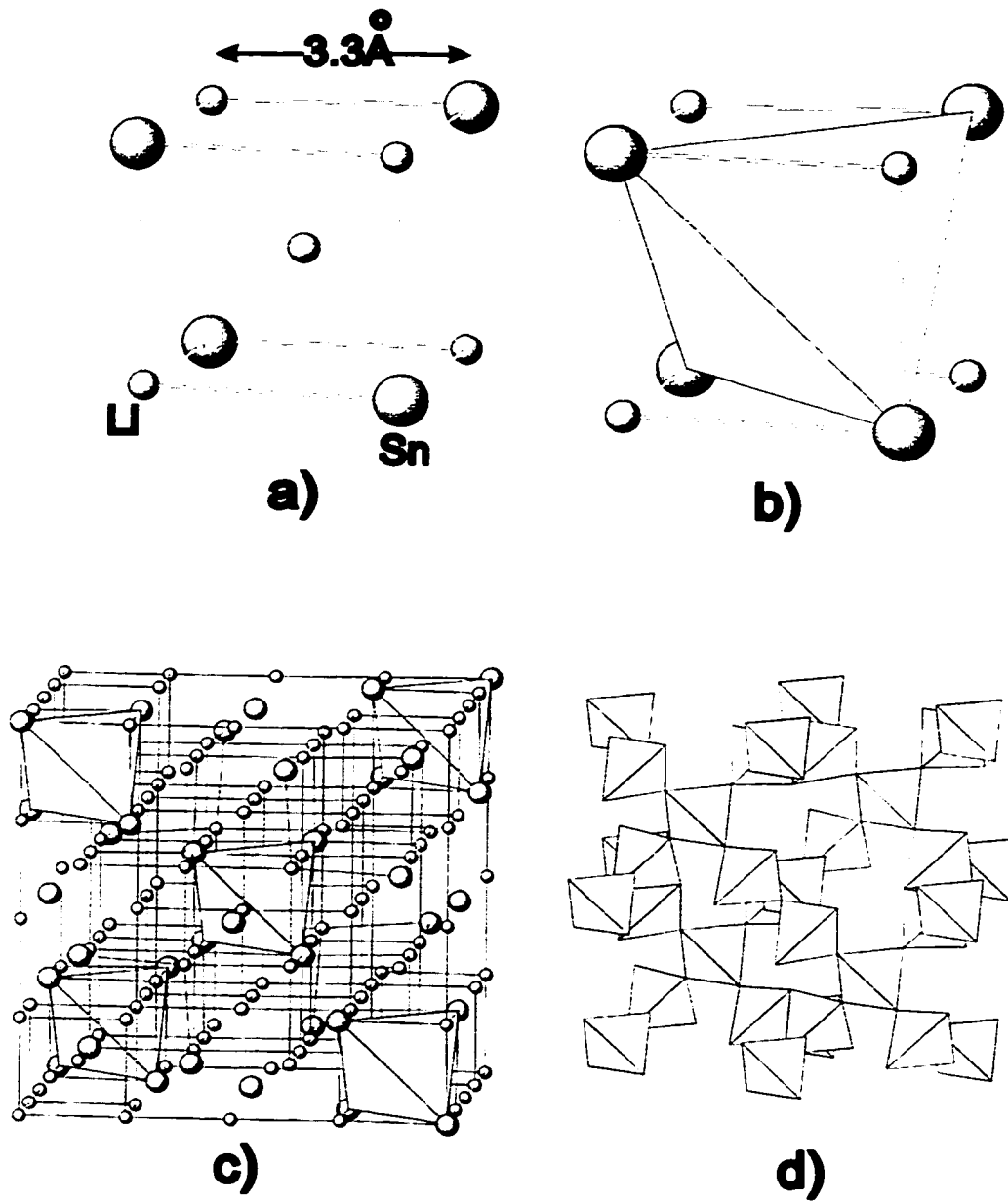
Figure 3-9 Powder diffraction patterns calculated for a) tin tetrahedron, b) tin tedrahedra randomly arranged on the underlying BCC lattice (see text), c) A calculation based on 5 tin clusters. The experimental data of figure 3-7 is shown for comparison in d).
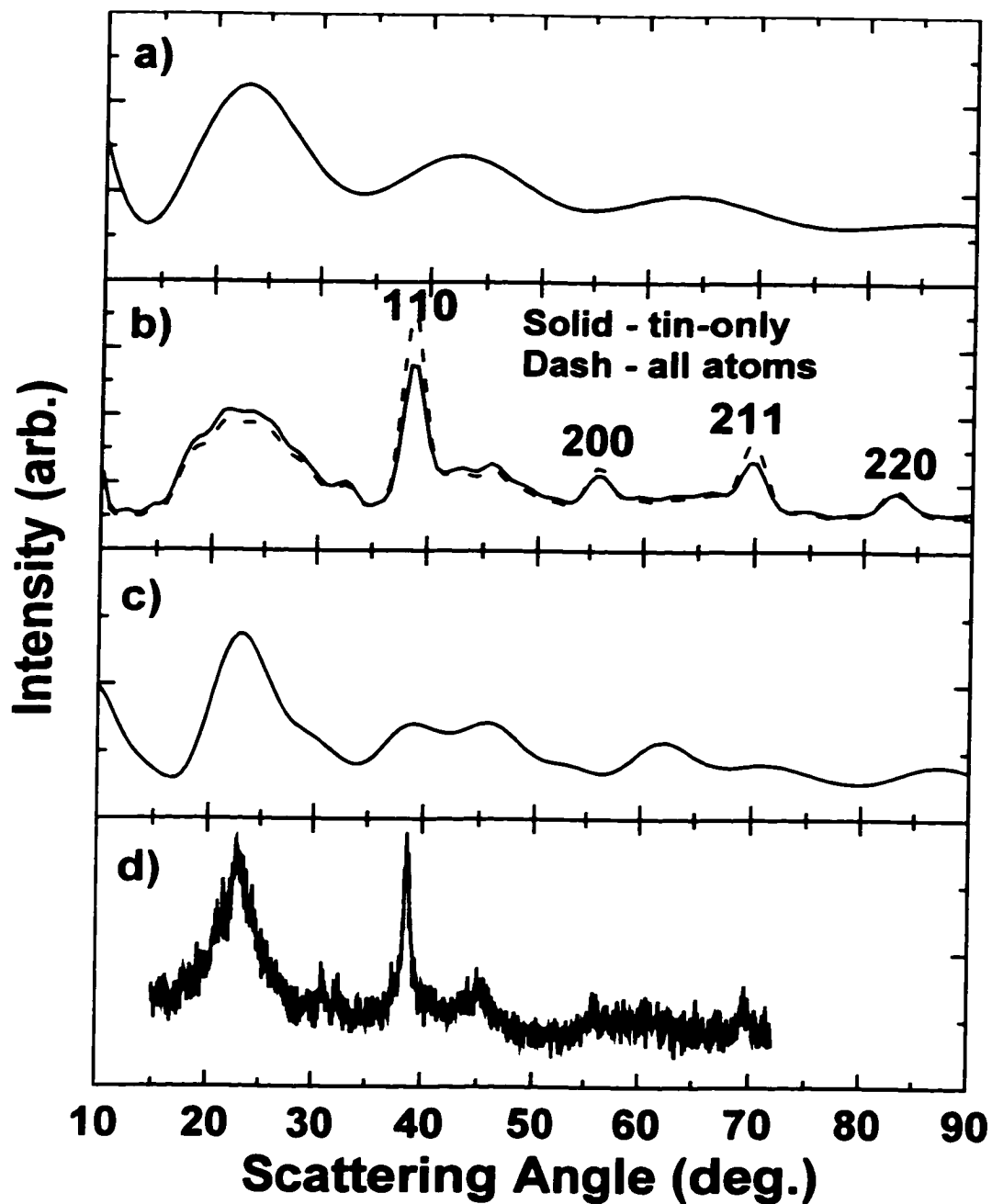
Figure 3-9 (b) shows a calculation for a lattice consisting of 1000 BCC sub-units arranged on a 10x10x10 grid. Tin atoms were placed on tetrahedra as shown in figure 3-8 (b), and these tetrahedra were located randomly throughout the lattice. The remaining sites were

filled with lithium, and a lithium:tin ratio of 4:1 was used. This pattern shows the same oscillatory pattern from the tin tetrahedra as does figure 3-9 (a), and in addition, the sharp Bragg peaks from the underlying BCC structure emerge from the calculated pattern. Figure 3-9 (b) also shows the result of the calculation for the same lattice if the lithium atoms are omitted. This is almost identical, because the scattering power of the lithium atom is small compared to the scattering power of a tin atom. However, the tin-only result shows that the sharp Bragg peaks arise due to the placement of the atoms making up the tin tetrahedra on the underlying BCC lattice. By comparing figures 3-9 (a) and 3-9 (b), the effects of the short-range order of the tin atoms can be investigated by doing calculations of tin clusters alone, assuming that the atoms of the clusters "fit" onto the underlying BCC lattice.

The calculations in figures 3-9 (a) and 3-9 (b) are suggestive that the correct explanation of the diffraction pattern of $Li_{4.4}Sn$ is at hand. However, the first broad peak in the calculation is much broader than experiment (figure 3-9 (d)). The width of the broad peak can be narrowed if the tin atoms are arranged into larger clusters. Figure 3-9 (c) shows the powder diffraction pattern that an arrangement of 5 tin tetrahedra would give. Notice that the shape of the first peak matches experiment more closely. This type of calculation was explored for various Li-Sn ratios (Li_xSn, $3.0 < x < 4.0$), with similar results (Dahn et al., 1998).

3.5 Summary

The purpose of this chapter has been to investigate the reaction of lithium with tin, as a fundamental understanding of the reaction of lithium with tin is important to most of the work in this thesis. The inter-metallic phases of the Li-Sn binary phase diagram have been studied by both XRD and ME spectroscopy. The ME spectra shall serve as 'fingerprints' for

in-situ ME experiments performed. The XRD patterns of the Li-Sn alloys show at least two distinct types of structure present. The alloys from Li_7Sn_3 to $Li_{22}Sn_5$, which shall become known as 'lithium-rich' alloys, have similar XRD patterns with several lower angle peaks $(20°$ to $25°)$ and a distinctive peak at around $38°$. This peak at $38°$ is as a result of the 110 reflection for BCC sub-structure.

The crystalline structures of the Li-Sn phase diagram exhibit long-range ordering of tin tetrahedra on an underlying BCC lattice $(38°$ peak). In the electrochemical reaction of lithium with tin at room temperature, the binary phase diagram is not followed exactly. The phases Li_2Sn_5 and LiSn form easily on discharge, however, the lithium-rich phases do not. A characteristic XRD pattern for all lithium-rich phases is understood in terms of model lattices. Short-range ordering of the tin atoms in the lithium-rich phases is apparent in XRD measurements. The broad feature at low angle $(20°-25°)$ of the XRD pattern of the poorly formed lithium rich alloys is explained by short-range ordering of clusters of tin tetrahedra.

Chapter 4

Effects of finite grain size on XRD, the ME and the electrochemical response

4.1 Motivation

The reaction mechanism of lithium with SnO is the basis for all of the work in this thesis. So how does lithium react with tin oxide? Let us suppose that SnO is first reduced by lithium to form Sn and Li_2O, which is shown by the reaction in equation 4-1.

$$SnO + 2Li \rightarrow Sn + Li_2O$$

$$(4-1)$$

According to thermodynamics, the reaction described in equation 4-1 is favourable. The free energies of formation of the reactants and products are: SnO (ΔG_f^o = -61.4 kcal/mol), Li (ΔG_f^o = 0), Sn (ΔG_f^o = 0) and Li_2O (ΔG_f^o = -134.13 kcal/mol) (Handbook of Chemistry and Physics, 70th edition). The free energy of formation for the reduction of SnO by Li is then,

$$\Delta G_{f,4-1}^o = -1.58 \frac{eV}{Li\ atom} ; (1 kcal/mol = 4.33 \times 10^{-2}\ eV/Li\ atom)$$

The equilibrium potential of such a reaction, measured with respect to lithium metal, will be V=1.58 volts. After SnO has been reduced to Sn, the reaction should proceed further with the alloying of lithium and tin. The alloying reaction should occur at less the 0.8V, as has been shown in chapter 3.

The reduction of a solid sample of SnO, at ambient temperature, may not result in well-ordered products, such as crystalline Sn and crystalline Li_2O having micrometer size grains. Therefore, grain size, where a grain is defined to be a single unit that coherently diffracts x-rays, could be an important factor in experimental work. We now examine how

53

grain size affects the experimental results of the techniques used; specifically, XRD, ME spectroscopy and the equilibrium voltage profile.

4.2 Finite grain size effects on XRD

Figure 4-1 shows the results of Debye calculations done on model Sn lattices of various grain sizes. The structure of Sn (Wyckoff, 1982) was used to build different sized lattices of Sn. A '5X5X5' model lattice is composed of five unit cells of Sn wide by 5 unit cells high by 5 unit cells long. The '20X20X30' model lattice has 20 unit cells each in the a and b crystallographic directions and 30 unit cells in the c direction. The calculations were performed with an atomic form factor of unity for all angles, as the form factor is not essential for the point of this discussion. The grain sizes quoted in figure 4-1 are based on the largest lattice constant of Sn ($a = 5.83$ Å) multiplied by the length of the model lattice. For example, the '5X5X5' lattice has an approximate 'diameter' of 5X5.83 = 29 Å.

Figure 4-1 (a) is a measured powder XRD pattern for crystalline Sn. Note that the characteristic 'doublet' at around 32 ° does not appear in any of figures 4-1 (d), (e), or (f), where grain sizes are less than 60 Å. It begins to appear in the calculation for the '15X15X15' model lattice (figure 4-1 (c)), or at 87 Å grain size. The '20X20X30' model lattice (figure 4-1 (b)) shows that the doublet at 32° is well defined, yet the higher angle doublet (44°) is not. The '20X20X30' model lattice represents 24,000 Sn atoms, and an approximate grain size of 115 Å.

Figure 4-1 Finite grain size effects on the XRD pattern, (a) Crystalline Sn (measured) and calculated patterns for, (b) 20X20X30 unit cells of Sn, (c) 15X15X15, (d) 9X9X9, (e) 5X5X5, and (f) 2X2X2.

The atomic positions and lattice constants of the crystal structure for Sn were used (Wyckoff, 1982). A '5X5X5' grain is a grain composed of 5 unit cells of Sn wide by 5 units cells long by 5 unit cells high. A '20X20X30' is 20 cells by 20 cells in the a and b crystallographic directions by30 cells in the c direction. The grain sizes quoted are the maximum dimension, which is based on the largest lattice constant of Sn (a = 5.83 Å). The calculations do not include the atomic form factor for Sn.
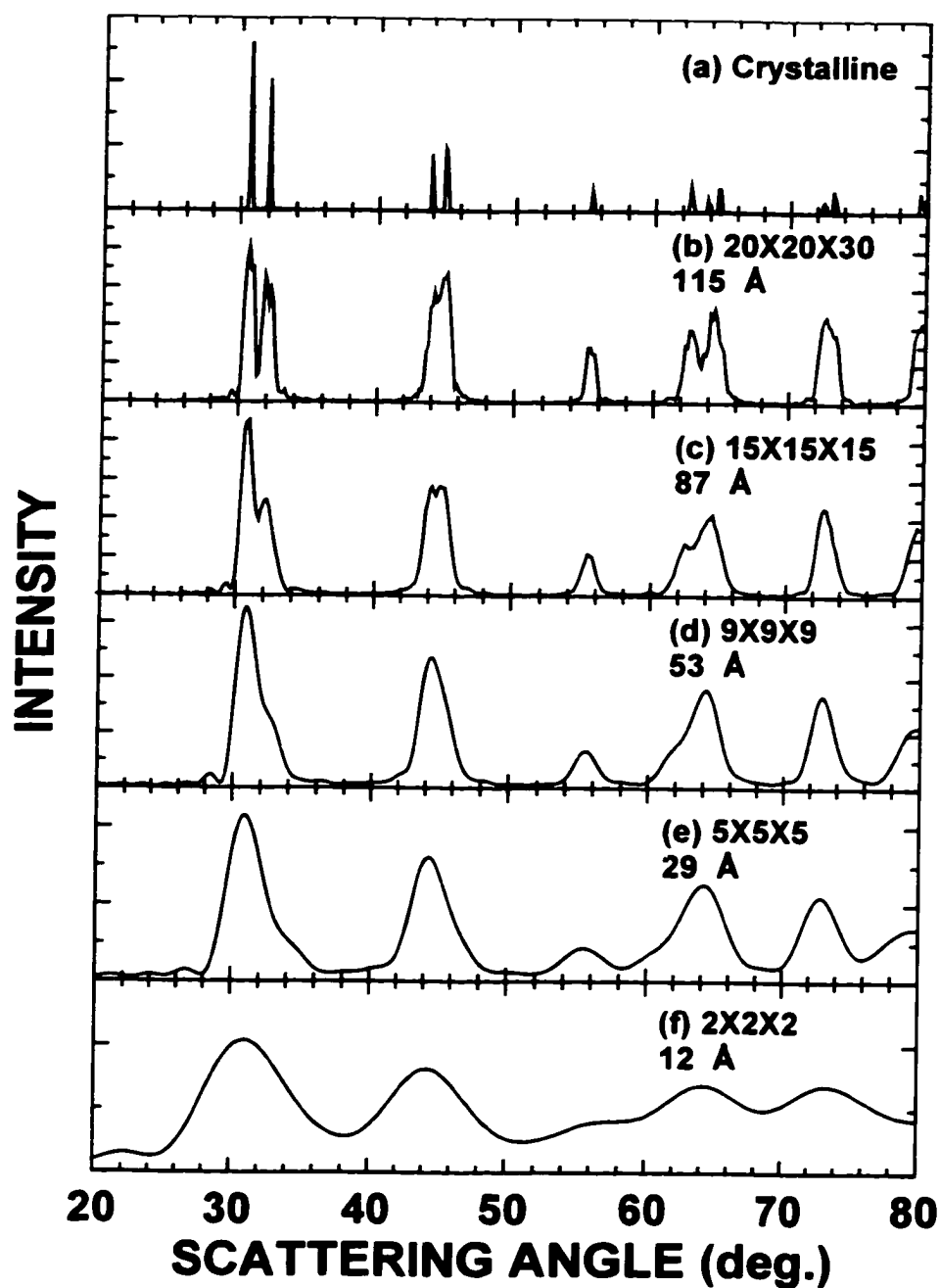
Figure 4-2 Peak width of the 301 reflection for the XRD patterns of figure 4-1: (a) Crystalline Sn (measured) and calculated patterns for, (b) 20X20X30 unit cells of Sn, (c) 15X15X15, (d) 9X9X9, (e) 5X5X5, and (f) 2X2X2.

The atomic positions and lattice constants of the crystal structure for Sn were used (Wyckoff, 1982). A '5X5X5' grain is a grain composed of 5 unit cells of Sn wide by 5 units cells long by 5 unit cells high. A '20X20X30' is 20 cells by 20 cells in the *a* and *b* crystallographic directions by30 cells in the *c* direction. The grain sizes quoted are the maximum dimension, which is based on the largest lattice constant of Sn (a = 5.83 Å). The calculations do not include the atomic form factor for Sn.
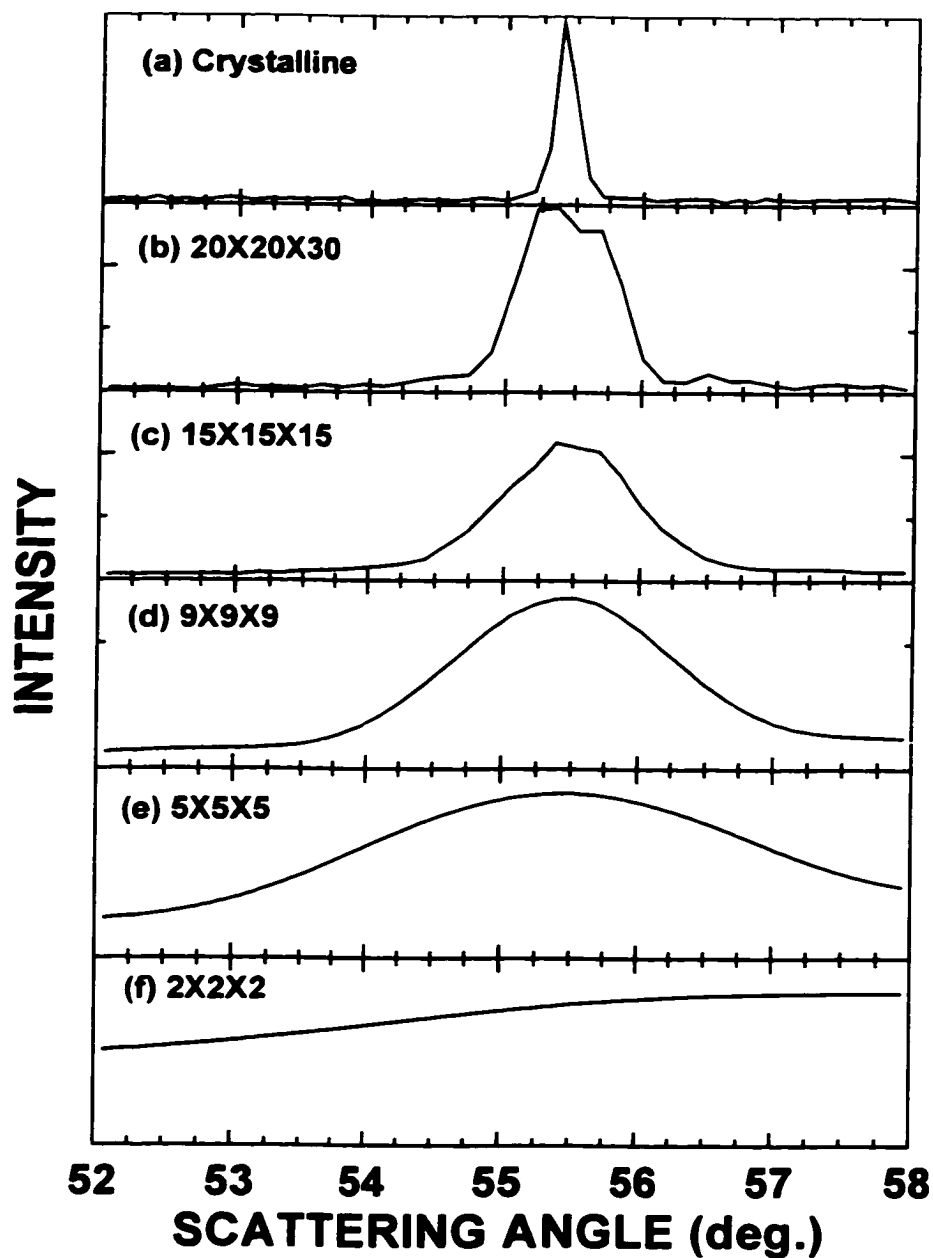
The Scherrer equation (equation 2-12) can be used to determine the grain sizes of the model lattices, and crystalline Sn, from their respective XRD patterns. Figure 4-2 shows the 301 reflection for Sn for the same model lattices described in figure 4-1. Table 4-1 lists the grain size (based on the maximum dimension of the model lattice), the FWHM for the 301 reflection (from figure 4-2), and the calculated grain size by the Scherrer equation.

Table 4-1 Grain size of the model lattices; by their maximum dimension, their average dimension and by the Scherrer equation applied to their XRD patterns

Lattice	Figure	Grain size by maximum dimension (Å)	Grain size by average dimension (Å)	FWHM of 301 peak (radians)	Grain size by Scherrer equation (Å)
Crystalline	4-1, 2 (a)	N/A	N/A	0.0044	368
20X20X30	4-1, 2 (b)	115	109	0.0174	93
15X15X15	4-1, 2 (c)	87	74	0.0218	74
9X9X9	4-1, 2 (d)	53	44	0.0414	39
5X5X5	4-1, 2 (e)	29	25	0.0709	23

The grain sizes, as calculated by the Scherrer equation, are consistently smaller than that of the maximum dimension of the model lattices. The Scherrer equation assumes a cube of length L (equation 2-12), but the structure of Sn is not cubic, it is tetragonal (a = 5.83 Å and c = 3.18 Å). An average dimension should be used for the grain size of the model lattice (Warren, 1969), and table 4-1 shows that this agrees well with the Scherrer formula. Therefore, application of the Scherrer equation to broad x-ray peaks allows a reliable estimate of grain size to be made.

4.3 Finite grain size effects on the ME

ME spectroscopy is an effect of condensed matter, '... the (ME) is not detectable in gases and non-viscous liquids' (Greenwood and Gibb, 1971). Consider a free atom that

undergoes an excited to ground state transition, resulting in the emission of a photon of energy E_γ. The emission of the photon causes recoil of the atom, with a corresponding change in its velocity. Assume that the atom had a non-zero velocity before the emission, for instance, velocity due to thermal vibration. The energy difference between the energy of the transition and E_γ is equal to the energy due to the thermal motion plus the energy due to recoil. For a free atom the recoil energy is of the order of 10^{-3} eV and the thermal, or 'Doppler-effect energy', is of the order of 10^{-2} eV. The Doppler effect energy leads to a distribution of photon energies. The natural width of the ^{119}Sn Mössbauer transition is only $\sim 10^{-8}$ eV. Therefore, the probability for the absorption of a γ-ray by a nucleus which is free to recoil and is vibrating thermally is of the order $10^{-8}/(10^{-2} + 10^{-3}) = 10^{-6}$. Therefore the ME is not observed for gases and most liquids.

The recoil energy, E_R, and the Doppler-effect energy, E_D, are related to E_γ and to the mass, M, of the emitting unit, as follows (Greenwood and Gibb, 1971),

$$E_R \propto \frac{E_\gamma^{\,2}}{M} \quad ; \quad E_D \propto E_\gamma \sqrt{\frac{1}{M}}$$

The ME can be observed in condensed matter because it is the mass of a grain ($\sim 10^{15}$ atoms), no longer the individual atom, that determines E_R. In solids, the recoil energy and Doppler-effect energy are negligible. For example, in an extended solid containing ^{119}Sn, E_R is ten orders of magnitude smaller than the natural line-width of the photon produced.

This is, of course, somewhat simplified. The emission of a photon can either lead to a 'recoil-free' event or can cause a phonon excitation in the lattice. The probability of the photon producing a recoil-free event is called the recoil-free-fraction (RFF), f, which is derived from quantum mechanics.

The RFF is determined from the mean atomic displacement squared, $\langle x^2 \rangle$, and the photon

energy. E_γ, as follows,

$$f = \exp\left[\frac{-E_\gamma^2 \langle x^2 \rangle}{(\hbar c)^2}\right]$$; $\hbar$ = planck's constant, c = speed of light

(4-2)

There is a simple relationship, based on a Debye-model of the phonon spectrum (for a

discussion of the Debye model, see Ahscroft and Mermin, 1976), that relates the RFF to the

ambient temperature, T, and to the Debye-temperature, Θ_D, of a material (Greenwood and

Gibb, 1971).

$$f \approx \exp\left[\frac{-6E_R T}{k_B (\Theta_D)^2}\right]$$

A word of caution, however, as the use of the Debye model to extract information from the

RFF is an approximation. The assumption that the mean atomic displacement is isotropic

(i.e., $\langle x^2 \rangle = \langle y^2 \rangle = \langle z^2 \rangle$) is not always valid (Shenoy et al., 1978).

Flinn (1978) calculated values for f(295K) for [119]Sn, as a function of Θ_D, which are

reproduced in table 4-2.

Table 4-2 Calculated recoil-free-fraction (RFF) at 295 K and second order doppler shift (SOD)(77-295) for [119]Sn as a function of the Debye temperature, Θ_D. (From Flinn, 1978).

Θ_D (K)	Recoil-free-fraction, f	Second order doppler shift (SOD) (mm/s) (at 295K with respect to 77K)
100	0.005	0.075
150	0.096	0.072
200	0.268	0.069
250	0.431	0.066
300	0.577	0.061
350	0.651	0.056
400	0.720	0.049

Table 4-2 also shows the 'second order doppler shift' (SOD) as a function of the Debye temperature of materials containing Sn. The SOD, which is a relativistic effect, is a change in the isomer shift of a transition due to lattice vibrational velocities,

$$\Delta(\text{Isomer Shift, IS}) = \frac{\langle v^2 \rangle}{2c^2}; v \text{ is the lattice vibrational velocity}$$

The isomer shift (IS) is for the resonant absorption at 0K, the SOD changes the IS at a given temperature, and the center shift (CS) (that is measured at the temperature of measurement) is the IS plus the SOD.

Collins et al. (1978) compare, by the ME, an Sn_x/SnO_{1-x} composite (grain size < 25 Å) and SnO_2 (grain size < 25 Å) to their crystalline equivalents, SnO and SnO_2, respectively. They infer the Debye temperatures of the materials by examining the temperature dependence of the RFF. A lower Debye temperature was inferred, in both cases, for the small grain samples compared to their crystalline counterparts. A summary of their results is shown in table 4-3. For both SnO and SnO_2, the linewidth of the resonant absorption becomes

Table 4-3 Summary of the results of Collins et al. (1978), who investigated grain size effects on ME spectroscopy of tin oxides

Linewidths quoted as full width at half maximum intensity (FWHM), and center shifts quoted relative to $CaSnO_3$

Sample	Linewidth (FWHM) (mm/s)	Center shift (295K) (mm/s)	Debye temperature, Θ_D (K)
Sn_x/SnO_{1-x} composite (< 25 Å)	1.23	2.871	181
SnO crystalline	0.916	2.678	203
SnO_2 (< 25 Å)	1.04	0.129	243
SnO_2 crystalline	0.965	0.004	313

broader for smaller grain size. Smaller grain size material typically has a distribution of Sn

sites due to the greater relative effect of the Sn sites on the surface than those in the bulk. The

sites on the surface are in slightly different electronic environments from the bulk sites, and

their center shifts are therefore different. This creates a distribution of center shifts resulting

in the broadening of the expected resonant absorption. Also notice the shift to higher center

shift for the small grain samples, consistent with a SOD effect. Hong et al. (1995) also

demonstrate the reduction in RFF for small grain Sn (70 Å, Θ_D = 133 K) compared with bulk

Sn (> 400 Å, Θ_D = 161 K).

There is a dramatic reduction in the melting points of many metals as their grain size

is reduced (see for example, Peters et al. (1998), Lai et al. (1996) and Martin et.al. (1994)).

Shi (1994) discusses and models the size dependant thermal vibrations and melting point

depression in nanocrystals. Shi's model relates the mean squared atomic displacement,

$\langle x(r) \rangle^2$, of the atoms in a grain of size, r, to the mean squared atomic displacement of the

atoms in a bulk crystal, $\langle x_B \rangle^2$, by a parameter α. This (α) is the ratio of the mean atomic

displacements of surface atoms to bulk atoms, in the limit of infinite grain size.

$$\frac{\langle x(r) \rangle^2}{\langle x_B \rangle^2} = \exp\left[(\alpha - 1)\frac{n_S}{n_B}\right] \quad ; n_S \text{ and } n_B \text{ are the number of surface and bulk atoms}$$

(4-3)

Assuming a spherical grain, then the ratio of the number of surface to the number of

bulk atoms can be expressed as a function of the radius, r, and the thickness, h, of a layer of

atoms on the crystallite surface.

This is incorporated into equation 4-3, as follows,

$$\frac{\langle x(r) \rangle^2}{\langle x_B \rangle^2} = \exp\left[\frac{(\alpha - 1)}{\left(\frac{r}{3h} - 1\right)}\right]$$

(4-4)

For face centered cubic crystals h = a/2, where a is the lattice constant, and for the diamond structure h = a/4. For a face centered tetragonal structure (for example, Sn), one could consider either face (i.e. h = a/2, c/2) or an average layer thickness, such as the average of the lattice constants (i.e. h = (a+b+c)/6). Shi's phomenological model is not expected to be accurate for r near 3h, or when r ~ 10 Å, since equation 4-4 diverges when r ≤ 3h.

Shi uses the Lindemann criterion for melting, which dictates that a crystal will melt when the root mean-square displacement of the atoms in the crystal exceeds a certain fraction of the inter-atomic distance. The Lindemann criterion has been shown to be valid for small grain size crystals (Hasegawa et al., 1993). Shi also uses the Debye model to obtain equation 4-5, which relates the melting point of a small grain, $T_m(r)$, to the bulk melting point, $T_m(bulk)$.

$$\frac{T_m(r)}{T_m(bulk)} = \exp\left[-\frac{(\alpha - 1)}{\left(\frac{r}{3h} - 1\right)}\right]$$

(4-5)

Equation 4-4 was used in conjunction with equation 4-2 in order to investigate the RFF (295 K) in Sn as a function of grain size. A value of f_{Sn}(295 K) = 0.039 (Greenwood and

Gibb, 1971) was used to obtain the mean squared atomic displacement of atoms in bulk Sn

(using equation 4-2, with E_γ = 24 keV). The results of these calculations, for various values

of α and h, are shown in figure 4-3. Phenomenologically, and considering a composite

material of small grain Sn in matrix that is not Sn, α is related to the 'stiffness' of the matrix

(Shi, 1994). Note the strong dependence on the RFF for small grain size (20 Å to 120 Å) on

the parameter α. The range encompassed by the particular values of α in figure 4.3 will be

used to model data in chapter 5. In section 5.4.2 the grain size dependent melting points of Sn

Figure 4-3 Recoil free fraction of Sn as a function of grain size
The calculations were based on the theory of Shi (1994) (see text). Three values of α were used, which are indicated. The surface layer thickness, h, is defined by the lattice constants for Sn (a, b = 5.83 Å and c = 3.125 Å), as shown on the graph. The plot for h = c/2 and α = 3.1 is not shown.
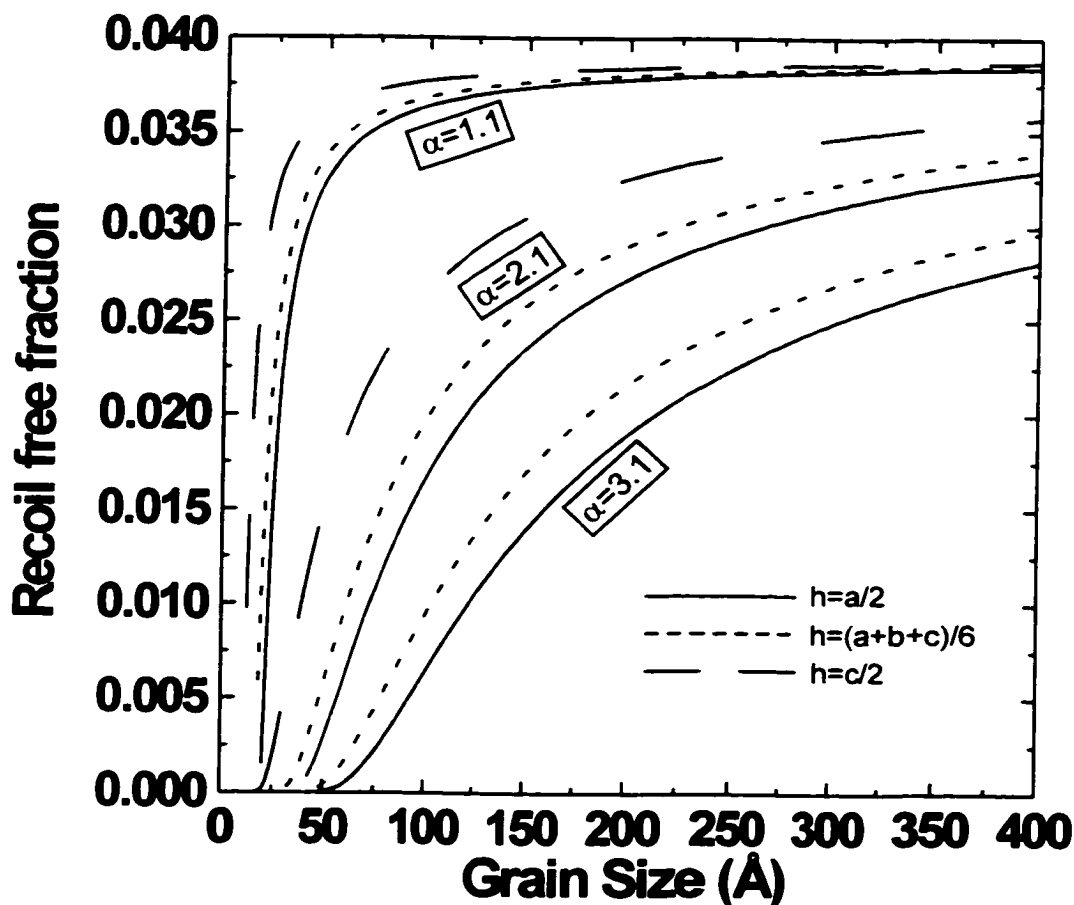
atoms in a SiO$_2$ matrix (Unruh et al., 1992) will be used to extract the value of α for this particular environment.

In summary, there are three factors of the ME measurement that may change during an in-situ ME experiment on a Li/SnO cell. The center shift (CS) will change as the Sn atom electronic environment differs in each of the Li-Sn alloy phases. The SOD may change for small grain size, which will change the CS, and the RFF, which can change as a function of grain size and matrix composition, will affect the total absorption counts.

4.4 Finite grain size effects on the voltage profile

A first-order phase transition shows as a region of constant voltage on a voltage profile, as was shown in chapter 3.

Figure 4-4 Differential capacity versus voltage for a Li/Sn cell (first discharge and first charge)
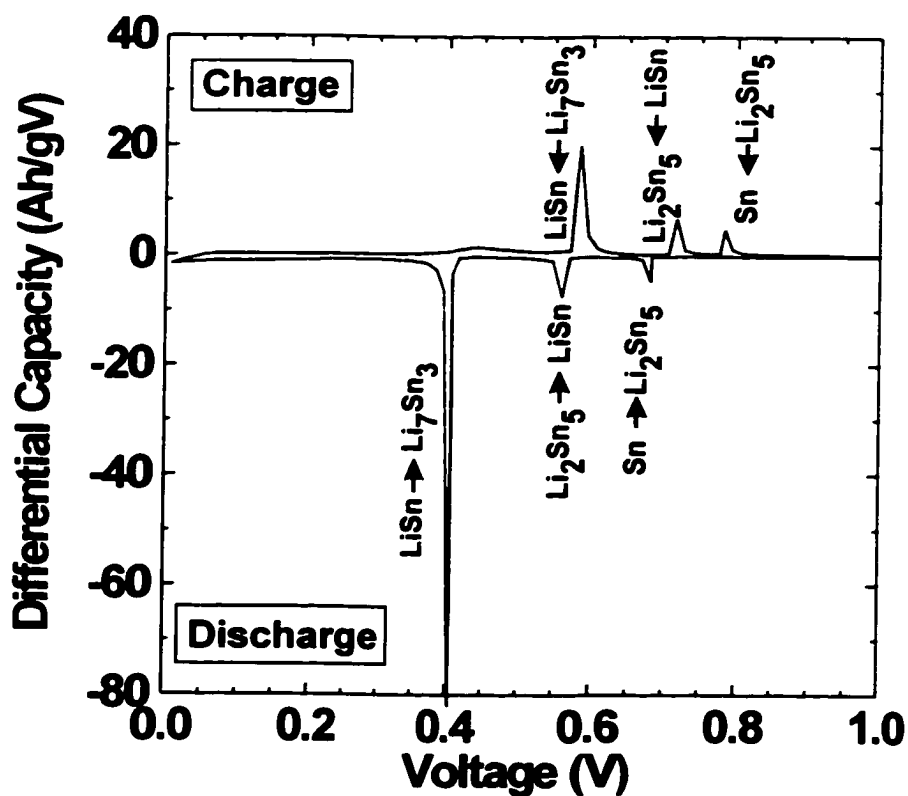
We often examine *differential capacity* (Ah/gV) versus voltage in order to investigate phase transitions more closely. A plateau (a two-phase co-existence region) will show as a peak on a differential capacity plot. Figure 4-4 shows differential capacity versus voltage for a Li/Sn cell. This is the same cell that was discussed in chapter 3. Note the well-defined peaks on the curve, which are indicative of two-phase regions. The appropriate two-phase reaction is indicated next to each peak.

An infinitesimal change in the free energy, dG, is produced by changes in the number of atoms, dx, and the temperature, dT, (assuming no change in pressure) as follows,

$$dG = -SdT + \mu dx$$

The differential capacity is proportional to $(\partial x/\partial \mu)_T$, which is a thermodynamic response in composition to a change in μ (McKinnon, 1980). This function will peak during a first-order phase transition (i.e. a plateau in voltage, in the absence of kinetic effects, means $\partial \mu \rightarrow 0$).

McKinnon also makes a useful analogy between the thermodynamic equation for a chemical reaction (in a cell, with no increase in pressure) and that of the magnetization, M, of a long cylinder in an external magnetic field, B. The thermodynamic equation for the latter is as follows,

$$dG = -SdT - MdB$$

The isothermal magnetic susceptibility, χ_T, is defined as,

$$\chi_T = \left(\frac{\partial M}{\partial B} \right)_T$$

The susceptibility is analogous to the differential capacity in that it measures the response of the magnetization to small changes in the applied field. There is a first order phase transition

for the magnetization at the critical point B = 0. This corresponds to the flipping of magnetic

spins in a ferromagnetic substance when the applied field changes direction.

Binder and Landau (1984) studied the effects of grain size on magnetic susceptibility

versus magnetic field at this first order phase transition. Their results, which were based on

calculations on model lattices with size parameter L, are reproduced in figure 4-5.

When the grain size is large (L = 10) the thermodynamic response function,

susceptibility, peaks around the first order phase transition. As the grain size is decreased the

response function broadens around the phase transition.

Figure 4-5 Magnetic susceptibility (χ_L) versus applied field (H)
as a function of grain size (from Binder and Landau, 1984)

The real value of size parameter, L, is unimportant. Larger L means larger grain size. This
calculation was assumed at $k_B T/J = 2.1$, where $k_B T_c/J = 2.269$.
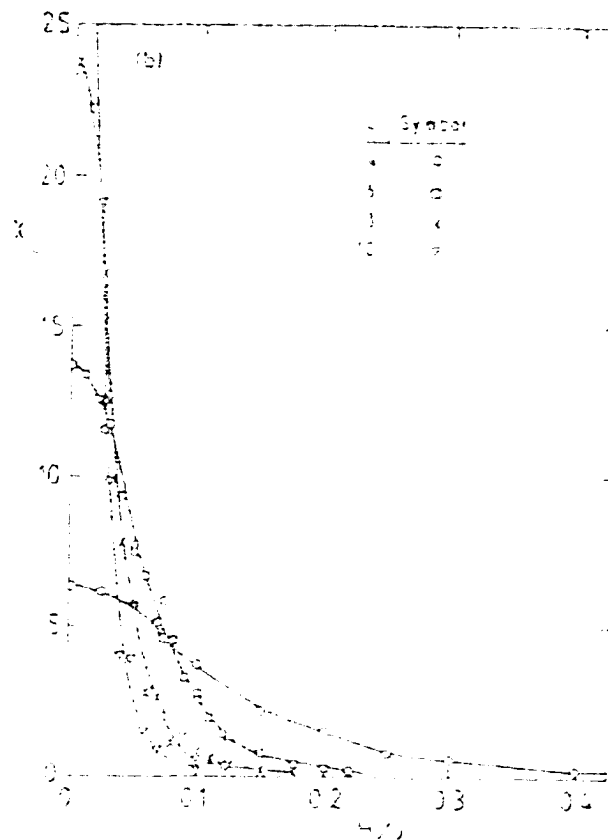
Having made the analogy with the electrochemical reaction response function, differential capacity, we can expect that the differential capacity will also become broader, around a first-order phase transition, as the grain size is reduced.

Figure 4-6 compares the differential capacity of two different grain-sized materials. Figure 4-6 (a) shows the differential capacity for the electrochemical reaction of lithium with bulk Sn (the same cell of figure 4-4). Figure 4-6 (b) is the differential capacity of the electrochemical reaction of lithium with small grain (< 45 Å) SnO_2. It is obvious that, like susceptibility versus applied magnetic field, the peaks of a differential capacity versus voltage plot become broader as the grain size is reduced.

Figure 4-6 Differential capacity versus voltage for cells of,
(a) Li/(Bulk Sn) and (b) Li/(Small grain SnO₂, 45Å)

Notice the change of vertical scale, The peaks in differential capacity are really much larger for bulk Sn than for small grain SnO_2 than the graph displays. By all rights, we should compare them on similar scales. However, the features of the small grain (b) material would be insignificant in comparison to the large grain (a).
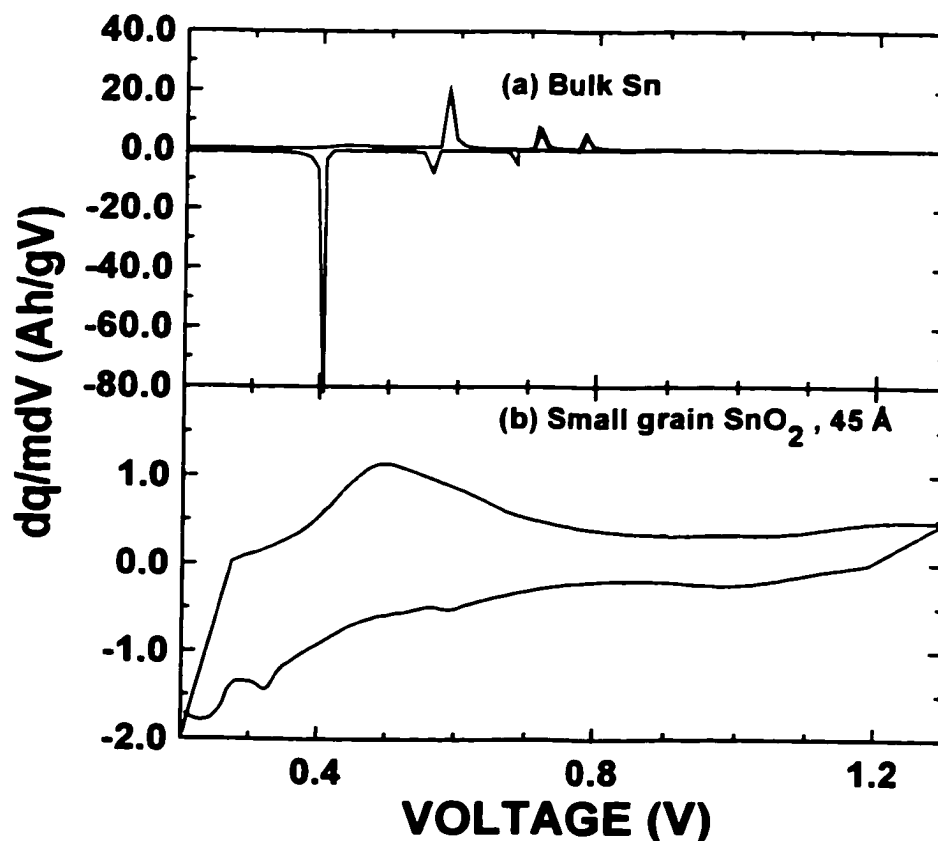
Chapter 5

First cycle reaction mechanism

5.1 Crystalline SnO

Equation 5-1 shows the suggested reaction mechanism of lithium with SnO, which has already been proposed in chapter 4. The reaction is two-step; 'step1' corresponds to the reduction of SnO by Li (at an expected potential difference of 1.58 V versus lithium metal, and 'step 2' is the Li-Sn alloying reaction which should occur at less than 0.8 V.

$$SnO + 2Li \xrightarrow{step\,1} (1.58V)\,Sn + Li_2O$$
$$Sn + Li_2O + 4.4Li \xrightarrow{step\,2} Li_{4.4}Sn\,(<0.8V) + Li_2O$$

$$(5-1)$$
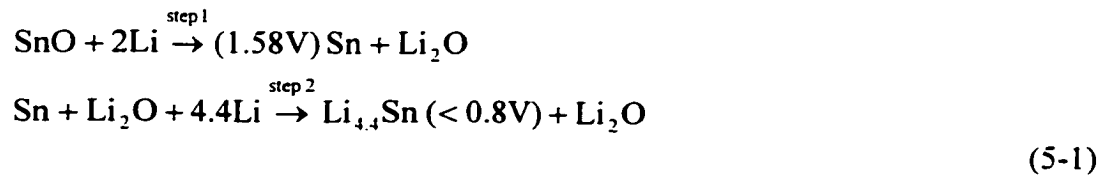
The specific capacity of reaction 5-1 (step 1) is easily calculated based on transferring 2 moles of lithium per mole of SnO,

$$specific\ capacity\ (step\,1) = 397\,\frac{mAh}{g\,(SnO)}$$

The specific capacity of reaction 5-1 (step 1 and step 2), the overall reaction, is calculated based on reacting 6.4 moles of lithium per mole of SnO,

$$specific\ capacity\ (step\,1 + step\,2) = 1270\,\frac{mAh}{g\,(SnO)}$$

The proposed reaction mechanism (equation 5-1) will be established, in the sections that follow, by electrochemical measurement, in-situ XRD and in-situ ME spectroscopy.

5.1.1 Electrochemical measurement

Li/SnO cells of SnO powder (Aesar, 99.9%) were constructed and were discharged and charged using a specific constant current of 18.6 mA/g, between lower and upper voltage limits of 0.0 and 2.5 V, respectively. The voltage profile for SnO is shown in figure 5-1.

Figure 5-1 Voltage profile for a Li/SnO cell (first 3 half-cyles)

The calculated capacity for 'step 1' (SnO + 2Li → Sn + Li_2O) is indicated by an arrow. The calculated capacity for 'step 2' (Li_2O + Sn + 4.4Li → $Li_{4.4}Sn$ + Li_2O), per gram SnO, is also indicated. The reverse reactions (for charge), '-step1' and '-step 2', are shown
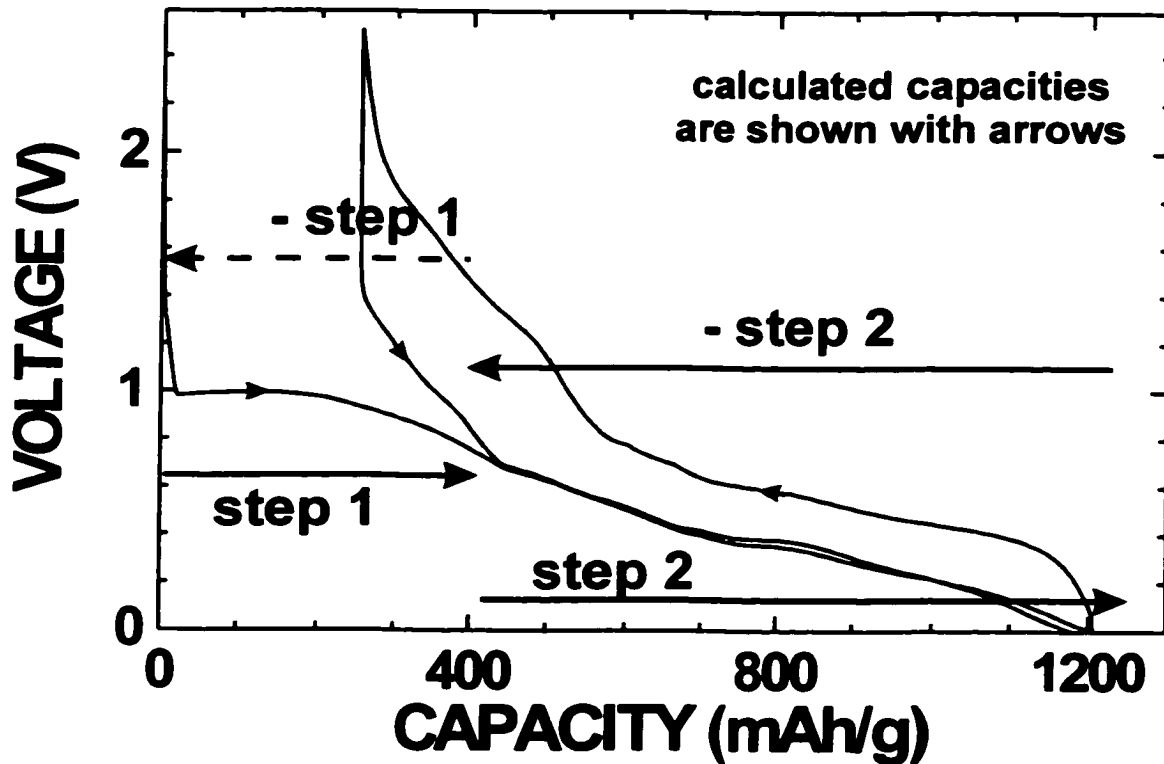
The reactions in steps 1 and 2 (of equation 5-1) appear to match experiment. There is a long sloping plateau at around 1.1 V on the first discharge, corresponding to step 1. The calculated capacity of the alloying of lithium with tin (step 2, at <0.8V) also matches well with experiment. During charge, the calculated capacity of the de-alloying reaction (- step 2) is indicated. The re-formation of SnO (- step 1) is indicated by a dashed arrow, as the calculated

capacity does not match with experiment. Apparently, SnO does not re-form completely during charge.

Figure 5-2 Differential capacity versus voltage for cells of (a) Sn and (b) SnO
The first discharge (dashed line), first charge (solid line) and second discharge (solid line) are shown. Note the large irreversible capacity of the SnO cell on the first discharge.
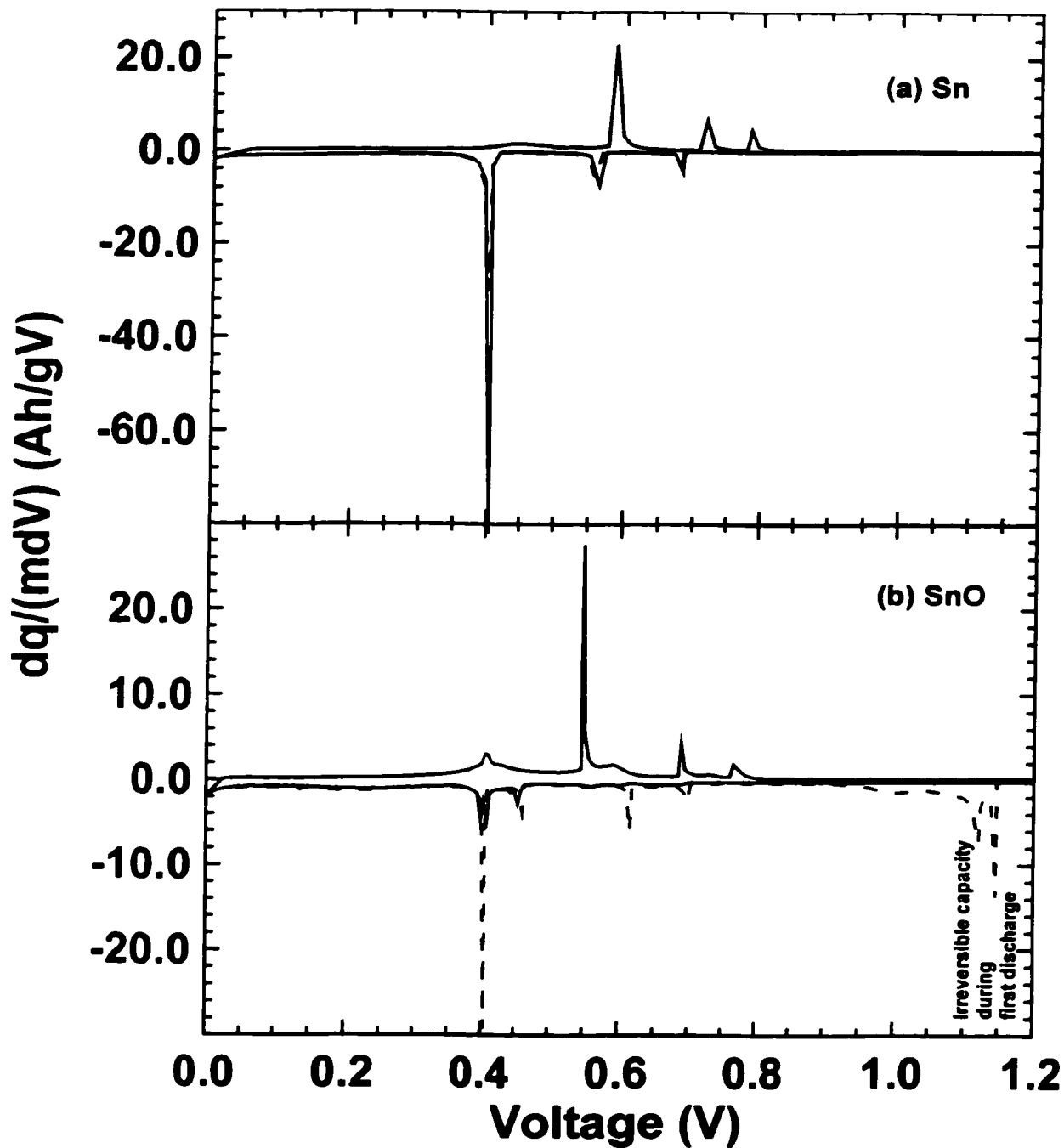
Figure 5-2 shows the differential capacity versus voltage for the same cell compared to the results for a Li/Sn cell of Sn metal powder (Aldrich, 99.9%). Note the large irreversible capacity for the SnO cell (figure 5-2(b)) at greater than 0.8 V during the first discharge. This is not present in the cell of metallic Sn (figure 5-2(a)). The differential capacity plots are also quite similar for SnO and Sn after the first discharge to (0.8 V). These data suggest that the reaction mechanism for lithium with SnO is similar to that of lithium with Sn after the initial portion of the first discharge.

5.1.2 In-situ XRD

A Li/SnO in-situ XRD cell was made with a 'Bellcore' type electrode. The cell was discharged to 0.0 V and subsequently charged to 2.5 V, using a specific current of 9.3 mA/g. XRD scans, of 3 hours duration, were taken continuously during the discharge and charge of the cell.

Figure 5-3 shows selected diffraction patterns from scan 1 to scan 12, which represent the discharge to 0.66 V. In each of the following five figures (figures 5-3 to 5-7), the (e) panel is the voltage profile (voltage versus scan number). The XRD intensities (panels (a) through (d)) are plotted on a logarithmic scale. Voltage versus capacity is not shown, however the cell achieved the expected capacity during both the discharge and during the subsequent charge. In all XRD scans there are peaks that are due to the in-situ cell; these are, 'cell part', Be and BeO, which are indicated on figure 5-3 (c). Figure 5-3 (d) shows scan 1, which represents the initial starting material, SnO, as indicated by the expected peak positions. All reference patterns are taken from the PDF database (PDF-2 JCPDS-ICDD, © 1993), unless otherwise stated.

The original SnO is consumed as lithium is added, as shown by the decrease in the SnO peaks from scan 1 (figure 5-3 (d)), scan 4 (figure 5-3 (c)) and scan 8 (figure 5-3 (b)). Scan 12 (figure 5-3 (a)) shows the formation of Sn by 0.66 V of discharge, which confirms the 'step 1' reaction as surmised at the beginning of this chapter. Figure 5-4 (c) shows the formation of the first Li-Sn alloy phase, Li_2Sn_5, at 0.55 V. Further discharge to 0.41 V leads to the formation of the second Li-Sn phase, LiSn (figure 5-4 (a)). Note the change of intensity scale from figure 5-3 to 5-4. Between scan 21 and scan 27 (figure 5-5 (c), (b) and (a)), or to the bottom of discharge, the characteristic XRD pattern of the disordered lithium rich Li-Sn phases prevails. The explanation for this pattern has already been discussed in chapter 3.

Figure 5-6 shows x-ray patterns collected during a portion of the subsequent charge of this cell to 0.78 V. The charge portion is similar to the discharge portion over the alloying reaction, but in reverse. Scan 45 (0.78V) shows that LiSn is formed again. Figure 5-7 shows the final series of scans from scan 47 (figure 5-7 (d)) to scan 55 (figure 5-7 (b), top of charge). Note the formation of Sn starting at scan 47 (figure 5-7 (d)) through to scan 55 (figure 5-7 (b)). Scan 55 represents the end of the experiment, as no additional lithium can be removed. Most important, is the fact that, at least by XRD, the original starting material. SnO, does not re-form. This explains the origin of the irreversible capacity in SnO. Scan 1 has been plotted on the same intensity scale as scan 55 in figure 5-7 (a). Note the increase in background from the start to the end of the experiment. No evidence for the formation of Li_2O was detected by XRD. Presumably, the Li_2O formed is amorphous, as an underlying amorphous compound will have a diffraction pattern that results in an increase in the background.

Figure 5-3 In-situ XRD results for a Li/SnO cell; (a) scan 12 – 0.66 V, (b) scan 8 – 0.94 V, (c) scan 4 – 1.05 V, (d) scan 1 – 1.04 V and (e) voltage profile (voltage versus scan number) for the constant current cycling of the cell.

Logarithmic intensities are plotted for the experiment using the left-hand vertical axis and linear intensities are plotted for the reference patterns (normalized to 100) using the right-hand vertical axis.
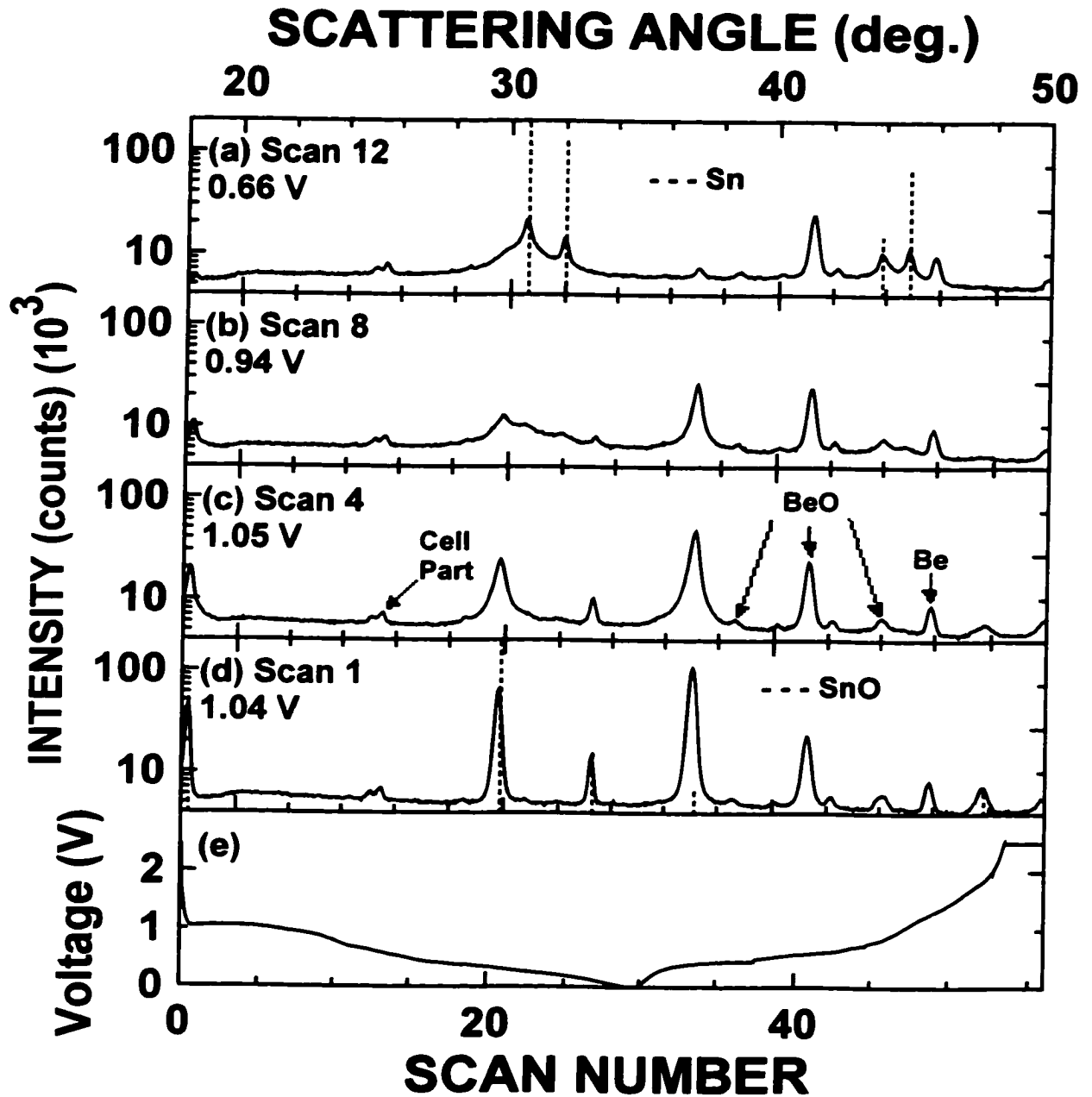
Figure 5-4 In-situ XRD results for a Li/SnO cell; (a) scan 17 – 0.41 V, (b) scan 15 – 0.50 V, (c) scan 14 – 0.55 V, (d) scan 12 – 0.66 V and (e) voltage profile (voltage versus scan number) for the constant current cycling of the cell.

Logarithmic intensities are plotted for the experiment using the left-hand vertical axis and linear intensities are plotted for the reference patterns (normalized to 100) using the right-hand vertical axis. Patterns were calculated for LiSn and Li_2Sn_5 (Courtney and Dahn, 1997a).
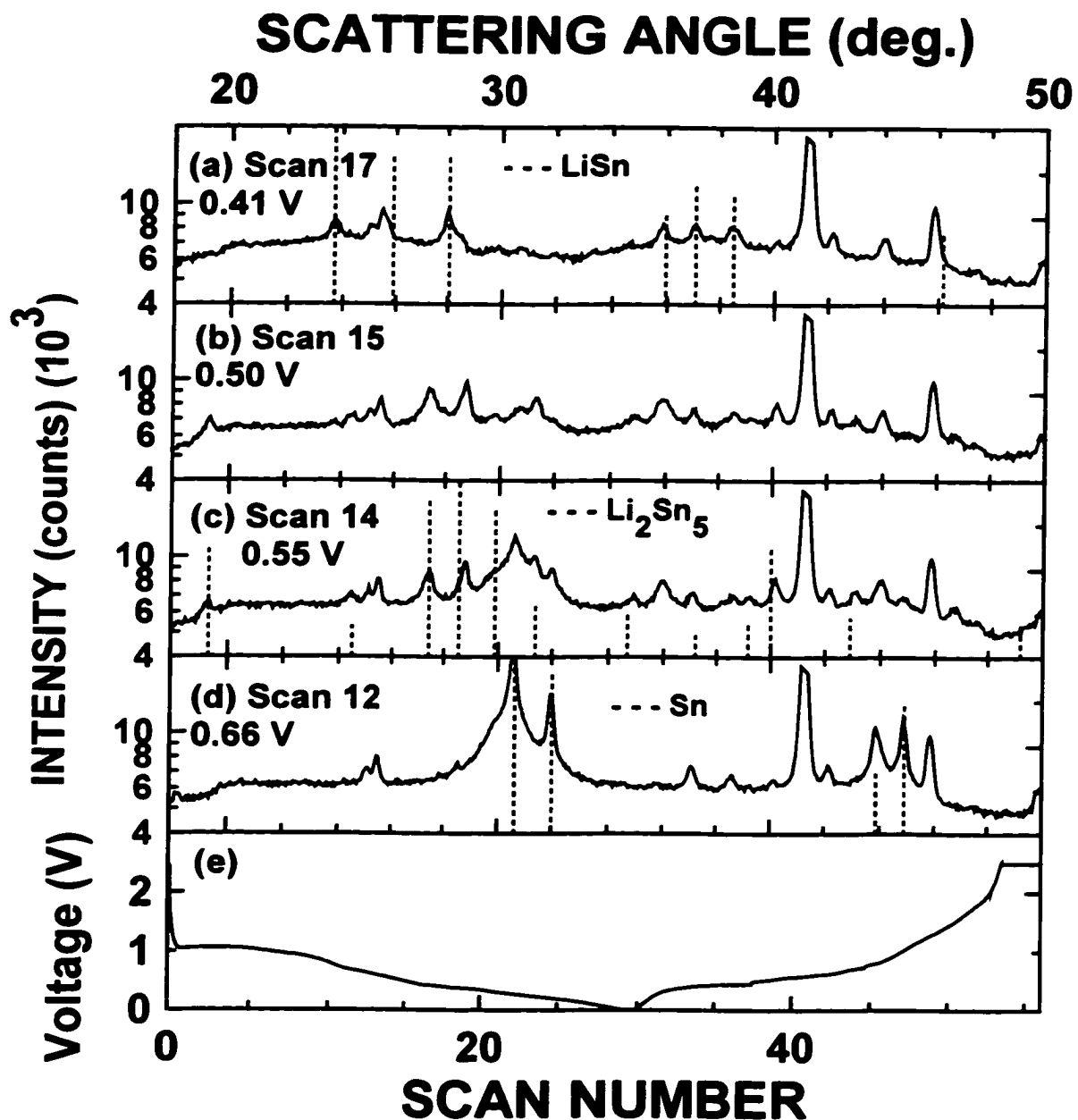
Figure 5-5 In-situ XRD results for a Li/SnO cell; (a) scan 27 – 0.10 V, (b) scan 22 – 0.23 V, (c) scan 21 – 0.31 V, (d) reference pattern for Li₇Sn₃ and (e) voltage profile (voltage versus scan number) for the constant current cycling of the cell.

Logarithmic intensities are plotted for the experiment using the left-hand vertical axis and linear intensities are plotted for the reference patterns (normalized to 100) using the right-hand vertical axis.
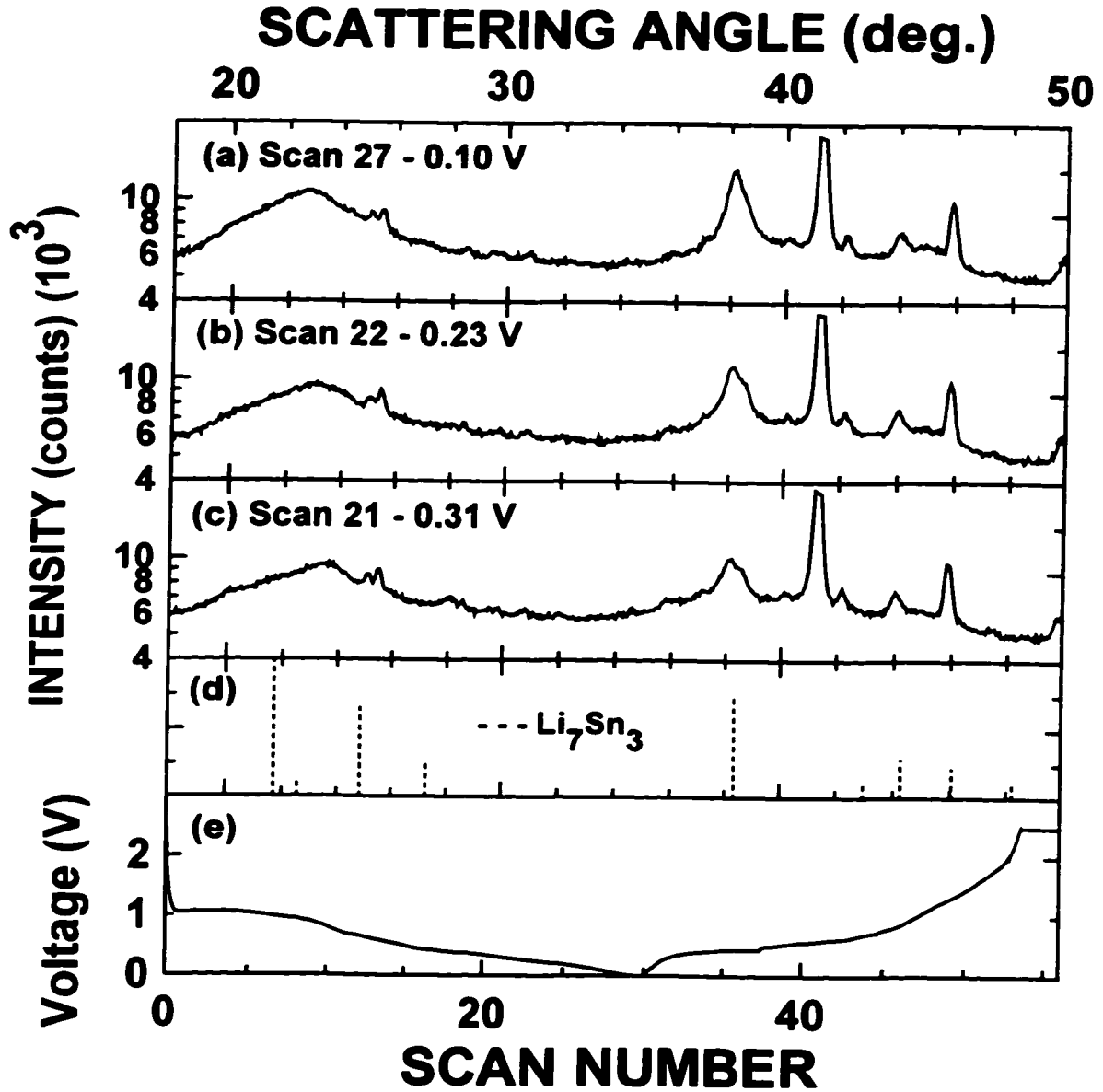
Figure 5-6 In-situ XRD results for a Li/SnO cell; (a) scan 45 – 0.78 V, (b) scan 43 – 0.64 V, (c) scan 31 – 0.23 V, (d) reference patterns for Li_5Sn_2, $Li_{13}Sn_5$, Li_7Sn_2 and $Li_{22}Sn_5$ and (e) voltage profile (voltage versus scan number) for the constant current cycling of the cell.

Logarithmic intensities are plotted for the experiment using the left-hand vertical axis and linear intensities are plotted for the reference patterns (normalized to 100) using the right-hand vertical axis.
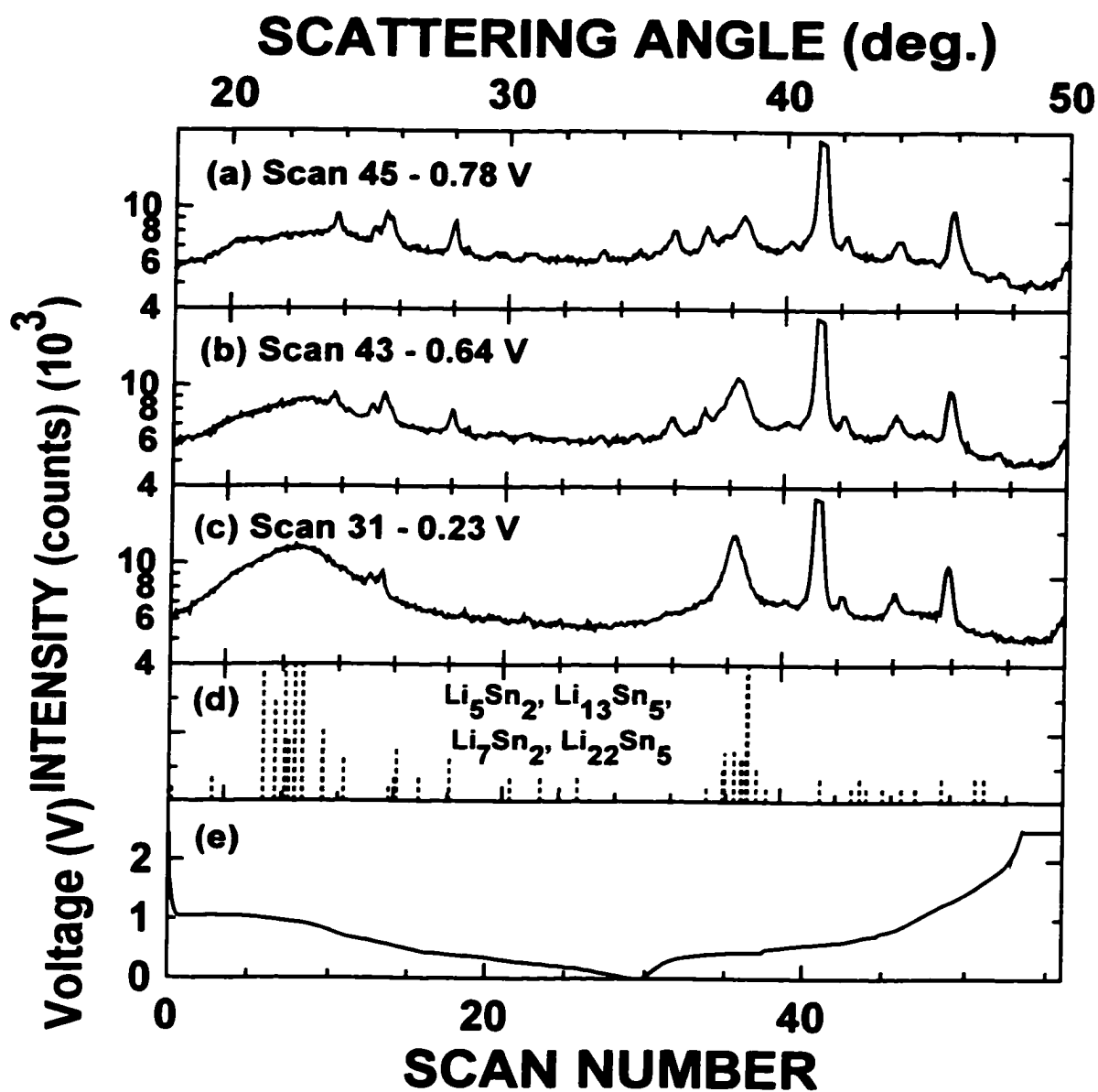
Figure 5-7 In-situ XRD results for a Li/SnO cell; (a) scan 1 – 1.04 V, (b) scan 55 – 2.55 V, (c) scan 50 – 1.44 V, (d) scan 47 – 1.00 V and (e) voltage profile (voltage versus scan number) for the constant current cycling of the cell.

Logarithmic intensities are plotted for the experiment using the left-hand vertical axis and linear intensities are plotted for the reference patterns (normalized to 100) using the right-hand vertical axis.
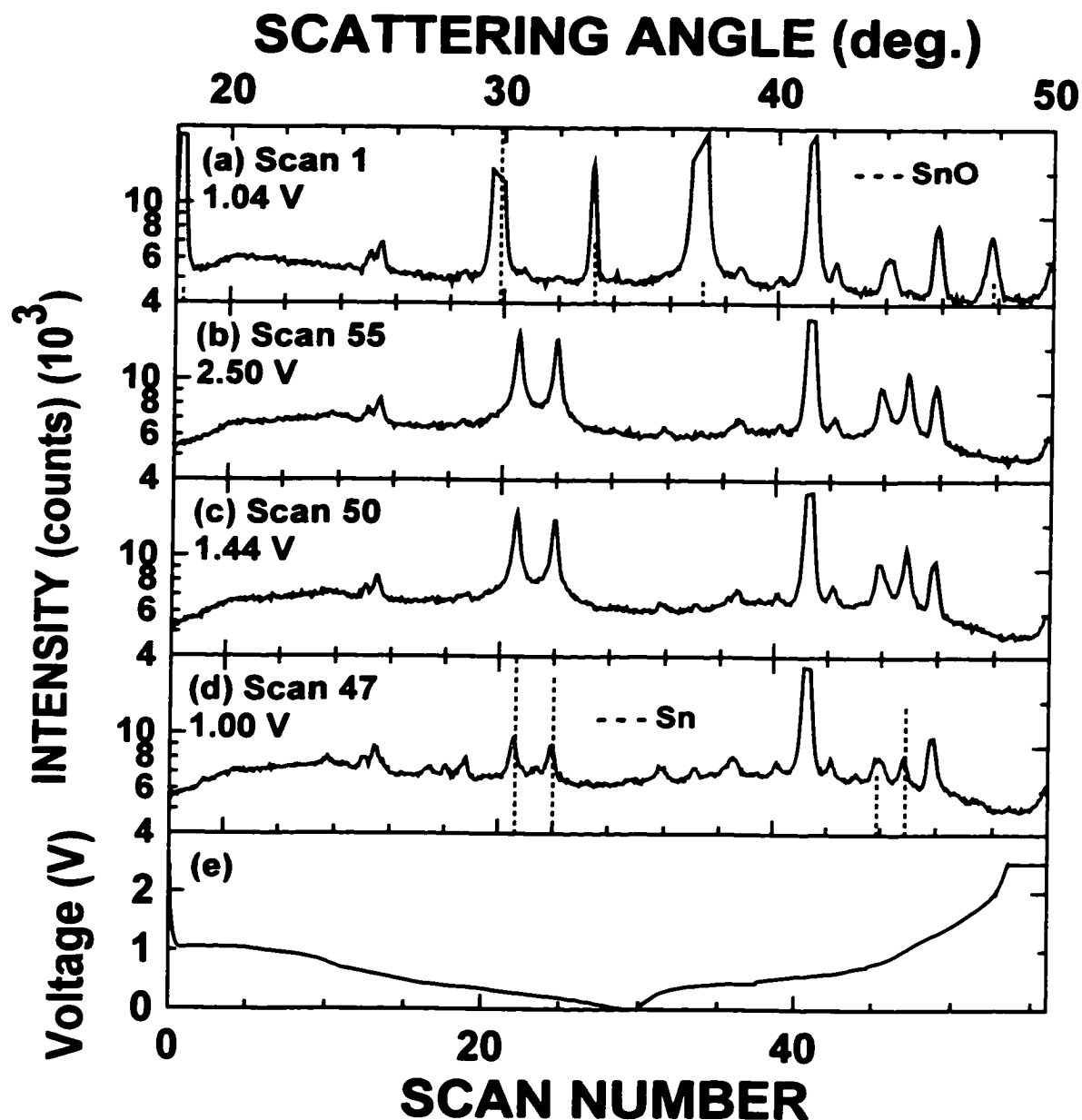
The in-situ XRD experiment on SnO showed:

1. The initial reduction of the SnO to Sn and Li_2O occurs, confirming 'step 1', and the Li_2O

formed is amorphous. The amorphous Li_2O formed helps explain why the initial plateau voltage is smaller than calculated (1.1 V - observed versus 1.58 V - calculated). The calculation in section 4.1 of $\Delta G_{f, 4-1}°$ assumed that the product Li_2O formed was crystalline. According to the in-situ XRD experiment, this is not the case. Since, $\Delta G_{f, amorphous}° > \Delta G_{f, crystalline}°$, then the formation of amorphous Li_2O would reduce the calculated voltage of this initial plateau.

2. 'Step 2' is confirmed, at least in part. The first two of the phases of the Li-Sn phase diagram are formed, Li_2Sn_5 and LiSn. The remaining XRD patterns found during the rest of the discharge suggest the formation of poorly ordered lithium-rich Li-Sn phases. The characteristic XRD patterns are understood, and have been explained in chapter 3.

3. The charge is the reverse of the discharge, with the exception that the starting material, SnO, does not re-form. It will be shown in the following section that SnO bonds do re-form, but the ordering of the structure is poor, which explains why it is not observed by XRD.

5.1.3 In-situ ME Spectroscopy

A Li/SnO in-situ ME spectroscopy cell was made. The cell was discharged using an initial specific current of 37.2 mA/g for 11 hours, then using 9.3 mA/g for 76 hours (to 0.0 V). The cell equilibrated for 6 hours with zero current then was further discharged using a specific current of 2.45 mA/g for 12 hours. The cell was subsequently charged using a specific current of 9.3 mA/g for 94 hours. ME spectra of three hours in duration were obtained throughout the discharge and charge of the cell.

Figures 5-8 and 5-9 show selected results from the Li/SnO in-situ ME spectroscopy cell. In both figures, the top panel (figure 5-8 (a) and figure 5-9 (a)) is the voltage profile of the cell. Selected summed spectra (three consecutive spectra, each of 3 hours in duration were summed for this analysis) shown in both these figures are indicated at their particular point on the discharge or charge. For example, figure 5-8 (b) shows the ME spectra of the in-situ cell at the start of discharge. The point at which this occurs (in capacity) is indicated on figure 5-8 (a) by the symbol '(b)'. The in-situ ME data is represented by the solid circles, and the reference scans, which are also indicated on the panels, are taken from the results of Dunlap et al. (1998) (see figure 3-3) and from measured powder ME spectra (see figure 2-6).

The cell is discharged, and, as expected, the SnO starting material (figure 5-8 (b)) is reduced to Sn during the first plateau reaction (figure 5-8 (c)). The broad shoulder at lower isomer shift is believed to be un-reacted oxide. It is important to keep in mind that the RFF of Sn is much lower than the RFF of SnO (RFF = 0.039 for Sn (Greenwood and Gibb, 1971) and RFF = 0.12 for SnO (Moreno and Mercader, 1994)). As such, any Sn atoms in the un-reacted oxide will absorb approximately 3 times more (i.e., RFF_{SnO} / RFF_{Sn} ≈ 3) than the Sn atoms in metallic tin. Therefore, the 'size' of the shoulder is not equal to the relative proportions of ^{119}SnO / ^{119} Sn, but is equal to one third of that ratio. This shoulder basically disappears by the formation of Li_2Sn_5 (figure 5-8 (d)), after the initial plateau. LiSn is then formed (figure 5-8 (e)), which is followed by the formation of Li_7Sn_3 (figure 5-8 (f)).

The in-situ XRD experiment, conversely, does not show a well-ordered structure for Li_7Sn_3 (figure 5-5 (c)), but it does indicate the formation of the characteristic Li-rich alloy phase disordered structure (as explained in section 3.4). Other than perhaps the effects of small grains, the ME does not investigate long range structure. The ME probes the local

environment of individual Sn atoms. Therefore when it is stated that a particular phase forms, it means that the local structure of the Sn atoms in that phase corresponds to the local structure of the Sn atoms in the pure phase. Notice that the widths of the spectra in both figure 5-8 (f) and (g) are slightly larger than the corresponding powder spectra, which could indicate broadening due to surface effects of small grain or poorly ordered material.

Pure alloy phase spectra of Li_5Sn_2 and $Li_{13}Sn_5$ (figure 5-8 (g)) do not match the in-situ ME spectra where they would be expected to occur in capacity. There are two possible explanations for this. The Li-Sn pure alloy phase ME spectra have a notable progression as lithium is added (see figure 3-3). The center shifts change from larger velocity to smaller velocity (in reference to a $CaSnO_3$ source). There are three distinct regions to these spectra, or more precisely, Sn environments. The 'Sn-like' phases (i.e. Sn, Li_2Sn_5 and LiSn) have one unresolved peak above 2 mm/s. The 'intermediate Li-rich' phases (i.e. Li_7Sn_3, Li_5Sn_2 and $Li_{13}Sn_5$) have two resolved peaks that are centered at around 2 mm/s, and this effect is especially pronounced for Li_7Sn_3 (figure 3-3 (d)). The 'final Li-rich' phases (i.e. Li_7Sn_2 and $Li_{22}Sn_5$) have one unresolved peak below 2 mm/s. The Li_7Sn_3 'like peaks' start to occur just after the formation of LiSn on the voltage profile, and is observed for some time. The spectra recorded in figure 5-8 (g) could be a mixture of poorly ordered phases of the 'intermediate Li-rich' region. Alternatively, these data could indicate that the local structures of the Sn atoms in Li_5Sn_2 and $Li_{13}Sn_5$ are not achieved in a Li/SnO cell at ambient temperature.

The local structures of Sn atoms in Li_7Sn_2 (figure 5-8 (h)), and, finally, $Li_{22}Sn_5$ (figure 5-8 (i)) at the bottom of discharge, are observed.

Figure 5-8 The discharge of theLi/SnO in-situ ME spectroscopy cell, (a) voltage versus capacity (with scans to be shown in (b) to (i) indicated by their point on the voltage profile, (b) initial scan (compared to SnO powder), (c) 390 mAh/g (compared to Sn powder), (d) 400 mAh/g (Li_2Sn_5), (e) 525 mAh/g (LiSn), (f) 780 mAh/g (Li_7Sn_3), (g) 810 mAh/g (Li_5Sn_2 – solid and $Li_{13}Sn_5$ – dashed), (h) 960 mAh/g (Li_7Sn_2), and (i) 1150 mAh/g ($Li_{22}Sn_5$)

Reference patterns taken from Dunlap et al. (1998) (see figure 3-3) and for SnO (see figure 2-6). The scaling of the reference patterns was done by inspection in order to aid interpretation of the center shift, these are not fitted spectra.
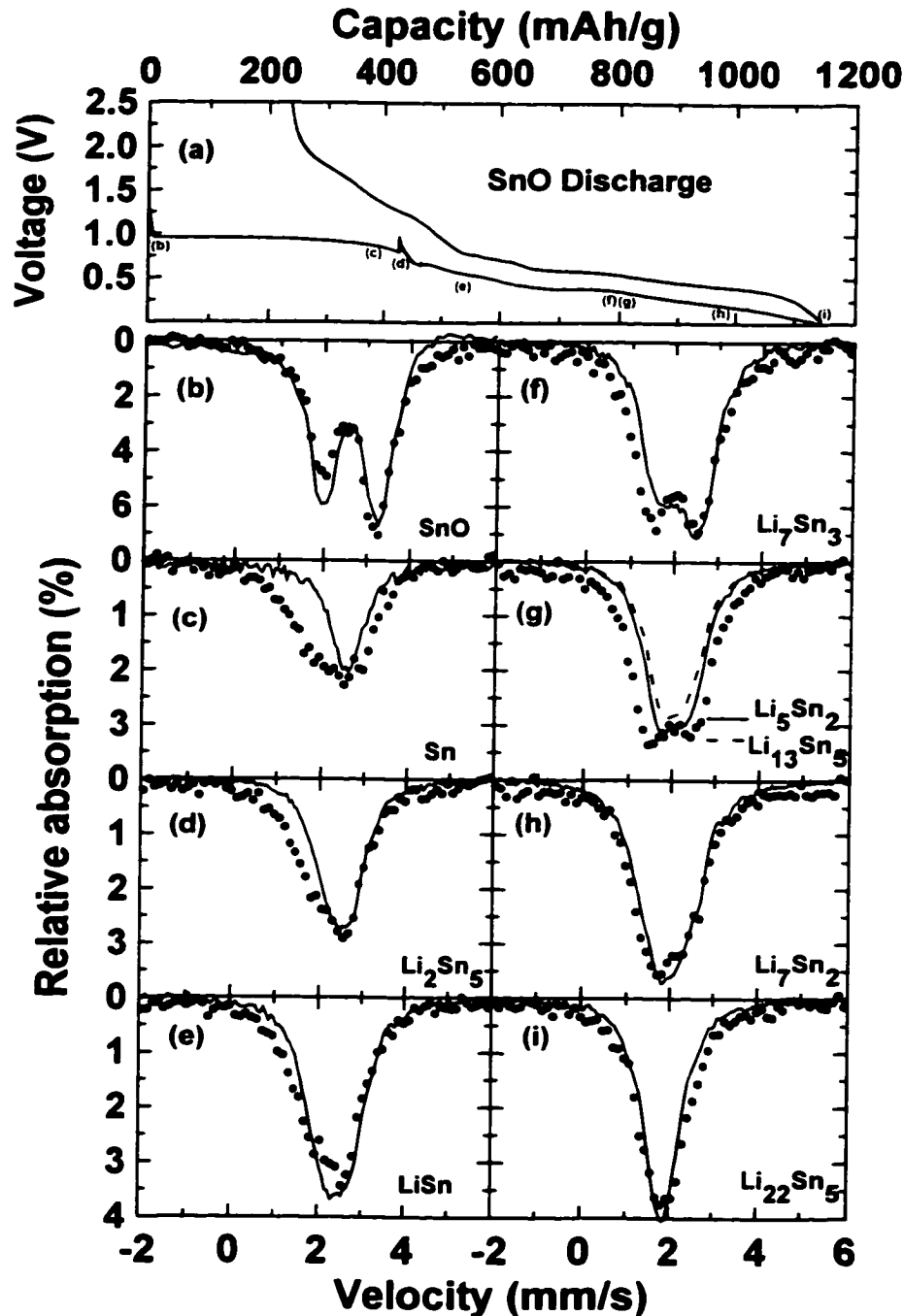
Figure 5-9 The charge of theLi/SnO in-situ ME spectroscopy cell, (a) voltage versus capacity (with scans to be shown in (b) to (h) indicated by their point on the voltage profile, (b) 1150 mAh/g (compared to $Li_{22}Sn_5$), (c) 1030 mAh/g (Li_7Sn_2), (d) 800 mAh/g (Li_7Sn_3), (e) 575 mAh/g (LiSn), (f) 525 mAh/g (Li_2Sn_5), (g) 480 mAh/g (Sn), and (h) 225 mAh/g (spectra at top of charge fit to Sn, SnO and SnO_2 as indicated)

Reference patterns taken from Dunlap et al. (1998) (see figure 3-3) and for SnO (see figure 2-6). . The scaling of the reference patterns was done by inspection in order to aid interpretation of the center shift, these are not fitted spectra.
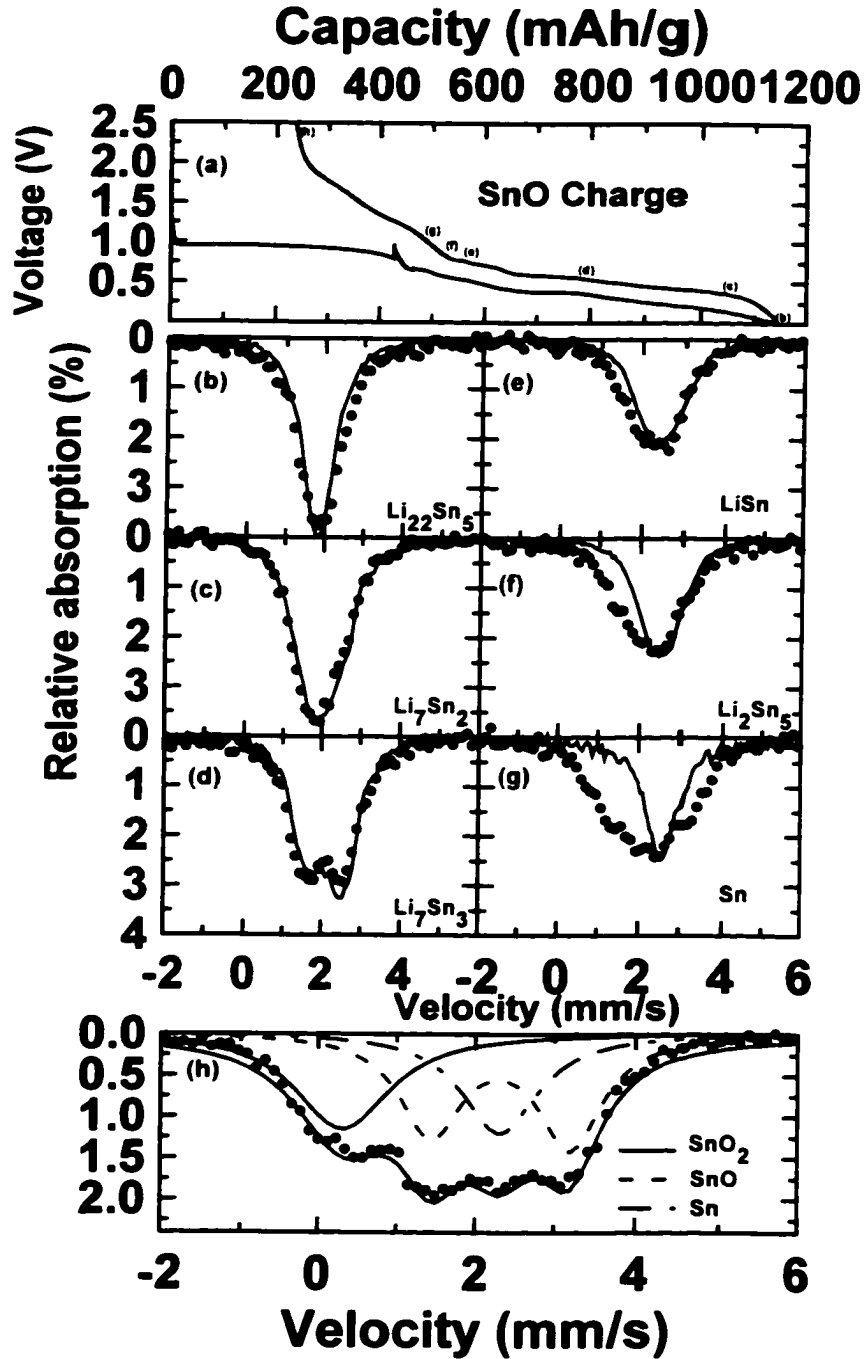
The sequence of spectra observed during the charge is exactly the reverse (figure 5-9). Li_7Sn_2 (figure 5-9 (c)) forms, then Li_7Sn_3 (figure 5-9 (d)), LiSn (figure 5-9 (e)), Li_2Sn_5 (figure 5-9 (f)), and finally Sn (figure 5-9 (g)).

Figure 5-9 (h) shows the ME spectra for the Li/SnO in-situ cell at the top of charge. This spectrum has been fit to the powder spectra of Sn, SnO and SnO_2, and the sum of these sub-spectra is also shown. This fit confirms the 'back-reaction' to the oxide that was suggested by electrochemistry, but was not seen by XRD. The back-reaction appears to commence at the same time as the formation of Li_2Sn_5 (figure 5-9 (f)). The in-situ experiment is not performed at an infinitesimally slow rate, and so does not represent the true equilibrium composition. Again, the relative intensities of the fitted sub-spectra in figure 5-9 (h) and the 'strong' shoulder of back-reaction in figure 5-9 (g) are not to be equated to actual quantities of the individual compounds.

The recoil free fraction, as was discussed in section 4-3, is dependent on the lattice properties of a particular material. RFF values are usually obtained by measuring the temperature dependant absorption of a material. An in-situ ME experiment, where the absorber material is nominally thin and the total number of Sn nuclei does not change, can also be used to study the RFF. The RFF is equal to the probability of an impinging photon producing a resonant absorption in the source. In other words, one can integrate above the absorption lines (relative to the background counts) and have a measure of the RFF. The RFF as a function of lithium content for the Li/SnO cell is shown in figure 5-10. Note that the values of the total relative intensity of absorption have been scaled so as to correspond with the accepted value of the RFF of crystalline SnO for the first scan.

Figure 5-10 Average Recoil free fraction (RFF) versus y in Li$_y$SnO as obtained by in-situ ME measurement of a Li/SnO cell
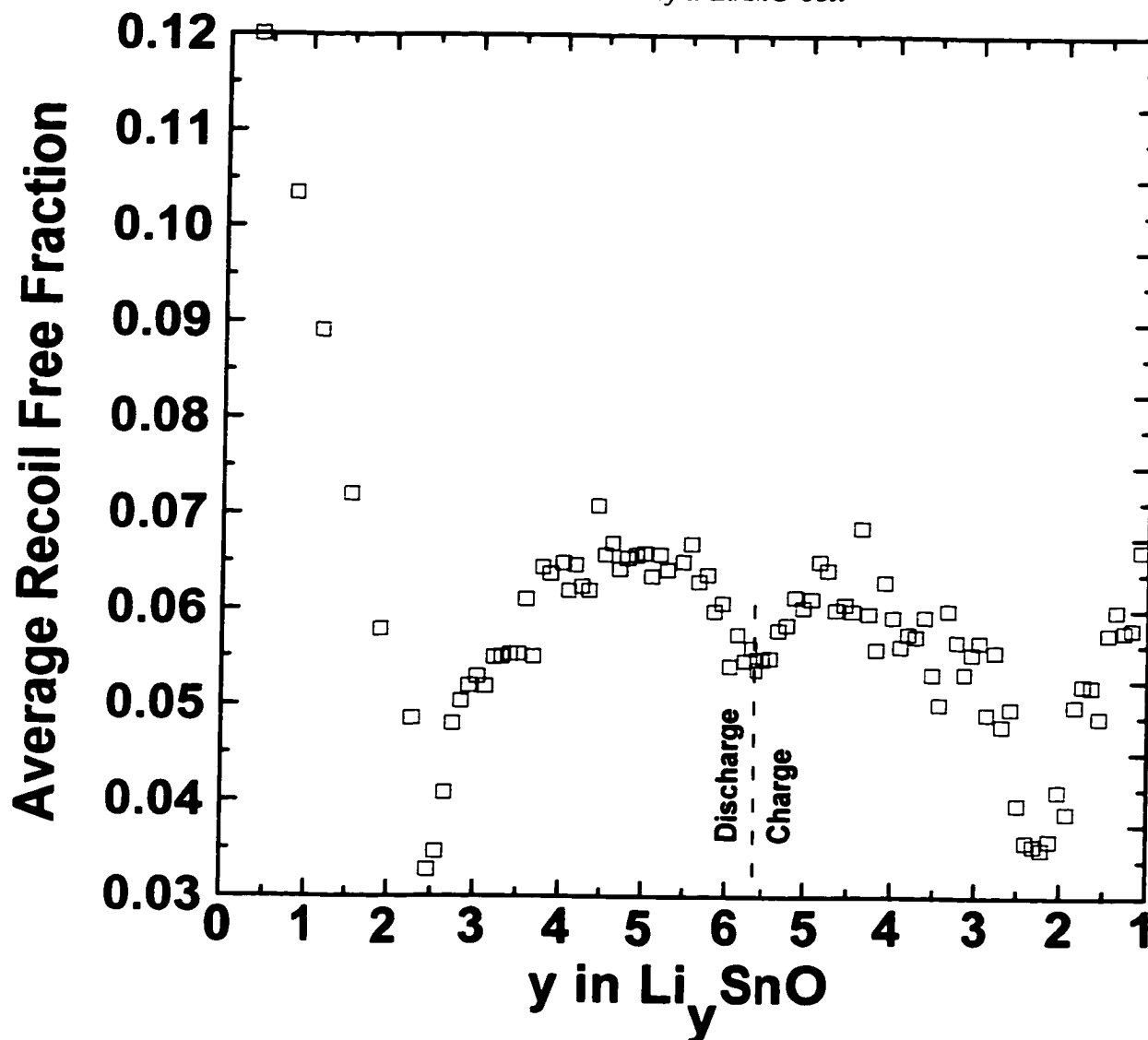
The lowest value of the RFF is obtained at an apparent stoichiometry of about Li$_{2.5}$SnO. This particular cell was discharged at a relatively fast rate over the initial discharge plateau, so the value of y does not represent the true equilibrium lithium concentration. In other words, the lowest value of the RFF should occur for metallic Sn (i.e. it has the lowest melting point of the Li-Sn phases), which corresponds to a stoichiometry of Li$_{2.0}$SnO. Note

that the observed value of the RFF at the lowest point is about 0.032, which is smaller than the accepted value for Sn of 0.039. This is possibly due to the fact that the Sn formed is small grain. The possible effects of small grain size on the RFF have been discussed in chapter 4, and will be investigated more fully later on in this chapter.

There should be no doubt, therefore, that equation 5-1 represents the reaction mechanism of lithium with tin oxide during the first cycle. We now use these ideas in studies of the reaction mechanism of lithium with other Sn-containing materials listed in the Fuji patent; first SnO_2 and then the SnO-containing glasses.

5.2 Crystalline SnO₂

A Li/SnO_2 test cell using a crystalline SnO_2 powder (Aesar, 99.9 %) electrode was made. The cell was tested with a specific current of 37.2 mA/g for both discharge and charge segments. The voltage profile for this cell is shown in figure 5-11.

Figure 5-11 Voltage profile for a Li/SnO_2 cell (first 3 half-cycles)
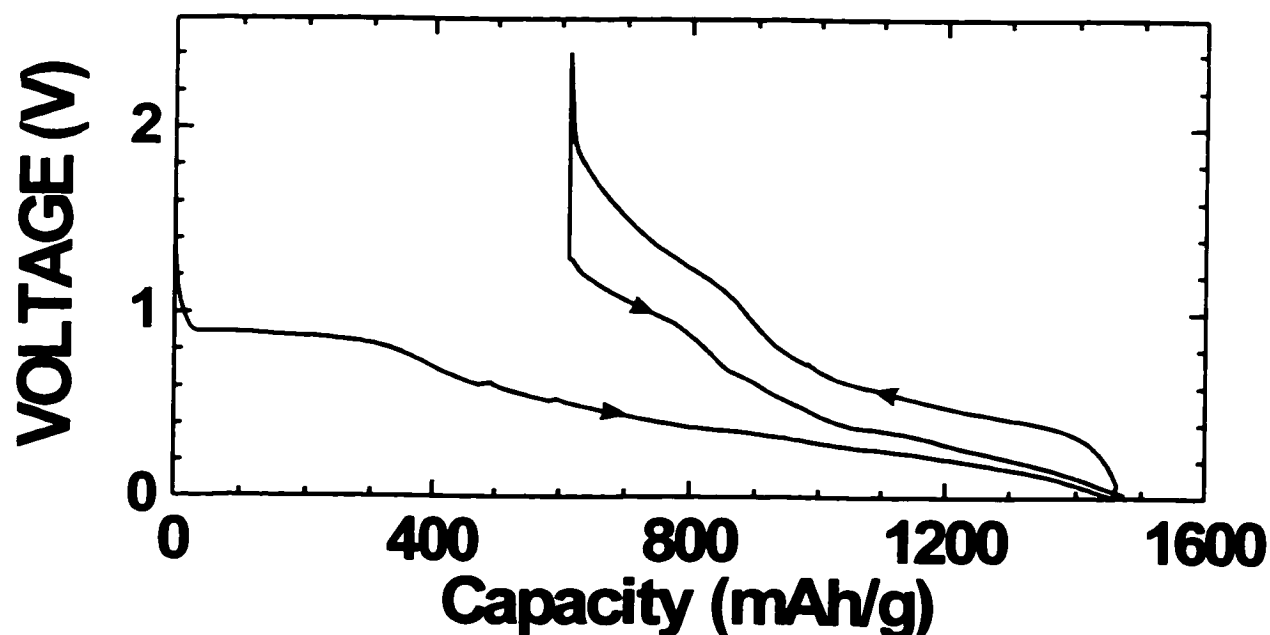
The overall shape of the voltage profile for SnO_2 (figure 5-11) is quite similar to that of SnO (figure 5-1). Notice the large first discharge capacity (~ 1450 mAh/g) and the large irreversible capacity (~ 600 mAh/g), as well as the plateau (~ 0.9 V) during the first discharge. To extend the established reaction mechanism for SnO to SnO_2, 4 equivalents of Li are needed to reduce SnO_2 to Sn and lithia , as shown in the reaction of equation 5-2.

$$SnO_2 + 4Li \xrightarrow{step\ 1} Sn + 2Li_2O$$

$$Sn + 2Li_2O + 4.4Li \xrightarrow{step\ 2} Li_{4.4}Sn + 2Li_2O$$

$$(5-2)$$
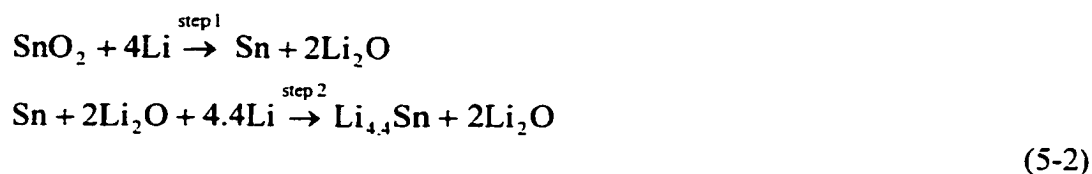
The calculated capacity for the complete reaction ('step 1' and 'step 2') is 1491 mAh/(g SnO_2), which compares well with the experimental first discharge capacity of 1450 mAh/g. The first charge capacity at less than 1.0 V, equivalent to '-step 2', is predicted to be 781 mAh/g, which is somewhat larger than the observed first charge capacity of 650 mAh/g to 1.0 V.

A Li/SnO_2 in-situ XRD cell was constructed. This cell, like the SnO cell, employed a 'Bellcore' electrode, and it was discharged and charged using a specific current of 18.6 mA/g. Figure 5-12 is a summary of the results of the in-situ XRD experiment on the Li/SnO_2 cell. The shift between the calculated and measured patterns on figure 5-12 is due to a vertical displacement of this particular XRD cell with respect to the goniometer axis.

Figure 5-12 confirms that SnO_2 follows a similar reaction mechanism as SnO when it reacts with lithium in an electrochemical cell. The starting material, SnO_2 (figure 5-12 (d)), is consumed during the first discharge plateau. The characteristic XRD pattern of the Li-rich alloy phases is also evident (figure 5-12 (b), compared with reference patterns in figure 5-12 (c)). The starting material does not re-form on charge (figure 5-12 (a)), but metallic Sn does,

thereby explaining the large irreversible capacity of SnO$_2$. There does appear to be back-reaction (to SnO$_2$ and possibly SnO), as was the case for SnO. The capacity on charge above 1.0 V is approximately 200 mAh/g. The calculated irreversible capacity (based on no back-reaction) is 710 mAh/g, whereas the actual irreversible capacity is 600 mAh/g.

Figure 5-12 *In-situ XRD results for Li/SnO$_2$, (a) end of charge (2.5V), (b) end of discharge (0.0V), (c) peak positions of some Li-rich alloy phases, and (d) first scan (2.5 V)*
The intensity (in counts per second) is plotted using the left-hand vertical axis. There is a change of scale from (b) to (d). Expected patterns use the right-hand vertical axis
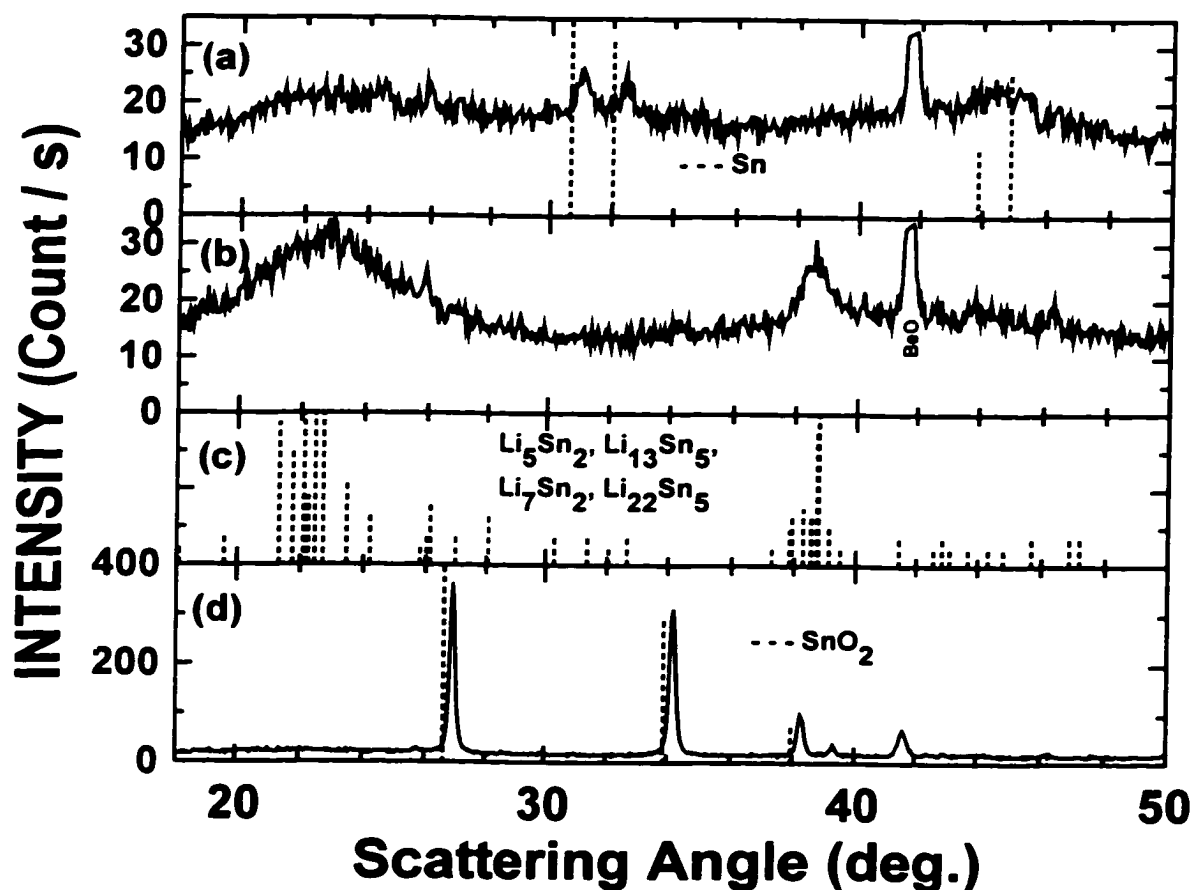
The next sections will show that the basic reaction mechanism (per equation 5-1) of lithium with SnO is the same for the SnO-containing glasses.

5.3 Glass preparation

5.3.1 Quartz tube furnace

Three of the glasses that were initially studied were made by the technique described in this section. Figure 5-13 shows the powder XRD patterns of these materials; $SnO:SiO_2$, $SnO:(B_2O_3)_{0.25}:(P_2O_5)_{0.25}$, and $SnO:(B_2O_3)_{0.25}:(P_2O_5)_{0.25}:(K_2CO_3)_{0.1}$ in (figures 5-13 (a), (b) and (c), respectively). The stoichiometries listed refer to the relative amounts of starting material that were used to make the glass. For example, $SnO:SiO_2$ was made from equimolar

Figure 5-13 XRD patterns of glasses made by quartz tube furnace method. (a) $SnO:SiO$, (b) $SnO:(B_2O_3)_{0.25}:(P_2O_5)_{0.25}$, and (c) $SnO:(B_2O_3)_{0.25}:(P_2O_5)_{0.25}:(K_2CO_3)_{0.1}$
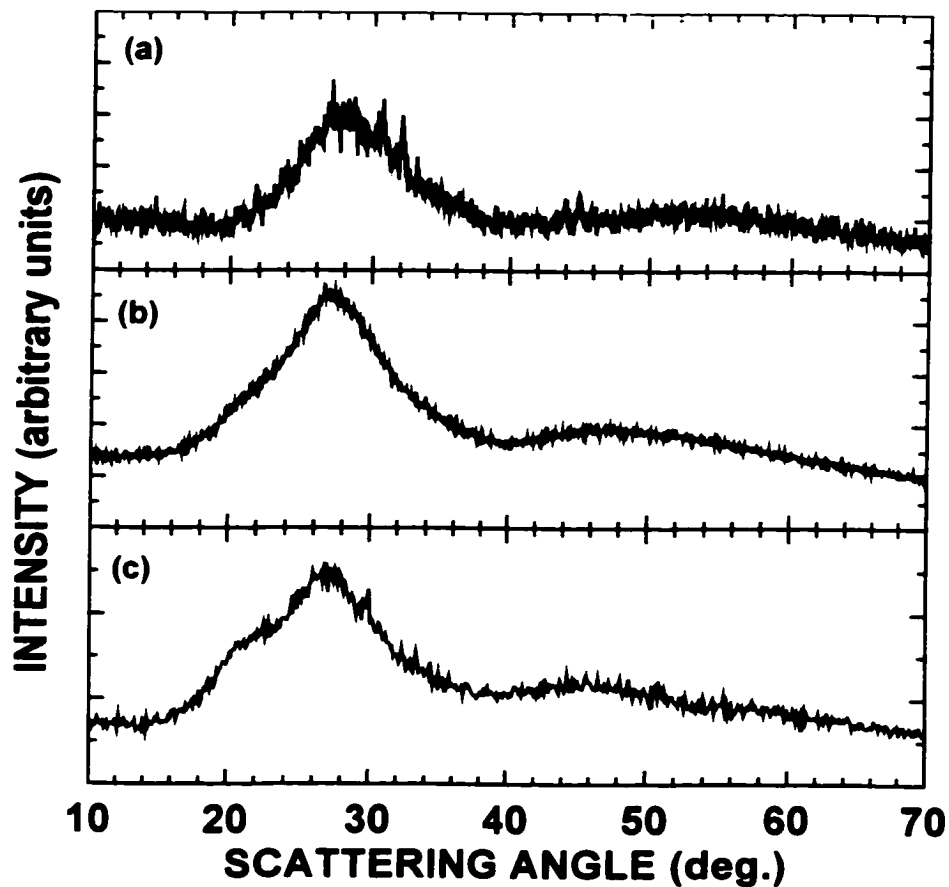
amounts of SnO (Aldrich 99.9 %) and SiO_2 (Aesar, 99.6 %) that were dry-blended (prior to heating) in an autogrinder. Other starting compounds used were P_2O_5, B_2O_3 and K_2CO_3

(Aldrich). A Lindberg horizontal tube furnace was used to heat samples at 10°C per minute to a temperature of 1000°C. The samples, which were contained in either graphite or alumina crucibles, were held at this temperature for 1 hour. The crucibles were located inside a quartz reaction tube (4ft long and 2 inches diameter) that was placed inside the furnace. A constant flow of argon (Linde, UHP) was maintained in the reaction tube throughout the heating and cooling periods. The material was quenched by taking the tube out of the furnace and allowing it to cool to room temperature. The materials were then separated from the crucible (a process that was not often satisfactory as the glass was always well-adheared to the crucible) and were ground in an auto-grinder. They were passed through a seive (-325 mesh). Large pieces of the SnO:SiO$_2$ glass was a yellowish-green colour. The powders made from this glass were white. Large pieces of the boro-phophate glasses were dark-green. The powders made from this glass were also white.

5.3.2 RF induction furnace with a rotating coil

There was a problem associated with the glass preparation technique described in the last section. In order to retrieve pieces of the glass for experimentation, one would have to 'chip away' at the glass in order to separate it from the crucible. Impurities, such as metal from the 'chipping instrument' would contaminate the sample, and quite often the separation process led to the crucible shattering.

A more efficient way of making the glasses was devised. It involved a RF induction furnace (with an ability to be able to pour a melt) that was located in an controllable atmosphere. A picture of this set-up is shown in figure 5-14. Stoichiometric ratios of constituent powders were thoroughly mixed and added to a graphite susceptor which was

placed inside a boron nitride radiation shield within the radio frequency (RF) coil of an induction furnace. The coil is of a special design which can be rotated perpendicular to its axis within the vacuum chamber of the induction furnace. Samples were loaded within the furnace, and a vacuum was slowly established over the period of an hour or so, to avoid ejection of the powders from the susceptor. Then the chamber was filled with argon to one atmosphere absolute and the RF power applied. The samples were heated to near 1000°C (measured with an optical pyrometer aimed through a view-port at the molten sample in the susceptor). Once it was confirmed that the sample was fully molten, the RF coil was rotated beyond the horizontal position (while RF power was still being applied) and the molten sample dumped and quenched onto a nickel sheet in contact with a massive copper plate at room temperature. Then the chamber was opened. In all cases, samples were uniform solid lumps of glass with smooth surfaces.

Figure 5-14 Picture of RF induction furnace set-up used for glass making

Boron nitride radiation shield

Alumina crucible with graphite "jacket"

controllable atmosphere chamber

arm able to be rotated

Ni foil - easy to separate glass from foil

Cu block
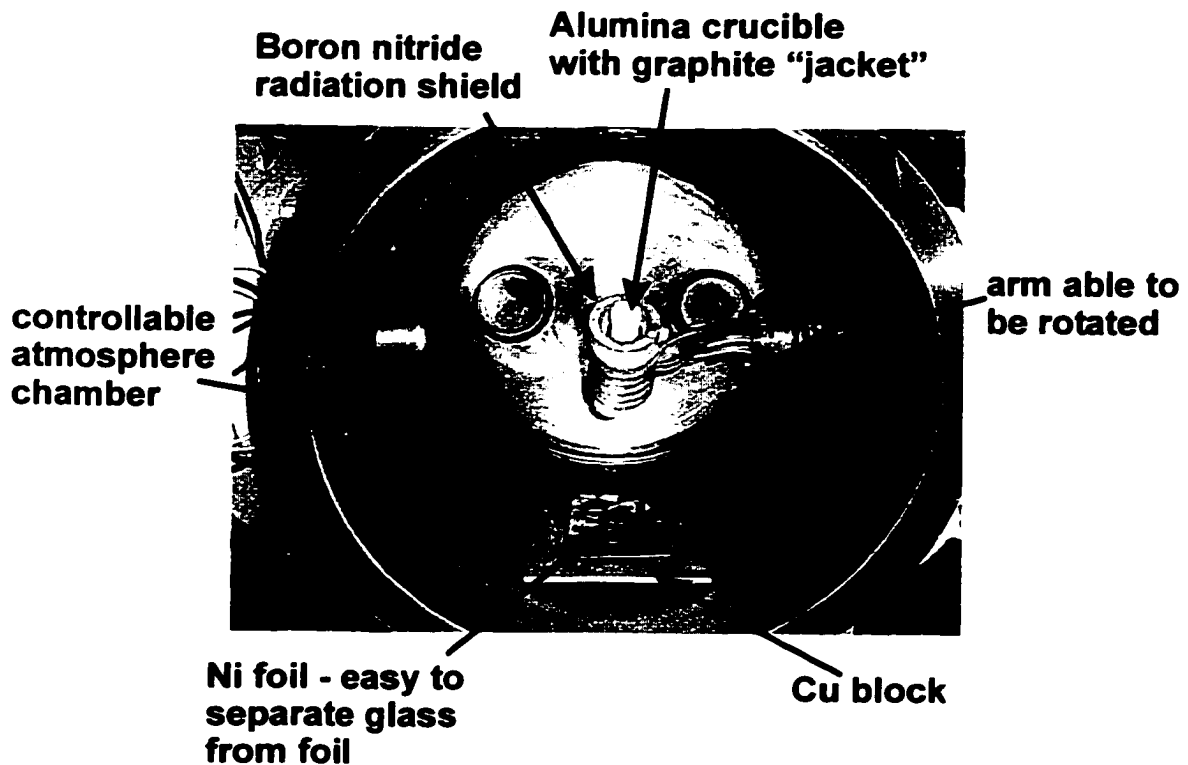
A series of SnO, PbO and Sb_2O_3 based boro-phosphate glasses were made using this set-up. The PbO and Sb_2O_3 based glasses shall be discussed in more detail in chapter 7. The powder XRD patterns of the SnO-based glasses are shown in figure 5-15.

Figure 5-15 Powder XRD patterns for SnO-based glasses made,
(a) $SnO:(B_2O_3)_{0.1}:(P_2O_5)_{0.1}$, *(b)* $SnO:(B_2O_3)_{0.4}:(P_2O_5)_{0.1}$, *(c)* $SnO:(B_2O_3)_{0.25}:(P_2O_5)_{0.25}$
(d) $SnO:(B_2O_3)_{0.1}:(P_2O_5)_{0.4}$, *(e)* $SnO:(B_2O_3)_{0.35}:(P_2O_5)_{0.35}$, *and (f)* $SnO:(B_2O_3)_{0.5}:(P_2O_5)_{0.5}$
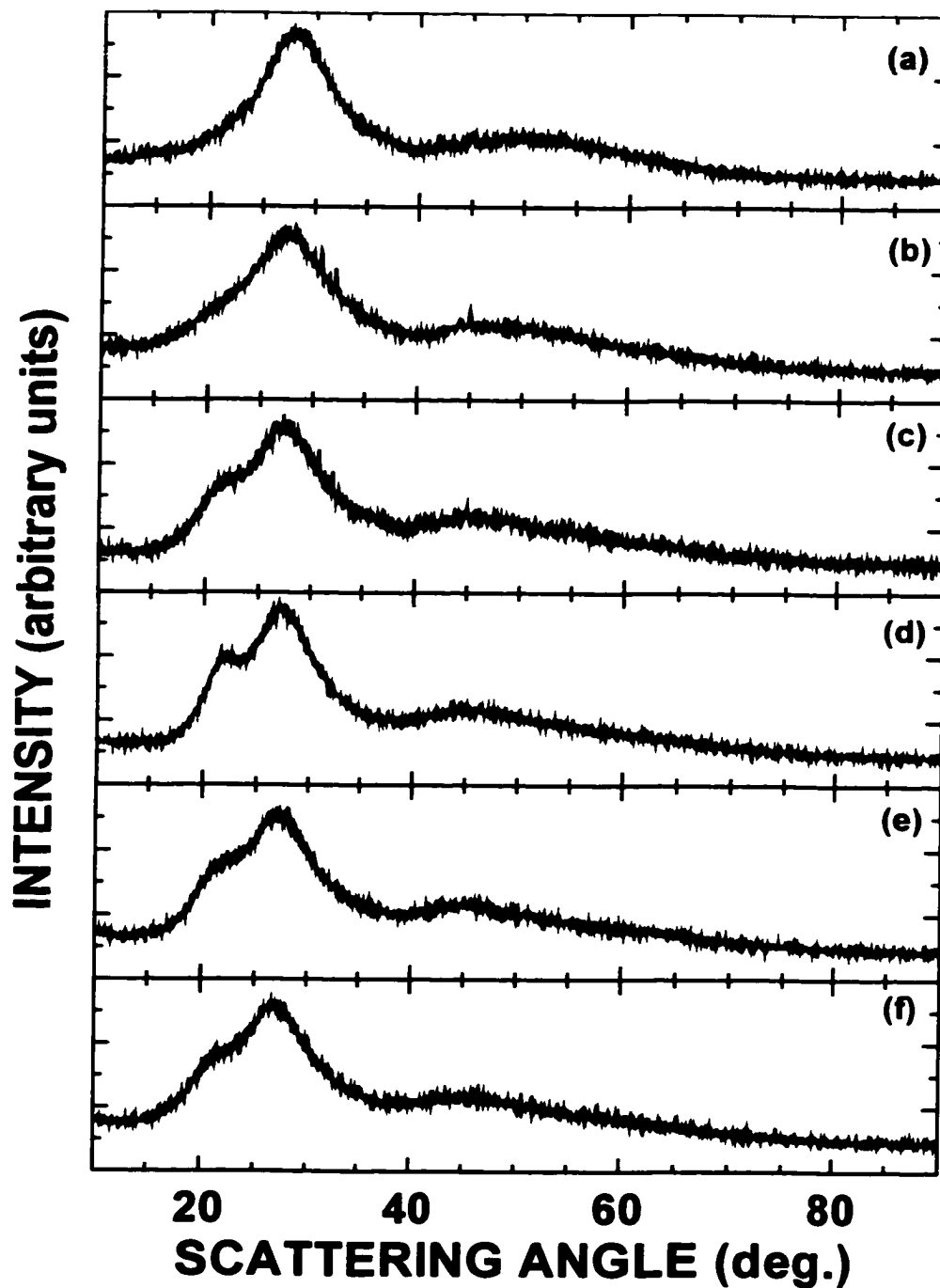
5.4 The reaction of lithium with SnO:$(B_2O_3)_{0.25}$:$(P_2O_5)_{0.25}$ glass

Figure 5-16 shows a voltage profile for a Li/SnO:$(B_2O_3)_{0.25}$:$(P_2O_5)_{0.25}$ cell. From now on, I will adopt a short hand notation for the glass compositions; SnO:(0.25/0.25) means a SnO:$(B_2O_3)_{0.25}$:$(P_2O_5)_{0.25}$ glass. This cell was discharged and charged using a specific current of 37.2 mA/g, between 0.0 and 2.5 V. The first 3 half-cycles of the cell are shown.

Figure 5-16 Voltage versus capacity for a Li/SnO:$(B_2O_3)_{0.25}$:$(P_2O_5)_{0.25}$ cell (Li/SnO:(0.25/0.25))
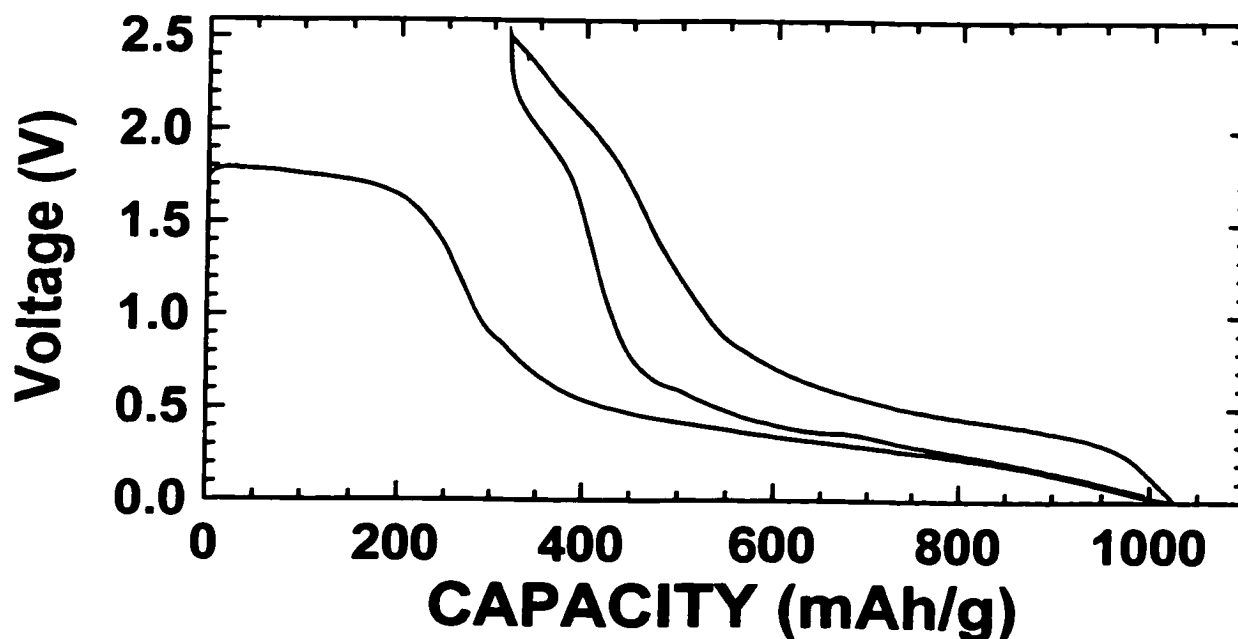
Notice that the voltage profile of the Li/SnO:(0.25/0.25) cell (figure 5-16) is similar to that of the Li/SnO cell (figure 5-1). The initial plateau at 1.7 V, for 250 mAh/g, is followed by a capacity of 750 mAh/g at lower voltage. It shall be shown that the reaction mechanism of lithium with this glass is based on the reaction mechanism of lithium with SnO. The first voltage plateau of the Li/SnO cell had a lower value than the calculated voltage (based on thermodynamics, see section 5.1). The formation of amorphous Li_2O, and not crystalline Li_2O, explained why the observed voltage was lower than the calculated voltage (1.58 V). The observed voltage plateau in the glass is higher than 1.58 V, and this can be understood

by the assumption that the initial SnO component of the glass is amorphous. An increase in the free energy due to amorphous reactants should increase this first voltage plateau.

The reaction mechanism of lithium with a SnO-based glass, is proposed in equation 5-3. Consider the reduction, by lithium, of the oxygen that is most intimately bonded with the Sn in the glass to form Li_2O. This lithia is incorporated within the framework of B_2O_3 and P_2O_5. The latter shall be termed as 'X' components, and they are inert to lithium. The lithium then alloys with the regions of Sn that remain.

$$SnO : X + 2Li \xrightarrow{step\,1} (1.58V)\,Sn + Li_2O : X$$

$$Sn + Li_2O : X + 4.4Li \xrightarrow{step\,2} Li_{4.4}Sn\,(<0.8V) + Li_2O : X$$

$$(5-3)$$
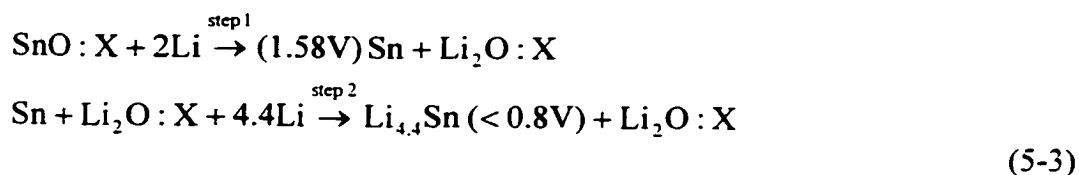
The calculated capacity of such a reaction (if $X = (B_2O_3)_{0.25}:(P_2O_5)_{0.25}$) is 915 mAh/g with an 'irreversible' capacity (assuming that it is truly irreversible, although the tendancy to back-react is possible) of about 380 mAh/g. These calculated capacities match reasonably well with experiment.

5.4.1 In-situ XRD

A Li/SnO:(0.25/0.25) in-situ cell was constructed. In this experiment, the electrode was coated directly onto the beryllium disk. The coating method was not optimal, and as a result some of the coated electrode 'flaked-off' before the cell was constructed. In effect, this creates a 'hole' for a significant portion of the x-rays to penetrate deeper into the region past the electrode. Thus, the XRD patterns of this particular in-situ cell have many 'cell-part' peaks in them (as shown in figure 5-17 (d)). The cell was subject to constant current discharge and charge at a specific current of 18.6 mA/g, between the lower and upper voltage

Figure 5-17 In-situ XRD results for Li / SnO (0.25/0.25) cell, (a) end of charge (2.5V). (b) end of discharge (0.0V), (c) peak positions of some Li-rich alloy phases, and (d) first scan (2.5 V)
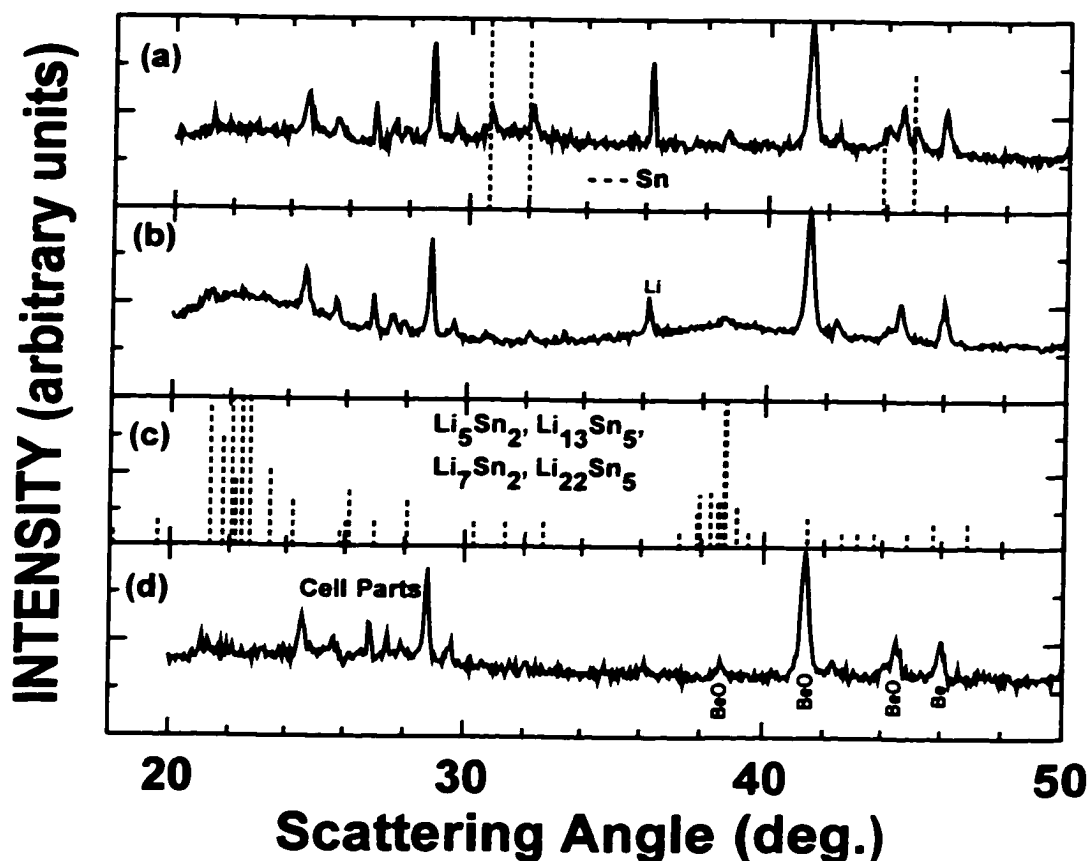
limits of 0.0 and 2.5 V, respectively. The cell was continuously measured by XRD of scans 3 hours in duration. A summary of the in-situ results for the SnO:(0.25/0.25) cell is shown in figure 5-17.

The starting material (figure 5-17 (d)) does not appear to change dramatically during discharge. Neither Sn, Li_2Sn_5, nor LiSn are observed as they were for the SnO in-situ XRD cell. The glass does, however, display the characteristic lithium-rich alloy phase at the bottom of discharge (figure 5-17 (b), with the reference patterns for some of the lithium-rich alloys given in figure 5-17 (c)). At the top of charge there is evidence to suggest that regions

of Sn are formed (figure 5-17 (a)). The Sn regions formed appear to be large, however, it is believed that this pattern (taken at the top of charge, 2.5 V) represents a mixture of both large grain Sn and small grain Sn. Chapter 6 will discuss the effects of the upper cut-off voltage on the size of Sn regions that form.

5.4.2 In-situ ME Spectroscopy

A Li/SnO:(0.25/0.25) in-situ ME spectroscopy cell was constructed. The cell was discharged using a specific current of 9.3 mA/g to 0.0 V, and subsequently charged using a specific current of 18.6 mA/g to 2.5 V. ME spectra, each of three hours in duration, were obtained throughout the discharge and charge of the cell. Figures 5-18 and 5-19 show selected results from this in-situ ME spectroscopy cell. In both figures the top panel (figure 5-18 (a) and figure 5-19 (a)) is the voltage profile of the cell. Selected scans to be shown in the figure are indicated at their particular point on the discharge or charge curves. For example, figure 5-18 (b) shows the ME spectra of the in-situ cell at the start of discharge. The point at which this occurs (in capacity) is indicated on figure 5-18 (a) by the symbol '(b)'. The in-situ data is represented by the solid circles, and the Li-Sn reference spectra, which are also indicated on the panels, are taken from the results of Dunlap et al. (1998) (see figure 3-3). The reference spectrum for SnO:(0.25/0.25) was presented in figure 2-6.

The first portion of the discharge, to the end of the initial plateau, leads to virtually zero Sn signal. The spectrum in figure 5-18 (c) shows some evidence for the existence of metallic Sn at this point. Apparently the RFF of the Sn nuclei is very low here. Chapter 4 contained some discussion as the effects of grain size on the RFF, which is now pursued using some of the experimental data in this chapter.

Figure 5-18 The discharge of the in-situ SnO (0.25/0.25) ME cell, (a) voltage versus capacity (with scans to be shown in (b) to (i) indicated by their point on the voltage profile, (b) initial scan (compared to SnO (0.25/0.25) powder), (c) 250 mAh/g (compared to Sn powder), (d) 275 mAh/g (Li_2Sn_5), (e) 325 mAh/g (LiSn), (f) 5700 mAh/g (Li_7Sn_3), (g) 670 mAh/g (Li_5Sn_2 – solid and $Li_{13}Sn_5$ – dashed), (h) 800 mAh/g (Li_7Sn_2), and (i) 900 mAh/g ($Li_{22}Sn_5$)

Reference patterns taken from Dunlap et al. (1998) (see figure 3-3) and for SnO (0.25/0.25) (see figure 2-6). The scaling of the reference patterns was done by inspection in order to aid interpretation of the center shift, these are not fitted spectra.
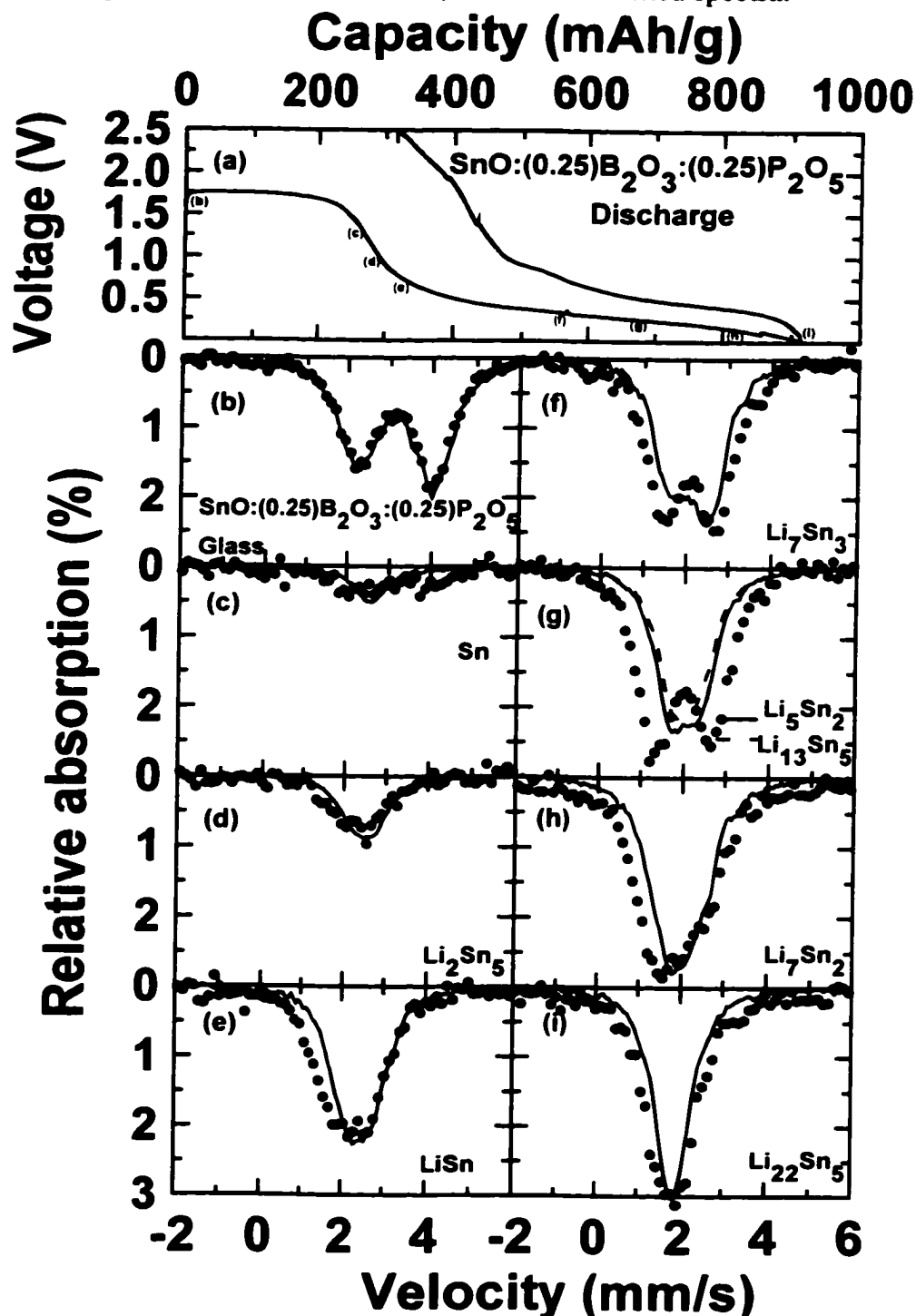
Figure 5-19 The charge of the in-situ SnO (0.25/0.25) ME cell, (a) voltage versus capacity (with scans to be shown in (b) to (h) indicated by their point on the voltage profile, (b) 900 mAh/g (compared to $Li_{22}Sn_5$), (c) 825 mAh/g (Li_7Sn_2), (d) 600 mAh/g (Li_7Sn_3), (e) 550 mAh/g (LiSn), (f) 500 mAh/g (Li_2Sn_5), (g) 475 mAh/g (Sn), and (h) 300 mAh/g (spectra at top of charge fit to Sn and SnO:(0.25/0.25)

Reference patterns taken from Dunlap et al. (1998) (see figure 3-3) and for SnO (0.25/0.25) (see figure 2-6). The scaling of the reference patterns was done by inspection in order to aid interpretation of the center shift, these are not fitted spectra.
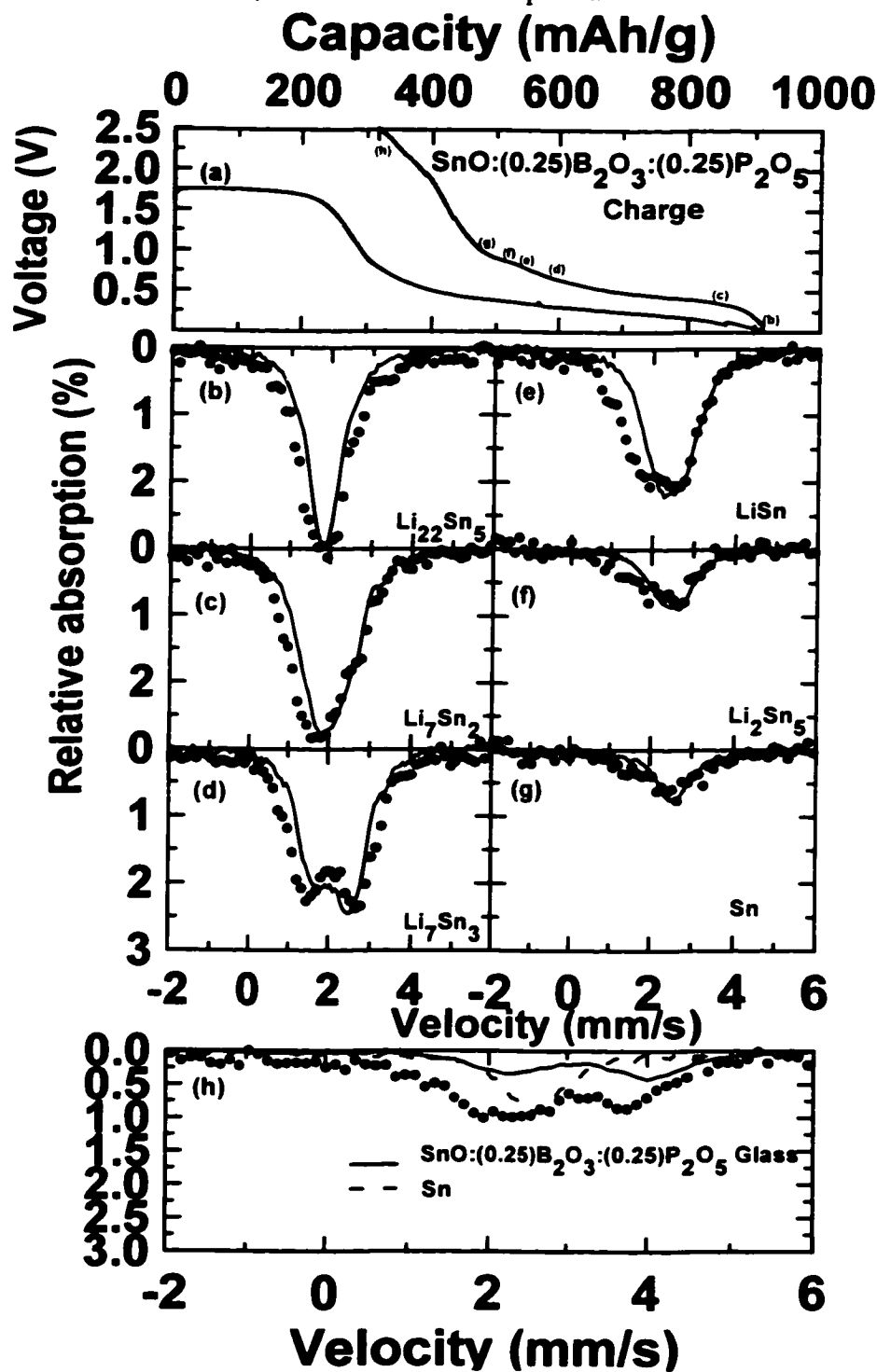
Equation 4-5 was used to estimate the value of α (the surface to matrix coupling

constant for a Sn-SiO$_2$ composite) for a series of experimental data measured by Unruh et

al.(1992). They measured, by differential scanning calorimetry (DSC), the melting point

Figure 5-20 Melting temperature as a function of Sn grain size
The data points are taken from the experimental results of Unruh et al. (1992). The solid line shows a fit to the experimental points with $\alpha = 2.1$ (from equation 4-5), whereas the dashed one represents a fit using $\alpha = 1.9$
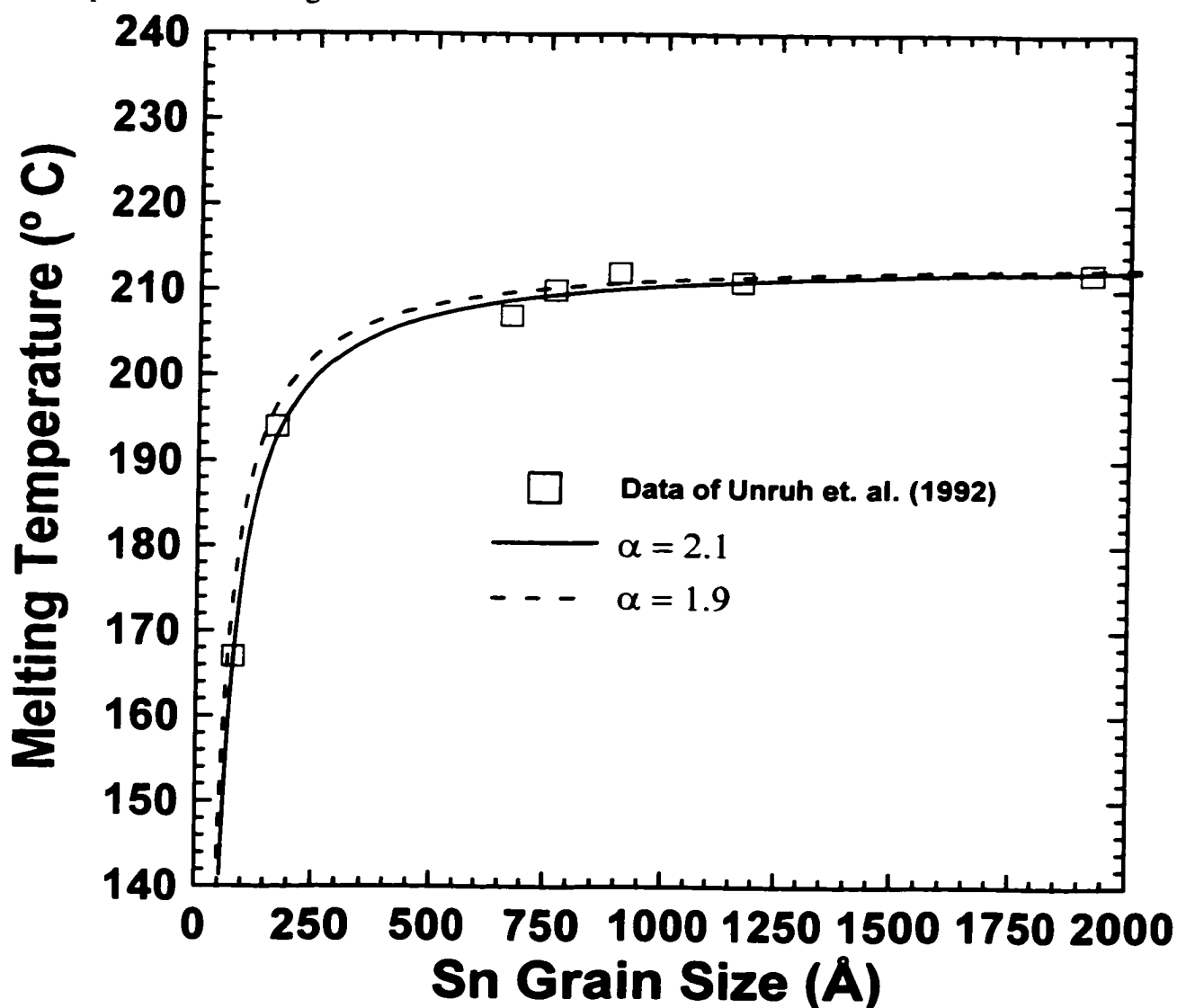
depression for small grain Sn embedded in an amorphous matrix of SiO$_2$. The materials were

prepared by RF magnetron sputtering. The observed melting points of the various sizes of Sn

grains is reproduced in figure 5-20. Equation 4-5 was used with an average monolayer thickness (h = (a+b+c)/6, where a, b and c are lattice constants for Sn) and two values of α were used (α = 2.1 and α = 1.9). The two limits provide a reasonable bound for the data of Unruh et al. (1992).

Figure 5-21 RFF as a function of Sn Grain size for α = 2.0

The solid curve represents the smallest monolayer thickness (h = c/2) and the largest monolayer thickness (h = a/2) is shown by the dashed line. The lattice constants of Sn (a and c were used).
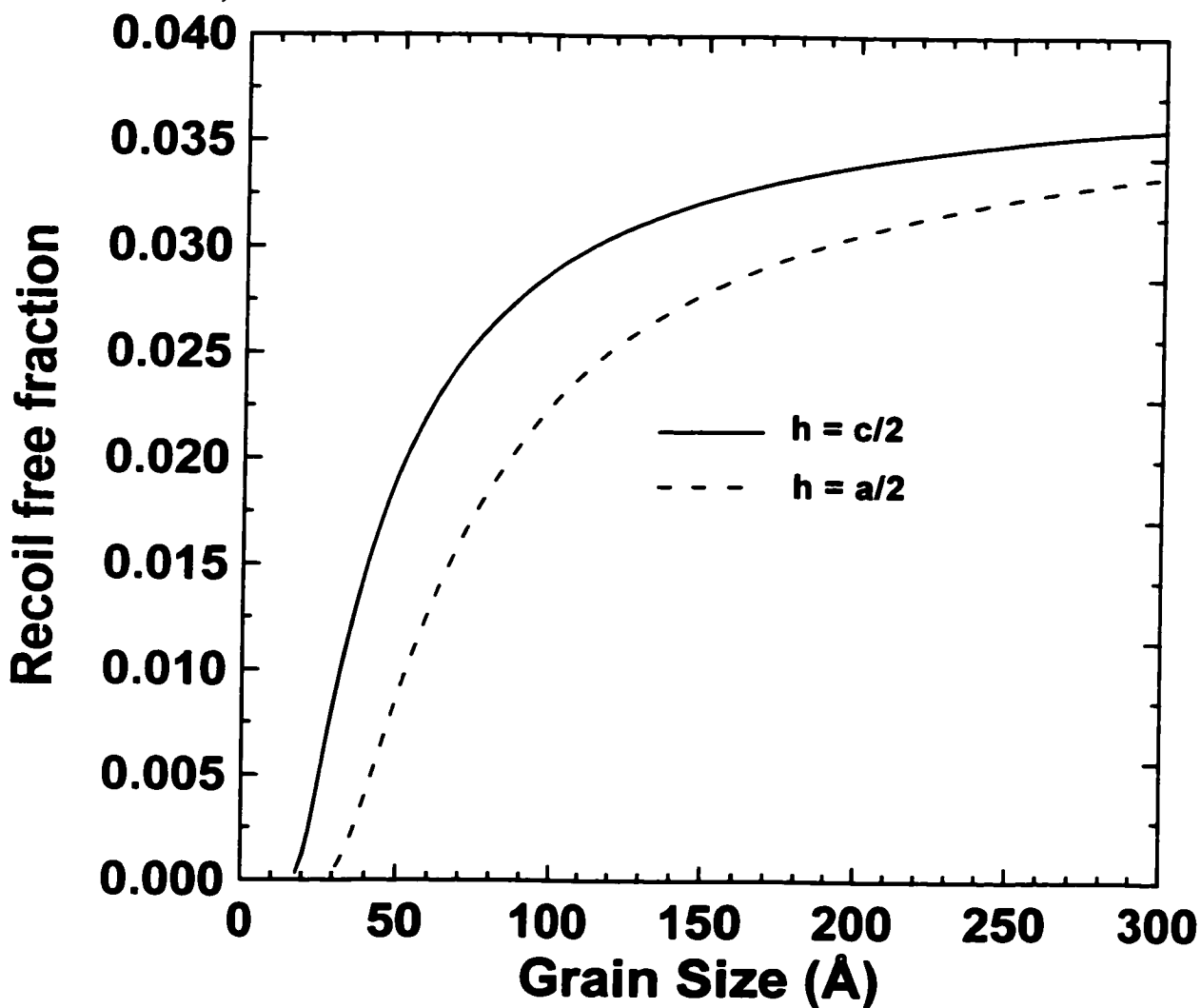
An average value of α = 2.0 was used to model the RFF of Sn, using equations 4-2 and 4-4, as a function of Sn grain size in a Sn:SiO$_2$ composite. The results of this are shown

in figure 5-21. In this figure, the upper and lower values of the monolayer thickness are shown.

An approximation for the RFF for different grain sizes of Sn embedded in an amorphous oxide matrix can now be made. It is assumed that the coupling constant, α, does not change for the types of matrix that are discussed in this chapter. The XRD patterns for the bottom of discharge of all of the in-situ XRD cells, as well as a $Li/SnO:SiO_2$ in-situ XRD cell (to be discussed in the next section), is shown in figure 5-22. The grain size, based on the FWHM of the 110 reflection for the BCC sub-structure (and the Scherrer equation), of the Li-rich phase (bottom of discharge) of the materials studied is calculated and shown in table 5-1. Table 5-1 also shows an estimate of the Sn grain size from which the lithium-rich phase was formed. This is based on the three-fold increase in volume per Sn from the crystal structure of Sn to the crystal structure of $Li_{22}Sn_5$ (chapter 3). The BCC 110 sub-structure peak was used to determine the Sn grain size as it is more pronounced than the Sn pattern for most of the materials. Figure 5-21 was used to estimate the RFF for the Sn in each of these materials, which is shown as a range (min, max) in table 5-1. These estimates have large

Table 5-1 Estimate of Li-rich Li-Sn phase grain size and Sn grain size from in-situ XRD

Material	Figure	FWHM of BCC 110 (radians)	$Li_{4.4}Sn$ Grain size estimate (Å)	Sn Grain size estimate (Å)	RFF (figure 5-21) (min, max)
SnO:(0.25/0.25)	5-22 (a)	0.061	26	18	(N/A, 0.0003)
$SnO:SiO_2$	5-22 (b)	0.056	27	19	(N/A, 0.0003)
SnO_2	5-22 (c)	0.035	44	30	(0.0001, 0.008)
SnO	5-22 (d)	0.013	117	81	(0.018, 0.027)

error bars due to the numerous assumptions made in the development of the model.

Figure 5-22 In-situ XRD patterns for the bottom of discharge, (a) SnO:(0.25/0.25) (figure 15-7 (b)), (b)SnO:SiO₂ (figure 5-24 (b)), (c) SnO₂ (figure 5-12 (b)), and (d) SnO (figure 5-6 (c))
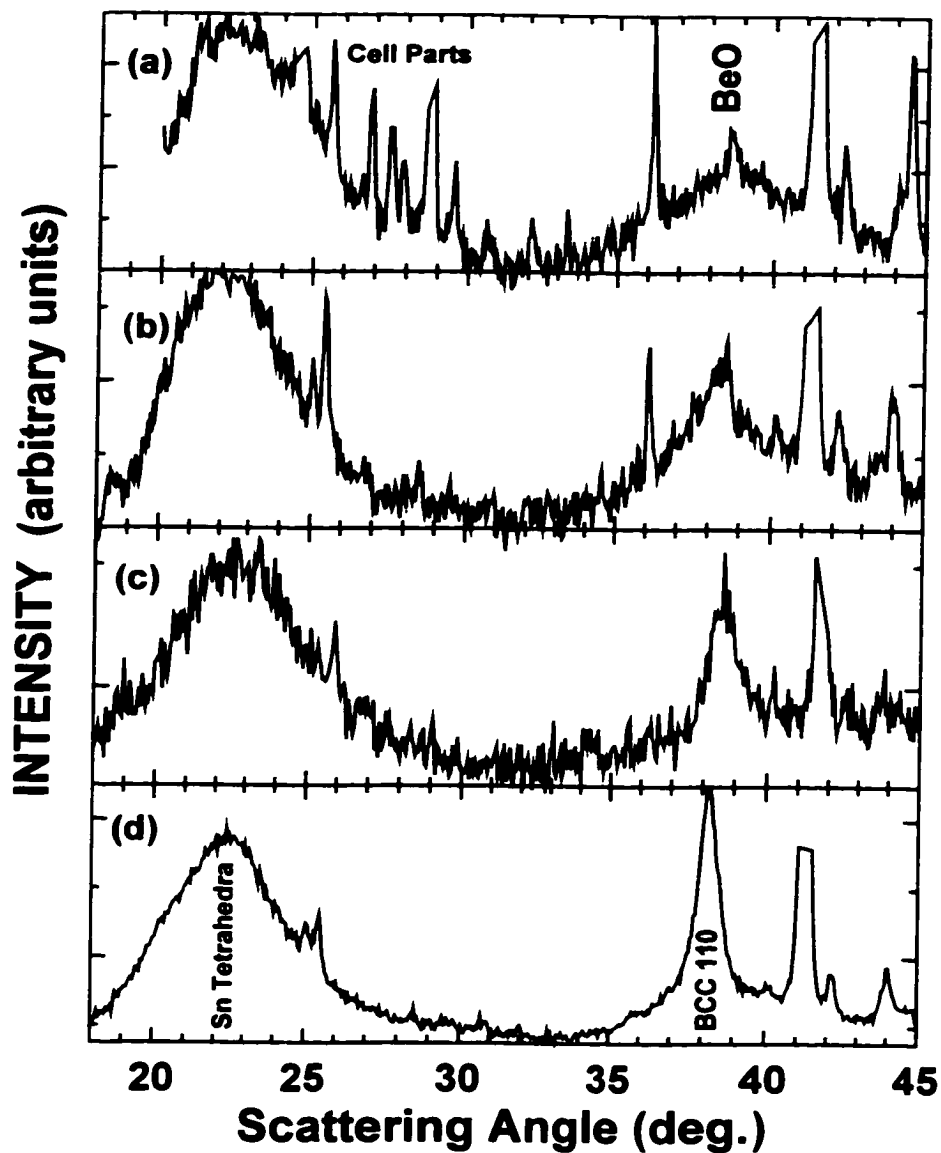
These estimates can be compared to those values obtained in the in-situ ME experiment. The RFF fractions were graphed for all of the spectra of the Li/SnO:(0.25/0.25) in-situ ME cell as they were for the Li/SnO cell (figure 5-10). These values are shown in figure 5-23.

Figure 5-23 RFF versus y in Li_ySnO as obtained by in-situ ME measurement of
Li/SnO and Li/SnO:(0.25/0.25)
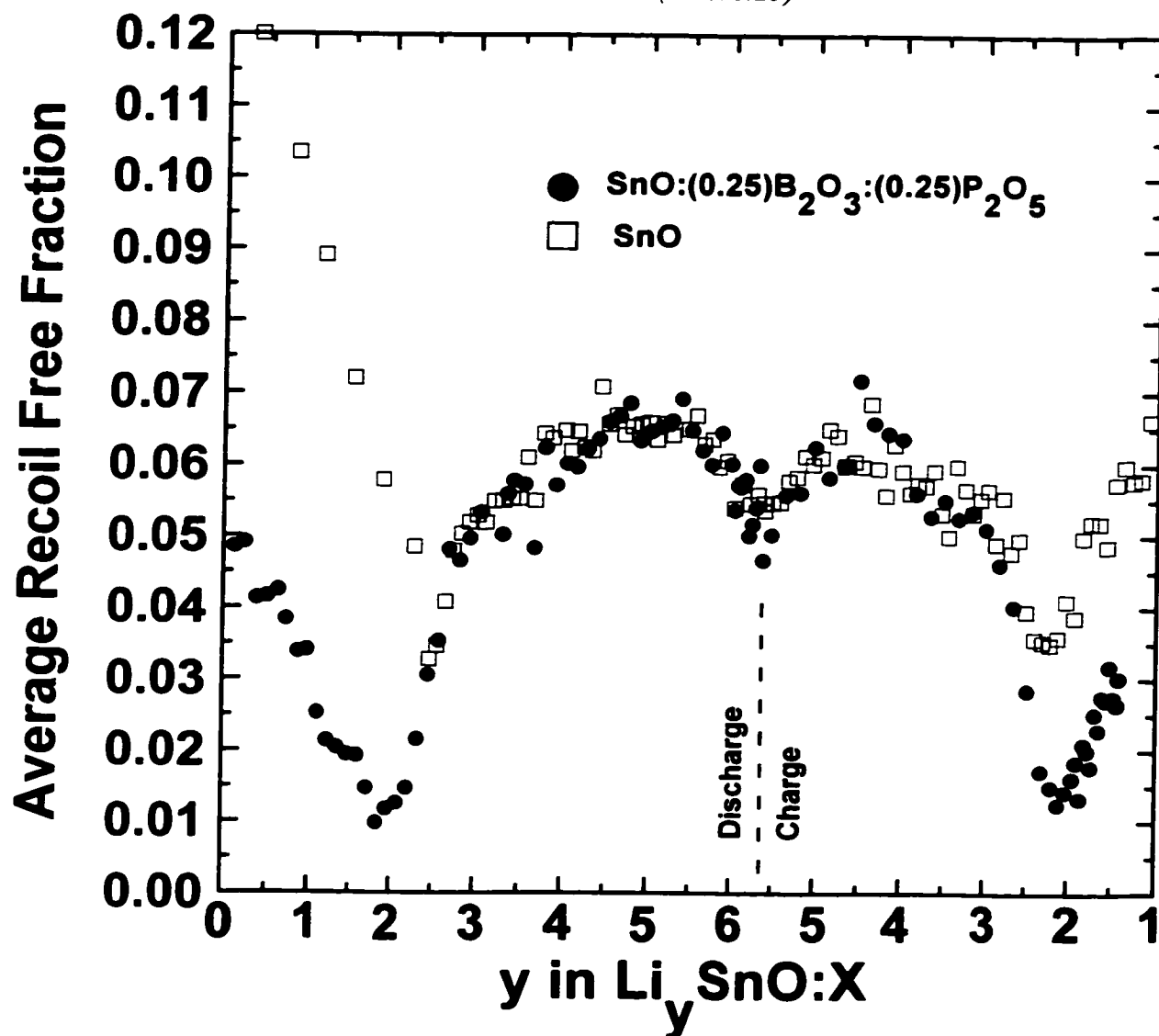
The number of Sn atoms in the coated SnO and SnO:(0.25/0.25) cathodes were within

10% of each other. Therefore, the SnO:(0.25/0.25) RFF values were scaled on the same scale

as the SnO RFF values. The observed RFF (of Sn at y = 2) for SnO:(0.25/0.25) was

approximately 0.01, and the observed value of the RFF for SnO (of Sn at y = 2) was 0.032.

The estimate of the RFF based on grain size (table 5-1) shows that the measured RFF of the

Sn atoms (at y=2) in SnO agrees somewhat with the upper bound of the calculation (RFF_{max}

= 0.030). However, the observed RFF value for the glass does not (RFF_{max} = 0.0003). There were, of course, several assumptions made in both the calculation and in the analysis of the measurement. The main point is that the RFF decreases markedly with grain size. This is the case both from a theoretical and from an experimental perspective. A more detailed pursuit of this theory and type of measurement could be quite useful.

More useful information can be gained from figure 5-23. Both samples match each other well on this graph. As shown in chapter 4, and again in chapter 5, the RFF is a measurement of the lattice and its surroundings (the matrix). Figure 5-23 suggests a strong similarity between the reaction of lithium with SnO and with SnO:(0.25/0.25) glass. Furthermore, note the slight increase in the RFF for both samples from y = 2 during discharge to y = 2 during charge. This suggests that the Sn atoms (as metallic Sn) could be **aggregating** to larger grain size. In fact, they are. The purpose of chapter 6 shall be to investigate this aggregation.

The remainder of the spectra of figures 5-18 and 5-19 show much the same behaviour as those of figures 5-8 and 5-9 (the Li/SnO cell). There is one potentially important difference between them, however. The characteristic spectra of Li_7Sn_3 (i.e. the two singlets at low and high velocity) are prevalent for a larger amount of capacity (y in $Li_ySnO:X$) than they are in the Li/SnO cell. This could be studied further.

Figure 5-19 (h) shows that the back-reaction also occurs in the glass. The original glass powder spectrum and the Sn spectrum have been plotted (not fit) on the spectrum at the top of charge.

Therefore, the SnO (0.25/0.25) glass follows the proposed reaction mechanism suggested by equation 5-3. In the following section the reaction mechanism shall be shown to

be consistent for all SnO-containing materials that were made and studied.

5.5 Other SnO-containing glasses

Figure 5-24 shows a summary of the results of a Li/SnO:SiO$_2$ in-situ XRD cell. This cell was made with a 'Bellcore' electrode. The cell was discharged and charged using a specific current of 9.3 mA/g, between upper and lower voltage limits of 2.5 and 0.0 V, respectively. As was the case for the Li/SnO:(0.25/0.25) in-situ XRD cell, the phases, Sn (at least not substantially, there may be some Sn impurity in this sample – see figure 5-12 (a)), Li$_2$Sn$_5$ and LiSn are not observed during the first discharge of this cell. The characteristic pattern of poorly formed lithium-rich alloys is definitely apparent at the bottom of discharge (figure 5-24 (b), whose peak positions are highlighted by the expected structure peak positions in figure 5-24 (c)). The difference between this glass and the SnO:(0.25/0.25) glass is that there is greater evidence for the formation of Sn on charge (compare figure 5-24 (a) to figure 5-17 (a).

Figure 5-25 shows the first 3 half cycles of cells made from the SnO boro-phosphate series of glasses (XRD of the series is shown in figure 5-14). These cells were discharged and charged between upper and lower voltage limits of 2.5 and 0.0 V, respectively, with a constant specific current of 37.2 mA/g.

Figure 5-25 has a capacity axis that has been plotted as mAh/(g Sn). If the reaction that was suggested in equation 5-3 is correct for all SnO-containing materials, then these voltage profiles should be similar when plotted on this scale, which they are.

Figure 5-24 In-situ XRD results for Li / SnO:SiO₂ cell, (a) end of charge (2.5V), (b) end of discharge (0.0V), (c) peak positions of some Li-rich alloy phases, and (d) first scan (2.5 V)
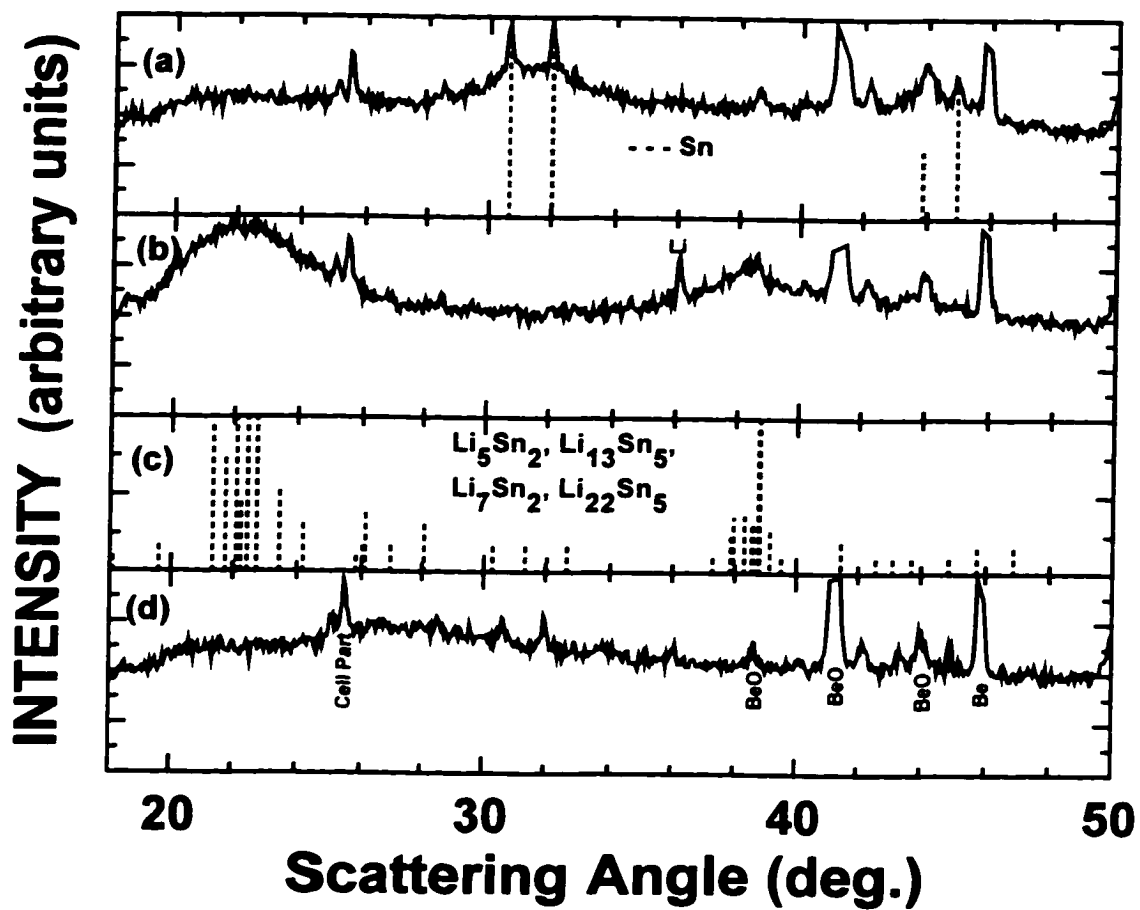
Figure 5-25 Voltage versus capacity (mAh/(g Sn)) for cells made from Li and, (a) SnO:(0.1/0.1), (b) SnO:(0.4/0.1), (c) SnO:(0.25/0.25), (d) SnO:(0.1/0.4), (e) SnO:(0.25/0.25), and (f) SnO:(0.5/0.5)
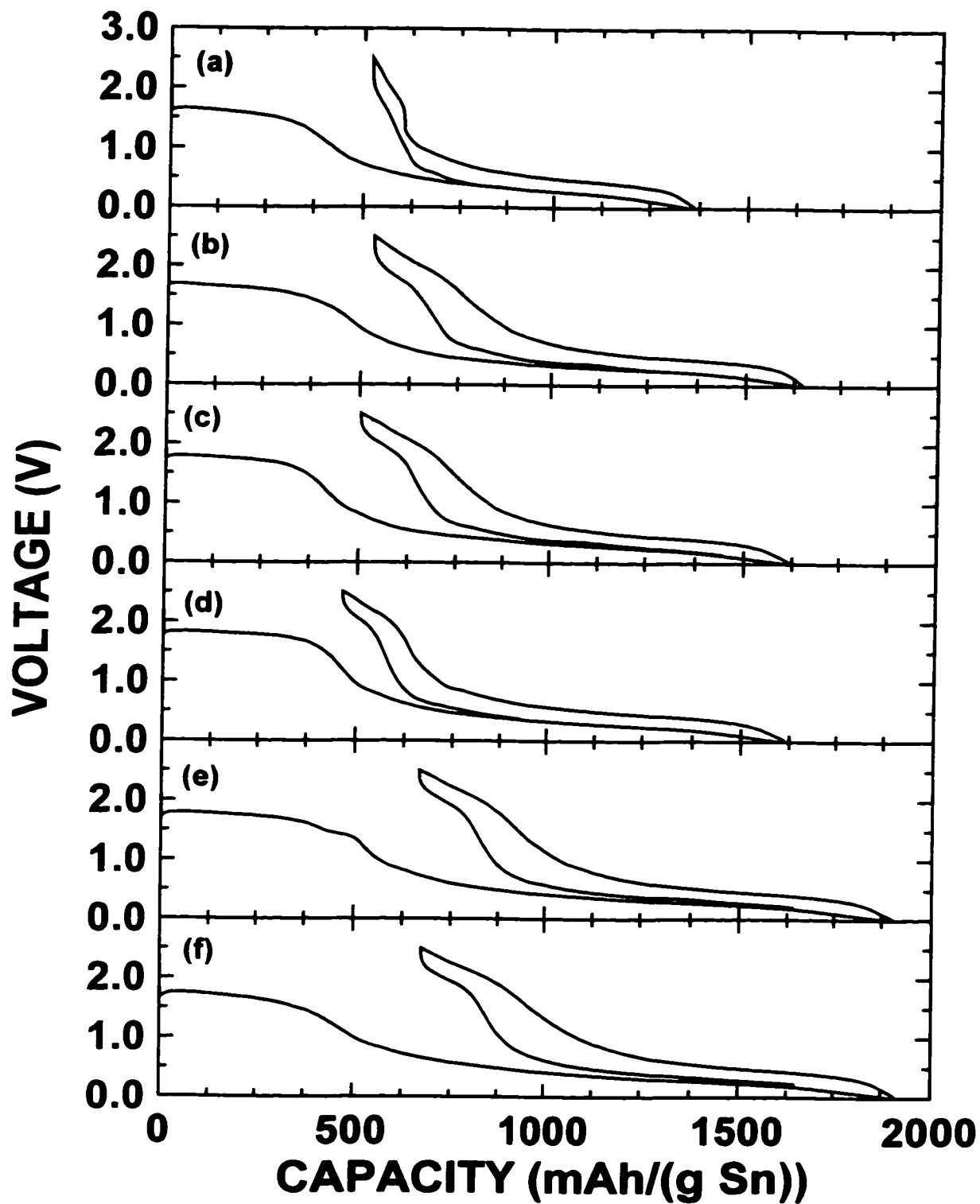
Figure 5-26 shows that a similar reaction mechanism exists in all of the SnO-based materials studied. The reversible capacity (for cells discharged and charged between 0.1 and 0.8 V, respectively) is plotted as a function of the weight percent Sn in the samples. The reaction given in equation 5-3 predicts that this should be a straight line.

Figure 5-26 Reversible capacity (mAh/g) versus weight % Sn for all SnO-containing materials studied
The cells were discharged and charged between 0.1 and 0.8 V, respectively.
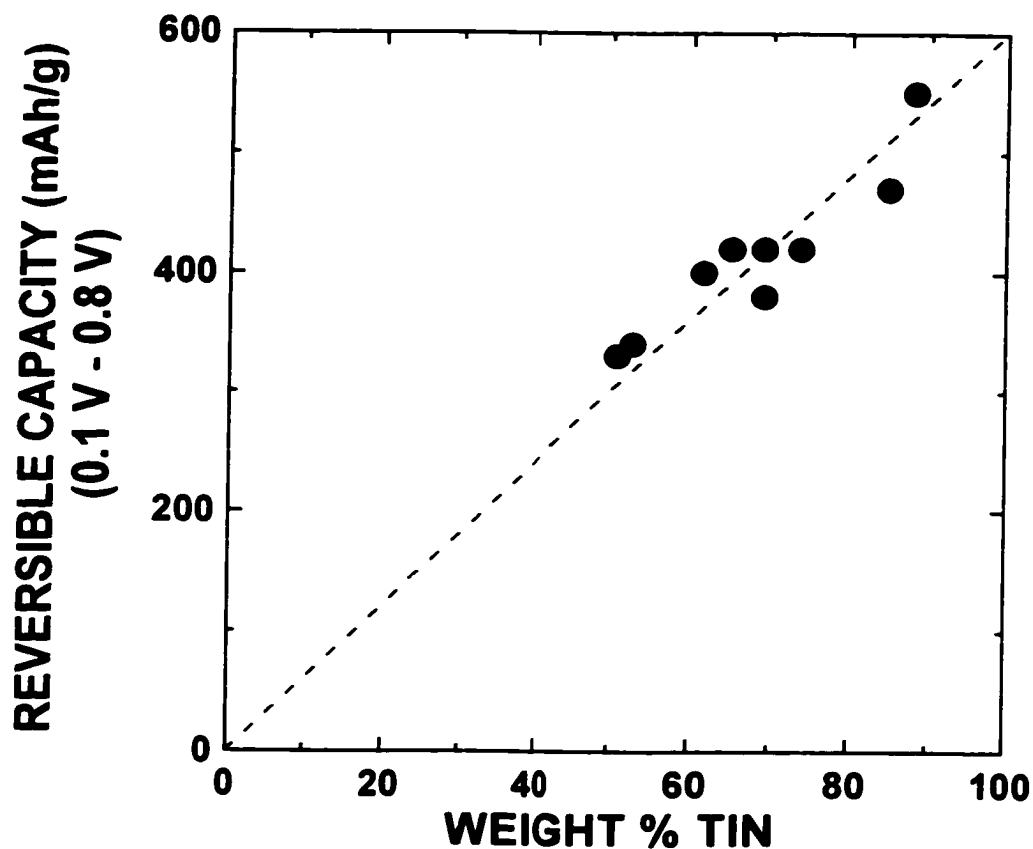
The first cycle reaction mechanism of lithium with SnO-based materials is now well understood. The next step is to investigate subsequent cycles, and therefore, the reversibility of these types of materials as they react with lithium.

Chapter 6

Subsequent cycles and reversibility

6.1 The effects of bulk phase transitions on reversibility

The first cycle reaction mechanism for the electrochemical reaction of lithium with tin oxide composites has been established in chapter 5. We now focus on subsequent cycles and reversibility. During the first discharge, the tin oxide component is reduced to tin which then alloys with lithium. The alloying reaction occurs in a lithium ion-conducting matrix (for SnO the matrix is amorphous Li_2O, and for SnO:X the matrix is amorphous X and amorphous Li_2O). The matrix is mostly inert. However, at high enough voltage (during lithium removal) the matrix can 'back react' to a degree. The back reaction, as it turns out, affects reversibility, and it shall be discussed later in the chapter. The first portion of the discussion, however, shall focus on the reversibility of the alloying reaction alone.

6.1.1 Background

The failure mechanism, or poor reversibility, of lithium alloy materials has to do with the loss of morphological integrity through many cycles. The 'cracking' of the grains, as it is often referred, is as a result of the large change in volume from adding lithium to the grain (for example, see Yang et al., 1996 and Anani et al., 1982). In addition, adding lithium to an alloying metal (with large grains) causes phase transformations through different crystallographic structures. Some of the alloy phases are described as brittle materials, which contributes to the problem of grain cracking (Fauteux and Koksbang, 1993). The alloying reaction, unlike an intercalation process (such as lithium insertion into graphite), is not

108

benign. A solution to this problem has been to 'dilute' the active alloying phase in either a lithium and electron-conducting matrix (e.g. Boukamp et al., 1981 and Huggins et al., 1984), or in an electron-conducting matrix of two different alloying metals (e.g. Besenhard et al., 1990). This way the expansion of the grains can occur in a 'softer' environment. The Fuji approach is similar to these methods, except that the active component is dispersed in a lithium ion-conducting matrix.

In this thesis, focus is given to the effects of grain size on reversibility. Chapter 4 was devoted to exploring the effects of grain size on some of the experimental measurements that will be used in this chapter and in the following chapter.

Figure 6-1 is a schematic of the addition of lithium to both a large grain (~ 400 Å, figure 6-1 (a)) and a small grain (~ 10 Å, figure 6-1 (b)) alloy phase ($Li_{\alpha}Sn$). In the case of the large grain, the addition of lithium, which has a finite diffusion constant in the alloy phase, causes a 'skin' of the new phase ($Li_{\beta}Sn$) to develop. Assume that both bulk phases are quite different crystallographic structures, which is certainly true for the Li-Sn alloy phases. There will be volume mismatch between these phases at the phase boundary. The resulting inhomogeneous expansion can create voids and cracks within the grain, which are impermeable to lithium ions and electrons. After several lithium insertions and removals, the growth of these voids and cracks can lead to the pulverization of the grain. Some of the alloy fragments become disconnected electrically (and ionically) from the rest of the grain, and as a result can no longer react electrochemically with lithium ions. By analogy, consider a lakebed after a period of drought; the fissures and cracks that develop are as a result of inhomogeneous contraction of the soil particles.

Figure 6-1 Schematic of the effects of grain size on bulk phase transitions, (a) Large grain (~ 400 Å) and (b) Small grain (~ 10 Å)
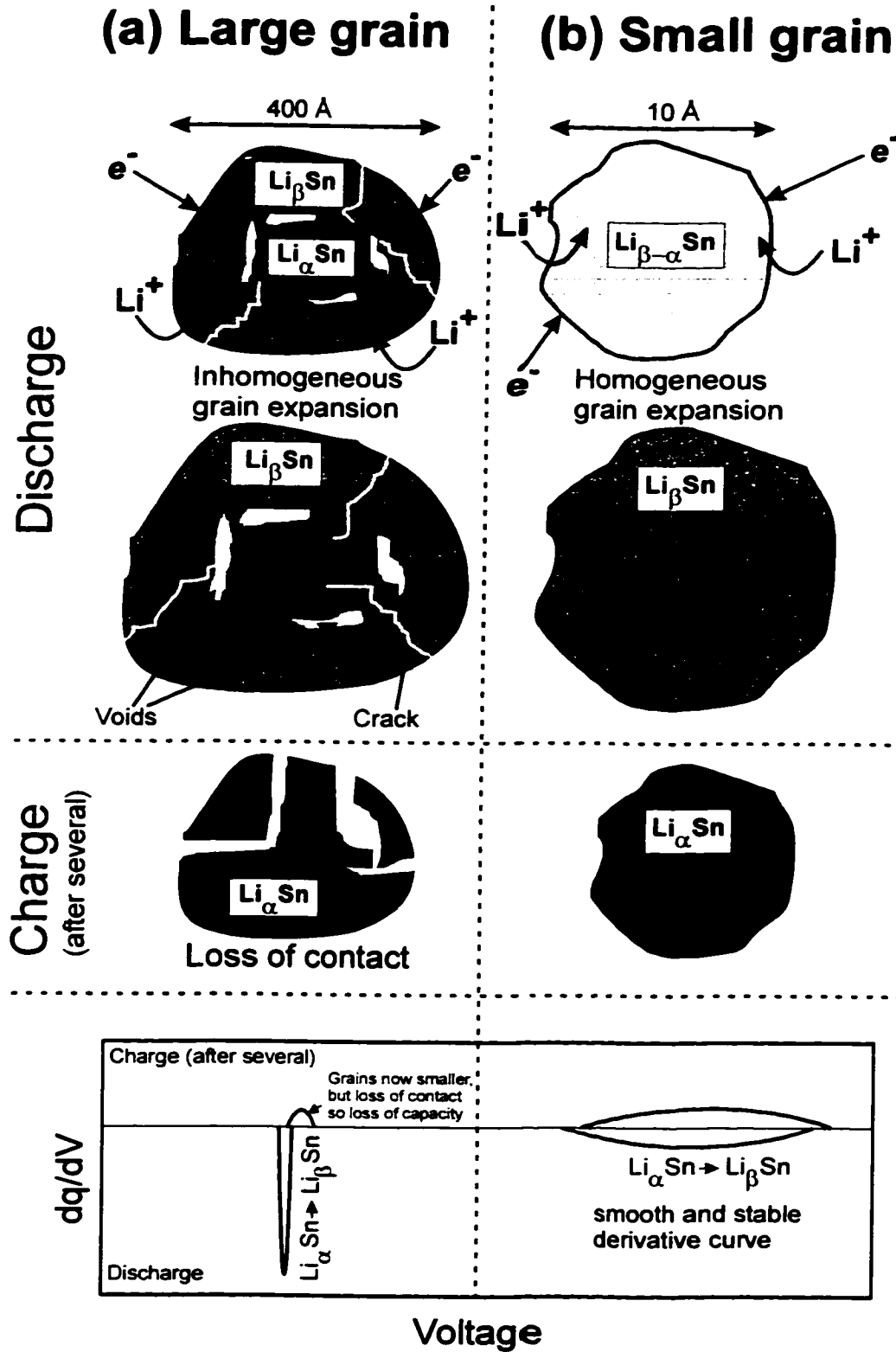
The bottom panel of figure 6-1 (a) shows the corresponding differential capacity versus voltage. A bulk phase transition during discharge would appear as a narrow peak in differential capacity. After several discharge and charge reactions, the electrochemically active components of the pulverized grain would now be smaller, so the differential capacity (shown on charge in the schematic) would broaden. The area under this broad peak, however, would be smaller than the area under the peak during the first discharge. Therefore, bulk phase transition in large grains lead to capacity loss after several cycles.

Small grain material (~ 10 Å), on the other hand, expands and contracts homogeneously as lithium is added and removed (figure 6-1 (b)). If the grain size is sufficiently small, lithium ions can diffuse readily from the grain surface to the grain center. In this case, a two-phase boundary region is meaningless and the grain expands, not as a phase mixture, but as a homogeneous Li_xSn phase. Small grain material will not develop voids and cracks as lithium is subsequently inserted and removed. Figure 6-1 (b) shows the corresponding differential capacity versus voltage. Small grain material would produce a broad peak that would be stable from discharge to charge after many cycles. Therefore, alloy materials with small grains should retain their initial capacity after many lithium insertions and removals.

6.1.2 Effect of grain size on the reversibility of the reaction of lithium with SnO_2

Low temperature thermal decomposition of Sn acetates and oxalates can be used to produce SnO_2 with small grain size (Dollimore et al., 1963). Using this method, small grain-sized SnO_2 was made and compared to bulk SnO_2 by XRD and electrochemical reaction. Figure 6-2 shows the XRD patterns of the various samples of SnO_2 used; bulk SnO_2 (1)

(Aesar Corp.) in figure 6-2 (c), SnO_2 (2) prepared by the thermal decomposition of Sn(II)

acetate (Aldrich) at 420°C in air in figure 6-2 (b), and SnO_2 (3) prepared by the thermal

decomposition of Sn(IV) acetate (Aldrich) at 390°C in argon in figure 6-2 (a).

Figure 6-2 XRD patterns of different grain-sized SnO_2
Impurity peaks from SnO in samples 2 and 3 are indicated
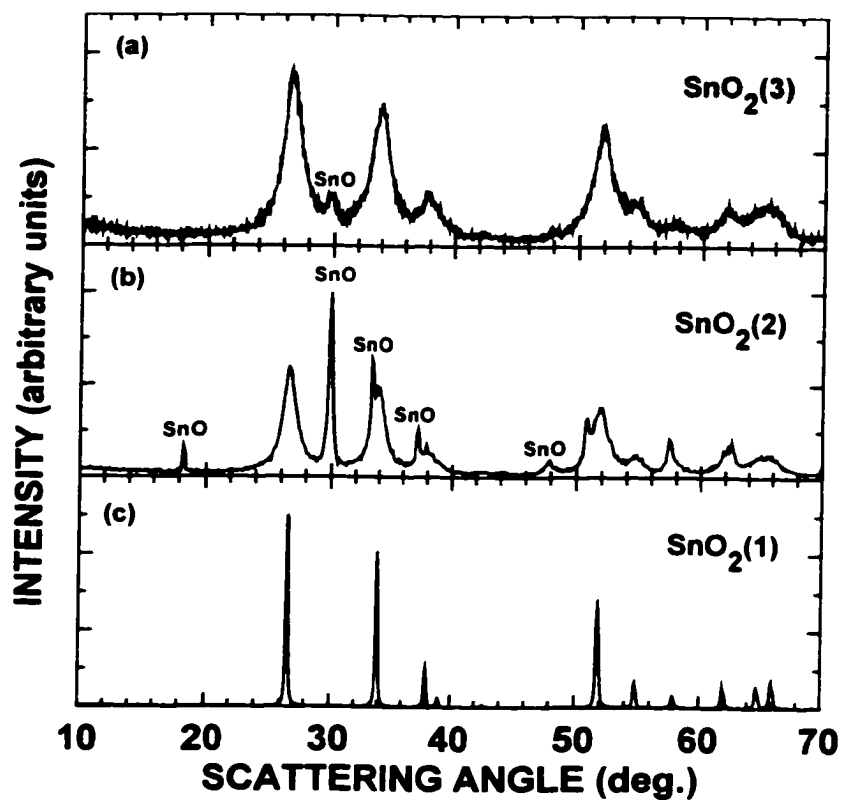
Table 6-2 The grain size of the SnO_2 samples studied

Sample	Description	FWHM for 110 reflection (Fig. 6-2) (deg.)	Grain size by Scherrer equation (Å)
SnO_2 (1)	Aeasar, as received	0.2	> 400
SnO_2 (2)	Sn(II) acetate at 420°C in air	1.4	58
SnO_2 (3)	Sn(IV) acetate at 390° C in argon	1.8	45

Table 6-1 lists the grain sizes calculated from the peak near 27° (the 110 reflection for SnO₂) by the Scherrer equation. The grain size decreases from sample 1 to sample 2 to sample 3.

Electrodes and cells of these materials were made. The cells were discharged and charged with a specific current of 37.2 mA/g, between various fixed voltage limits.

Figure 6-3 Capacity versus cycle number for different grain-sized SnO₂ samples
Cells were discharged and charged between 0.2 and 1.3 V.
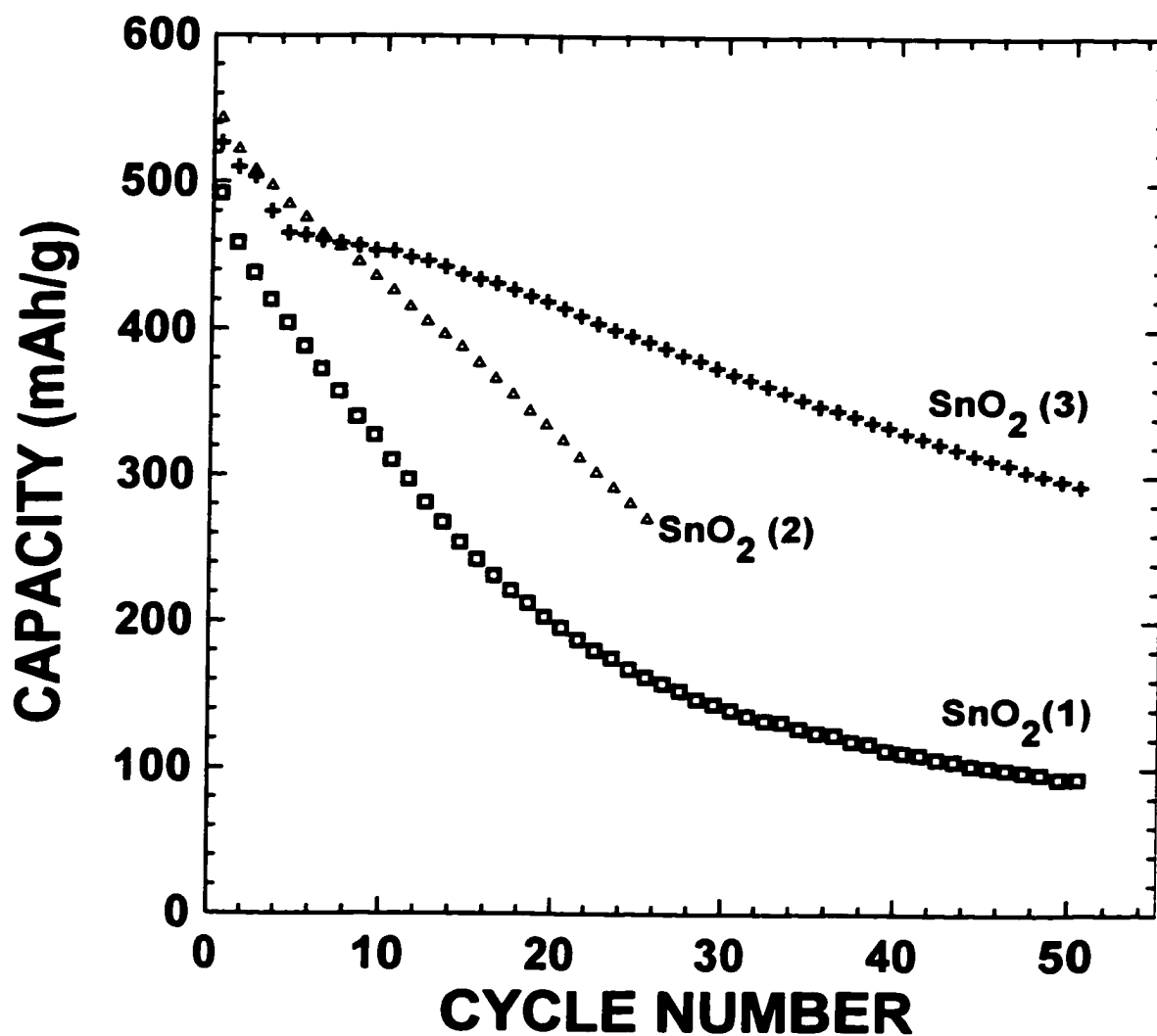
Figure 6-3 shows the capacity versus cycle number for cells of samples 1, 2, and 3

discharged and charged between 0.2 and 1.3 V. It is clear that the capacity retention is best

for the sample with the smallest grains (SnO_2 (3), 45 Å), and worst for the sample with the

largest grains (SnO_2 (1), > 400 Å).

Figure 6-4 Differential capacity versus voltage for cells of,
(a) Li/(SnO₂ (3) – grain size 45 Å), and (b) Li/(SnO₂ (1) – grain size > 400 Å)
The 2nd discharge and charge cycle is shown by the solid line, and the dashed line is the 5th
cycle. Cells were discharged and charged between 0.2 and 1.3 V.
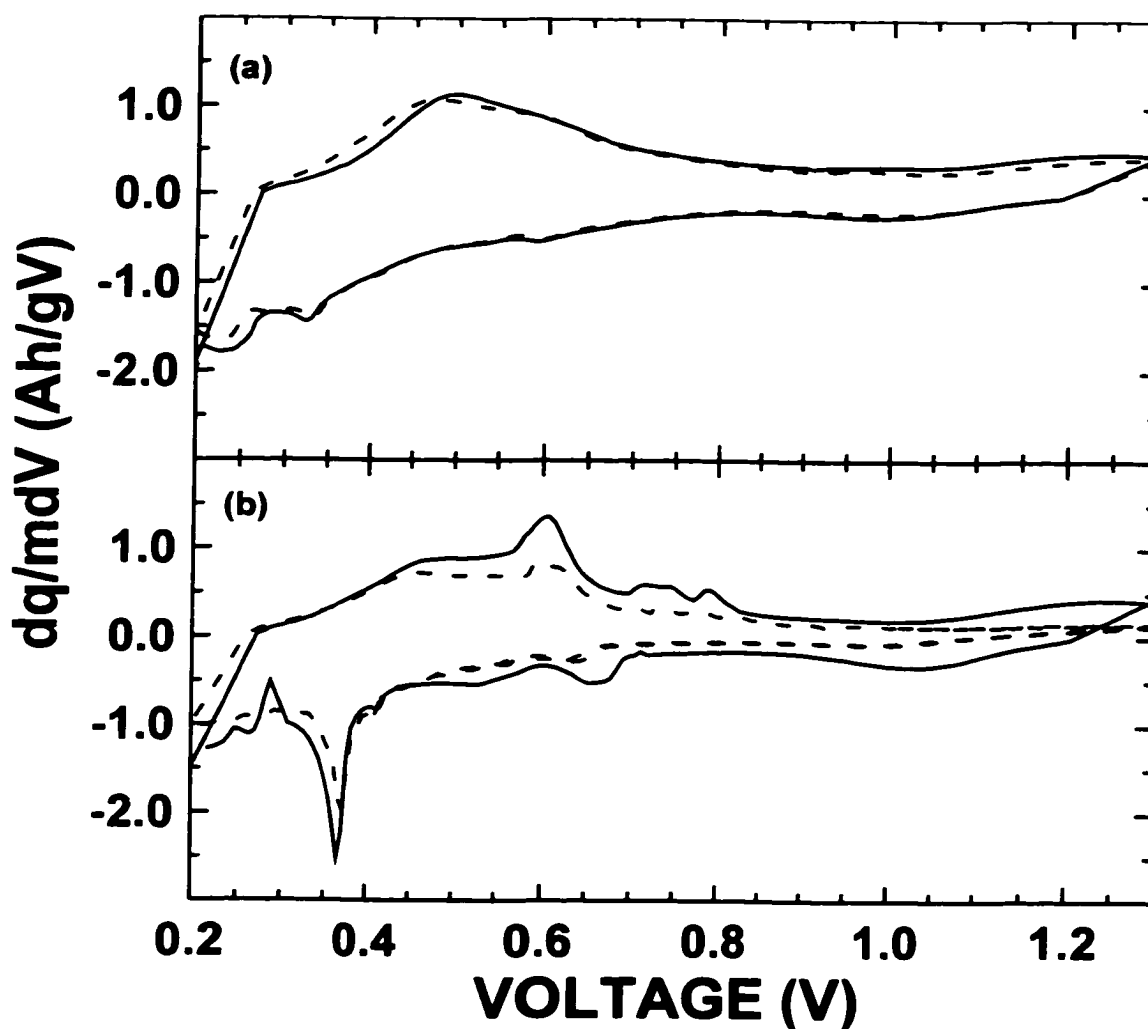
Figure 6-4 shows the differential capacity versus voltage for the 2nd (solid line) and

5th (dashed line) cycles of the largest and smallest grain size materials of figure 6-2. SnO_2

(1), the largest grain size (> 400 Å), displays sharp peaks in differential capacity which

diminish in width and intensity by the 5th cycle (figure 6-4 (b)). Presumably the large grain size material has lost capacity due to pulverization of the grains. The small grain material, SnO_2 (3) (45 Å), however, shows a smooth differential capacity response that is stable over these four cycles (figure 6-4(a)). The starting grain size of the SnO_2 (3) sample was not as small as the schematic of figure 6-1 (b) suggests in order to have inhomogeneous expansion of grains (i.e. 10 Å). However, the grain size of the Sn regions that result from the reduction of SnO_2 (of 45 Å grain size) during the first discharge are what is important, and these are probably smaller than that of the starting material. In any event, the 10 Å estimate of figure 6-1 (b) is not precise.

The purpose of the acetate decomposition experiment was to make materials to investigate the effects of grain size on reversibility. It is clear that 'smaller is better' is one key factor for good reversibility.

6.2 Aggregation of Sn after the first discharge

It has been shown in the previous section that small grain size alloy materials have better capacity retention. The SnO composites described in chapter 5 produce small grain alloy material during the first discharge. The remainder of this chapter shall demonstrate that the Sn regions that are created during the first discharge grow to larger grain size by the repeated discharge and charge of the cell.

Figure 6-5 Schematic of aggregation of Sn in SnO:X Glass,
(a)Original SnO:X glass, (b) After first discharge to 0.8 V, and
(c) Glass after several cycles showing cluster growth

The 'X' regions in panel (a) include oxygen that is bonded to the Sn, and the 'X' regions in panels (b) and (c) include lithium that forms lithia during first discharge.

(a) Original SnO:X Glass

(b) After first discharge to 0.8 V (nucleation)

(c) After several cycles showing Sn cluster growth
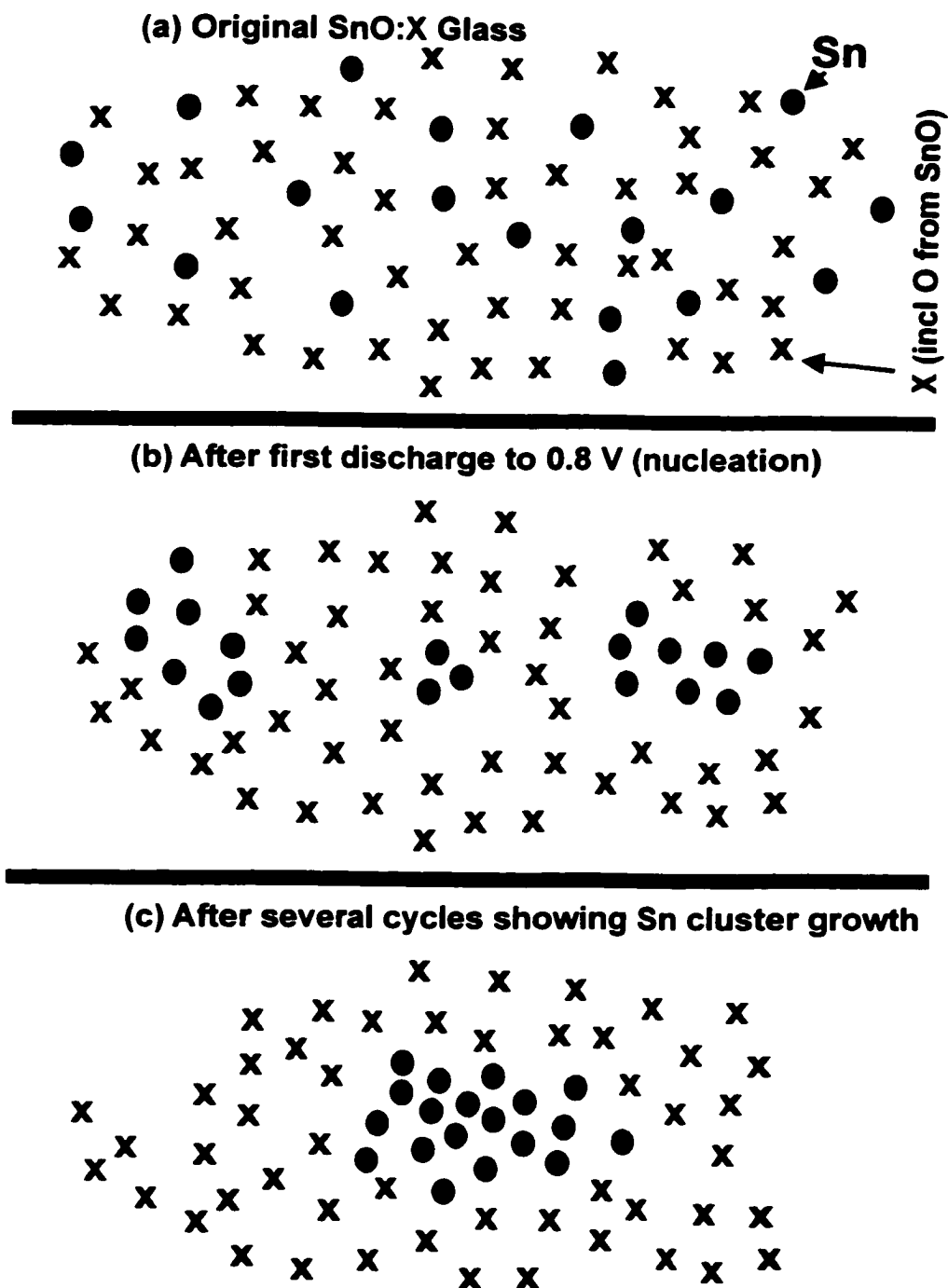
Figures 6-5 (a), (b) and (c) is a schematic of the aggregation of Sn regions in the SnO composites. The Sn atoms are shown by the solid circles in figures 6-5 (a), (b) and (c), and the 'X' regions are composed of the 'X + O' atoms (as in SnO:X) in panel (a), and include lithium (as in Li_2O) in panels (b) and (c). Initial addition of lithium to the SnO:X composite (during first discharge) produces clusters of Sn of this approximate size (figure 6-5 (b)), as shown by the in-situ XRD experiments in chapter 5.

Landau and Lifshitz (1993) discuss nucleation in phase transitions, 'If a substance is in a meta-stable state, it will sooner or later enter another state which is stable.' The oxide glass that has been reduced after the initial discharge plateau is such a meta-stable state. Early efforts to make a glass from metallic Sn, Li_2O, B_2O_3 and P_2O_5 invariably failed. The Sn would precipitate out of the quenched melt in large grain and particle size. Therefore, it is reasonable to assume that the small regions of Sn that are created during first discharge will attempt to aggregate to larger and larger grain size. The most stable state (i.e. bulk Sn) will provide the driving force for the aggregation.

There are numerous examples of nucleation and growth in the solid state. The process of *Coarsening* is an important technique used to produce materials with desirable characteristics. Karpov (1995) describes some examples of coarsening used in materials processing. Coarsening, or 'Diffusive Decomposition' as the author also calls it, can be used to create semiconductor micro-crystals in insulating glass, for example. The examples that the author provides are heated above room temperature, but the materials are not melted. It will be shown that in the case of Sn:(X + Li_2O), the subsequent cluster growth (aggregation) proceeds at room temperature in the electrochemical reaction of the material with lithium. The progression from SnO:X (figure 6-5 (a)) to the schematic of figure 6-5 (b) and then, by

further reaction with lithium (many cycles), to the situation shown in figure 6-5 (c), shall serve as the model for the rest of this chapter. If the aggregates become sufficiently large then the material will show poor reversibility. The aggregation of Sn (or the retardation of it) is the key factor for the reversibility of these materials as they react with lithium in an electrochemical cell.

Figure 6-6 (b) shows an XRD pattern which demonstrates aggregation of Sn in the SnO:(0.5/0.5) glass after 75 cycles. This cell was discharged and charged using a specific current of 37.2 mA/g, between fixed voltage limits of 0.1 and 0.8 V. The XRD pattern was obtained by ex-situ XRD of a retrieved cell electrode material (the cell was disassembled in an inert atmosphere glove box after charging the cell to 1.5 V). The electrode material was maintained in an argon atmosphere in an air-tight holder during measurement.

The approximate size of the Sn clusters is obtained by comparison to one of the model lattice Debye calculations that were described in chapter 4. The dashed line in figure 6-6 (b) represents a Debye calculation on a Sn lattice of 25 Å in size (i.e. the '5X5X5' model lattice). The Sn atoms in the material have aggregated (figure 6-6 (b)) from the smaller Sn clusters created after the first cycle (figure 6-6 (a)). Aggregation is also apparent in the differential capacity graph (figure 6-6 (c)). The differential capacity is smooth during the first cycle (solid line), and it develops peaks (dashed line) by repeated discharge and charge. The dashed line in figure 6-6 (c) represents the 75th cycle.

Figure 6-6 Aggregation of Sn in $SnO:(B_2O_3)_{0.5}:(P_2O_5)_{0.5}$ glass by electrochemical reaction with lithium, (a) Ex-situ XRD after one cycle, (b) Ex-situ XRD after 75 cycles, and (d) differential capacity versus voltage for the 1st (solid) and 75th (dashed) cycles

The dashed line in figure 6-6 (b) represents a calculated XRD pattern by the Debye formalism for a model Sn lattice of approximately 25 Å grain size.
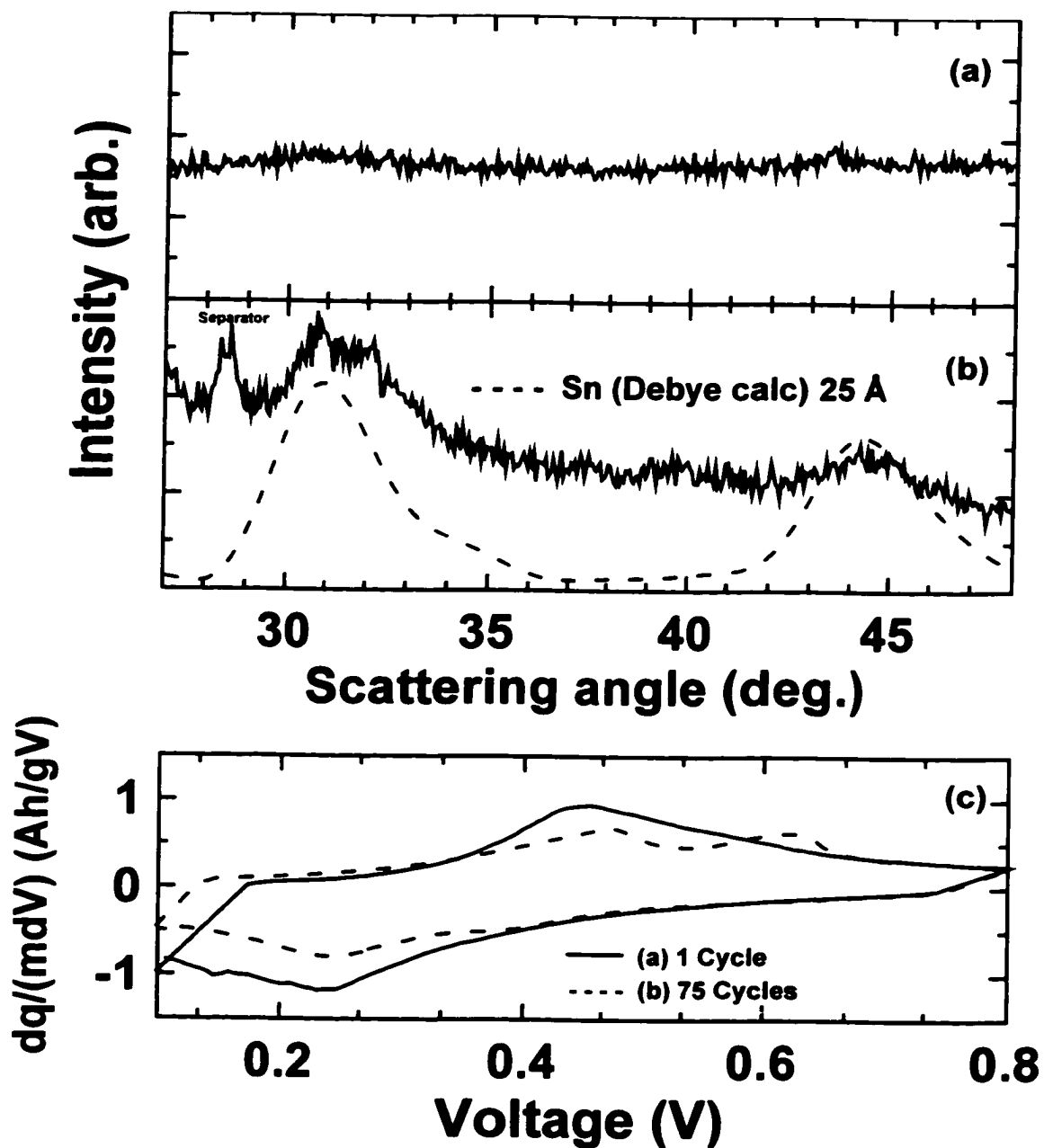
6.3 Volume fraction Sn (in SnO:X) and reversibility

The series of $SnO:B_2O_3:P_2O_5$ glasses (XRD patterns in figure 5-15) was synthesized to study Sn aggregation. A glass containing small amounts of Sn (e.g. SnO:(0.5/0.5)) should result initially in smaller regions of Sn than a glass that contains more Sn (e.g. SnO:(0.1/0.1)). The distances over which the Sn must traverse in order to nucleate and grow is greater in the dilute glass than it is in the concentrated glass. Figure 6-7 shows the XRD patterns taken of cathode materials that were discharged and charged for two cycles using a specific current of 37.2 mA/g, between upper and lower voltage limits of 2.5 V and 0.0 V, respectively. The cells were disassembled in an inert environment, after being held at a constant voltage of 1.5 V for a period of no less than one day. It is clear that the initial size of the Sn clusters that are formed is related to the number of 'spectator atoms' (i.e X and O) of the glass. Those materials with a large number of spectator atoms (figure 6-7 (d)) produce smaller Sn regions than those materials with the least number of spectator atoms (figure 6-7 (a)).

Figure 6-7 Ex-situ XRD after 2 cycles (0.0-2.5 V) for various SnO:X materials,
(a) Li/SnO:(0.1/0.1) cell cathode, (b) Li/SnO:(0.25/0.25), (c) Li/SnO:(0.35/0.35) and (d)
Li/SnO:(0.5/0.5)

The cells were discharged and charged between 0.0 and 2.5 V for 2 cycles. Figure 6-7 (d) shows the expected peak positions for Sn
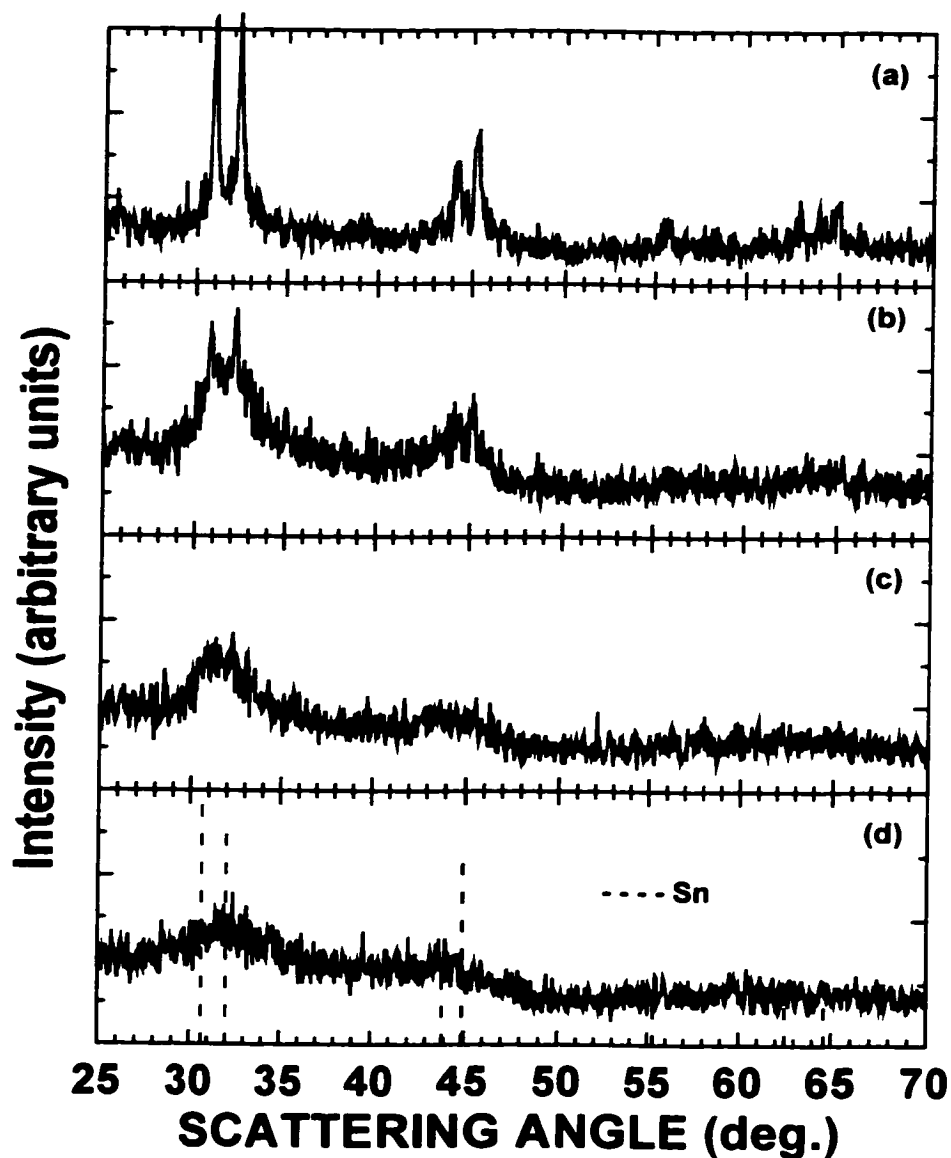
Therefore, the initial dispersion of Sn clusters that are far apart (as in the glass containing the least Sn) and that are structurally separated by more spectator atoms should cycle better as the ability to aggregate is reduced.

6.3.1 Spectator:Sn series and reversibility

The spectator:Sn designation that is used is calculated from the X plus oxygen atom count to the number of Sn atoms in a sample. For example, SnO has a spectator:Sn ratio of 1.0, whereas the SnO:(0.25/0.25) glass has a spectator:Sn ratio of 4.0. In order to help quantify the cycling stability of different samples, a capacity retention index, $R_{x/1}$, is used. This is the capacity of the xth charge cycle as a percentage of the 1st charge cycle capacity.

Figure 6-8 Capacity versus cycle number for cells made from the $SnO:(B_2O_3)_x:(P_2O_5)_y$ series of glasses, (a) SnO:(0.1/0.1), (b) SnO:(0.4/0.1), (c) SnO:(0.25/0.25), (d) SnO:(0.1/0.4), (e) SnO:(0.35/035), and (f) SnO:(0.5/0.5)

The spectator:Sn count, as well as the capacity retention index for the 40th cycle, $R_{40/1}$, is indicated for each sample. The cells were cycled between 0.1 and 0.8 V.
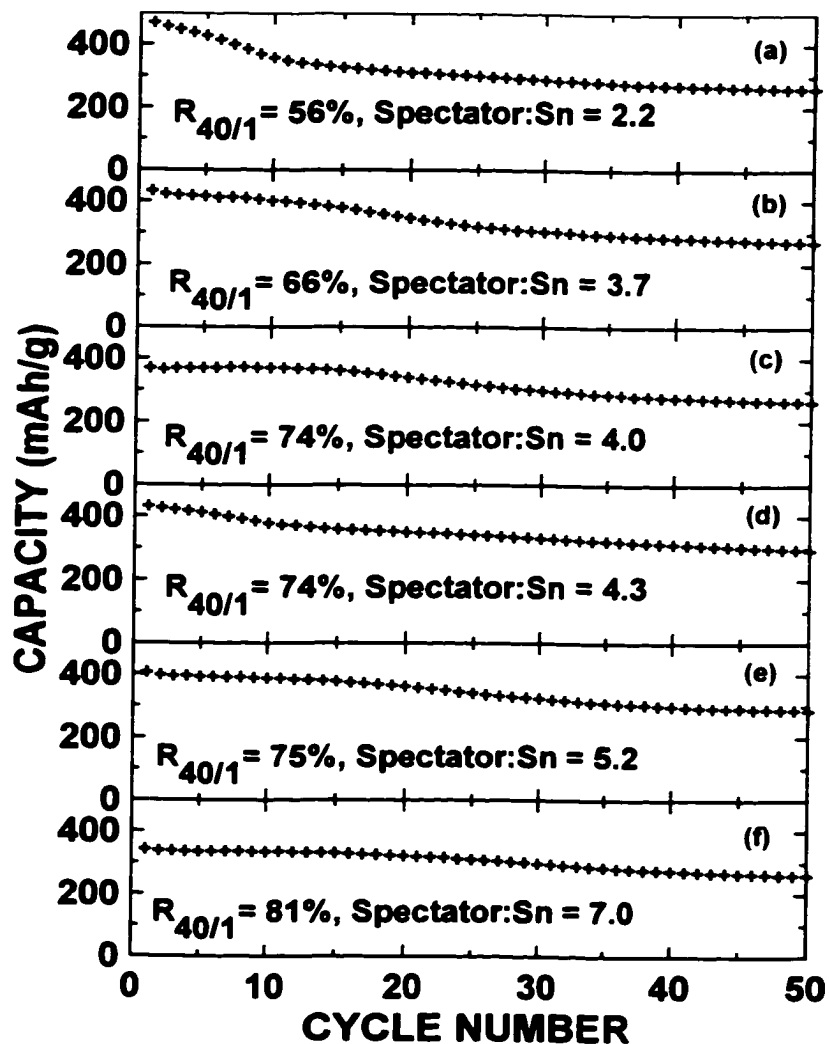
Figure 6-9 'Trade-off' between capacity and reversibility for SnO:X materials,
(a) First charge capacity versus X:Sn, (b) $R_{40/1}$ versus X:Sn

These are data for all SnO:X materials studied, where the cells were cycled between 0.1 and 0.8 V.
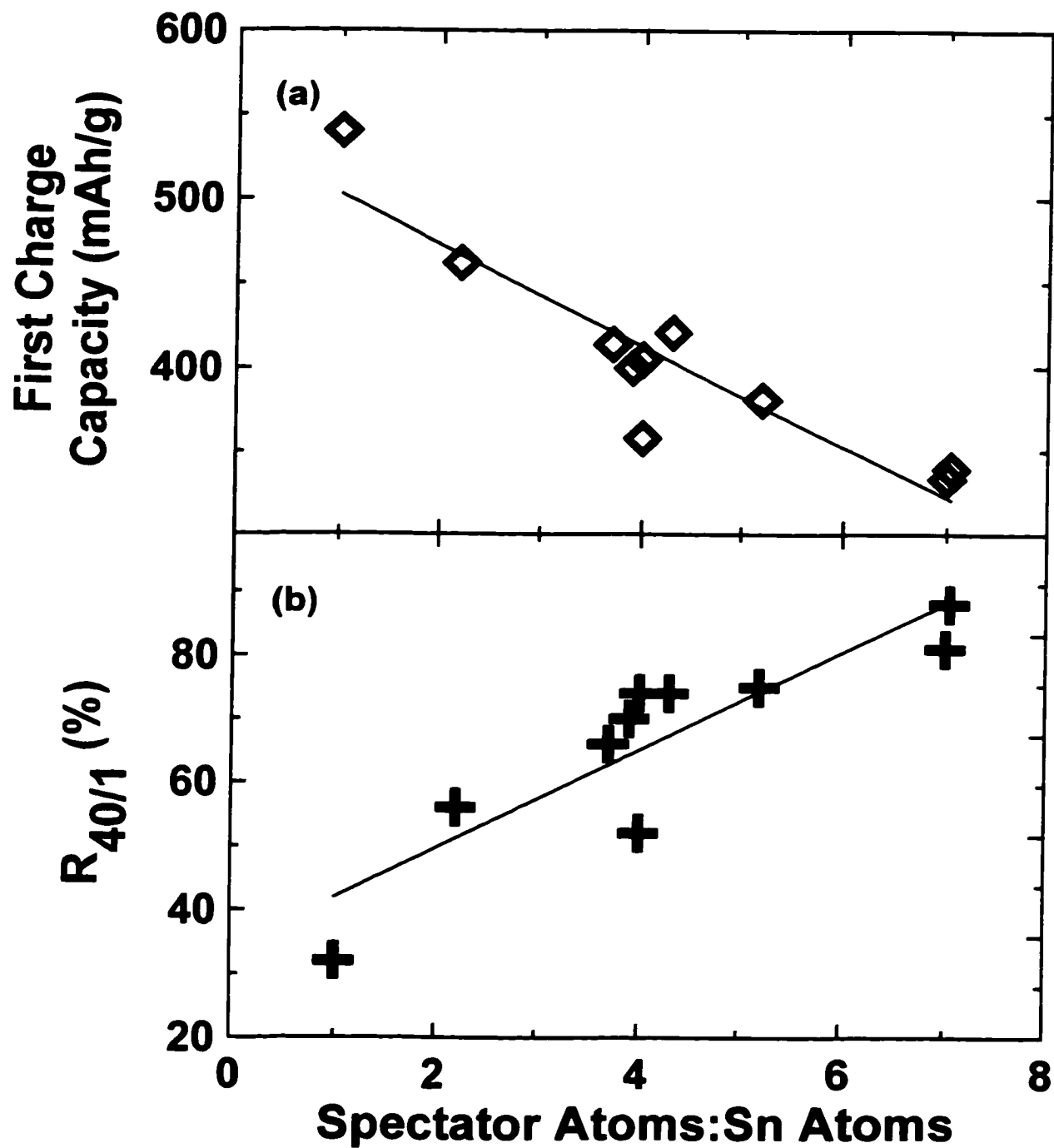
Figure 6-8 shows the capacity versus cycle number for the cells of the $SnO:(B_2O_3)_x:(P_2O_5)_y$ series of glasses that were cycled between 0.1 and 0.8 V with specific currents of 37.2 mA/g. As the X:Sn ratio increases, the capacity loss with cycle number decreases. However, this is at the expense of the specific capacity, because the spectator atoms add weight to the electrode, but not capacity. Figure 6-9 shows both $R_{40/1}$ and the first cycle reversible specific capacity plotted versus the X:Sn ratio for all SnO:X samples studied that were cycled over this voltage range.

6.3.2 Investigation of aggregation by differential capacity

The top five panels in figure 6-8 clearly show that the capacity with cycle number curves have an anomalous behaviour. There is a range in each curve at intermediate cycle numbers where the capacity is decreasing more rapidly than earlier and later in the life of the cell. In order to probe this behaviour, the differential capacity versus voltage for all the cycles of each sample were carefully examined. Figure 6-10 shows the differential capacity versus voltage for the first 60 cycles of the SnO:(0.1/0.1) glass. The differential capacity versus voltage graph is initially smooth in the first cycle, but by cycle 6, a peak at 0.6 V during charge is clearly emerging (figure 6-10 (d)). The same trends continue during cycles 7 to 15, that is, the peak at 0.6 V during charge and a corresponding peak at 0.45 V during discharge continue to grow (figure 6-10 (c)). After cycle 15, the peak at 0.45 V shrinks and is replaced by a strong peak near 0.35 V (figure 6-10 (b)). Finally, after cycle 24, the differential capacity pattern is more or less constant with cycle number (figure 6-10 (a)).

Figure 6-10 Differential capacity versus voltage for a Li/SnO:(0.1/0.1) cell cycled between 0.1 and 0.8 V at various cycles, (a) Cycles 24-60, (b) Cycles 16-24, (c) Cycles 7-15, and (d) Cycles 1-6

The changes in differential capacity for the respective graphs are indicated
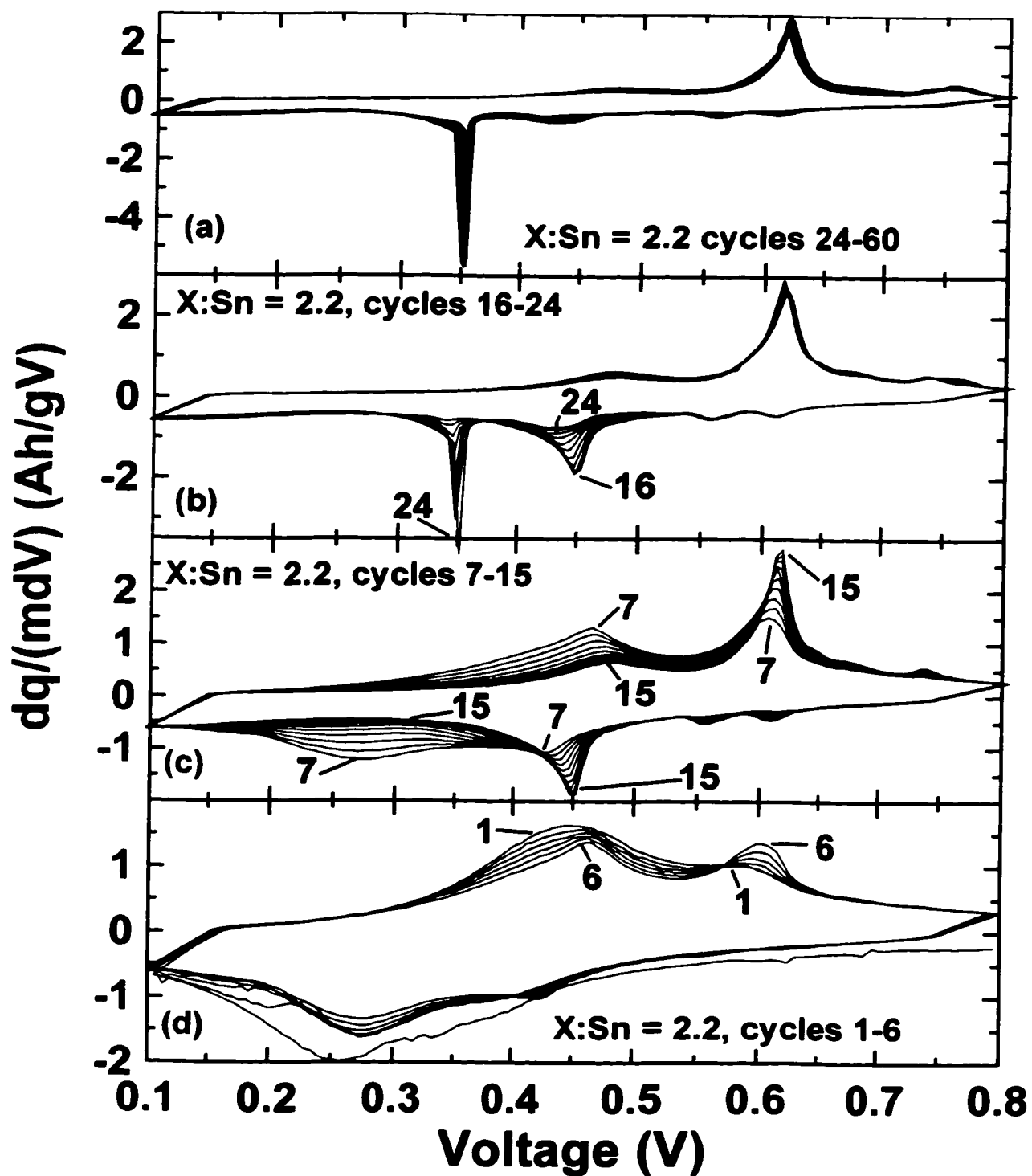
Figure 6-11 Differential capacity versus voltage for a Li/SnO:(0.4/0.1) cell cycled between 0.1 and 0.8 V at various cycles, (a) Cycles 24-60, (b) Cycles 16-24, (c) Cycles 7-15, and (d) Cycles 1-6

The changes in differential capacity for the respective graphs are indicated
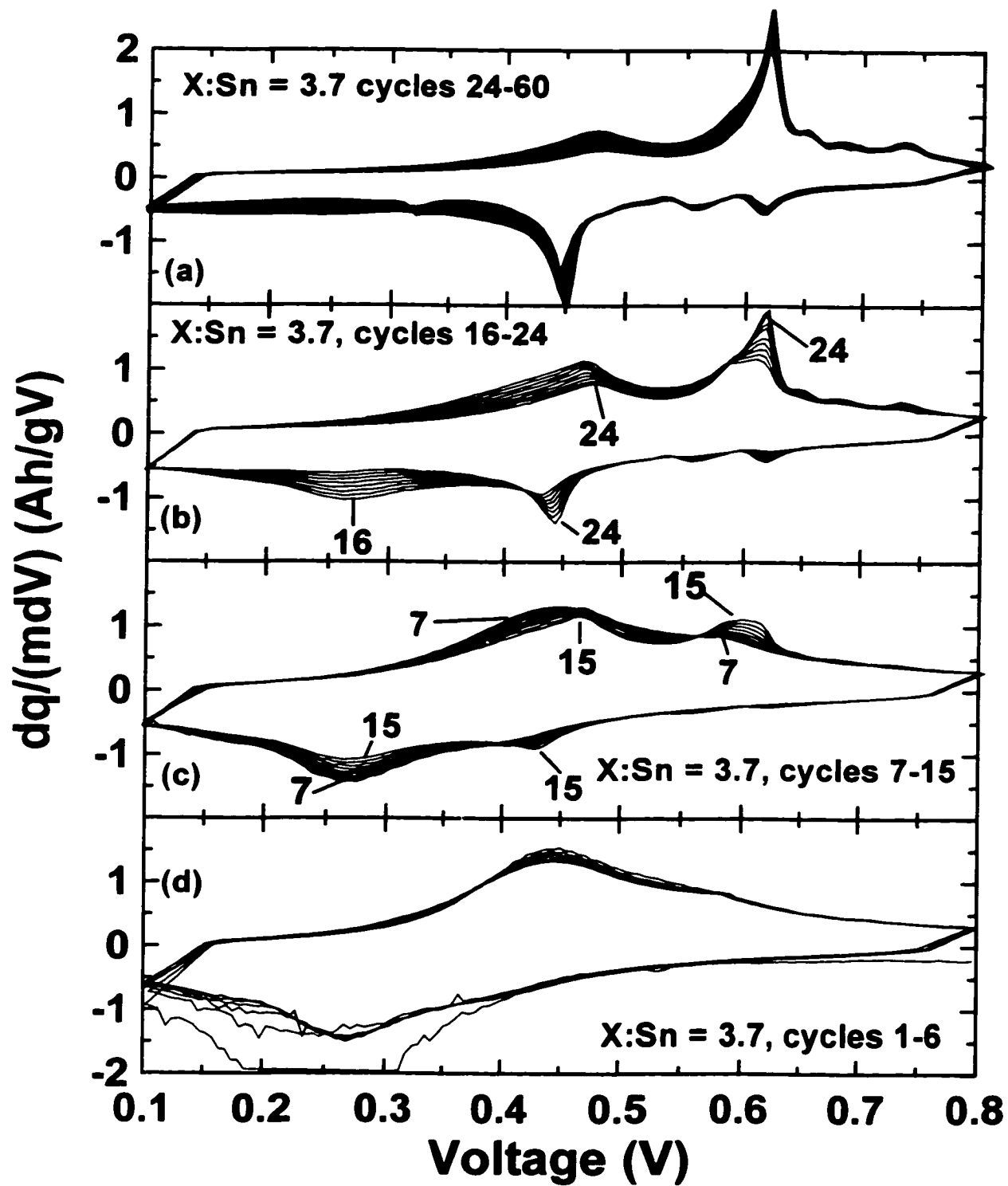
Figure 6-11 shows the same information as figure 6-12, except the SnO:(0.4/0.1) glass is examined. Again, the differential capacity is smooth in the early cycles (figure 6-11(d)). After 15 cycles, the SnO:(0.4/0.1) sample (figure 6-11 (c)) has almost the same differential capacity as the SnO:(0.1/0.1) sample did after 6 cycles (figure 6-10 (d)). After 24 cycles, the SnO:(0.4/0.1) sample reaches a stable differential capacity, shown in figure 6-11 (a). This shape is similar to that of the SnO:(0.1/0.1) sample after 15 cycles (figure 6-10 (c)). This suggests that both samples, which were initially glassy materials with well-dispersed tin atoms, move through the same sequence of tin cluster sizes, but at different rates. Furthermore, the stable cluster size in each case is different, judging by the shape of the steady state (cycle 60) differential capacity curve. The SnO:(0.1/0.1) sample, with X:Sn=2.2 forms larger regions of tin than does the SnO:(0.4/0.1) sample, with X:Sn=3.7.

Most curious is the change in appearance of the differential capacity between cycles 16 and 24 for SnO:(0.1/0.1). Why does the discharge peak at 0.45 V disappear, to be replaced by a peak at 0.35 V? Section 6.5 shall discuss this more fully. For now though, it is sufficient to realize that these materials aggregate to larger grain size through cycling with lithium.

Figure 6-12 shows the differential capacities for the first, 30th, and 60th cycles of the series of glasses. Each sample has a smooth differential capacity at cycle one suggesting very small (a few atoms) tin clusters. After 30 cycles, there is a clear trend shown by the samples. Those with small X:Sn ratios have sharp features in differential capacity suggesting large clusters of tin while those with large X:Sn ratios have broad features suggesting small clusters. Careful examination of all the cycles for all the samples shows that there is a common set of differential capacity profiles.

Figure 6-12 Differential capacity versus voltage for the $SnO:(B_2O_3)_x:(P_2O_5)_y$ series of glasses, at the 1st (column 1), 30th (column 2) and 60th (column 3) cycles for cells cycled between 0.1 and 0.8 V; (a),(b) and (c) Li/SnO:(0.1/0.1) , (d),(e) and (f) Li/SnO:(0.4/0.1) , (g),(h) and (i) Li/SnO:(0.25/0.25) , (j),(k) and (l) Li/SnO:(0.1/0.4) , (m),(n) and (o) Li/SnO:(0.35/0.35) , and (p),(q) and (r) Li/SnO:(0.5/0.5)
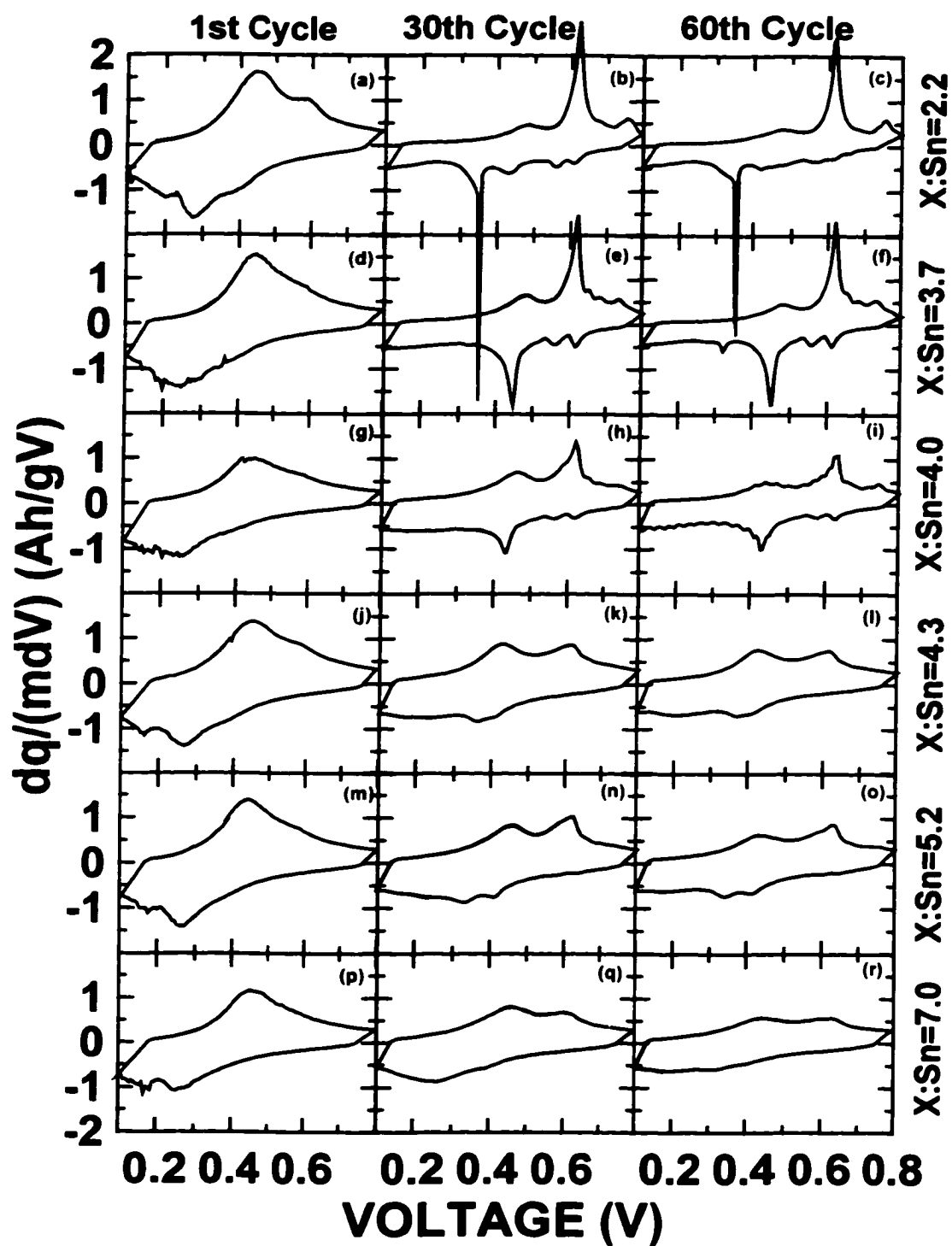
The differential capacities exhibited by the SnO:(0.5/0.5) sample can be found at small cycle numbers in the cycling behaviour of the SnO:(0.1/0.1) sample, and so on. Thus, there is a one to one correspondence between a differential capacity profile of a given shape and a particular tin cluster size. The variation of differential capacity versus voltage as a function of cycle number is a mapping of the growth of tin aggregate size with cycle number. Furthermore, it is clear (figure 6-12) that all the samples reach a steady state tin cluster size (stable differential capacity) after about 30 cycles. The steady state cluster size is smallest, in general, for the samples with the largest X:Sn ratio.

6.4 An investigation of the steady state tin cluster size

Figure 6-5 (a) shows a schematic view of the tin oxide composite glass. The tin and X atoms are indicated and are well dispersed, as expected, in an amorphous, uniform glass. Figure 6-5 (b) shows the situation after the first discharge to 0.8 V (Li atoms in the X-regions and in the tin clusters are not shown for clarity). The tin atoms have nucleated into clusters of tens of atoms. Assume that the growth will proceed (figure 6-5 (c)) until the distance between tin clusters reaches some maximum length, r.

6.4.1 Consequences of maximum distance between tin clusters

If this speculation is correct, then the steady state tin cluster size which results will depend on the initial volume fraction of tin in the glass. Glasses with little tin (large X:Sn ratios) will only be able to form small tin clusters before the cluster-cluster separation reaches r. On the other hand, if there is substantial tin initially (small X:Sn ratio), then big clusters are possible before the cluster-cluster separation becomes as large as r.

In order to make some estimates consider the following model. Assume that tin is initially dispersed in the glass with volume fraction, v. Assume that the maximum allowable separation between equal sized spherical tin clusters is r. Then one can solve for the maximum radius, R, of the equal-sized spherical clusters. Assuming that the clusters are packed on a simple cubic lattice (one sphere of radius R in a cube of edge 2R+r), one obtains,

$$v = \frac{4\pi R^3}{3(2R + r)^3}$$

which can be solved to give,

$$R = \frac{r(3v)^{0.33}}{(4\pi)^{0.33} - 2(3v)^{0.33}}$$

(6-1)

If the clusters were packed on a face centered cubic lattice (4 spheres of radius R in a cube of edge $2^{0.5}$(2R+r)), one obtains,

$$v = \frac{16\pi R^3}{3(\sqrt{2}(2R + r))^3}$$

which can be solved to give

$$R = \frac{\sqrt{2}r(3v)^{0.33}}{(16\pi)^{0.33} - \sqrt{8}(3v)^{0.33}}$$

(6-2)

Simple cubic packing is one of the least efficient forms of packing spheres and face-centered cubic, or cubic close packing is the most efficient method of packing spheres (Ashcroft and Mermin, 1976). It is likely that the clusters of tin formed in these materials will not be

exactly homogeneous in size and that they will adopt more random packing than these will. Nevertheless, the packing cases that are considered represent the bounds of quite inefficient packing and efficient packing.

Figure 6-13 shows the steady state radius of the formed clusters assuming a maximum inter-cluster distance, $r = 10$ Å, as a function of the volume fraction of tin, v, in the initial glass. Since each of equations 6-1 and 6-2 are linear in r, the curves in figure 6-13 simply shift for changes to the value of r. The key point of figure 6-13 is that R shows a very strong dependence on v. In order to relate the volume fraction of tin to the X:Sn ratio, we assume that all atoms have the same radius and all bond lengths are the same. Then the volume fraction tin is simply the reciprocal of the X:Sn ratio. (This assumption is, of course, inexact, but it is accurate enough given the speculative nature of the model.). Figure 6-14 shows the steady state cluster radius, R, versus the X:Sn ratio. Note that the y-axis is on a logarithmic scale. This shows that materials with small X:Sn ratios should have large steady state tin clusters formed and materials with large X:Sn ratios should have much smaller steady state tin clusters formed (as the differential capacity measurements in figure 6-12 imply). The tin cluster size found for the SnO:(0.5/0.5) sample (X:Sn = 7.2) after 75 cycles is about 25 Å in diameter (figure 6-6) and is in rough agreement with the predictions of figure 6-14. The simple model that is presented may capture the physics of tin aggregation in these materials, but we now speculate on the origin of the maximum intercluster distance, r.

*Figure 6-13 Calculated steady state Sn cluster radius (logarithmic axis)
versus volume fraction Sn assuming;
simple cubic packing (SCP) and cubic close packing (CCP) of Sn clusters.*
The maximum inter-cluster distance, r, was taken to be r = 10 Å for these curves.
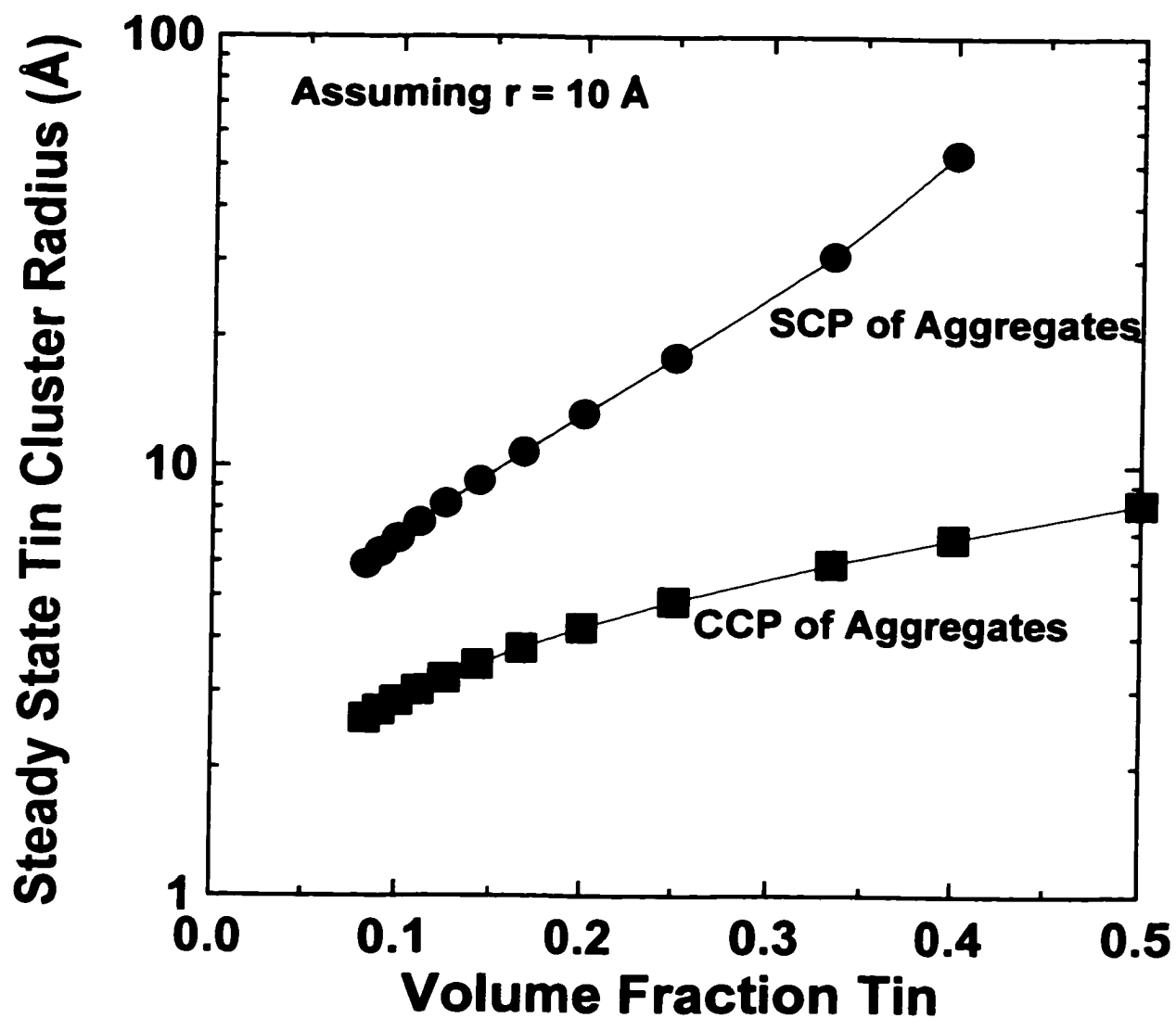
Figure 6-14 Calculated steady state Sn cluster radius (logarithmic axis)
versus X:Sn ratio assuming
simple cubic packing (SCP) and cubic close packing (CCP) of Sn clusters
The maximum inter-cluster distance, r, was taken to be r = 10 Å for these curves.
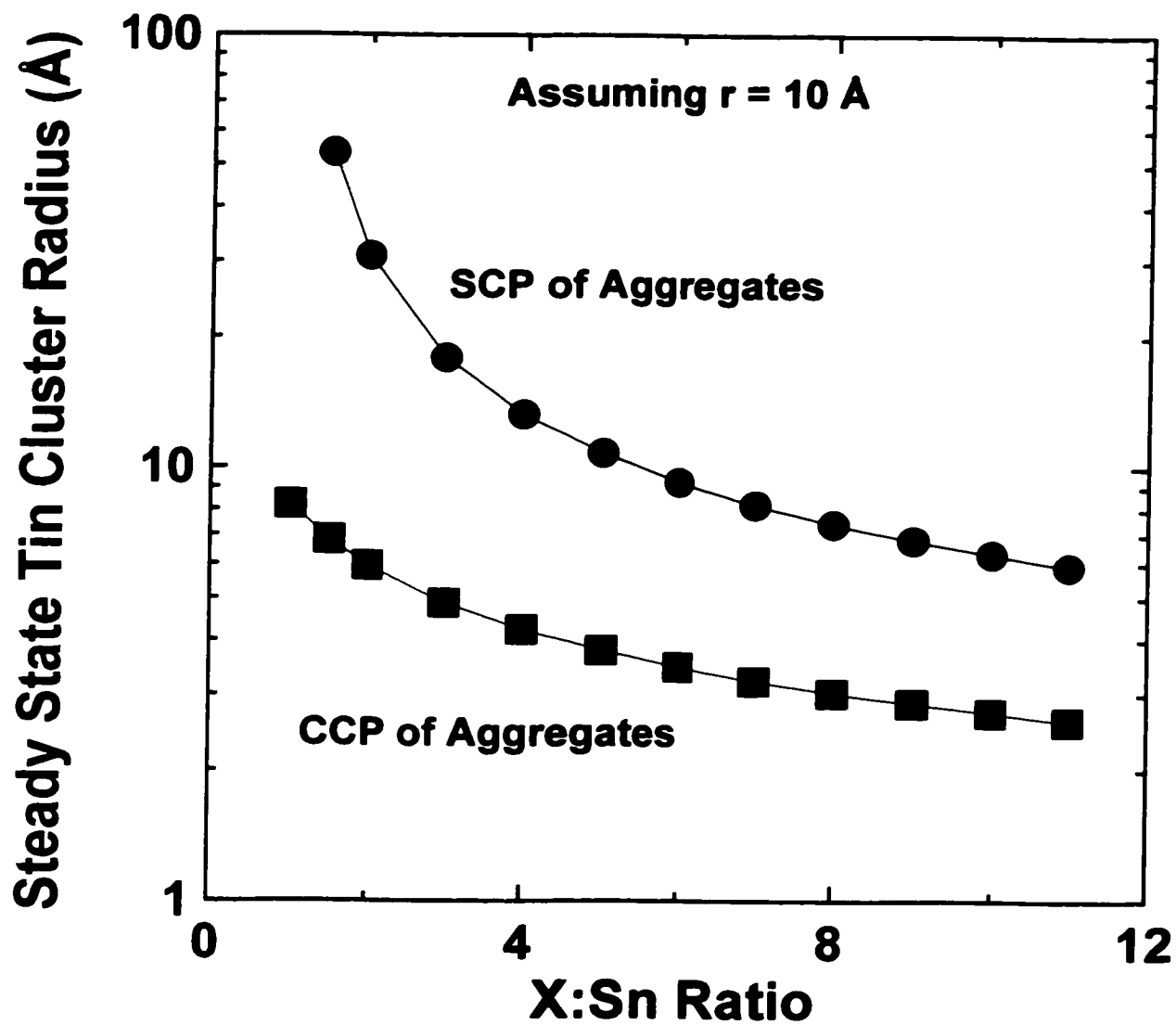
6.4.2 Possible origin of the maximum Sn intercluster distance

The results in the last section raise a number of important questions. What is the origin of the maximum intercluster separation? How do the tin atoms move in the glass in order to aggregate into larger and larger clusters? How do lithium atoms and electrons move between the tin clusters?

It is reasonable to assume that Li^+ ions can diffuse readily from one tin cluster to the next since the Li-X glass (remember, the glass consumes lithium irreversibly in the first discharge) will certainly be a Li^+ ion conductor. A possibility is that electrons will transport from cluster to cluster by tunneling (since the glasses are electrically insulating) as long as the cluster-cluster distance is not longer than an electron tunneling length. This tunneling length sets one length scale that may determine the maximum intercluster separation. Once clusters have formed, it is presumably favorable for large Li-Sn clusters to form at the expense of small ones, in order to minimize the surface interaction energy between the regions of X and the Li-Sn clusters. Thus, larger tin clusters attempt to "swallow up" small ones. In order for this to occur, tin atoms must move from the small clusters to neighboring big ones. It is possible that the motion of tin atoms will be similar to that of lithium atoms. That is Sn^{++} ions will be mobile in the X-Glass, and the corresponding electron must tunnel from one cluster to the next.

6.4.3 Effects of temperature on aggregation

If the aggregation process is similar to coarsening, or diffusive decomposition, then increased temperature should increase both the rate of growth and the size of the aggregates.

Figure 6-15 The effect of temperature on aggregation, (a) Differential capacity versus voltage for Li/SnO:(0.5/0.5) cell at 30°C (solid) and 55°C (dashed) on the first cycle, (b) second cycle, (c) third cycle, (d) fourth cycle, (e) fifth cycle, (f) sixth cycle, and (g) Capacity retention versus cycle number for the same cells
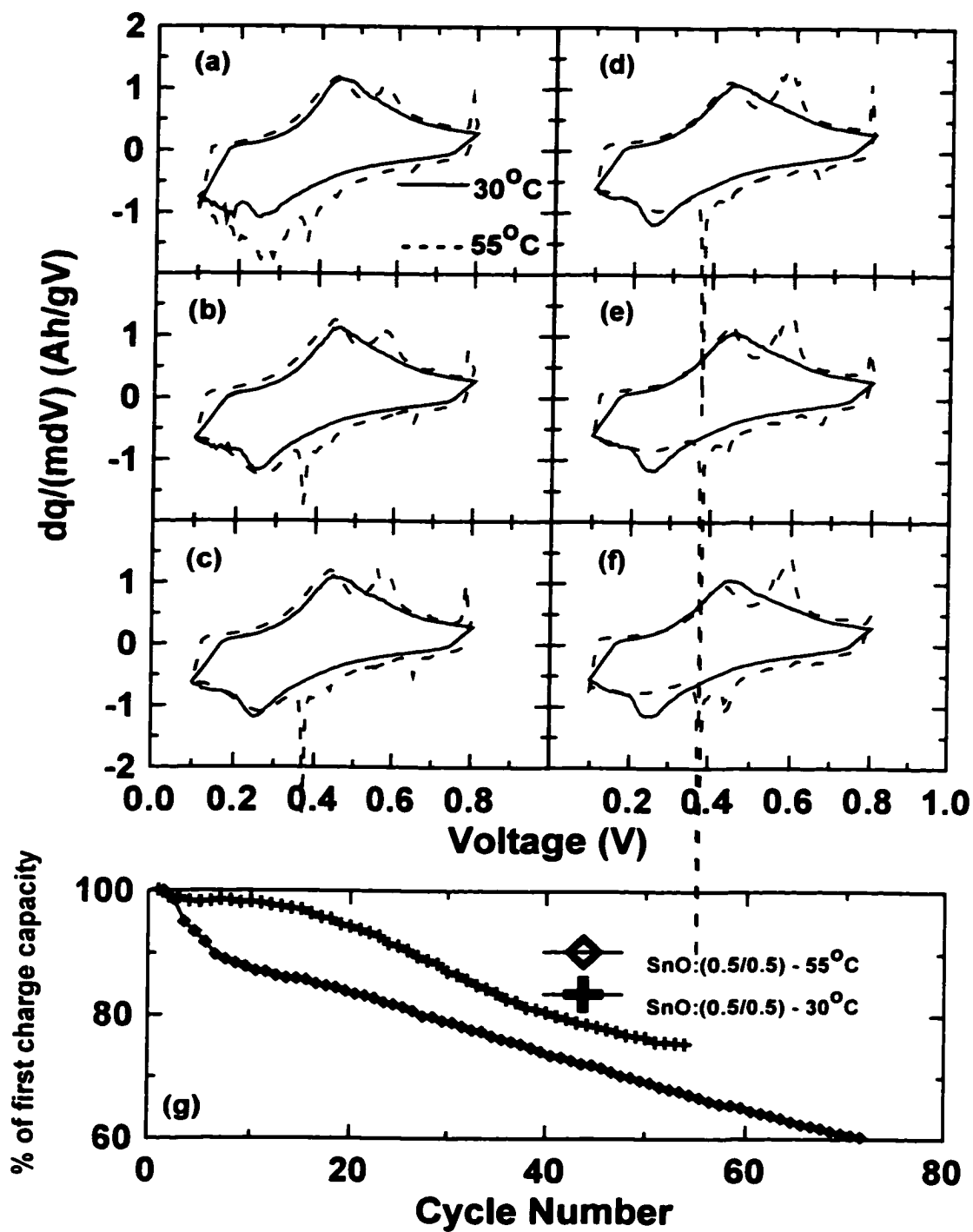
The aggregation of tin does proceed more rapidly at higher temperatures. As an example, figure 6-15 (g) shows capacity versus cycle number for cells of the SnO:(0.5/0.5) sample cycled at 30° C and 55°C. The cells were cycled between 0.1 and 0.8 V, using a specific current of 37.2 mA/g. The cells reach the region of rapid capacity loss first at higher temperature, which is the region where the capacity is changing rapidly with cycle number, or where the tin atoms are undergoing aggregation up to a stable cluster size. This, therefore, occurs earlier for the same sample when it is cycled at higher temperature. Figure 6-15 (a) shows the differential capacity versus voltage for the same cells during the 1st cycle. The difference in the aggregation rates due to a 25° C temperature difference is astounding. Notice also that the peak at 0.35 V during discharge (figure 6-15 (a)) appears readily in the cell that was maintained at 55° C during discharge and charge. The discharge peak at 0.35 V appeared only for the SnO:(0.1/0.1) glass at 30°C (figure 6-12 (b) and (c)). This peak during discharge, therefore, must be a part of the aggregation that is not normally realized for most glass compositions other than in extreme conditions. The peak at 0.35 V during discharge continues to grow for the cell at 55° C (figures 6-15 (b), (c), (d) and (e)), while the cell at 30° C does not appear to aggregate over this voltage range during these first six cycles.

6.5 The effect of voltage range on aggregation

It was clear early on in the research that these materials displayed extreme sensitivity to the choice of voltage range used for cycling. Figure 6-16 shows the capacity versus cycle number for both small grain samples of SnO_2 that were discussed in section 6.1. When the voltage limits are changed from 0.3-1.0 V to 0.0-1.3 V for SnO_2 (3) (figure 6-16 (a)) at cycle 25, the capacity loss increases dramatically. Figure 6-16 (b) shows the effect of changing the

voltage range for the SnO₂ (2) sample to 0.2-1.0 V at cycle 38, where the capacity loss also increased dramatically.

Figure 6-16 Capacity versus cycle number as a function of voltage range,
(a) Li/(SnO₂ (3) — see section 6.1 for a description of this material), and
(b) Li/(SnO₂ (2) — see section 6.1 for a description)
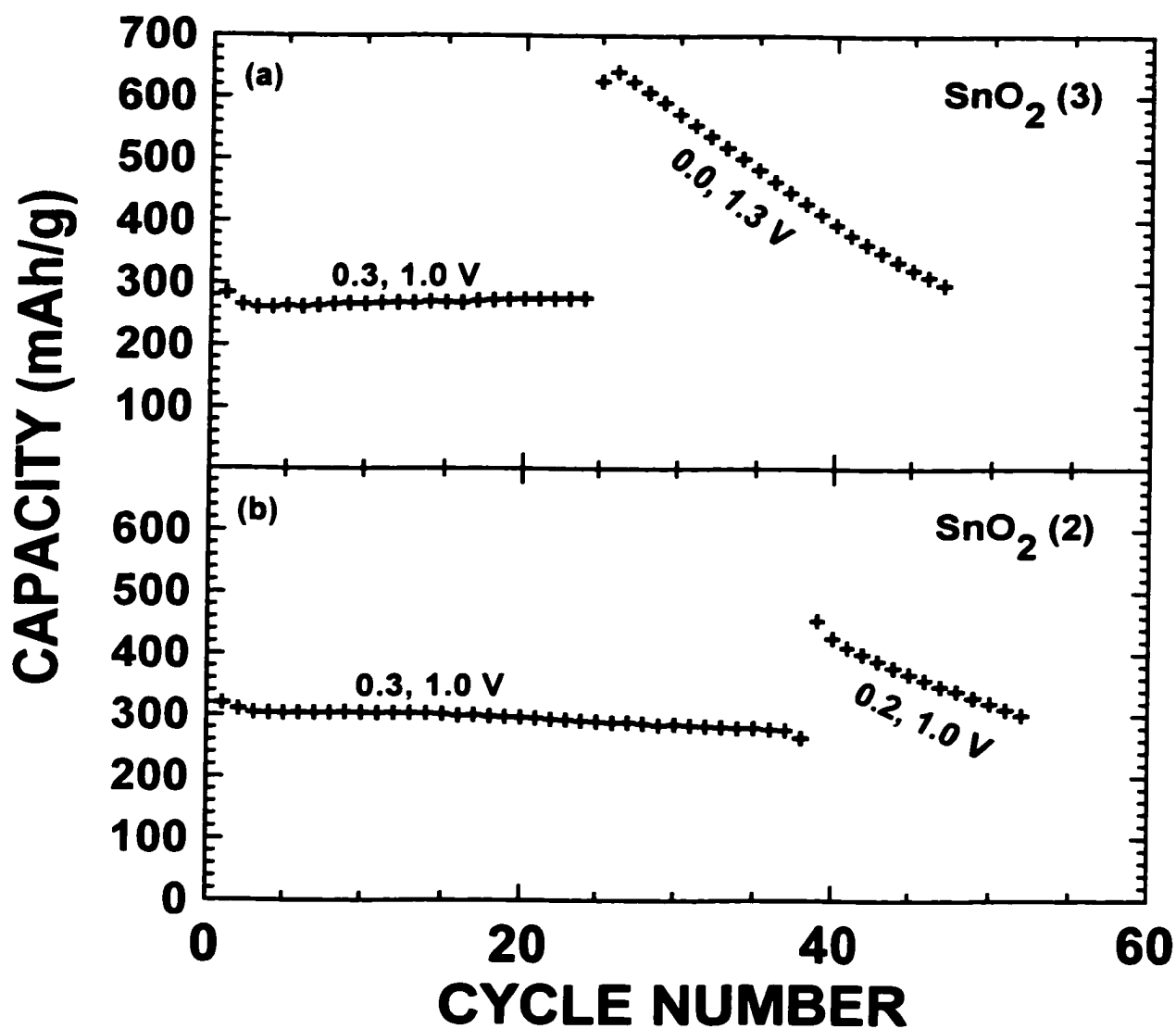
In order to optimize the cycling behaviour one might envisage undertaking a vast testing matrix where both the charge and discharge cut-off voltages were varied in 0.1 V

increments. This would involve a large number of cells and materials. A more analytical approach was adopted in order to understand why the reversibility of these materials is sensitive to the voltage range chosen for cycling.

6.5.1 Choosing optimum voltage range by differential capacity

Figure 6-17 (a) shows dq/(mdV) versus voltage for the first (defined as the first charge and second discharge) and fifth cycle of a Li/SnO:(0.5/0.5) cell cycled between 0.2 and 1.3V. The derivative is not stable, as large peaks begin to appear as the cell is cycled. Figure 6-17 (b) shows the corresponding capacity versus cycle number for the same cell. $R_{10/1}$ is 0.78 for this cell.

Figure 6-17 (c) shows similar data for a cell cycled between 0.3 and 1.0V. Although the differential capacity is more stable than in figure 6-17 (a), it does still change and we do not expect this cell to have good long-term cycling. Over the first 10 cycles, however, $R_{10/1}$ is 1.00, as shown in figure 6-17 (d). The specific capacity of the material over this voltage range is much smaller than that needed for practical applications. Therefore, other voltage ranges were investigated.

Figures 6-17 (e), 6-17 (g) and 6-17 (i) show the same information as figure 6-17 (a), except for the voltage ranges 0.0-1.0V, 0.1-1.0V and 0.2-1.0V respectively. In all cases, the differential capacities are not stable over the first five cycles. The capacity is largest for the widest voltage limits, but the capacity retention for all the samples is poor as indicated in figures 6-17 (f), 6-17 (h) and 6-17 (j).

Figure 6-17 A Li/SnO:(0.5/0.5) cell cycled between various voltage ranges; 0.2-1.3 V in (a)
Differential capacity versus voltage (the first and fifth charge cycles are shown) and (b)
Capacity versus cycle number, 0.3-1.0 V in (c) and (d), 0.0-1.0 V in (e) and (f), 0.1-1.0 V in
(g) and (h), 0.2-1.0 V in (I) and (j), and 0.0-0.8 V in (k) and (l)
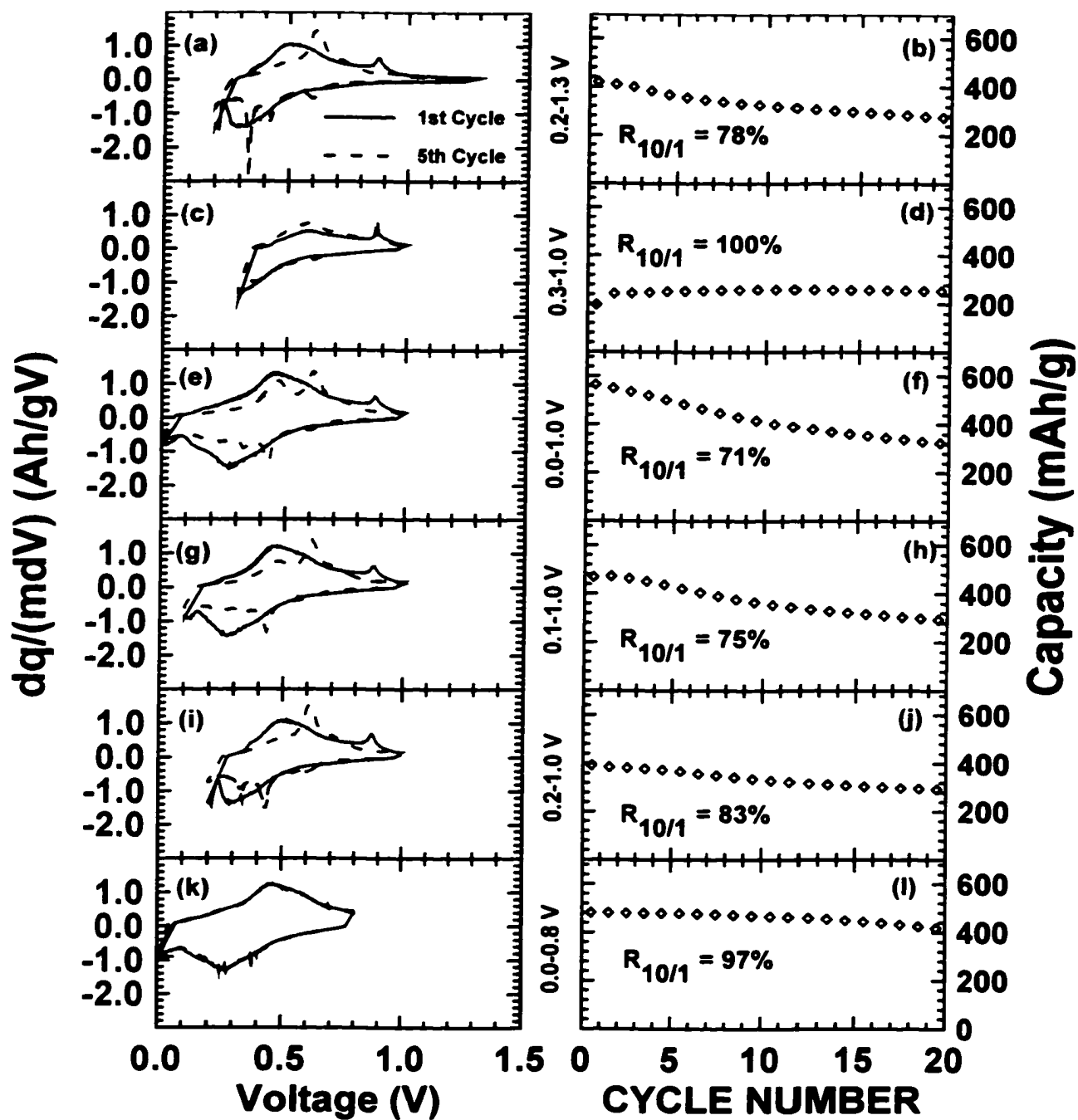
Figure 6-18 A Li/SnO₂ (3)cell cycled between 0.0 and 0.8 V, (a) Differential capacity versus voltage (the first and fifth charge cycles are shown) and (b) Capacity versus cycle number
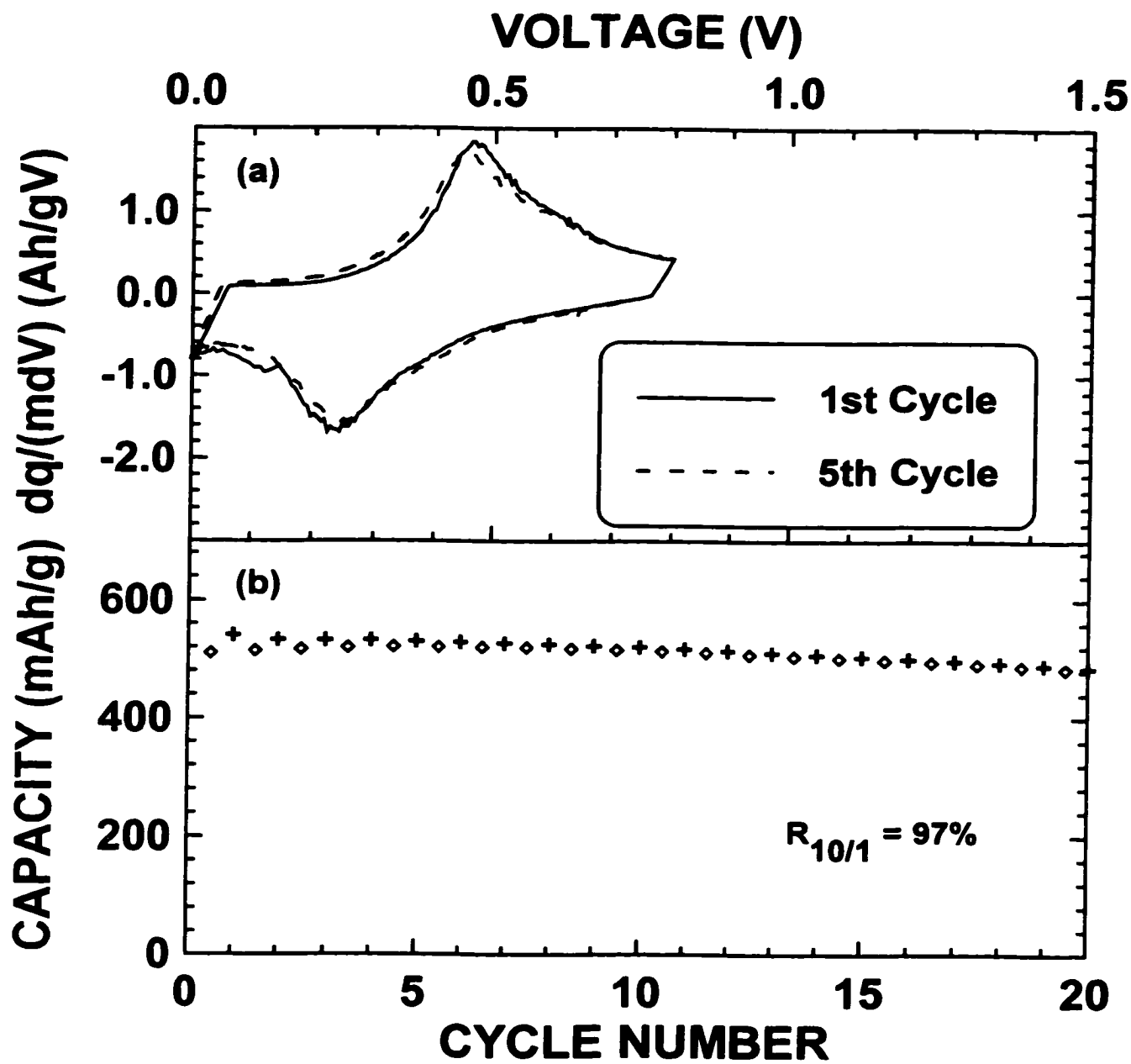
An examination of figures 6-17 (a), 6-17 (c), 6-17 (e), 6-17 (g) and 6-17 (i), suggests that all peaks in dq/(mdV) in the initial cycle can be avoided if the charge cutoff voltage is limited to about 0.8V, to avoid the peak at 0.87V in the first charge. This peak may correspond to the initiation of the back reaction.

Figure 6-17 (k) shows dq/(mdV) versus voltage for the first and fifth cycle of a Li/SnO:(0.5/0.5) cell cycled between 0.0 and 0.8V. The differential capacity is completely stable (for at least five cycles) when cells are cycled between these cutoff voltages. Aggregation of Sn does, however, eventually occur, as shown in figure 6-12. Figure 6-17 (l) shows that there is little capacity loss with cycle number (at least for the first 10 cycles) for this cell. This is expected based on the arguments presented above. The specific capacity is near 500 mAh/g for this material in this voltage range.

Finally, figure 6-18 shows an application of the same ideas to SnO_2 sample 3. When the voltage limits are constrained to 0.0-0.8V, no sharp peaks in dq/(mdV) are traversed and the cycling is stable (for at least 5 cycles) as measured by both the stability of the differential capacity (fig. 6-18 (a)) and the good capacity retention (for at least 10 cycles) shown in figure 6-18 (b).

Notice also that the peak during discharge at 0.35 V (the same one that was displayed for the 55° C cycling of this material, and the same one that was only realized for the SnO:(0.1/0.1) sample over the voltage range 0.1-0.8 V) is more prevalent as the upper voltage is increased, regardless of the lower voltage limit. In order to investigate these peaks on differential capacity, ex-situ XRD experiments were performed.

6.5.2 Ex-situ XRD study of SnO:X differential capacity on cycling

Specific features of the differential capacity versus voltage for some of the SnO:$(B_2O_3)_x$:$(P_2O_5)_y$ series of glasses were investigated by ex-situ XRD. Cells of Li/SnO:(0.1/0.1), Li/SnO:(0.25/0.25), Li/SnO:(0.35/0.35) and Li/SnO:(0.5/0.5) were made and discharged and charged using a specific current of 37.2 mA/g between 0.0 and 1.5 V voltage limits. Cell electrodes were harvested at the end of each of the 2nd, 6th and 10th charge cycles. Prior to XRD of the electrode material, the cells were maintained at a voltage of 1.5 V for a period of not less than one day in order for the electrode material to equilibrate. The cells were disassembled in the charged state in an inert atmosphere glove box, and the electrode material was mounted in the ex-situ XRD holder. The materials were then x-rayed. In some cases the material was well-adhered to the separator material, so separator peaks show on the XRD patterns and are indicated, as appropriate, in the graphs of the XRD patterns.

An ex-situ XRD pattern is displayed on the left-hand side of the graph in each of figures 6-19, 6-20 and 6-21. The corresponding differential capacity graph for the terminating cycle of that particular experiment is shown immediately to the right of the XRD pattern as a solid line. A relevant prior cycle is shown as a dashed line. For the 2nd cycle ex-situ experiment the prior cycle is the first cycle, for the 6th cycle the prior cycle is the 2nd cycle, and for the 10th cycle the prior cycle is the 6th cycle. Capacity versus cycle number for each of these cells is given in figure 6-22.

Figure 6-19 Ex-situ XRD at 1.5 V for cells cycled for 2 cycles between 0.0 and 1.5 V, for samples; Li/SnO: (0.1/0.1) (a) XRD and (b) Differential capacity, Li/SnO: (0.25/0.25) (c) XRD and (d) Differential capacity, Li/SnO: (0.35/0.35) (e) XRD and (f) Differential capacity, Li/SnO: (0.5/0.5) (g) XRD and (h) Differential capacity

The expected peak locations for Sn (white) are shown in panel (g), as is the separator peak
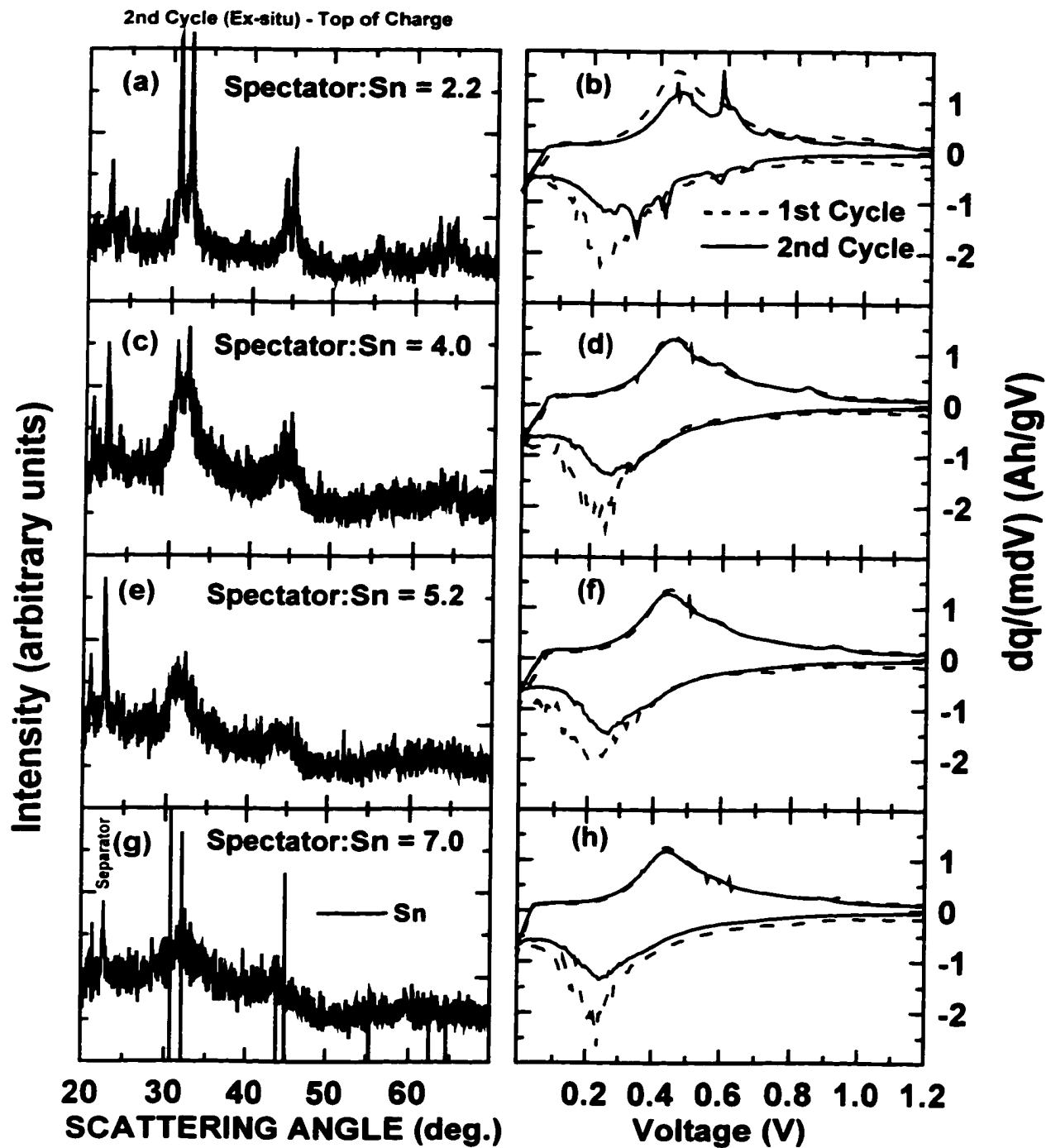
Figure 6-20 Ex-situ XRD at 1.5 V for cells cycled for 6 cycles between 0.0 and 1.5 V, for samples; Li/SnO: (0.1/0.1) (a) XRD and (b) Differential capacity, Li/SnO: (0.25/0.25) (c) XRD and (d) Differential capacity, Li/SnO: (0.35/0.35) (e) XRD and (f) Differential capacity, Li/SnO: (0.5/0.5) (g) XRD and (h) Differential capacity

The expected peak locations for Sn (white) are shown in panel (g). The expected peak locations for Sn (grey) are shown in panel (e). The separator peak is shown in panel (c)

6th Cycle (Ex-situ) - Top of Charge
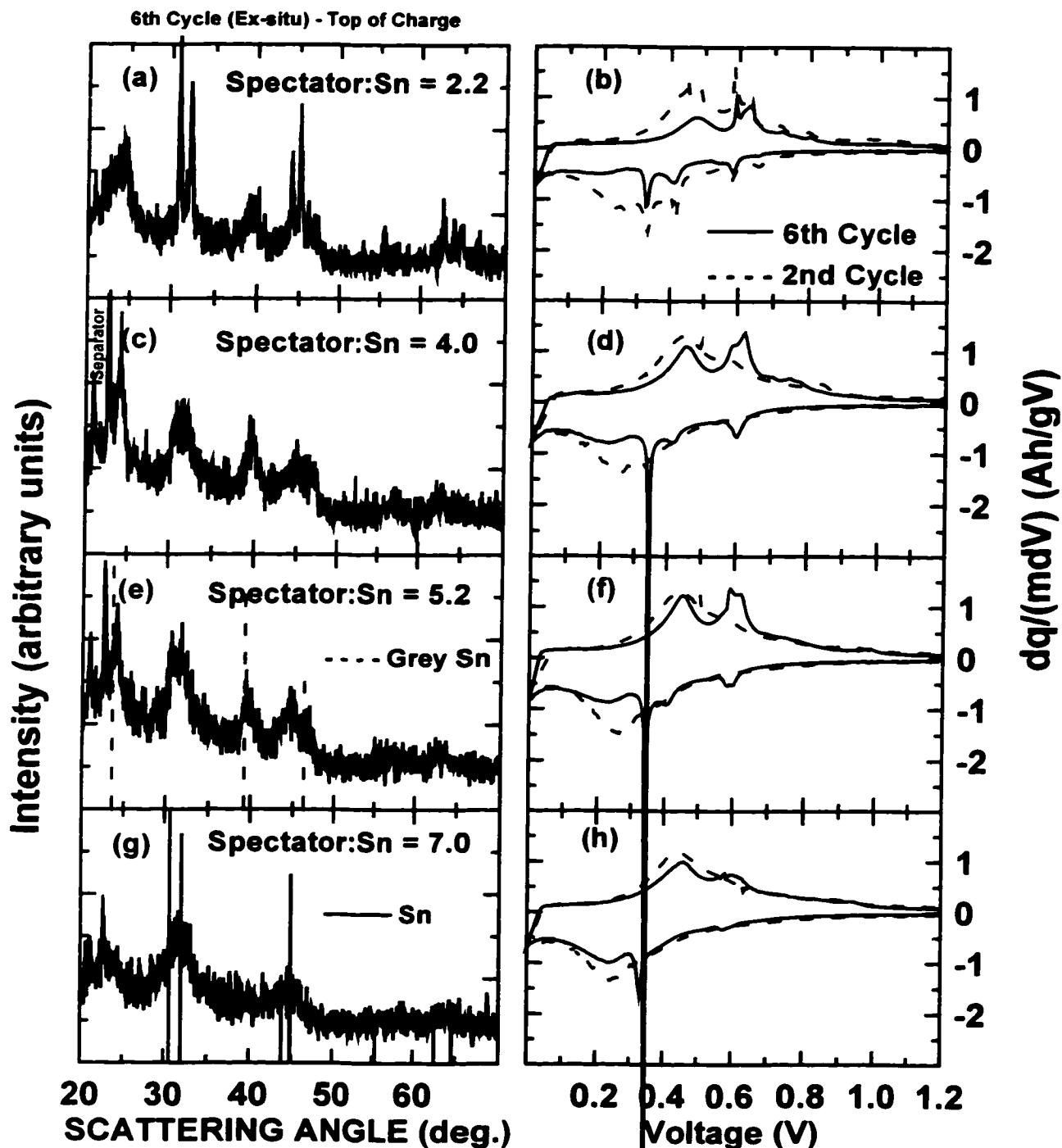
Figure 6-21 *Ex-situ XRD at 1.5 V for cells cycled for 10 cycles between 0.0 and 1.5 V, for samples; Li/SnO: (0.1/0.1) (a) XRD and (b) Differential capacity, Li/SnO: (0.25/0.25) (c) XRD and (d) Differential capacity, Li/SnO: (0.35/0.35) (e) XRD and (f) Differential capacity, Li/SnO: (0.5/0.5) (g) XRD and (h) Differential capacity*

The expected peak locations for Sn (white) are shown in panel (g). The expected peak locations for Sn (grey) are shown in panel (e). The separator peak is shown in panel (c)
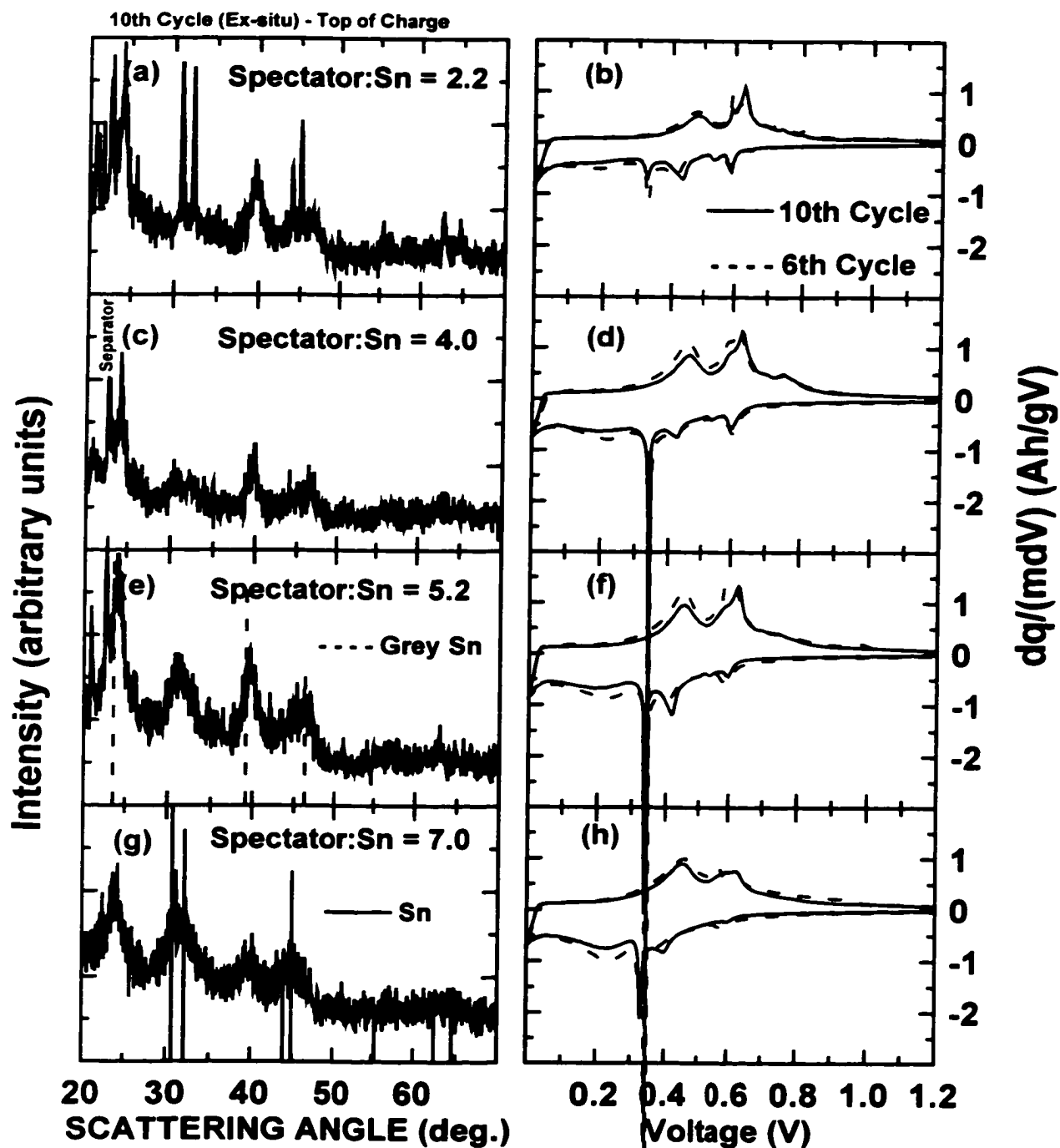
Figure 6-22 Capacity (as a % of first charge capacity) versus cycle number for Li/:SnO(y/y) cells (y = 0.1, 0.25, 0.35 and 0.5)

Actual first charge capacities are also indicated
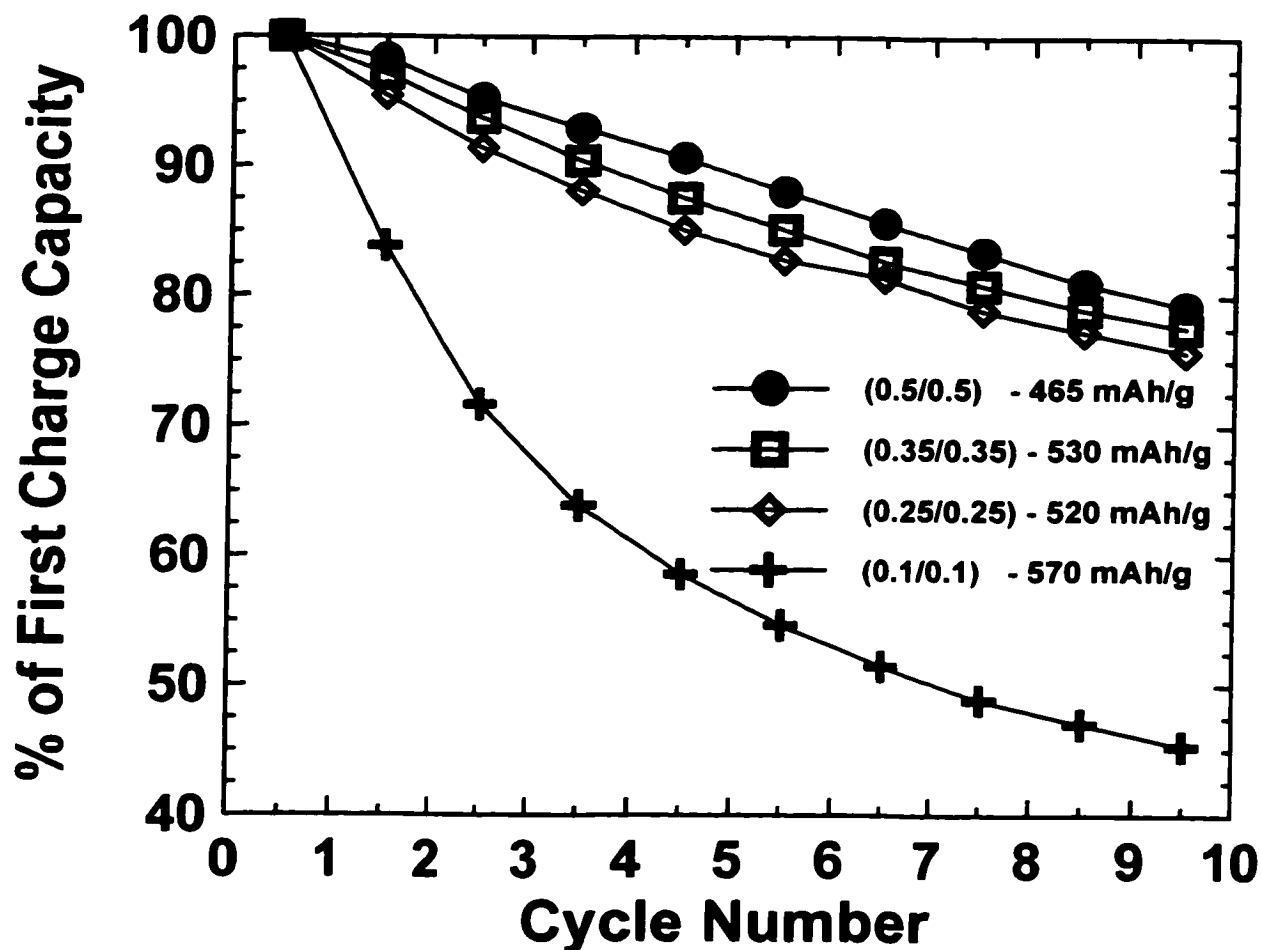
Figure 6-19 shows the results of ex-situ XRD performed on the materials after the second cycle. As expected, the glass that contains most Sn produces the largest regions of Sn (figure 6-19 (a)). Starting materials that contain less Sn lead to decreasing Sn region sizes (progressively smaller in figures 6-19 (c), (e) and (f)). During the 2nd cycle, the size of the Sn regions is also suggested by emergent peaks on the differential capacity graphs (e.g. figure 6-19 (b)).

Figure 6-20 provides the results of ex-situ XRD performed after 6 cycles. The SnO:(0.1/0.1) glass has lost almost half of its initial charge capacity (as shown in figure 6-22), and as is also evident by the diminished peaks on differential capacity (figure 6-20 (b)). The peaks at around $24°$ and $38°$ are believed to be remnants of pulverized Li-rich alloy phase. The SnO:(0.25/0.25) glass, on the other hand, has only lost about 15 % of its initial capacity (figure 6-22), yet there appears to be substantial Li-rich remnant material. Also note the huge peak on differential capacity at 0.35 V discharge. This mystery can be resolved by realizing that the other allotropic form of Sn, grey Sn, is formed. Grey Sn is a diamond structure (Wyckoff, 1982) and is supposed to be stable at temperatures less than $13.2°C$ (Musgrave, 1962). Perhaps some lithium in this structure stabilizes it at room temperature. The shift in observed scattering to a higher angle than expected pattern indicates a slightly smaller lattice constant. Presumably, grey Sn containing small amounts of substitutional lithium would have a smaller lattice constant than grey-Sn without lithium.

The formation of grey Sn is believable when one considers that the poorly formed Li-rich alloy phases are based on Sn tetrahedra (chapter 3), and that the Sn atoms in the grey Sn structure are also in the same tetrahedra (diamond structure). So why should this manifest itself as a peak on discharge? After all, the XRD patterns are measured at the top of charge.

It is possible that the addition of lithium at the line phase (Li_7Sn_3) occurs at lower voltage when the Sn atoms have already adopted a tetrahedral coordination, than if they have not. This could be investigated more fully by at least two ways; an ab-initio calculation, similar to that presented in chapter 3, could be performed on clusters of Sn atoms with the appropriate cluster symmetry. An in-situ (or ex-situ) ME experiment could also be conducted. There is a significant difference in center shift between white and grey Sn of 0.56

mm/s (Greenwood and Gibb, 1971), where grey Sn has a smaller center shift of 2.00 mm/s (relative to SnO_2, white Sn has a center shift of 2.56 mm/s relative to SnO_2).

The peak in differential capacity at 0.35 V discharge is also observed for the SnO:(0.35/0.35) glass (figure 6-20 (f)), with a corresponding XRD pattern showing some grey and white Sn (figure 6-20 (e)). The SnO:(0.5/0.5) glass shows less grey Sn by XRD and differential capacity (figures 6-20 (g) and (h), respectively). The formation of grey Sn seems to be also linked to the initial volume fraction of Sn in the glass.

The SnO:(0.1/0.1) glass has achieved a stable differential capacity over this voltage range by the 10th cycle (figures 6-21 (a) and 6-21 (b)). It is difficult to surmise, in this case, which of the components are electrochemically active. This glass has lost 55 % of its first charge capacity, and since the structures of the Li-rich alloy phases and grey Sn are similar, it is difficult to retract stoichiometric information. The other glass compositions have also achieved stable differential capacity by the 10th cycle, as indicated by the remainder of figure 6-21.

It would appear, therefore, that under certain conditions (elevated temperature and charging to 1.5 V) the aggregation rate proceeds much more quickly. If the initial regions of Sn (on the first discharge) are quite large (e.g. as in the SnO:(0.1/0.1) glass cycled 0.0-1.5 V) then the electrode material pulverizes quickly, but the grey Sn phase is not achieved substantially. If, however, the initially formed regions of Sn are of 'intermediate' size (e.g. as in the SnO:(0.25/0.25) glass and in the SnO:(0.35/0.35) glass) then the grey Sn phase is realized. For the most dilute case, e.g. the SnO:(0.5/0.5 glass, the grey Sn phase will occur at 55° C cycling, but not substantially at a higher charge voltage limit.

6.6 Summary

The reversibility of the reaction of lithium with SnO:X composite materials is now better understood. What has been learned is given in point form as follows:

1. Small grain Sn has better capacity retention than large grain Sn. Morphological integrity of the grains is maintained when bulk phase transitions are eliminated. Differential capacity versus voltage graphs are a way by which to examine this. The smoother the initial differential capacity versus voltage, the smaller the initial Sn regions that are formed, and, therefore, the material will be have better capacity retention.

2. Smaller regions of Sn can be made using a starting material with smaller volume fraction Sn. However, there is a price to pay in reversible capacity.

3. The aggregation of Sn in the meta-stable state that has been created on the first discharge is key to understanding the reversibility of these materials. Materials where the Sn is initially finely dispersed (i.e. high spectator:Sn ratio) will aggregate to a lesser extent than those materials where the initial regions of Sn are larger. Presumably, the distance over which the Sn atoms can diffuse is a factor in determining the possible aggregate size. A speculative model, based on a limiting cluster-cluster distance that is controlled by electron tunneling or ionic transport, was proposed. This model shows reasonable agreement with experiments conducted over a voltage range of 0.1 to 0.8 V.

4. The aggregation rate and steady state cluster size (and therefore reversibility) of these materials is quite sensitive to both the voltage range and to the temperature. Increasing the upper voltage limit to greater than 0.85 V, causes rapid acceleration of the aggregation process. The back reaction (to the oxide) is apparently conducive with aggregation. The reason why this is so is not clear, and could be examined in more detail. Increasing temperature has a similar effect, which suggests that aggregation involves a diffusion mechanism of some kind.

Chapter 7

The choice of alloying metal

7.1 Motivation

The previous chapters have investigated the reaction mechanism of lithium with Sn and SnO composite materials. Lithium alloys with metals other than Sn, for example, Pb, Si, Sb, Al and Bi. Idota et al. (1994), in addition to reporting SnO composite anode materials, describe the use of PbO and Sb_2O_3 composites. It therefore makes sense to study these in order to generalize the reaction mechanism of lithium with all materials listed in the Fuji patent. This chapter will raise more questions than it will answer. unfortunately, but this is often the way of scientific research. The data and ideas that are presented here could serve as a starting point for future work.

The lead oxide and antimony oxide composites may react with lithium in a manner similar to that of tin oxide, so it is useful to be aware of the binary reaction of lithium with Sb and Pb. Weppner and Huggins (1977) investigated the Li-Sb electrochemical reaction, and report a maximum of three lithium atoms per antimony atom (i.e. Li_3Sb). The Li-Pb binary system is similar to the Li-Sn binary system (Moffat, 1990), and this has also been investigated by electrochemical reaction (Wang, et al., 1985). The maximum lithium concentration in a Li-Pb alloy corresponds to the compound $Li_{22}Pb_5$.

A series of $PbO:(B_2O_3)_x:(P_2O_5)_y$ and $Sb_2O_3:(B_2O_3)_x:(P_2O_5)_y$ glasses were made in accordance with the methods described in section 5.3.2, and their XRD patterns are given in figure 7-1. Crystalline PbO (Aldrich) and Sb_2O_3 (Aldrich) were also studied.

151

Figure 7-1 Powder XRD patterns for PbO and Sb₂O₃ based glasses,
(a) PbO:(0.35/0.35), (b) PbO:(0.5/0.5), (c) Sb₂O₃:(0.1/0.1), (d) Sb₂O₃:(0.25/0.25),
(e) Sb₂O₃:(0.35/0.35), and (f) Sb₂O₃:(0.5/0.5)
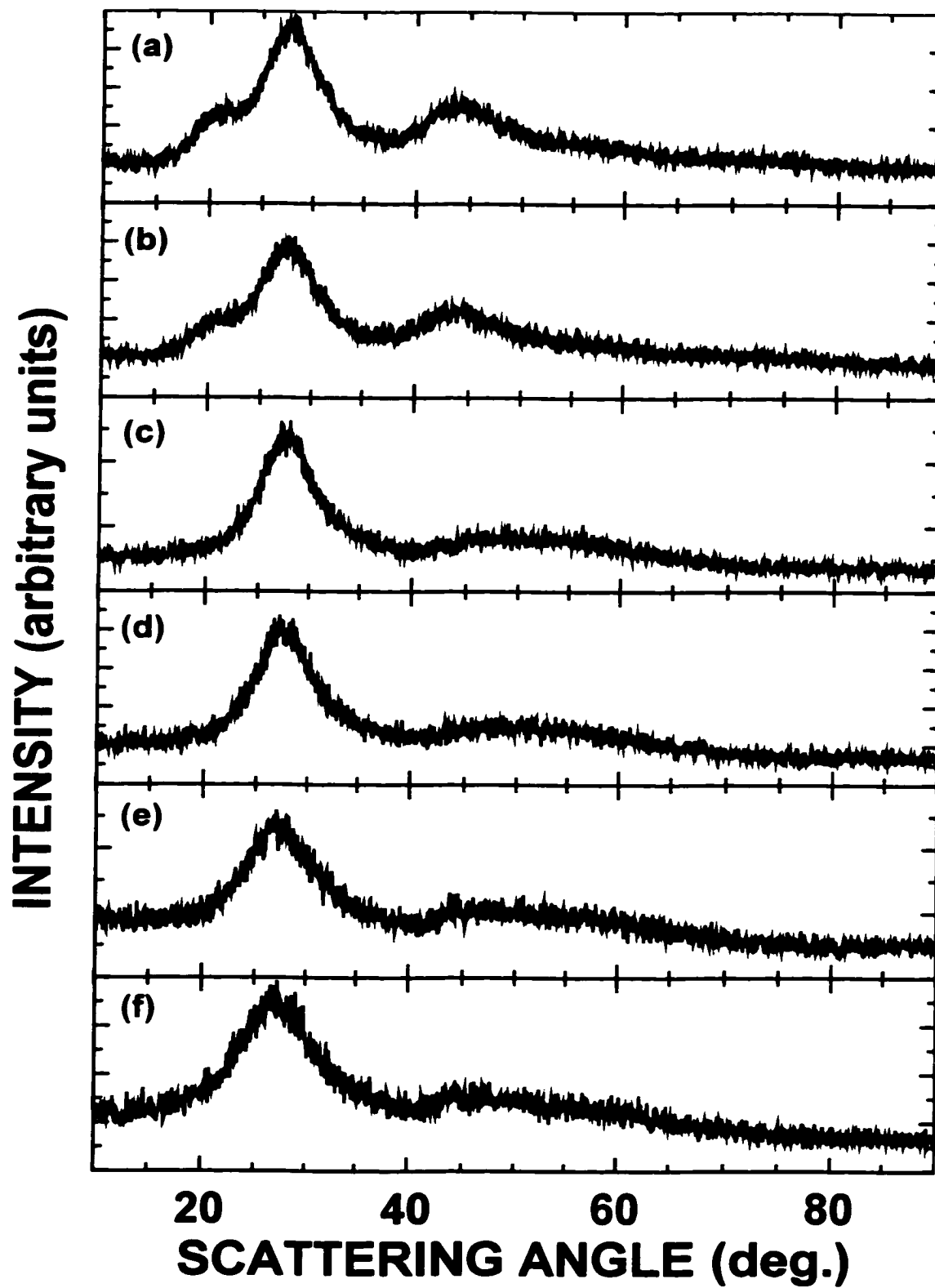
7.2 PbO and the PbO:(B₂O₃)ₓ:(P₂O₅)ᵧ series of glasses

The general reaction mechanism of lithium with SnO:X (equation 5-3) can be modified for a PbO:X composite as follows;

$$PbO:X+2Li \xrightarrow{step 1} Pb+Li_2O:X$$

$$Pb+Li_2O:X+4.4Li \xrightarrow{step 2} Li_{4.4}Pb+Li_2O:X$$

$$(7-1)$$
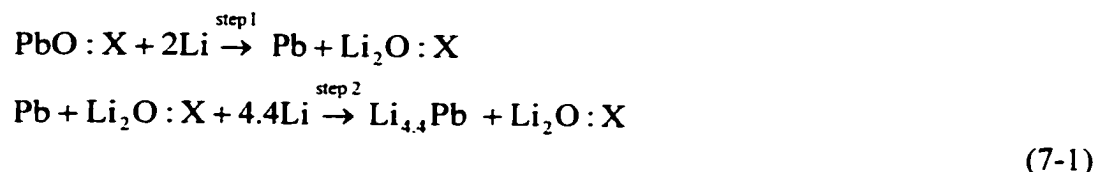
The theoretical capacities for step 1 and step 2 for the PbO:X materials that were studied are easily calculated and are given in table 7-1.

Table 7-1 Theoretical capacities for PbO:X materials studied

Name	Step 1 (eqn. 7-1) capacity (mAh/g)	Step 2 (eqn. 7-1) capacity (mAh/g)	Step 1 plus step 2 capacity (mAh/g)
PbO	240	529	769
PbO:(0.35/0.35)	177	391	569
PbO:(0.5/0.5)	163	360	523

7.2.1 Electrochemical results

Coin cells, composed of cathodes of the materials listed in table 7-1 and lithium anodes, were constructed and were discharged and charged using a specific current of 37.2 mA/g, between lower and upper voltage limits of 0.0 and 1.5 V, respectively. Voltage profiles, as well as capacity versus cycle number, for the PbO-containing materials are shown in figure 7-2.

Figure 7-2 (a) shows the voltage profile for a Li/PbO cell. The plateaus in the voltage versus capacity graph (therefore peaks in differential capacity versus voltage graph) are pronounced, suggesting that an alloying reaction with bulk phase transitions (similar to a Li/SnO cell) is occurring. The capacity fade (figure 7-2 (b) of PbO) is severe, and the

observed first discharge capacity (680 mAh/g) is lower than the expected first discharge capacity (769 mAh/g).

Figure 7-2 Electrochemical results for various Li/PbO:X cells;
PbO in (a) Capacity versus voltage and (b) Capacity versus cycle number,
PbO:(0.35/0.35) glass in (c) and (d), and PbO:(0.5/0.5) glass in (e) and (f)
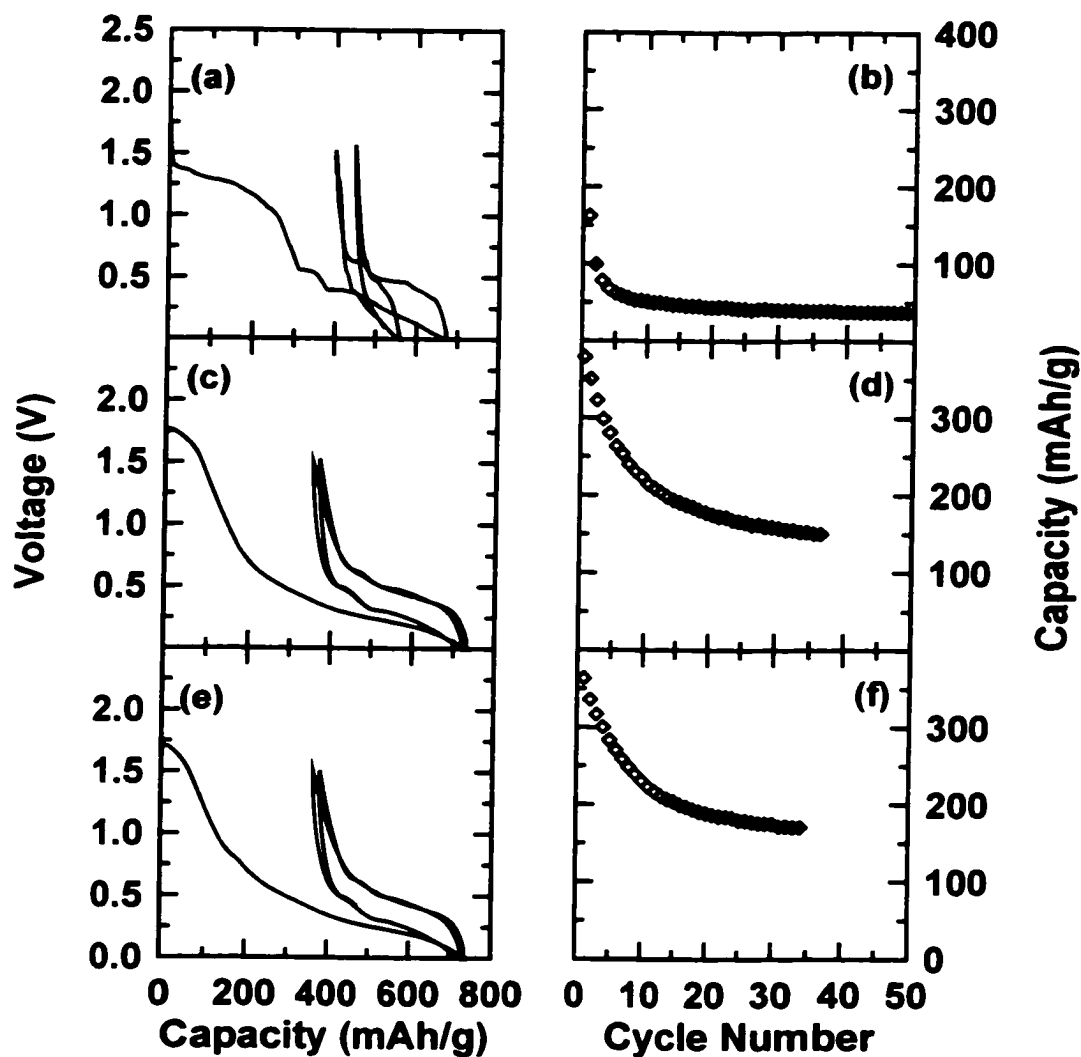
Figures 7-2 (c) and 7-2 (e) show the capacity versus voltage for cells of Li/PbO:(0.35/0.35) and Li/PbO:(0.5/0.5), respectively. The observed first discharge capacity for these materials is between 100 and 150 mAh/g higher than the expected first discharge

capacity (column 3, table 7-1). The reason for this is not clear. Perhaps the lithium bonds to additional oxygen in the matrix (as in B_2O_3 and P_2O_5). The observed reversible capacities, however, match quite well with the expected capacity of the alloying reaction (column 2 in table 7-1). Notice the plateaus that exist on the capacity versus voltage for the two glassy materials (figures 7-2 (c) and 7-2 (e)) after the first discharge, which suggests aggregation to larger grain size Pb. The capacity retention of the PbO:X glasses is poor, as shown in figures 7-2 (d) and 7-2 (f). It will be shown, by ex-situ XRD that Pb aggregates faster than does Sn in a similar environment, and this is why PbO-containing glasses display poorer capacity retention than the SnO-containing glasses do.

7.2.2 Ex-situ XRD results

A Li/PbO cell was discharged and charged using a specific current of 18.6 mA/g, between 0.0 and 1.5 V. The cell was maintained at a voltage of 1.5 V prior to disassembly, where the electrode of the cell was retrieved for ex-situ XRD in a manner similar to that described in chapter 6.

Figure 7-3 (a) shows the differential capacity versus voltage for this cell. The first discharge is shown (dashed) as is the first charge and second discharge (both solid). Notice the irreversible capacity during the first discharge (> 1.0 V), which is similar to the irreversible capacity for a Li/SnO cell (figure 5-2 (b)). The Li/PbO cell loses capacity more quickly than does a Li/SnO cell (compare the second discharge of figure 7-3 (a) to the second discharge of figure 5-2 (b)), which suggests that Pb aggregates faster and to larger grain size than Sn does. Figure 7-3 (b) is the ex-situ XRD pattern for the electrode of a Li/PbO cell after one cycle (0.0-1.5 V using 18.6 mA/g). Large grain size Pb is obviously present.

Figure 7-3 Electrochemical and ex-situ XRD results for a Li/PbO cell,
(a) Differential capacity versus voltage and
(b) Ex-situ XRD of a cell electrode after one cycle (0.0-1.5 V)
The expected peak positions for Pb are indicated in panel (b)
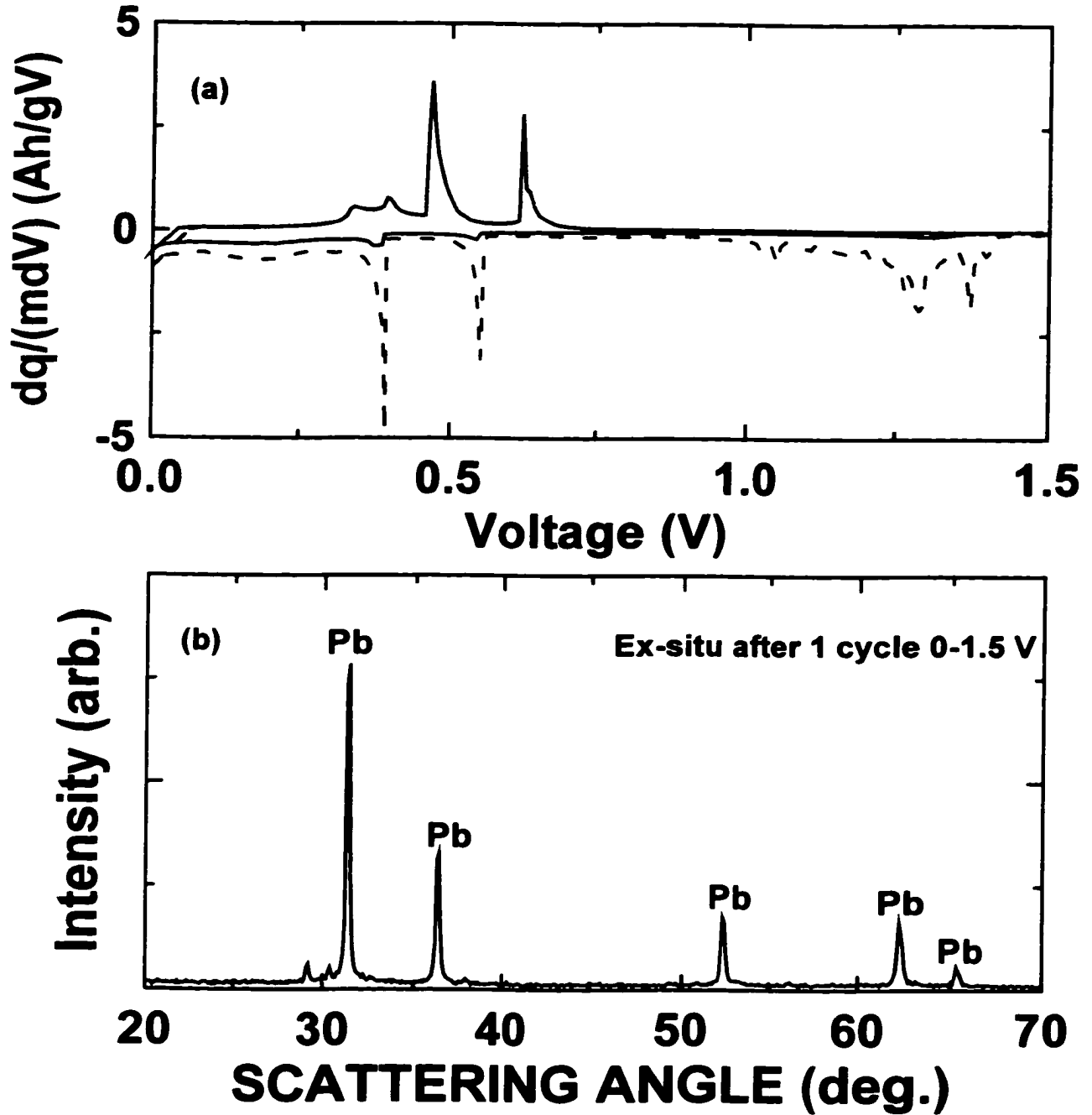
Figures 7-4 and 7-5 show ex-situ XRD and differential capacity versus voltage for Li/PbO:(0.35/0.35) and Li/PbO:(0.5/0.5) cells, respectively. The (b), (d) and (f) panels in both figures 7-4 and 7-5 show differential capacity versus voltage at various cycle numbers. A solid line in differential capacity in these figures (7-4 and 7-5) corresponds to the second (panel (b)), sixth (panel (d)) and tenth (panel (f)) cycles. The ex-situ XRD pattern of the cell electrode after these cycles is shown in the panel immediately to the left (panels (a), (c) and (e), respectively). The dashed lines on the differential capacity versus voltage panels are from a relevant prior cycle (to the solid line), as is indicated on the figures.

It is clear that PbO:X composites follows a similar first cycle reaction mechanism with lithium to the SnO:X composites. The metal oxide component of the glass is reduced to the metal (Pb), as shown in figure 7-4 (a) and figure 7-5 (a).

The size of the regions of Pb that form, and subsequently aggregate, is inversely related to the number of spectator atoms in the glass (compare figure 7-4 (a) and figure 7-5 (a), figure 7-4 (c) and figure 7-5 (c), and, figure 7-4 (e) and figure 7-5 (e)).

Furthermore, the PbO-containing glasses aggregate faster to larger grain size than the SnO-containing glasses. For example, compare figure 7-5 (a) to figure 6-19 (g), figure 7-5 (c) to figure 6-20 (g), and figure 7-5 (e) to figure 6-21 (g), which contrasts Li/PbO:(0.5/0.5) and Li/SnO:(0.5/0.5) at the same cycle number. The faster rate of Pb aggregation helps explain the poorer capacity retention of the PbO-containing glasses (i.e. $R_{10/1}$ for the PbO:(0.5/0.5) glass equals 57 % (figure 7-2 (f)), while the SnO:(0.5/0.5) glass has a capacity retention of 80 % at the tenth cycle (figure 6-22).)

Figure 7-4 Ex-situ XRD at 1.5 V for Li/PbO:(0.35/0.35) cells cycled between 0.0 and 1.5 V at various cycle numbers. (a) XRD and (b) Differential capacity versus voltage for the 2nd cycle, (c) and (d) the 6th cycle, and (e) and (f) the 10th cycle.

The expected peak locations for Pb are shown in panel (a). The separator peak is shown in panel (e).
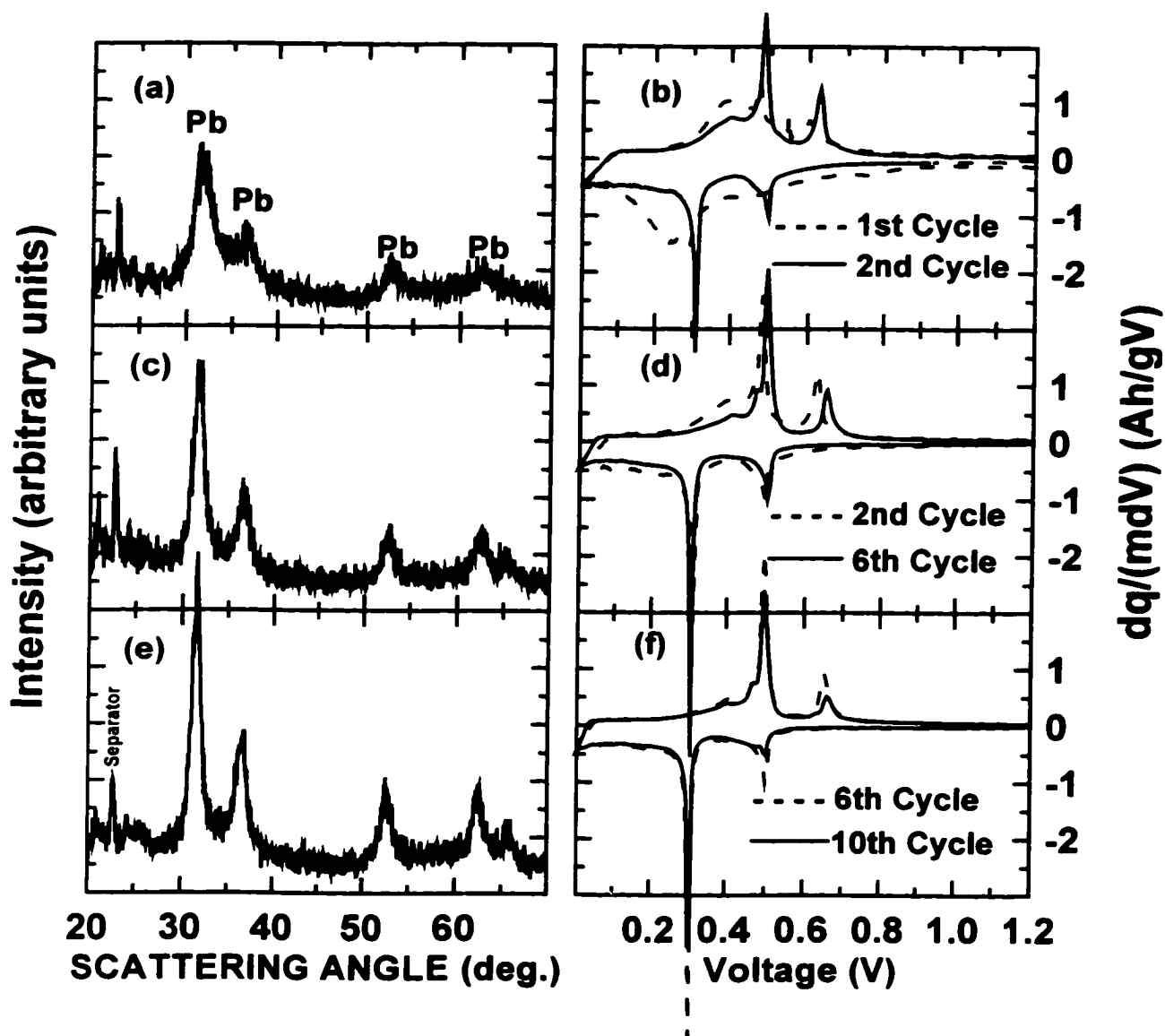
Figure 7-5 Ex-situ XRD at 1.5 V for Li/PbO:(0.5/0.5) cells cycled between 0.0 and 1.5 V at various cycle numbers. (a) XRD and (b) Differential capacity versus voltage for the 2nd cycle, (c) and (d) the 6th cycle, and (e) and (f) the 10th cycle.

The expected peak locations for Pb are shown in panel (c). The separator peak is shown in panel (e).
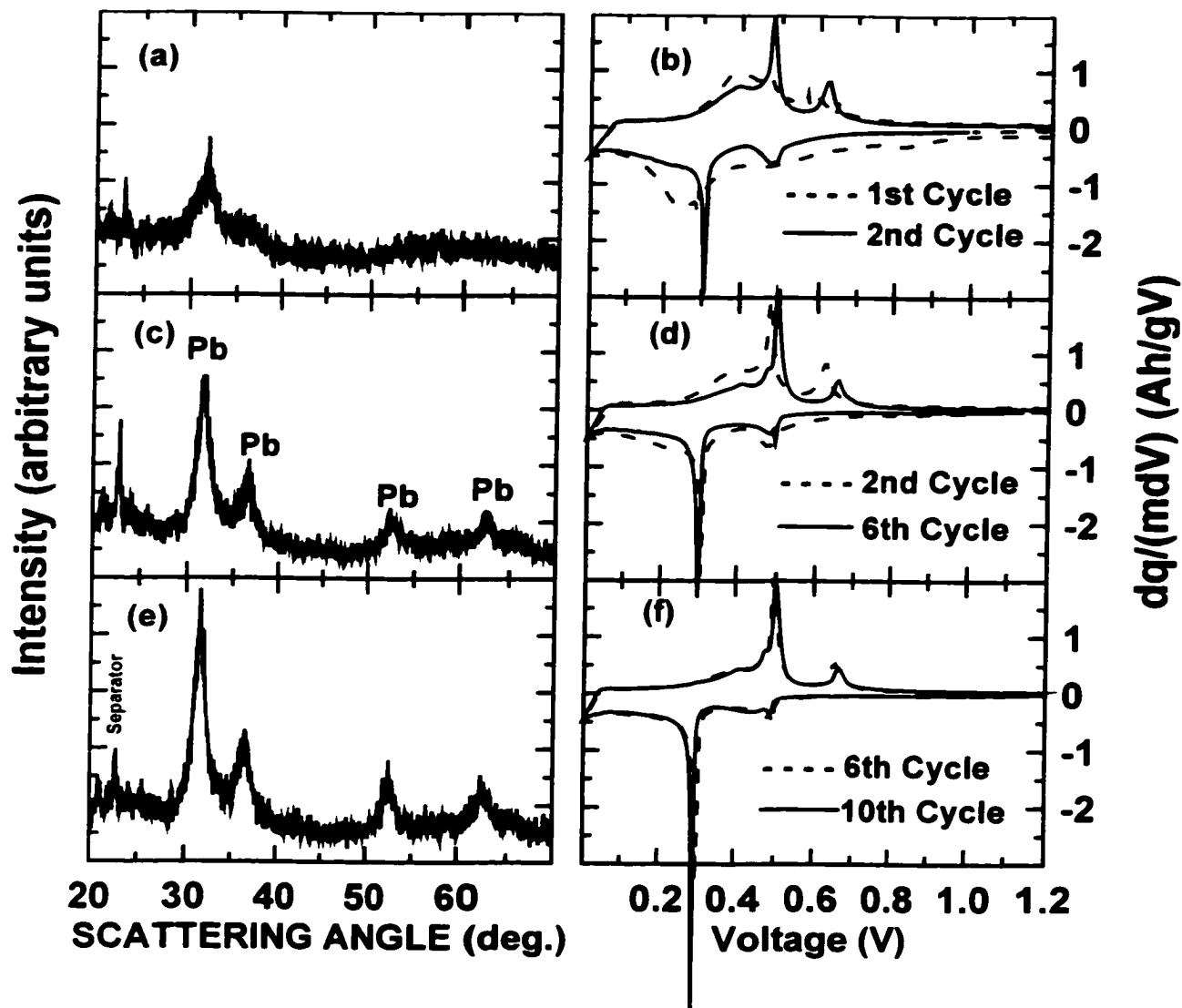
7.3 Sb$_2$O$_3$ and the Sb$_2$O$_3$:(B$_2$O$_3$)$_x$:(P$_2$O$_5$)$_y$ series of glasses

The reaction mechanism given in equation 7-1 (from equation 5-3) is easily extended

to Sb$_2$O$_3$:X composite starting materials, and is shown in equation 7-2.

$$Sb_2O_3 : X + 6Li \xrightarrow{step\ 1} 2Sb + (Li_2O)_3 : X$$

$$2Sb + (Li_2O)_3 : X + 6Li \xrightarrow{step\ 2} 2Li_3Sb + (Li_2O)_3 : X$$

$$(7-2)$$
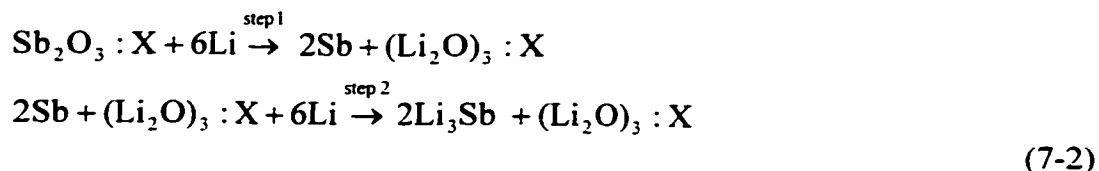
The theoretical capacities for step 1 and step 2 for the Sb$_2$O$_3$:X materials that were studied

are shown in table 7-2.

Table 7-2 Theoretical capacities for Sb$_2$O$_3$:X materials studied

Name	Step 1 (eqn. 7-2) capacity (mAh/g)	Step 2 (eqn. 7-2) capacity (mAh/g)	Step 1 plus step 2 capacity (mAh/g)
Sb$_2$O$_3$	553	553	1106
Sb$_2$O$_3$:(0.1/0.1)	515	515	1030
Sb$_2$O$_3$:(0.25/0.25)	468	468	935
Sb$_2$O$_3$:(0.35/0.35)	440	440	881
Sb$_2$O$_3$:(0.5/0.5)	406	406	812

7.3.1 Electrochemical results

Coin cells, composed of cathodes of the materials listed in table 7-2 and lithium

anodes were constructed and were discharged and charged using a specific current of 37.2

mA/g, between lower and upper voltage limits of both 0.0 and 1.5 V, and 0.2 and 1.3 V,

respectively. Voltage profiles, as well as capacity versus cycle number, for the Sb$_2$O$_3$-

containing materials are shown in figure 7-6.

Figure 7-6 Electrochemical results for various Li/Sb₂O₃:X cells;
Sb₂O₃ in (a) Capacity versus voltage and (b) Capacity versus cycle number,
Sb₂O₃:(0.1/0.1) glass in (c) and (d), Sb₂O₃:(0.25/0.25) glass in (e) and (f), Sb₂O₃:(0.35/0.35)
glass in (g) and (h), and, Sb₂O₃:(0.5/0.5) glass in (i) and (j)
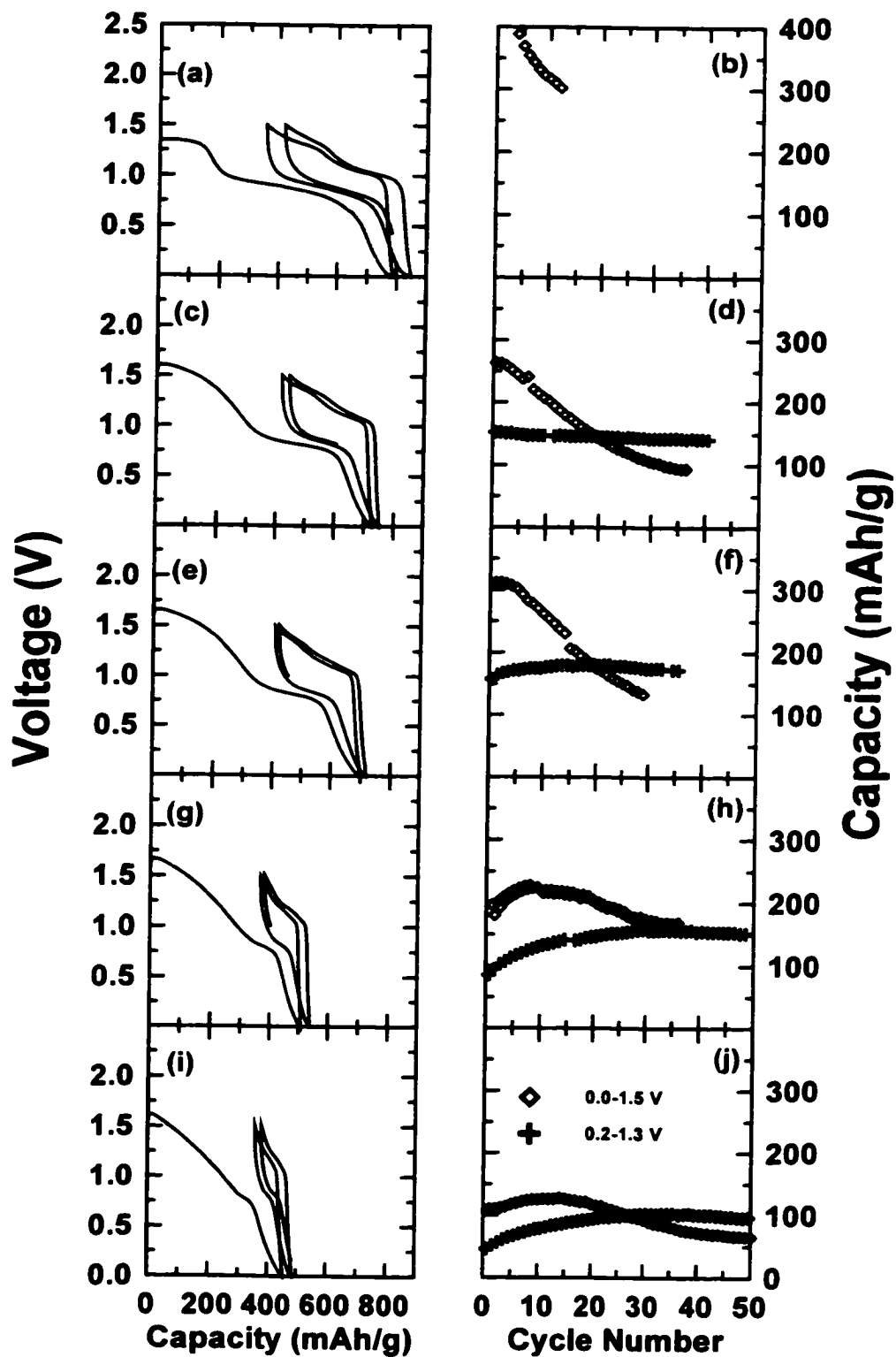
The observed first discharge capacities and first charge capacities (to 1.5 V) of the materials shown in figure 7-6 are given in table 7-3, and are compared to the expected capacities from table 7-2.

Table 7-3 Expected and observed discharge and charge capacities for Sb_2O_3:X materials

Name	Expected first discharge capacity (mAh/g)	Observed first discharge capacity (mAh/g)	Expected first charge capacity (mAh/g)	Observed first charge capacity (mAh/g)
Sb_2O_3	1106	800	553	450
Sb_2O_3:(0.1/0.1)	1030	725	515	325
Sb_2O_3:(0.25/0.25)	935	700	468	300
Sb_2O_3:(0.35/0.35)	881	500	440	200
Sb_2O_3:(0.5/0.5)	812	450	406	110

The observed capacities are consistently smaller than expected. It is possible that the proposed reaction in equation 7-2 is not fully achieved during the first discharge, which could be due to poor kinetics, for example. Alternatively, the reaction that is proposed in equation 7-2 could be incorrect. Further work could be done to establish the correct reaction mechanism. It is likely, however, that the reaction presented in equation 7-2 is correct in principle. The Sb_2O_3 materials have an irreversible capacity that is proportional to the amount of oxygen that is initially bonded to the antimony, and a reversible capacity that is proportional to the antimony content. The voltage profiles for all the materials, after first discharge, are similar in appearance to voltage profiles for a Li/Sb cell (as reported by Wang et al., 1986). We will therefore proceed with the assumption that it is the alloying of lithium with antimony that represents the reaction mechanism in subsequent cycles.

7.3.2 Ex-situ XRD results

Figure 7-7 (a) shows the ex-situ XRD pattern of an electrode of a Li/Sb$_2$O$_3$ cell. The cell was discharged and charged for one cycle between 0.0 and 2.5 V using a specific current of 18.6 mA/g. The cell was maintained at 1.5 V for one day prior to being measured by x-ray. The expected peak positions (from the PDF data base) for Sb$_2$O$_3$ (solid line) and Sb (dashed line) are given in figure 7-7 (c), and the expected peak positions for the two phases of the Li-Sb phase diagram, Li$_2$Sb (solid line) and Li$_3$Sb (dashed line), are given in figure 7-7 (b).

Figure 7-7 Ex-situ XRD results for a Li/Sb$_2$O$_3$ cell after one cycle (0.0-2.5 V)
(a) Ex-situ XRD pattern, (b) Expected peak positions for Li$_2$Sb (solid) and Li$_3$Sb (dashed),
and (c) Expected peak positions for Sb$_2$O$_3$ (solid) and Sb (dashed)
Expected peak positions taken from PDF data-base.
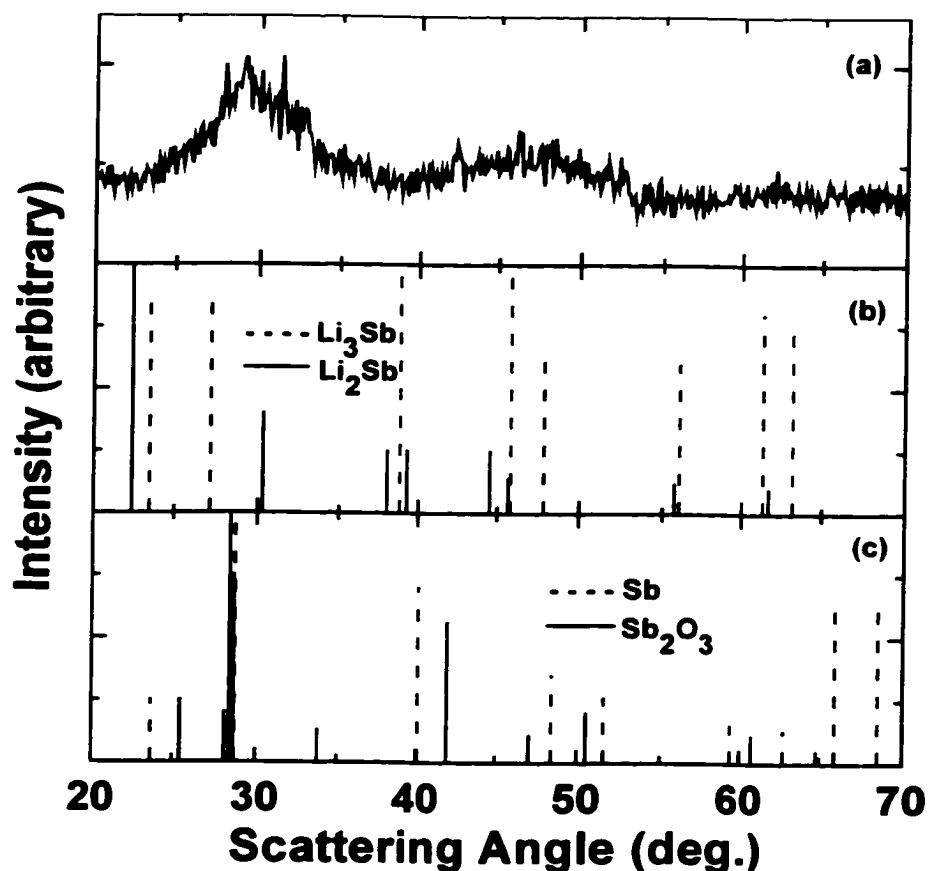
The ex-situ XRD pattern in figure 7-7 (a) shows that Li/Sb_2O_3 forms much smaller grains of product than either Li/SnO (figure 5-7 (b)) or Li/PbO (figure 7-3 (b)). The starting material is crystalline and it becomes amorphous after one discharge and charge cycle. There an indication of un-reacted (or back-reacted) Sb_2O_3 in figure 7-7 (a) (compare to expected pattern in figure 7-7 (c) for Sb_2O_3), although extracting such a conclusion on two peaks is difficult to defend. The other crystalline patterns (i.e. Li_3Sb (dashed) and Li_2Sb (solid) in figure 7-7 (b) and Sb (dashed) in figure 7-7 (c)) do not appear on the ex-situ XRD pattern. It would appear that the reaction of lithium with Sb_2O_3 (and the subsequent removal of Li) leads to amorphous products at the top of charge.

Figure 7-8 and figure 7-9 shows the results of ex-situ XRD experiments performed on cells of Li/Sb_2O_3:X glass series. These cells were discharged and charged using a specific current of 37.2 mA/g, between 0.0 and 1.5 V. Cells were maintained at 1.5 V for a period of not less than one day prior to disassembly. Electrodes were retrieved and measured by x-ray, as has been described previously.

Figure 7-8 shows the XRD pattern obtained after the cells were discharged and charged for two cycles. The differential capacity versus voltage for all materials shows neither aggregation nor substantial change from the first to the second cycle (as shown in panels (b), (d), (f) and (h)). The ex-situ XRD patterns show the same amorphous pattern as was obtained for crystalline Sb_2O_3 after one cycle (i.e. compare panels (a), (c), (e) and (g) to each other and to figure 7-7 (a)). This observation is the same at the 10th cycle, as shown in figure 7-9. The same XRD pattern that was obtained for Sb_2O_3 is prevalent in the Sb_2O_3 series of glasses after ten cycles (see panels (a), (c), (e) and (g) of figure 7-9, compare them to the same panels in figure 7-8 and with figure 7-7 (a)).

Figure 7-8 Ex-situ XRD at 1.5 V for cells cycled for 2 cycles between 0.0 and 1.5 V for various Sb₂O₃-containing samples; Li/Sb₂O₃:(0.1/0.1) in (a) XRD and (b) Differential capacity versus voltage, Li/Sb₂O₃:(0.25/0.25) in (c) and (d), Li/Sb₂O₃:(0.35/0.35) in (e) and (f), and, Li/Sb₂O₃:(0.5/0.5) in (g) and (h)

The separator peak is indicated in panel (e)
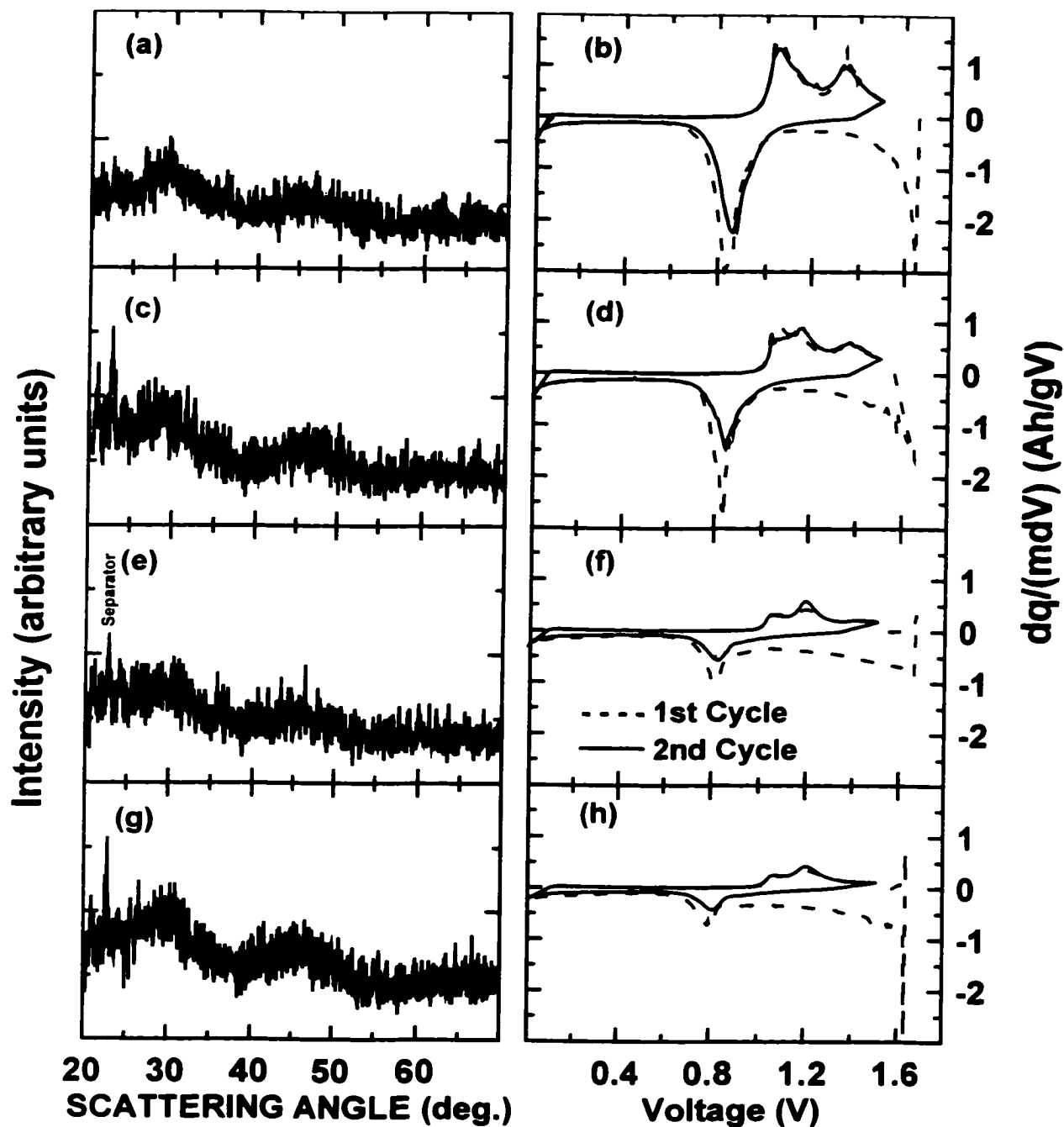
Figure 7-9 Ex-situ XRD at 1.5 V for cells cycled for 10 cycles between 0.0 and 1.5 V for various Sb_2O_3-containing samples; $Li/Sb_2O_3:(0.1/0.1)$ in (a) XRD and (b) Differential capacity versus voltage, $Li/Sb_2O_3:(0.25/0.25)$ in (c) and (d), $Li/Sb_2O_3:(0.35/0.35)$ in (e) and (f), and, $Li/Sb_2O_3:(0.5/0.5)$ in (g) and (h)

The separator peak is indicated in panel (e), and lithium metal in panel (c). In this case, the lithium metal was most likely present as an impurity in the separator.
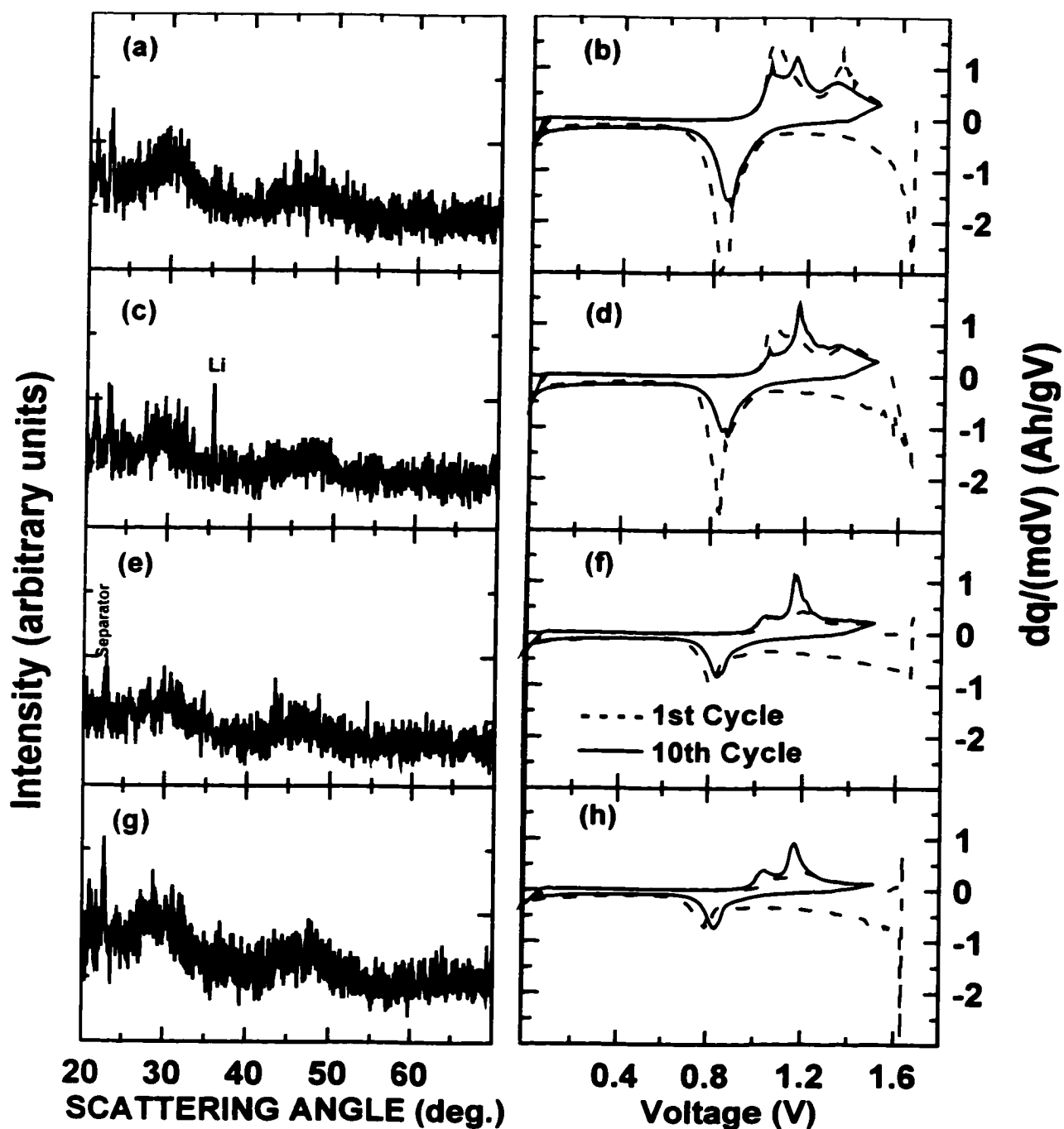
The Sb_2O_3 series of glasses do change somewhat in differential capacity after 10 cycles (compare dashed and solid lines on figures 7-9 (b), (d), (f) and (h)), but this change does not manifest itself as an observable change in structure (compare the XRD patterns in figure 7-9 to those in figure 7-8). It is clear that more work should be done to attempt to figure this out. The message is that Sb is quite different from Sn and Pb. Apparently, Sb does not nucleate or aggregate to the same degree as Sn and Pb in these types materials as they react with lithium. The reason why this is possible is explored in the next section.

7.4 Explanations for the different rates of aggregation observed in composites containing Sn, Pb and Sb based on solid state diffusion and the onset of back-reaction

The simple model for steady state cluster size that was presented in section 6.4.2 is not atom specific. The steady state cluster sizes for Sn, Pb and Sb in SnO:X, PbO:X and Sb_2O_3:X glasses are expected to be the same if the spectator:(alloying metal) ratios are equal. The results that have been presented in this chapter clearly shows that this is not true. A model (based on electron tunneling setting the length scale for the cluster-cluster distance) worked reasonably well for SnO:X materials, but there are obviously some other factors that need to be considered in order to explain the differences in aggregation rates between Sn, Pb and Sb.

In this section two different approaches are adopted. First we investigate, in a qualitative manner, the effects of metal type on solid state diffusion. We assume that the alloying metal 'desires' to aggregate with others of its kind (perhaps to reduce the number of more energetic surface atoms in relation to the number of bulk atoms, which provides the driving for aggregation), and we examine the differences between the diffusion of Sn, Pb and Sb. The conclusion of this section is highly speculative, but tempting none-the-less, and

could be a good starting point for future work.

Kittel (1971) describes diffusion of impurity atoms (or vacancies) in solid as a flux moving through the solid that is governed by Fick's law. The flux is proportional to the diffusion constant, 'In order to diffuse, an atom must surmount the potential energy barrier presented by its neighbours.' He goes on to define a probability, p, also called the *jump frequency*, that an atom will have enough thermal energy to pass over the barrier as,

$$p \approx v \exp(-E/k_B T)$$

$$(7-3)$$

The term, v, in equation 7-3 is a characteristic atomic vibrational frequency, and the activation barrier energy is expressed as E. Notice that the probability is exponentially dependant on the activation barrier energy and temperature, but linear in the vibrational frequency. We therefore consider the exponential terms only, as changing them will produce the most dramatic effects on the diffusion probability.

Equation 7-3 predicts a higher probability of diffusion for atoms that are presented with small barriers for diffusion. It also states that the probability of diffusion will be larger at higher temperatures, which has already been shown to be true for Sn in section 6.4.3. We now discuss barrier heights, in a qualitative manner, for our Sn, Pb and Sb containing composite materials.

The first question to answer is what causes the barrier for each metal atom in the composite? We assume that alloying metal (Me) atoms, such as Sn, Pb or Sb, are intimately bonded to one of two other species in the composites materials after one discharge cycle; that is, either another Me atom or a lithium atom. This of course ignores any interaction with the oxide matrix (for instance, a Me-O interaction or a Me-P/B interaction), but it is reasonable to assume that any such interactions will be of the same order for all types of Me in similar

environments of B, P and O.

A comparative gauge of the Me-Me and Me-Li barrier energy can be obtained by comparing the melting points of the respective Li-Me binary phase diagrams. In order to melt, the atoms in a compound must break the bonds that exist between the atoms of the compound. These are the same bonds that must be overcome if an atom is to break free from a small cluster in order to diffuse to a larger cluster. Thus, we have a crude estimate of the diffusive activation energy barriers by examination of melting temperatures. Table 7-4 shows the melting temperatures of all the binary Li-Me and Me phases of Sn, Pb and Sb (from Moffat, 1990). It is clear that the Sb phases have the highest melting points. In other words, the Sb-Sb and Sb-Li activation barriers are higher than the corresponding Pb and Sn

Table 7-4 Melting temperatures of all Me and Li-Me phases (Me = Sn, Pb and Sb)
(After Moffat, 1990)

Pb phase	Melting Temp. ($^{\circ}$C)	Sn phase	Melting Temp. ($^{\circ}$C)	Sb phase	Melting Temp. ($^{\circ}$C)
Pb	327	Sn	232	Sb	630
LiPb	482	Li_2Sn_5	400	Li_2Sb	1300
Li_8Pb_3	642	LiSn	486	Li_3Sb	1400
Li_3Pb	658	Li_7Sn_3	716		
Li_7Pb_2	726	Li_5Sn_2	730		
$Li_{22}Pb_5$	649	$Li_{13}Sn_5$	762		
		Li_7Sn_2	783		
		$Li_{22}Sn_5$	765		

activation barriers are. The Sn and Pb phase melting points are of the same order as shown in table 7-4. However, careful examination of the total areas (therefore cumulative melting temperatures) under the liquid phase lines of the respective binary phase diagram shows that Sn and Sn-Li phase melting temperatures are slightly higher than those of the Pb and Pb-Li phases.

Figure 7-10 Differential capacity versus voltage and ex-situ XRD for various Li/MeO:X cells after the 10th cycle (0.0-1.5 V); Me = Pb in (a) and (b), Me = Sn in (c) and (d), and, Me = Sb in (e) and (f)

In this figure, X = $(B_2O_3)_{0.5}(P_2O_5)$. For Me = Sb, the stoichiometry is actually $SbO_{1.5}$:X. The horizontal dashed lines in panels (a) and (c) are drawn to distinguish the charge and discharge segments. The vertical dashed line drawn in panels (c) to (a) represents the voltage at which the SnO:X sample (panel (c)) has achieved approximately half of its charge capacity. Notice that PbO:X has achieved more than half of its charge capacity at this point in voltage.
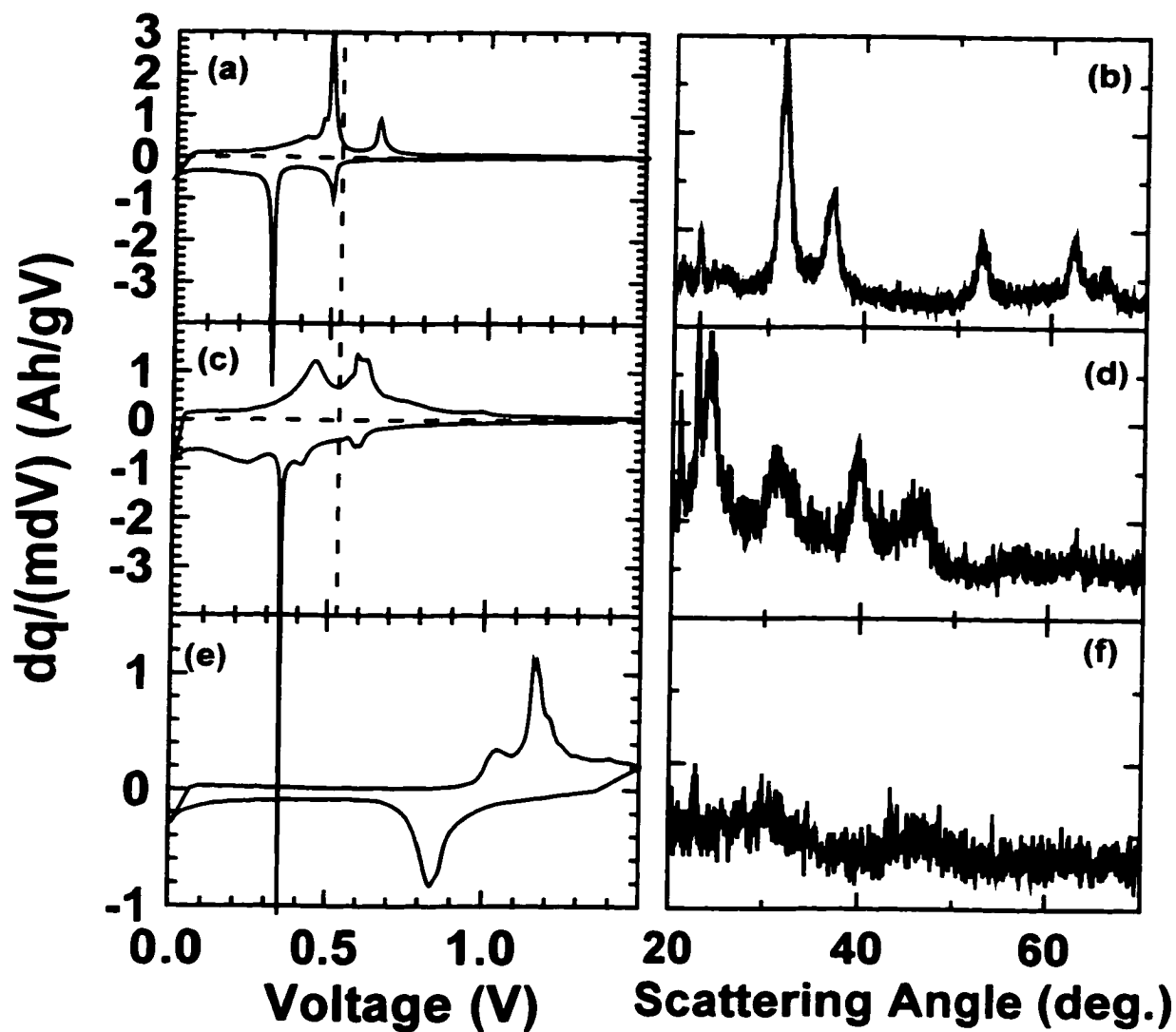
The relative strength of the Me-Li bond can also be obtained from the differential capacity versus voltage graphs of the Li/MeO:X cells. A large Me-Li bond strength would result in a high potential difference (in reference to lithium metal) on a differential capacity versus voltage graph. Figure 7-10 shows the differential capacity versus voltage and ex-situ XRD patterns after 10 cycles (0.0-1.5 V) for Li/MeO:X cells. These results have been previously shown in this chapter and in chapter 6.

Figure 7-10 shows that, for a similar matrix, X, Pb will aggregate to larger grain size (figure 7-10 (b)), than Sn (figure 7-10 (d)) and Sb (figure 7-10 (f)). Sb aggregates to the least extent. Differential capacity versus voltage shows that the majority of Pb-Li bonds are broken at a lower energy (figure 7-10 (a)) than Sn-Li bonds (figure 7-10 (c)) and certainly at a lower energy than Sb-Li bonds (figure 7-10 (e)).

In summary, in order for a Me to aggregate (by diffusion) an activation barrier must be overcome. This activation barrier is determined by the potential energy of the surroundings of the atom that is diffusing. The surroundings of the various Me are examined by examining the bond strengths (Me-Me and Me-Li) by two methods; melting points (from the binary Me-Li phase diagrams) and differential capacity versus voltage graphs. It is clear that Sb-Sb and Sb-Li bonds (and therefore activation barriers for diffusion) are higher in energy than those of Sn and Pb, which is evident from melting points and differential capacity. The same is true when comparing Sn to Pb. This qualitative model explains the different aggregation rates in various Li/MeO:X samples that have been studied. More work on a broader range of MeO:X composites (e.g Me = Si, Bi, Al, Cd, Zn, etc.) could pursue this hypothesis further. A second approach, which examines the differences in the onset of the back-reaction between the alloying metal composites, is now discussed.

Figure 7-11 Voltage profiles (first charge) of cells of various metal oxides,
(a) Li/PbO, (b) Li/SnO, and (c) Li/Sb₂O₃

*Figure 7-11 Voltage profiles (first charge) of cells of various metal oxides,
(a) Li/PbO, (b) Li/SnO, and (c) Li/Sb₂O₃*

The capacity axis, which is not important here, is not shown as it is different for each cell. The end of De-alloying as well as the start of Back reaction (to the oxide) is shown for Li/PbO and Li/SnO.
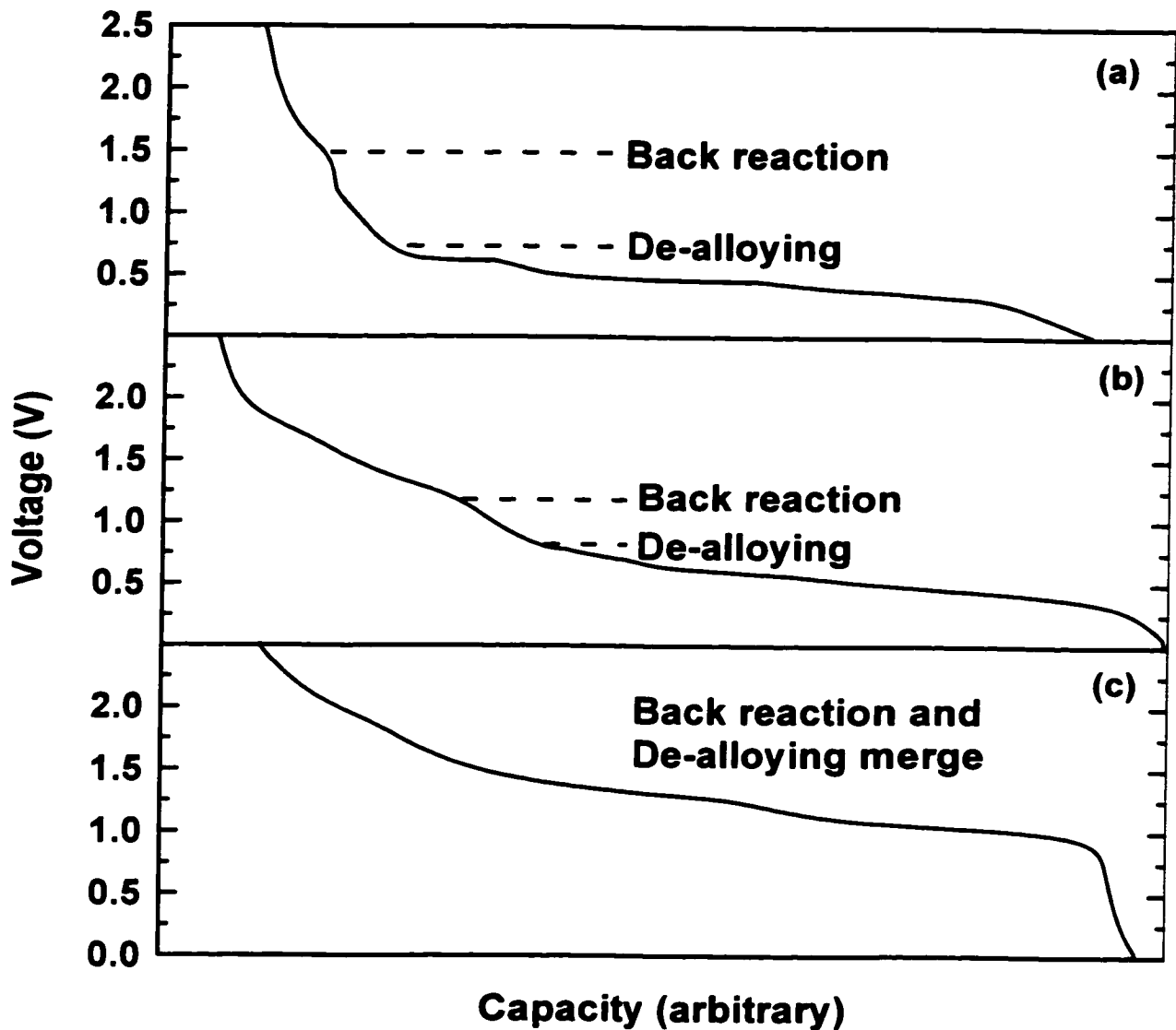
Figure 7-11 shows voltage profiles measured for the first charge of Li/PbO (figure 7-11 (a)), Li/SnO (figure 7-11 (b)) and Li/Sb₂O₃ (figure 7-11 (c)) cells that were discharged and charged using a specific current of 9.3 mA/g, between fixed voltage limits of 0.0 and 2.5

V. The points at which de-alloying ceases and back reaction (to the oxide starting material) commences are indicated for Li/PbO (figure 7-11 (a)) and Li/SnO (figure 7-11 (b)) cells by the horizontal dashed lines. These points are based on the features of the respective voltage profiles and on in-situ ME spectroscopy work.

The difference in voltage between the de-alloying and back reaction is largest for the Li/PbO cell (figure 7-11 (a)), smaller for the Li/SnO cell (figure 7-11 (b)), and indistinguishable for the Li/Sb$_2$O$_3$ cell (figure 7-11 (c)). One reason for the difference in aggregation rates that is now put forth is based on the differences (in voltage) between these reactions for the respective metal oxide. The Pb in the Li/PbO cell has ample time and opportunity to aggregate before the commencement of the back reaction, whereas, the Sb in the Li/Sb$_2$O$_3$ is back reacting concurrently while de-alloying. Presumably, this concurrent back reaction retards aggregation in the case of Sb.

The two speculative explanations that have been put forth to explain the differences in the tendency to aggregate are exactly that, and more work should be done to follow up on these ideas.

"...If it's free, it can't be any good..."

(Ian Courtney, Summer 1998, discussing Linux OS, and life in general.)

Chapter 8

Conclusions

The starting point for the work reported in this thesis was a 200 page patent application (Idota et al., 1996). The patent contained many recipes, but little scientific information. The patent was the product of 8 years of work, by over 50 investigators and with a 100 million dollar investment (Jun Okuda, Divisional Manager, Fuji Photo Film Co., private conversation, January 1998). This may sound like an excuse for not totally understanding every aspect of these new materials – it is, but it is a valid one none-the-less. This work represents the first published scientific explanation for various mechanistic aspects of a new range of anode materials for lithium ion batteries, and it has been useful to many other research groups (e.g. see citations in the meeting abstracts of the 9th International Meeting on Lithium Batteries, 12 July 1998, Edinburgh, Scotland, and in the meeting abstracts of the 194th meeting of the Electrochemical Society, 01 November 1998, Boston, MA). Having said all that, let us summarize what has been learned.

The binary reaction of lithium with alloying metals (e.g., Sn, Pb and Sb) has been thoroughly researched by other groups (e.g., Anani et al., 1982, Wang et al., 1986, and Yang et.al., 1996). Chapter 3 contains a useful summary of the reaction of lithium with tin. The results of an ab-initio calculation of the lithium-tin electrochemical voltage profile is shown in section 3.3. From this, and in conjunction with the XRD experiments (in-situ and ex-situ), it was realized that the Li-Sn binary phase diagram is not followed exactly in the electrochemical reaction of lithium with tin at ambient temperatures. The first two phases of

174

the Li-Sn phase diagram (i.e. Li_2Sn_5 and LiSn) form in ordered crystalline structures. The remaining five phases, however, do not form well-ordered structures. These phases, also called 'lithium-rich' Li-Sn phases, share a BCC substructure, on which clusters of tin tetrahedra are positioned (see section 3.4).

The first cycle reaction mechanism of lithium with SnO is the basis for all of the other Sn-containing materials studied (i.e., SnO:X). This reaction was first surmised from basic thermodynamics considerations (section 4.1) and was confirmed by three independent experimental measurements, notably, electrochemical reaction (section 5.1.1), in-situ x-ray diffraction (section 5.1.2), and in-situ Mössbauer spectroscopy (section 5.1.3). The first lithium insertion (first discharge) causes the reduction of SnO to Sn and Li_2O (see equation 4-1). The remaining Sn is free to alloy with lithium to a stoichiometry of $Li_{4.4}Sn$. This overall reaction is mostly reversible. The $Li_{4.4}Sn$ de-alloys as lithium is removed (charge) to re-form metallic Sn. The reaction proceeds further by the removal of small amounts of lithium from Li_2O at a voltage greater than about 1.0 V during charge. This 'back-reaction' (to the original oxide) was suggested by electrochemical measurements (section 5.1.1), could not be detected in the in-situ XRD experiment (section 5.1.2), but was apparent in the in-situ ME spectroscopy experiment (section 5.1.3). These three experimental techniques were gainfully applied to one particular problem, and as a result, a strong conclusion was obtained.

The first cycle reaction mechanism for Li/SnO cells was extended to include Li/SnO:X (where X is a glass forming oxide that is inert to lithium, such as, B_2O_3, P_2O_5, and SiO_2). The first cycle reaction mechanism is exactly the same, where the X component does not change the basic reaction described above (or see the reaction given in equation 5-3). This reaction was also confirmed by electrochemical measurement (section 5.4), in-situ XRD

(section 5.4.1) and in-situ ME spectroscopy (section 5.4.2).

The reversibility (i.e. subsequent discharges and charges) of these materials as they react with lithium became the focus after chapter 5. Other work, as well as our own, suggested that small grain size alloying material shows better capacity retention than large grain size material. One of the reasons for this is that bulk phase transitions in Li-Sn alloy phases leads to inhomogeneous expansion of grains, which eventually lose morphological integrity, crack (pulverize), and become electrochemically inactive. Small grain size material, on the other hand, leads to homogeneous expansion of grains as lithium is inserted. In this situation, bulk phase transitions are meaningless, and the grains do not pulverize as lithium is added and removed from them. This is discussed and demonstrated in section 6.1. The effects of small grain size material on the experimental measurements that were performed (i.e., XRD, ME and electrochemical measurement) is the subject of chapter 4. It is shown, in section 6.3, that the size of the regions of Sn that are formed during first discharge is proportional to the volume fraction of Sn in the starting material. Those materials with high volume fraction Sn (e.g., SnO and SnO:(0.1/0.1)) produce, during first discharge, larger regions of Sn than those materials with a small volume fraction Sn (e.g. SnO:(0.5/0.5)). The materials that produce that smallest regions of Sn during the first discharge show better capacity retention than those materials that produce the largest regions of Sn on first discharge (see figure 6-9).

Further research showed that these materials (the Sn-containing ones at least) do not have a steady state structural arrangement after the first discharge. The Sn regions that are created during first discharge aggregate to larger and larger cluster size by the repeated discharge and charge of the cell, and, under constrained voltage limits (0.1-0.8 V) and at 30°

C, will eventually reach a steady state Sn-cluster size. This aggregation explains the poor capacity retention of these materials at higher cycle number. A model for the steady state cluster size is proposed in section 6.4. The limiting cluster size (steady state) is based on the initial volume fraction Sn in the glass and a maximum inter-cluster distance, $r \sim 10$ Å. A possible origin of this maximum inter-cluster distance is an electron tunneling distance (section 6.4.2).

The model for steady state aggregate size, however, does not explain how other factors affect the rate of aggregation, notably, increased aggregation with higher temperature (section 6.4.3) and increased rate of aggregation at higher upper voltage limits (section 6.5). The increased rate of aggregation at higher temperature can be understood within the context of a model for diffusion in solids (see section 7.1), but the reason why the Sn aggregates more readily at higher charge voltages is unclear, and could be the subject of future work.

The reaction mechanism of lithium with SnO:X composites is extended to similar composites of other alloying metal oxides, for instance, PbO:X in section 7.2 and Sb_2O_3:X in section 7.3. These types of materials were also noted in the Fuji patent. The first cycle reaction mechanism of lithium with PbO:X is similar to that of lithium with SnO:X, and is given in equation 7-1. The first cycle reaction mechanism of lithium with Sb_2O_3:X is proposed in equation 7-2. This reaction is not well established, however, and could be the focus of future work.

The most intriguing aspect of chapter 7 is that the type of alloying metal (Me, as in MeO:X, Me = Pb, Sn and Sb) apparently controls the rate aggregation of the alloying metal in subsequent cycling. Lead aggregates the fastest, tin next fastest, and antimony aggregates the least. The reason for this is not clear, but some speculative models are proposed (section

7.4).

The first explanation examines the respective Me-Li bond strengths by two methods; melting point temperatures of the Li-Me phase diagrams (table 7-4), and Me-Li bond strength as shown in differential capacity versus voltage (figure 7-10). This explanation assumes that aggregation of the alloying metal will proceed if the metal atoms in smaller clusters can break free in order to diffuse (by hopping) to the larger clusters. In order to break free, the metal must overcome an activation energy barrier (see equation 7-3). This activation barrier is related to the Me-Li bond strength. The aggregation tendency trend (Pb, Sn, Sb) is obvious in the energies of the respective Me-Li bonds.

Another approach examines the onset of the back reaction in the different composites (see figure 7-11). There is a distinct difference (in voltage) when the Li/PbO cell changes from de-alloying to back reaction (figure 7-11 (a)). In the Li/Sb$_2$O$_3$ cell, however, there is no obvious distinction between de-alloying and back reaction (figure 7-11 (c)). The suggestion is that in Sb, the concurrent back reaction retards the aggregation of the alloying metal, whereas in Pb, the alloying metal has ample opportunity and time to aggregate. Both these explanations are highly speculative, and represent a logical starting point for future work.

References

Anani, A., Crouch-Baker, S., and Huggins, R.A., 'Investigation of the Mixed-Conducting Matrix Concept Employing A Ternary Lithium Alloy At Ambient Temperature.', in *Lithium Batteries*, edited by A.N. Day, The Electrochemical Society Proceedings Series, Pennington, NJ, 1987.

Anani, A.A., Crouch-Baker, S., and Huggins, R.A., 'Investigation of a Ternary Lithium Alloy Mixed-Conducting Matrix Electrode at Ambient Temperature.', *Journal of the Electrochemical Society*, 135, 1988, pp 2103-2104.

Ashcroft, N.W. and Mermin, N.D., *Solid State Physics*, Holt, Reinehart and Winston, New York, 1976.

Aydinol, M.K., Kohan, A.F., Ceder, G., Cho, K., and Joannopoulos, J., 'Ab initio study of lithium intercalation in metal oxides and metal dichalcogenides.', *Physical Review B*, 56, 1997, pp 1354-1365.

Besenhard, J.O., Hess, M., and Komenda, P., 'Dimensionally Stable Li-Alloy Electrodes for Secondary Batteries.', *Solid State Ionics*, 40/41, 1990, pp 525-529.

Binder, K. and Landau, D.P., 'Finite-size scaling at first-order phase transitions.', *Physical Review B*, 30, 1984, pp 1477-1485.

Boukamp, B.A., Lesh, G.C., and Huggins, R.A., 'All-Solid Lithium Electrodes with Mixed-Conductor Matrix.', *Journal of the Electrochemical Society*, 128, 1981, pp 725-728.

Butler, P.C. and Klassen, S.E., in *Handbook of Batteries* (2nd edition), edited by D. Linden, McGraw-Hill, New York, 1995.

Collins, G.S., Kachnowski, T., and Benczer-Koller, N., 'Applications of the Mössabuer effect to the characterization of an amorphous tin-oxide system.', *Physical Review B*, 19, 1979, pp 1369-1373.

Courtney, I.A., McKinnon, W.R., and Dahn, J.R., 'On the Aggregation of Tin in SnO Composite Glasses Caused by the Reversible Reaction with Lithium.', *Journal of the Electrochemical Society*, 146, 1999, in press.

Courtney, I.A., Tse, J.S., Mao, Ou, Hafner, J., and Dahn, J.R., 'Ab initio calculation of the lithium-tin voltage profile.', *Physical Review B*, 58, 1998, in press.

Courtney, Ian A. and Dahn, J.R., 'Electrochemical and In Situ X-Ray Diffraction Studies of the Reaction of Lithium with Tin Oxide Composites.', *Journal of the Electrochemical Society*, 144, 1997, pp 2045-2052.

Courtney, Ian A. and Dahn, J.R., 'Key Factors Controlling the Reversibility of the Reaction of Lithium with SnO_2 and Sn_2BPO_6 Glass.', *Journal of the Electrochemical Society*, **144**, 1997, pp 2943-2948.

Cullity, B.D., *X-ray Diffraction*, Addison-Wesley Publishing Company, Inc., Reading, MA, 1967.

Dahn, J.R., Courtney, I.A., and Mao, Ou, 'Short-Range Sn ordering and crystal structure of $Li_{4.4}Sn$ prepared by ambient temperature electrochemical methods.', *Solid State Ionics*, **111**, 1998, pp 289-294.

Dahn, J.R., Py, M.A., and Haering, R.R., *Canadian Journal of Physics*, **60**, 1981, p 307.

Dahn, J.R., von Sacken U., Juzkow, M.W., and Al-Janaby, H., 'Rechargeable $LiNiO_2$/Carbon Cells.', *Journal of the Electrochemical Society*, **138**, 1991, p 2207.

Deiss, E., Wokaun, A., Barras, J.L., Daul, C., and Dufek, P., 'Average Voltage, Energy Density, and Specific Energy of Lithium-Ion Batteries. Calculation Based on First Principles.', *Journal of the Electrochemical Society*, **144**, 1997, pp 3877-3880.

Dollimore, D., Griffiths, D.L., and Nicholson, D., 'The Thermal Decomposition of Oxalates. Part II. Thermogravimetric Analysis of Various Oxalates in Air and in Nitrogen.', *Journal of the Chemical Society*, 1963, pp 2617-2623.

Dunlap, R.A., Small, D.A., McNeil, D.D., Obrovac, M.N., and Dahn, J.R., 'A Mössbauer effect investigation of the Li-Sn system.', to be submitted.

Fauteux, D. and Koksbang, R., 'Rechargeable lithium battery anodes: alternatives to metallic lithium.', *Journal of Applied Electrochemistry*, **23**, 1993, pp 1-10.

Flinn, P.A., 'Tin Isomer Shifts' in *Mössbauer Isomer Shifts*, edited by G.K. Shenoy and F.E. Wagner, North-Holland, New York, 1978.

Frank, U. and Müller, W., 'The Crystal Structure of $Li_{13}Sn_5$.', *Z. Naturforsch. B*, **30**, 1975, pp 316-319.

Frank, U., Müller, W. and Schäfer, H., 'The Crystal Structure of Li_5Sn_2.', *Z. Naturforsch. B*, **30**, 1975, pp 1-5.

Frank, U., Müller, W. and Schäfer, H., 'The Crystal Structure of Li_7Sn_2.', *Z. Naturforsch. B*, **30**, 1975, pp 6-9.

Gladyeshevskii, E.I., Oleksiv, G.I., and Kripyakevich, P.I., 'New examples of the structural type $Li_{22}Sn_5$.', *Soviet Physics-Crystallography*, **9**, 1964, pp 269-271.

Greenwood, N.N. and Gibb, T.C., *Mössbauer Spectroscopy*, Chapman and Hall Ltd., London, 1971.

Ibers and Hamilton, in *International Tables for Crystallography* (4th edition) Volume 4, Kluwer Academic Publishing, Boston, MA, 1996.

Hansen, D.A. and Chang, L.J., 'Crystal Structure of Li_2Sn_5.', *Acta Crysta.*, **B25**, 1969, pp 2392-2395.

Herold, A., *Bull. Soc. Chim. Fr.*, 1955, p. 999.

Hong, L.B., Ahn, C.C., and Fultz, B., 'The Debye temperature of nanocrystalline β-Sn measured by x-ray diffraction.', *Journal of Materials Research*, **10**, 1995, pp 2408-2410.

Hossain, S., in *Handbook of Batteries* (2nd edition), edited by D. Linden, McGraw-Hill, New York, 1995.

Huggins, R.A. and Boukamp, B.A., 'All-solid electrodes with mixed conductor matrix.', *US Patent*, # 4,436,796, 1984.

Idota, Y., Matsufuji, A., Maekawa, Y., and Miyasaki, T., 'Tin-Based Amorphous Oxide, A High Capacity Lithium-Ion Storage Material.', *Science*, **276**, 1997, p 1395

Idota, Y., Nishima, M., Miyaki, Y., Kubota, T., and Miyasaki, T., *Canadian Patent Application*, # 2,134,053, 1994.

Karpov, V.G., 'Ostwald ripening in disordered systems.', *Physical Review B*, **52**, 1995, pp 15846-15853.

Kittel, C., *Introduction to Solid State Physics* (4th edition), John Wiley & Sons, Inc., New York, 1971.

Kresse G. and Hafner, J., 'Ab initio molecular-dynamics simulation of the liquid-metal-amorphous-semiconductor transition in germanium.', *Physical Review B*, **49**, 1994, pp 14251-14269.

Lai, S.L., Guo, J.Y., Petrova, V., Ramanath, G., and Allen, L.H., 'Size-Dependent Melting Properties of Small Tin Particles: Nanocalorimetric Measurements.', *Physical Review Letters*, **77**, 1996, pp 99-102.

Landau, L.D. and Lifshitz, M., *Statistical Physics Part 1* (3rd edition), Pegamon Press, New York, 1993.

Mao, O., Dunlap, R.A., Courtney, I.A., and Dahn, J.R., 'In Situ Mössbauer Effect Studies of the Electrochemical Reaction of Lithium with Mechanically Alloyed Sn_2Fe.', *Journal of the Electrochemical Society*, **145**, pp 4195-4202.

Martin, T.P., Nüher, U., Schaber, H., and Zimmermann, U., 'Evidence for a size-dependent melting of sodium clusters.', *Journal of Chemical Physics*, **100**, 1994, pp 2322-2324.

McKinnon, W.R., PhD Thesis, The University of British Columbia, Vancouver, B.C., 1980.

McKinnon, W.R., in *Solid State Electrochemistry*, edited by P.G. Bruce, Cambridge University Press, London, 1995.

Moffat, W.G., *The Handbook of Binary Phase Diagrams*, Genium Publishing Corp., Schenectady, New York, 1990.

Moreno, M.S. and Mercader, R.C., 'Mössbauer study of SnO lattice dynamics.', *Physical Review B*, **50**, 1994, pp 9875-9881.

Müller, W. and Schäfer, H., 'The Crystal Structure of LiSn.', *Z. Naturforsch. B*, **28**, 1973, pp 246-248.

Müller, W., 'Preparation and Crystal Structure of Li_7Sn_3.', *Z. Naturforsch. B*, **29**, 1974, pp 304-307.

Musgrave M.J.P., 'On the relation between grey and white tin (α-Sn and β-Sn).', *Proceedings of the Royal Society (London):A*, 1962, pp 503-527.

Peters, Kevin F., Cohen, Jerome B., and Chung Yip-Wah, 'Melting of Pb nanocrystals.', *Physical Review B*, **57**, 1998, pp 13430-13438.

Reimers, J.N., 'Can first principles calculations aid in lithium-ion battery design?', *Journal of Power Sources*, **54**, 1995, pp 16-19.

Richard, M.N., Koetschau, I., Dahn, J.R., 'A Cell for In Situ X-Ray Diffraction Based on Coin Cell Hardware and Bellcore Plastic Electrode Technology.', *Journal of the Electrochemical Society*, **144**, 1997, pp 554-557.

Shenoy, G.K., Wagner, F.E., and Kalvius, G.M., 'The Measurement of Isomer Shifts' in *Mössbauer Isomer Shifts*, edited by G.K. Shenoy and F.E. Wagner, North-Holland, New York, 1978.

Shi, Frank G., 'Size dependent thermal vibrations and melting in nanocrystals.', *Journal of Materials Research*, **9**, 1994, pp 1307-1313.

Unruh, K.M., Patterson, B.M., and Shah, S.I., 'Melting behavior of $Sn_x(SiO_2)_{100-x}$ granular metal films.', *Journal of Materials Research*, 7, 1992, pp 214-218.

Wang, Jiqiang, King Paul, and Huggins R.A., 'Investigations of Binary Lithium-Zinc, Lithium-Cadmium and Lithium-Lead Alloys as Negative Electrodes in Organic Solvent-Based Electrolyte.', *Solid State Ionics*, 20, 1986, pp 185-189.

Wang, Jiqiang, Roistrick, I.D., and Huggins, R.A., 'Behavior of Some Binary Lithium Alloys as Negative Electrodes in Organic Solvent-Based Electrolytes.', *Journal of the Electrochemical Society*, 133, 1986, pp 457-460.

Warren, B.E., *X-ray Diffraction*, Addison-Wesley Publishing Company, Inc., Reading, MA, 1969.

Way, B., *Lithium Intercalation in B_zC_{1-z} solid solution*, PhD Thesis, Simon Fraser University, Burnaby, B.C., 1995

Weppner, W. and Huggins, R.A., 'Determination of the Kinetic Parameters of Mixed-Conducting Electrodes and Application to the System Li_3Sb.', *Journal of the Electrochemical Society*, 124, 1977, pp 1569-1578.

Weppner, W. and Huggins, R.A., 'Electrochemical Investigation of the Chemical Diffusion, Partial Ionic Conductivities, and Other Kinetic Parameters in Li_3Sb and Li_3Bi.', *Journal of Solid State Chemistry*, 22, 1977, pp 297-308.

Wyckoff, R.W.G., *Crystal Structures* (2nd edition), volume 1, Kreiger, Florida, 1982.

Yang, Y., Winter, M., and Besenhard, J.O., 'Small particle size multiphase Li-alloy anodes for lithium-ion batteries.', *Solid State Ionics*, 90, 1996, pp 281-287.

Zheng, T., *The Physics and Chemistry of High Capacity Carbonaceous Materials for Lithium-Ion Batteries*, PhD Thesis, Simon Fraser University, Burnaby, B.C., May 1996.